

Heterobimetallic Catalysis:
***E*-Selective Semi-Hydrogenation via Spectroscopic and Theoretical Studies**

BY

Pushpa Malkanthi K. Karunananda
B. Sc., University of Kelaniya, Sri Lanka. 2010

THESIS

Submitted as partial fulfilment of the requirements
for the degree of Doctor of Philosophy in Chemistry
in the Graduate College of the
University of Illinois at Chicago, 2017

Chicago, Illinois

Defense Committee:

Neal Mankad, Chair and Advisor
Vladimir Gevorgyan
Donald Wink
Michael Trenary
Emily Tsui, University of Notre Dame

To my father, my sister and the memory of my mother.....

Acknowledgements

The last five years spent in grad school, has been a truly amazing time for me. Although there were ups and downs, highs and lows, I've had an awesome experience that has helped me grow, and transformed me to be the person I am today. But, none of that would have been possible had it not been for a number of wonderful people who have been there for me. While my words are not enough, this is an attempt to express my gratitude towards them ever so briefly.

Professor Neal Mankad, my advisor, has been a pillar of strength throughout these last years. He has been truly an inspiration to work for, and has a brilliant mind that every time I walk out of his office after a meeting, I feel like I've learned something new and need to learn much more before I see him again. He has guided me throughout my graduate life and given me the freedom to pursue research in which ever the direction my interests have led me. His door has always been open and I have always enjoyed the long conversations we've had on chemistry and science. Thank you, Professor! (I still can't call you Neal)

I would also like to thank the Professors in my thesis committee, Prof. Vladimir Gevorgyan, Prof. Donald Wink, Prof. Michael Trenary and Prof. Emily Tsui for taking the time off from their busy schedules to be there for my thesis defense and for giving me insightful feedback and suggestions.

Prof. Scott Shippy, my graduate advisor has been a great mentor in my time at UIC. I'd like to extend my gratitude towards him for not only being a great professor when I took my first year grad courses, but also for being supportive of me throughout my time here.

Dr. Frank Vazquez has been my mentor in computational chemistry when I first started calculations. He's been great at helping me get out of fixes and has shown me some useful tricks of the trade. Thank you, Frank.

Dr. Dan McElheny has been a great resource with NMR experiments. Thank you, Dan for all the help with my kinetic experiments and results analysis.

I have also had the pleasure of working with some collaborators during my graduate years. I have especially enjoyed my time at the beamline with the synchrotron at Argonne National Laboratory. Thank you Dr. Soma Chattopadhyay and Dr. Tomohiro Shibata for all the help with the XANES analysis. I would also like to extend my thanks to Prof. Ercan Alp and Dr. Wenli Bi for their contribution on Mössbauer Spectroscopy. Another group of collaborators I would like to thank is the Ess group at Brigham Young University. Thank you Prof. Dan Ess and Ying Zhang for those cool calculations that you did on our heterobimetallic chemistry.

During the last five years, I was fortunate enough to work alongside a fantastic group of lab mates in the Mankad group. A special thank you goes out to our first postdoc, Dr. Upul Jayarathne. Thank you Upul, for teaching me how to work in an inorganic lab when I've had no prior experience and for training me to work independently. Thank you, Dr. Dominic Pye, Dr. Lijie Cheng and Dr. Chia-Wei Hsu for helping me get my thesis in shape. A special shout out goes to Dr. Brittany Johnson, Dr. Tom Mazzacano and soon-to-be-Dr.s Sharareh Bagherzadeh & Greyson Waldhart, my fellow batch mates from the first class of students in the Mankad group. It's been awesome setting up the lab and growing up with you over the years. Thank you, Brittany for teaching me about life in the US and for always keeping us in good spirits. It's always fun to be around you. I miss sitting next to you already. Thank you very much, Sheri for being a dear friend all these years. You're one of the kindest people I've ever met. I'm going to miss going out for coffee with you and all our random conversations. Thank you Greyson for always having my back. I'm going to miss you my friend, and your delicious pizzas. Thanks Tom for keeping us all in line and for your brotherly sense of humor. Thank you, Noel, Suresh and Siling for all the help around the lab. Siling, I'm really going to miss you, my sweet friend and our dinner conversations with Kyle. Good luck in Irvine, Kyle. Best of luck to the new members of the group, Antonio, Rickey

and Dibbendu as well. I would also like to thank former members of the group, Dr. Suparna Banerjee and Sean Parmelee who has worked hard and co-authored papers with me.

Another group of people who has been tremendously supportive has been the staff at the department of Chemistry at UIC. I would especially like to thank Rhonda Staudohar who has been my go to person since day one. Thank you for being so patient with all my silly little inquiries Rhonda. You've always been kind to me. Thank you, Silvia, Maggie, Nilo, Shirley, Jennifer, Tanya, Frances, Randy, Miranda and Don for helping me out in numerous ways.

I'd also like to give my thanks to my dear friends who have helped get me through grad school. A special thanks goes out to Erwin, Bhagya and Ayesha, my former roommates and dear friends. Thank you guys, for sticking by me since my undergrad years in our home country, Sri Lanka. I'm going to miss all the late-night card games, dinner parties, your delicious cooking and most of all, waking up to your music in the morning. Another person who misses that music already is Angeliki Papathanasiou, my dear friend in grad school. Thank you, Angel, for all your help with my school work and for always being there. You're the first friend I made in grad school and a keeper at that. Thank you, Dhanushka ayya, for always believing in me and encouraging me. I miss you, brother. And two people that have always been there for me in the last few years are my dearest friends, Dr. Shyamalee Dassanayake and Dr. Sujeewa Piyankarage. Thank you, akka and ayya, for welcoming me to Chicago and making me feel at home here. I've always enjoyed your company and appreciated your guidance. You've been my family away from home and I look forward to more adventures with you as we go through life.

Of course, none of my achievements would have been possible if not for the love and the support of my family here and back home. A special thank you goes to my uncle, Dr. Muthu Wijesundara, an alumnus of UIC for travelling to Chicago, to first get me settled in and for constantly checking in and being there for me. Thank you, bappa. My aunt and uncle in California, Lalitha and Sunny Chandrasena have always had their door open for me over the years. Thank

you chutti amma and bappa for everything. A special thank you goes out to my two aunts, Visakha and Tikiri Garihagama. Thank you, dearest loku amma and kiri loku amma. I cannot put in to words how much strength you've given me over the years. You've always been the biggest motivators I've had and your unconditional love and unwavering faith in my abilities has been my biggest strength, not only in grad school, but also in life.

Finally, my deepest and heartfelt gratitude goes out to my sister, my father and my late mother for their unconditional love and support over the years. Thank you, darling sis, you've always been my best friend and hearing your voice, even for a few minutes, makes my day brighter. My father has always been the biggest inspiration of my life. Thank you, dearest Appachchi! Everything I am today is because of you and any good there is in me, it all came from you. Dearest Amma, even though you're not here to see me today, you've always believed in me and knew that I would get here, even when I didn't. This is for you. Thank you!

Contribution of Authors

Chapter one is adapted and reproduced in part from the just accepted manuscript, Cooperative Strategies for Catalytic Hydrogenation of Unsaturated Hydrocarbons, Karunananda, M. K.; Mankad, N. P. *ACS Catal.*, **2017**, DOI: 10.1021/acscatal.7b02203. I was the primary author of this article and Prof. N. P. Mankad contributed to the preparation of the manuscript.

Chapter two is adapted and reproduced in part from the published manuscript, Experimental Determination of Redox Cooperativity and Electronic Structures in Catalytically Active Cu-Fe and Zn-Fe Heterobimetallic Complexes, Karunananda, M. K.; Vázquez, F. X.; Alp, E. E.; Bi, W.; Chattopadhyay, S.; Shibata, T.; Mankad, N. P. *Dalton Trans.* **2014**, 43, 13661-13671, DOI: 10.1039/c4dt01841a. I was the primary author of this article and synthesized the complexes studied and conducted the sample preparations for spectroscopic measurements. Dr. F. X. Vázquez calculated the Mössbauer parameters using DFT calculations. The optimization of the structures and the rest of the DFT calculations along with the IR spectroscopic experiments were carried out by me. Prof. E. E Alp and Dr. W. Bi carried out the data collection in Mössbauer experiments and aided with the results analysis. Dr. S. Chattopadhyay and Dr. T. Shibata carried out the data collection in XANES experiments and helped with the results analysis. Prof. N. P. Mankad contributed to the preparation of the manuscript.

Chapter three is adapted and reproduced in part from two published manuscripts. The first manuscript is Experimental and Computational Characterization of the Transition State for C-X Bimetallic Oxidative Addition at a Cu-Fe Reaction Center, Karunananda, M. K.; Parmelee, S. R.; Waldhart, G. W.; Mankad, N. P. *Organometallics*. **2015**, 34, 3857-3864, DOI:10.1021/acs.organomet.5b00476. I was one of the co-first authors and conducted computational characterization in the manuscript. S. R. Parmelee conducted the experimental characterization. Prof. N. P. Mankad contributed to the preparation of the manuscript. The second

manuscript is Synthesis and Characterization of Heterobimetallic Complexes with Direct Cu-M Bonds (M = Cr, Mn, Co, Mo, Ru, W) Supported by N-Heterocyclic Carbene Ligands: A Toolkit for Catalytic Reaction Discovery, Banerjee, S.; Karunananda, M. K.; Bagherzadeh, S.; Jayarathne, U.; Parmelee, S. R.; Waldhart, G. W.; Mankad, N. P. *Inorg. Chem.* **2014**, 53, 11307-11315., DOI: 10.1021/ic5019778. I was one of the co-first authors and conducted the entire computational characterization and analysis in the manuscript. The synthesis and the experimental characterization was carried out by Dr. S. Banerjee, S. Bagherzadeh, Dr. U. Jayarathne, S. R. Parmelee, and G. W. Waldhart. Prof. N. P. Mankad contributed to the preparation of the manuscript. The bimetallic N₂O activation section, was based off a manuscript that we prepared, but never published. The initial catalytic experiments were carried out by S. R. Parmelee. The computational analysis was done by me. Prof. N. P. Mankad contributed to the preparation of the manuscript.

Chapter four is adapted and reproduced in part from the published manuscript, *E*-Selective Semi-Hydrogenation of Alkynes by Heterobimetallic Catalysis, Karunananda, M. K.; Mankad, N. P. *J. Am. Chem. Soc.* **2015**, 137, 14598-14601. DOI: 10.1021/jacs.5b10357. I was the primary author of this article and conducted all the experiments and calculations. Prof. N. P. Mankad contributed to the preparation of the manuscript.

Chapter five is adapted and reproduced in part from the published manuscript, Heterobimetallic H₂ Addition and Alkene/Alkane Elimination Reactions Related to the Mechanism of *E*-selective Semi-Hydrogenation, Karunananda, M. K.; Mankad, N. P. *Organometallics* **2017**, 36, 220-227. DOI: 10.1021/acs.organomet.6b00356. I was the primary author of this article and conducted all the experiments and calculations. Prof. N. P. Mankad contributed to the preparation of the manuscript. The kinetic section consists of unpublished results on kinetic experiments conducted by me. The calculations mentioned in this section were done by a graduate student, Ying Zhang in Prof. Daniel H. Ess's group in Brigham Young University.

Table of Contents

	Page
Acknowledgements.....	iii
Contribution of Authors.....	vii
Table of Contents.....	ix
List of Tables.....	xiii
List of Figures.....	xv
List of Schemes.....	xix
List of Abbreviations.....	xxiii
Summary.....	xxvii
 1. Introduction.....	 1
1.1. Opening Remarks.....	2
1.2. Evolution of C-C Hydrogenation Reactions with the Development of Cooperative Catalyst Paradigms.....	3
1.2.1. Single Site Strategy.....	6
1.2.2. Cooperative Strategies.....	9
1.2.2.1. Metal-Ligand Cooperativity.....	9
1.2.2.1.1. Metal-Base Cooperativity.....	10
1.2.2.1.2. Metal-Acid Cooperativity.....	17
1.2.2.2. Frustrated Lewis Acid-Base Pair Cooperativity.....	19
1.2.2.3. Bimetallic Cooperativity.....	26
1.3. Heterobimetallic Catalysts as a Cooperative Strategy by Mankad Group....	28
1.3.1. Potential for Hydrogenation Reactions.....	32
1.4. Research Goals.....	34
 2. Experimental Determination of Redox Cooperativity and Electronic Structure in Catalytically Active Cu–Fe and Zn–Fe Heterobimetallic Complexes.....	 36
2.1. Opening Remarks.....	37
2.2. Introduction.....	37

Table of Contents (continued)

2.3. Results & Discussion.....	41
2.3.1. Mössbauer Spectroscopy.....	42
2.3.2. X-Ray Absorption Spectroscopy.....	50
2.3.2.1. Cu K-Edge Spectroscopy.....	50
2.3.2.2. Zn K-Edge Spectroscopy.....	53
2.3.2.3. Fe K-Edge Spectroscopy.....	56
2.3.3. Elucidation of Redox Cooperativity.....	59
2.4. Conclusions.....	62
2.5. Experimental Procedures.....	63
2.5.1. Synthesis.....	63
2.5.1.1. General Considerations.....	63
2.5.1.2. Preparation of $[K(18\text{-crown-}6)_2]^+[\text{Fp}]^-$	63
2.5.2. Mössbauer Spectroscopy.....	64
2.5.3. Computational Methods.....	64
2.5.4. X-Ray Absorption Spectroscopy.....	65
3. Theoretical Investigations of the Structure and Reactivity of Heterobimetallic complexes.....	67
3.1. Opening Remarks.....	68
3.2. Bimetallic Oxidative Addition.....	68
3.2.1. Introduction.....	68
3.2.2. Results & Discussion.....	70
3.2.3. Conclusions.....	75
3.3. Bimetallic N_2O Activation.....	75
3.3.1. Introduction.....	75
3.3.2. Results & Discussion.....	78
3.3.3. Conclusions.....	83
3.4. Key Functional Components of Heterobimetallic Catalysts.....	83
3.5. Development and Characterization of a Toolkit of Heterobimetallics.....	84
3.5.1. Introduction.....	84
3.5.2. Results & Discussion.....	86
3.5.3. Conclusions.....	94
3.6. Computational Methods	95

Table of Contents (continued)

4. <i>E</i>-selective Semi-Hydrogenation of Alkynes by Heterobimetallic Catalysis.	98
4.1. Opening Remarks.....	99
4.2. Introduction.....	99
4.3. Results & Discussion.....	103
4.3.1. Catalyst Screening Using Thermodynamic Calculations.....	103
4.3.2. Catalyst Optimization.....	105
4.3.3. Hydrogenation Mechanism	108
4.3.4. Time-Dependent Robustness Screening.....	111
4.4. Conclusions.....	113
4.5. Experimental Procedures.....	113
4.5.1. General Considerations.....	113
4.5.2. Physcial Measurements.....	114
4.5.3. Computational Methods.....	114
4.5.4. Synthesis of Catalysts.....	115
4.5.4.1. (IMes)AgRp.....	115
4.5.4.2. (IPr)AgRp.....	116
4.5.4.3. (IMes)AgFp.....	117
4.5.5. General Procedure of Catalyst Optimization.....	117
4.5.6. General Procedure for Catalytic Semi-Hydrogenation of Alkynes by (IMes)AgRp.....	118
4.5.7. General Procedure for the Akene Isomerization.....	119
4.5.8. Procedure for the Control of the Alkene Isomerization.....	119
4.5.9. General Procedure for the Robustness Screen Using Additives.....	120
5. Mechanistic Investigations into <i>E</i>-selective Semi-Hydrogenation of Alkynes by Heterobimetallic Catalysis.....	121
5.1. Opening Remarks.....	122
5.2. Introduction.....	122
5.3. Results & Discussion.....	126
5.3.1. Control Experiments and Catalyst Decomposition.....	126
5.3.2. Bimetallic H ₂ Activation.....	128
5.3.3. Alkene/Alkane Elimination and Selectivity Effects.....	139
5.3.4. Kinetic Studies.....	143
5.3.4.1. Potential for Cheaper Hydrogenation Catalyst Development..	145
5.4. Conclusions.....	147
5.5. Experimental Procedures.....	148

Table of Contents (continued)

5.5.1. General Considerations.....	148
5.5.2. Physical Measurements.....	149
5.5.3. Computational Methods.....	149
5.5.4. Preparation of HRp.....	150
5.5.5. Preparation of HRuCp(CO)(IMes).....	150
5.5.6. Catalytic Trials.....	151
5.5.7. Preparation of 4.....	151
5.5.8. Alkene/Alkane Elimination Reactions with HRp.....	152
5.5.9. General Procedure for the Kinetic Runs.....	152
5.5.10. Preparation of (6Dipp)Cu-Rp.....	153
6. Conclusions and Current/Future Directions.....	154
6.1. Conclusions.....	155
6.2. Current/Future Directions.....	156
6.2.1. Trapping Intermediates of hydrogenation to Develop Bifunctional Reactions.....	156
6.2.1.1. CO ₂ activation.....	157
6.2.1.2. Hydro-Carboxylation of Alkynes.....	159
6.2.2. Hydrogenation of Unsaturated C=E (E = C, O, N) Double Bonds.....	162
6.3. Concluding Remarks.....	163
References.....	164
Appendix.....	185
Copyright Permissions.....	190
Vita	198

List of Tables

Table		Page
Table 1:	Mössbauer parameters for Fp-X complexes as a function of X.....	44
Table 2:	Calculated Mössbauer parameters predicted by DFT.....	47
Table 3:	Asymmetry parameters for CO ligands determined experimentally and computationally.....	48
Table 4:	Cu K-Edge data.....	51
Table 5:	Zn K-Edge data.....	54
Table 6:	Fe K-Edge data.....	56
Table 7:	Experimentally determined bimetallic cooperativity during oxidative addition.....	60
Table 8:	Computed partial charges during bimetallic oxidative addition.....	61
Table 9:	Calculated natural charges along the reaction coordinate.....	73
Table 10:	Selected Wiberg and Mayer bond index values along the reaction coordinate.....	74
Table 11:	Calculated and experimental bond distances for (IMe)Cu-[M] model complexes.....	87
Table 12:	Calculated and experimental vibrational frequencies for (IMe)Cu-[M] model complexes.....	88
Table 13:	Calculated charges (<i>q</i>) from natural population analysis for (IMe)Cu- MCp _n (CO) _m model complexes.....	91
Table 14:	Calculated charges (<i>q</i>) for Cp and CO ligands from natural population analysis for (IMe)Cu-[M] model complexes.....	92
Table 15:	Wiberg bond indices for (IMe)Cu-MCp _n (CO) _m model complexes.....	93
Table 16:	Thermodynamics for H ₂ activation by (NHC)Cu-[M].....	104

List of Tables (continued)

Table		Page
Table 17:	Alkyne semi-hydrogenation catalyst optimization.....	106
Table 18:	Alkyne semi-hydrogenation by (IMes)Ag-Rp.....	107
Table 19:	Alkene isomerization studies.....	110
Table 20:	Alkyne semi-hydrogenation catalyst optimization.....	112
Table 21:	Ag-free and Ru-free control experiments.....	127
Table 22:	Kinetic parameters for hydrogenation by (IMes)M-Rp; (M=Cu, Ag).....	145
Table 23:	Catalytic hydrogenation of alkynes.....	147
Table A1:	Deconvolution parameters used for XAS spectra analysis using Athena software.....	187

List of Figures

Figure		Page
Figure 1:	Mössbauer data (black) and fit (red) for (IPr)Cu-Fp.....	43
Figure 2:	Cu \rightarrow Fe π -backdonation evident in calculated HOMO and HOMO-1 of a model (NHC)Cu-Fp complex. Calculated surfaces (0.04 isocontours).....	46
Figure 3:	Cu K-edge spectra for (a) (IPr)CuCl (red), (IMes)CuCl (blue), IPrCuI (green) (b) (IPr)Cu-Fp (blue), (IMes)Cu-Fp (red) and (IPr)Cu-Mp (green)	52
Figure 4:	(a) Zn K-edge spectra for Zn foil (dashed black), anhydrous ZnCl ₂ (dashed blue), (IPr)ZnCl ₂ .THF (solid red), (IPr)(Cl)Zn-Fp (solid green) (b) First derivative Zn K-edge spectra for (IPr)ZnCl ₂ .THF (red) and (IPr)(Cl)Zn-Fp (green).....	55
Figure 5:	Fe K-edge spectra for (a) FpI (pink), KFp (blue), FpMe (orange), Fp ₂ (green) (b) (IPr)Cu-Fp (pink), (IPr)(Cl)Zn-Fp (green), (IMes)Cu-Fp (blue).....	57
Figure 6:	First derivative of Fe K-edge spectra for KFp (red), FpI (blue) and Fp ₂ (green).....	58
Figure 7:	a) Calculated reaction coordinate diagram for reactants (IMe)Cu-Fp + CH ₃ Cl to products (IMe)Cu-Cl + Fp-CH ₃ with relative free energies given in kcal/mol at 298 K. b) Structure of TS1.....	72

List of Figures (continued)

Figure		Page
Figure 8:	Intermediates of N ₂ O activation by (IMe)Cu-Fp B) μ -1,1-N isomer C), μ -1,3-N,O isomer D) μ -1,2-N,N isomer E) N ₂ dissociated (IMe)Cu(μ -O)Fp species modelled by DFT calculations. Bond distances are shown in angstroms, and all displayed angles refer to \angle N-N-O. Color code: C, grey; H, white; Cu, bronze; Fe, orange; N, blue; O, red.....	79
Figure 9:	Reaction energy profile, determined by DFT modelling.....	80
Figure 10:	Calculated reaction coordinate diagram for reactants (IMe)Cu-Fp (A) + N ₂ O to (IMe)Cu-(μ -O)Fp (E) + N ₂ through transition state TS3 with relative free energies given in kcal/mol in 298 K.....	81
Figure 11:	Orbital surface for the LUMO of E calculated by DFT (0.04 isovalue)....	82
Figure 12:	a) Two independent (IPr)Cu-Wp molecules found in the same asymmetric unit, depicted as 50 % probability thermal ellipsoids. Hydrogen atoms and co-crystallized solvent molecules have been omitted ⁷⁵ . b) Optimized structures of (IMe)Cu-Wp and (IMe)Cu-Mc determined by density functional theory (DFT) energy minimization (BVP86/LANL2TZ(f)/6-311+G(d)).....	89
Figure 13:	Frontier molecular orbital diagram calculated for (IMe)Cu-Mc (BVP86/LANL2TZ(f)/6-311+G(d), 0.04 isocontours). In this case, the HOMO and HOMO-2 orbitals possess Cu-Mn π^* character, the HOMO-1 orbital possesses Cu-Mn σ character, the LUMO (not shown) does not involve Cu-Mn or Cu-CO interactions, and the LUMO+1 exhibits Cu-CO through-space overlap.....	90

List of Figures (continued)

Figure		Page
Figure 14:	a) Hypothetical mechanism for alkyne semi-hydrogenation by (NHC)M'-[M] catalysts (M = Fe or Ru, M' = Cu or Ag, L = IPr or IMes). b) Transition state for H ₂ activation TS4 by (IMe)Cu-Rp calculated by DFT.....	108
Figure 15:	Computational modeling of the reaction between (IMe)-CuRp and H ₂ . a) Relative energies of the structures from the intrinsic reaction scan that were analyzed for this study b) Transition state structure TS4, with key inter-nuclear distances labeled in units of Å. // = discontinuity.....	131
Figure 16:	Selected inter-nuclear distances for the reaction between (IMe)-CuRp and H ₂ , plotted along the calculated intrinsic reaction coordinate scan. // = discontinuity.....	132
Figure 17:	Selected Wiberg bond index values for the reaction between (IMe)-CuRp and H ₂ , plotted along the calculated intrinsic reaction coordinate scan. // = discontinuity.....	133
Figure 18:	Selected natural charge values derived from natural population analysis for the reaction between (IMe)-CuRp and H ₂ , plotted along the calculated intrinsic reaction coordinate scan. // = discontinuity.....	134
Figure 19:	Selected NBO occupancy values for the reaction between (IMe)-CuRp and H ₂ , plotted along the calculated intrinsic reaction coordinate scan. Lewis occupancies of the H ₂ bonding and antibonding NBOs and of a key Cu acceptor NBO are plotted on the left axis. Total non-Lewis occupancy of the system is plotted on the right axis. // = discontinuity.....	136

List of Figures (continued)

Figure		Page
Figure 20:	Surface plots (0.04 isovalues) of the LP*1(Cu) (left) and BD(Cu-Ru) (right) NBOs in R that are crucial acceptor and donor orbitals, respectively, for bimetallic H ₂ cleavage. For clarity, the distant H ₂ molecule has been omitted from the images.....	137
Figure A1:	IR Spectrum of [K(18-crown-6) ₂][Fp].....	185
Figure A2:	Deconvoluted Cu K-edge spectrum for (IPr)CuFp.....	186
Figure A3:	Deconvoluted Cu K-edge spectrum for (IMes)CuFp.....	186
Figure A4:	Deconvoluted Cu K-edge spectrum for (IPr)CuMp.....	187
Figure A5:	Sample stacked plot for the kinetic run for the hydrogenation of diphenylacetylene by (IMes)AgRp: Y2 = Disappearance of monitored peak for diphenylacetylene and Y3 = Appearance of the monitored peak for <i>E</i> -stilbene.....	188
Figure A6:	Sample concentration vs time plot for the kinetic run for the hydrogenation of diphenylacetylene by (IMes)AgRp: Time per one experiment = 30 s.....	189

List of Schemes

Scheme		Page
Scheme 1:	Evolution of H-H activation modes with cooperative strategies.....	5
Scheme 2:	Orbital interactions during single-site H ₂ activation.....	6
Scheme 3:	Olefin hydrogenation by Wilkinson's catalyst.....	7
Scheme 4:	Olefin hydrogenation by Schrock-Osborn catalyst.....	8
Scheme 5:	Olefin hydrogenation by Crabtree's catalyst.....	8
Scheme 6:	Orbital interactions during H ₂ activation with metal-base cooperativity	10
Scheme 7:	Hydrogenation by Shvo's catalyst.....	11
Scheme 8:	<i>E</i> -selective semi-hydrogenation of alkynes by Milstein's catalyst.....	11
Scheme 9:	Iron catalyzed hydrogenation of alkenes by Jones's catalyst.....	12
Scheme 10:	a) Nickel b) cobalt catalyzed hydrogenation of alkenes by Hanson and co-workers.....	13
Scheme 11:	Zirconium catalyzed hydrogenation by Erker and co-workers.....	14
Scheme 12:	Rhenium catalyzed olefin hydrogenation by Ison and co-workers.....	16
Scheme 13:	Orbital interactions during H ₂ activation with metal-acid cooperativity..	17
Scheme 14:	Cobalt and Nickel catalyzed alkene hydrogenation by Peters and co-workers.....	18
Scheme 15:	Ruthenium catalyzed <i>Z</i> -selective semi-hydrogenation of alkynes by Szymczak and co-workers.....	19
Scheme 16:	Reversible H ₂ activation by FLPs by Stephan and co-workers.....	20
Scheme 17:	Orbital interactions during H ₂ activation with FLP cooperativity.....	20
Scheme 18:	Olefin hydrogenation by FLPs by Paradies, Grimm, Stephan and co-workers.....	21
Scheme 19:	Alkyne hydrogenation using FLPs by Repo and co-workers.....	22

List of Schemes (continued)

Scheme		Page
Scheme 20:	<i>Z</i> -selective semi-hydrogenation of alkynes by Du and co-workers.....	23
Scheme 21:	Hydrogenation of electron poor alkynes and alkenes.....	24
Scheme 22:	Hydrogenation of <i>tert</i> -butylaniline by Stephan and co-workers.....	25
Scheme 23:	Hydrogenation of a) pyridines by Du and co-workers b) <i>N</i> -heterocycles and c) polyaromatics by Stephan and co-workers.....	26
Scheme 24:	<i>E</i> -selective semi-hydrogenation of alkynes by Williams and co-workers	27
Scheme 25:	Zirconium and iridium catalyzed hydrogenation by Bergman and co-workers.....	27
Scheme 26:	Olefin hydrogenation by Lu and co-workers.....	28
Scheme 27:	Heterobimetallic cooperative strategy to mimic bimetallic oxidative addition by Mankad and co-workers.....	30
Scheme 28:	Heterobimetallic C-H borylation by Mankad and co-workers.....	31
Scheme 29:	Heterobimetallic CO ₂ reduction by Mankad and co-workers.....	32
Scheme 30:	Proposed a) heterolytic H ₂ activation by heterobimetallic complexes b) catalytic cycle for C-C bond hydrogenations.....	34
Scheme 31:	Bimetallic oxidative addition using Pd complexes by a) Ritter and co-workers b) Ozerov and co-workers.....	38
Scheme 32:	Bimetallic oxidative addition by Chan and co-workers.....	39
Scheme 33:	Bimetallic oxidative addition by Uyeda and co-workers.....	39
Scheme 34:	Heterobimetallic reactivity during catalysis.....	40
Scheme 35:	Heterobimetallic cooperative strategy to mimic bimetallic oxidative addition by Mankad and co-workers.....	41

List of Schemes (continued)

Scheme		Page
Scheme 36:	Representative fragment abbreviations.....	42
Scheme 37:	Bimetallic oxidative addition of MeCl.....	70
Scheme 38:	Proposed homobimetallic N ₂ O binding to Cu-containing actives sites..	77
Scheme 39:	Hypothetical catalytic scheme for N ₂ O activation.....	78
Scheme 40:	Synthesis of (NHC)Cu-[M] complexes.....	85
Scheme 41:	<i>Z</i> -selective semi-hydrogenation of alkynes by Lindlar and co-workers.	101
Scheme 42:	<i>E</i> -selective semi-hydrogenation of alkynes by Fürstner and co-workers	101
Scheme 43:	<i>E</i> -selective semi-hydrogenation of alkynes by Fout and co-workers....	102
Scheme 44:	<i>E</i> -selective semi-hydrogenation of alkynes by Mashima and co-workers.....	102
Scheme 45:	Hypothetical mechanism for alkene isomerization under hydrogenation conditions by (NHC)M'-[M] catalysts.....	111
Scheme 46:	Orbital interactions during H ₂ activation.....	124
Scheme 47:	Possible orbital interactions during bimetallic H ₂ activation.....	125
Scheme 48:	<i>E</i> -selective semi-hydrogenation of alkynes.....	125
Scheme 49:	Experimental evidence for heterobimetallic H ₂ activation.....	129
Scheme 50:	Transition states and orbital interactions involved in a) monometallic and b) bimetallic H ₂ addition.....	138
Scheme 51:	a) Proposed alkyne hydrogenation mechanism b) Model alkene elimination reaction.....	139
Scheme 52:	a) Proposed alkene isomerization mechanism b and c) Model alkene vs alkane elimination.....	141

List of Schemes (continued)

Scheme		Page
Scheme 53:	Calculated rate limiting steps for the catalytic cycle of alkyne semi-hydrogenation by (IMe)M-[RuCp(CO) ₂] catalysts.....	144
Scheme 54:	a) Stable [(6Dipp)Cu-H] ₂ reported by Sadighi group b) Analogous heterobimetallic catalyst (6Dipp)Cu-Rp.....	146
Scheme 55:	Trapping intermediates of hydrogenation for bifunctional reactions.....	157
Scheme 56:	Proposed CO ₂ insertion step in the catalytic cycle of CO ₂ hydrogenation by Appel and co-workers.....	158
Scheme 57:	Reversible CO ₂ insertion into a Cu-C bond by Sadighi and co-workers	158
Scheme 58:	Potential CO ₂ trapping pathways.....	159
Scheme 59:	Hydrocarboxylation of alkynes by heterobimetallic catalysts.....	160
Scheme 60:	Hydrocarboxylation of alkynes by Tsuji and co-workers.....	160
Scheme 61:	Hydrocarboxylation of alkynes by Ma and co-workers.....	161
Scheme 62:	Hydrocarboxylation of alkynes by Martin and co-workers.....	161
Scheme 63:	Proposed heterobimetallic hydro-functionalization reactions.....	162

List of Abbreviations

6Dipp	1,3-bis(2,6-isopropylphenyl)-3,4,5,6-tetrahydropyrimidin-2-ylidene
7Dipp	1,3-bis(2,6-isopropylphenyl)-4,5,6,7-tetrahydro-1,3-diazepin-2-ylidene
Å	Angstrom
BAr ^F	tetrakis[3,5-bis(trifluoromethyl)phenyl]borate
BD	Bonding
BINAP	2,2'-Bis(diphenylphosphino)-1,1'-binaphthyl
BOA	Bimetallic Oxidative Addition
BRE	Bimetallic Reductive Elimination
cat	catalyst
Cc	Co(CO) ₄
cod	1,5-Cyclooctadiene
Cp	cyclopentadienyl
Cp*	Pentamethylcyclopentadienyl
Crp	CrCp(CO) ₃
Cy	Cyclohexyl
d	doublet
DFT	Density Functional Theory
diphos	1,2-Bis(diphenylphosphino)ethane
DMF	Dimethyl Formamide
<i>E</i>	<i>trans</i>
ECP	effective core potentials
equiv	equivalent
eu	entropy unit
eV	electron Volt

List of Abbreviations (continued)

FLP	Frustrated Lewis Pairs
Fp	$\text{FeCp}(\text{CO})_2$
FSR	Formal Shortness Ratio
FT-IR	Fourier Transform Infra Red
h	hours
HOMO	Highest Occupied Molecular Orbital
IMe	<i>N,N</i> -dimethylimidazol-2-ylidene
IMes	<i>N,N'</i> -bis(2,4,6-trimethylphenyl)imidazol-2-ylidene
iPr	isopropyl
IPr	<i>N,N</i> -bis(2,6-diisopropylphenyl)-imidazol-2-ylidene
IR	Infra-Red
IRC	Intrinsic Reaction Coordinate
<i>J</i>	NMR coupling constant
K	Kelvin
K _a	Acid dissociation constant
kcal	Kilocalorie
KIE	Kinetic Isotope Effect
LP	Lone Pair
LUMO	Lowest Unoccupied Molecular Orbital
<i>m</i> -	<i>meta</i>
Mc	$\text{Mn}(\text{CO})_5$
Me	Methyl
Mes	Mesityl
MHz	Mega Hertz

List of Abbreviations (continued)

mL	milliliter
mm	millimeter
Mp	MoCp(CO) ₃
NBD	norbornadiene
NBO	Natural Bond Orbital
NHC	N-heterocyclic carbene
N _{His}	Histidine
NMR	Nuclear Magnetic Resonance
<i>o</i> -	<i>ortho</i>
OA	Oxidative Addition
<i>p</i> -	<i>para</i>
Ph	Phenyl
pin	pinacol
pK _a	-log ₁₀ K _a
PNP	Phosphorus Nitrogen Phosphorus
py	pyridine
<i>q</i>	charge
Q	quadrupole moment
<i>rac</i>	racemic
RE	Reductive Elimination
Rp	RuCp(CO) ₂
RT	Room Temperature
s	singlet

List of Abbreviations (continued)

s^{-1}	per second
sept	septet
t	triplet
^t Bu	tertbutyl
THF	Tetrahydrofuran
triphos	Bis(diphenylphosphinoethyl)phenylphosphine
TS	Transition State
UV	Ultra Violet
WBI	Wiberg Bond Index
Wp	WCp(CO) ₃
XANES	X-Ray Absorption Near-Edge Spectroscopy
XAS	X-Ray Absorption Spectroscopy
Z	cis
//	discontinuity
ΔE_Q	quadrupole splitting
°	degree
‡	Transition State
α	asymmetry parameter
δ	Isomer shift
δ	Chemical shift
η	electric field gradient asymmetry parameter
ν	Frequency
ρ	reaction constant

Summary

The reaction development of *E*-selective semi-hydrogenation of alkynes by heterobimetallic catalysis is presented in this thesis.

Chapter one provides a background on homogeneous hydrogenation reactions of unsaturated hydrocarbons and highlights how switching to cooperative strategies from the classical single-site metal strategy has given rise to the development of rare selectivity modes and the use of non-precious catalyst elements. The potential of employing heterobimetallic catalysts developed by the Mankad group for catalytic hydrogenation is discussed.

To design catalysts methodically using this strategy, it is vital to gain insight about the structure and function of these heterobimetallic complexes. The next two chapters provide an experimental and a theoretical analysis of the heterobimetallic complexes.

Chapter two probes the electronic structure and the function of heterobimetallic complexes using XANES, IR and Mössbauer spectroscopy. Bimetallic oxidative addition is studied extensively using these spectroscopic techniques and the individual roles of the metals and ligands during reactivity are elucidated spectroscopically.

Chapter three examines the function of heterobimetallic complexes further using theoretical calculations. A DFT analysis of a bimetallic oxidative addition and a bimetallic N₂O activation is presented. The calculated transition states and thermodynamic parameters are comparable to experimental values. The key components of the catalysts relevant to reactivity are identified, and a series of heterobimetallic complexes conserving these components are synthesized by the Mankad group. A theoretical analysis of these complexes is presented and structural trends are interpreted.

Chapter four is devoted to the actual implementation of the heterobimetallic strategy into reaction development. The initial catalyst screening is carried out by thermodynamic energy calculations using DFT. A robust heterobimetallic catalyst that utilizes H₂ under atmospheric pressure for *E*-selective semi-hydrogenation of alkynes, a rare selectivity mode in high yields is developed.

Chapter five discusses the mechanistic features of the *E*-selective semi-hydrogenation reaction. Experimentally, the proposed mechanism is probed using model complexes. Theoretically, the transition state of the bimetallic H₂ activation step, bond orders and fragment charges along the reaction coordinate, and the key orbital interactions involved are calculated. Furthermore, a kinetic study inspired by calculations from a collaborating group is presented.

Chapter six discusses the current and future directions inspired by the work in this dissertation. Preliminary work on the development of bifunctional catalytic reactions by trapping the intermediates of the initial hydrogenation reaction, are presented, revealing a gateway for many future developments.

“Forget about the results. Creating the causes; that’s your work. The results will come by themselves.”

-Ajahn Brahm

Chapter 1

Introduction

Reproduced in part with permission from Karunananda, M. K.; Mankad, N. P. *ACS catal.*, Just
Accepted Manuscript, **DOI:** 10.1021/acscatal.7b02203.

© 2017 American Chemical Society

1.1. Opening Remarks

This dissertation narrates the story behind the reaction development of *E*-selective semi-hydrogenation of alkynes by heterobimetallic catalysis.

Chapter one unfolds the background of homogeneous hydrogenation reactions of C-C multiple bonds highlighting the main strategies employed today. It reveals how switching to cooperative strategies from the classical single-site metal strategy has given rise to the development of rare selectivity modes and the use of non-precious catalyst elements. It brings to light, the potential of using heterobimetallic catalysts developed by the Mankad group as a cooperative strategy to advance hydrogenation reactions.

In order to design catalysts methodically using this strategy, it's important to gain insight into the structure and function of these heterobimetallic complexes. The next couple of chapters are dedicated to understanding the heterobimetallics thoroughly using experimental and theoretical studies.

Chapter two investigates the electronic structure and the function of heterobimetallic complexes using XANES, IR and Mössbauer spectroscopy. The individual roles of the metals and ligands in oxidative addition, a key step in catalysis is studied extensively using these spectroscopic techniques.

Chapter three investigates the function of heterobimetallic complexes further using theoretical calculations. A DFT analysis of a bimetallic oxidative addition and a bimetallic N₂O activation is presented including calculated thermodynamic parameters and transition states which are comparable to experimental values. The key functional components of the catalysts relevant to reactivity are identified. Keeping these components intact, a series of heterobimetallic complexes available for catalysis synthesized by several

members of the Mankad group is mentioned. A theoretical analysis of these complexes along with the structural trends that emerged are presented.

Chapter four unveils the actual implementation of the heterobimetallic strategy into reaction development. Energy calculations by DFT are utilized for the initial catalyst screening. The development of a robust heterobimetallic catalyst that utilizes H₂ under atmospheric pressure for *E*-selective semi-hydrogenation of alkynes, a rare selectivity mode in high yields is discussed.

Chapter five features the mechanistic aspects of the *E*-selective semi-hydrogenation reaction. Experimentally, evidence for the proposed mechanism is given using model complexes. Theoretically, the transition state of the bimetallic H₂ activation step, bond orders and fragment charges along the reaction coordinate, and the key orbital interactions involved are calculated.

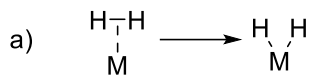
Chapter six concludes the narrative by discussing the lessons learned and future directions.

1.2. Evolution of C-C Hydrogenation Reactions with the Development of Cooperative Catalyst Paradigms

Catalytic hydrogenation of unsaturated C-C bonds is a well-developed area of organometallic chemistry that has been studied extensively for decades. It's a key transformation that has a multitude of applications in pharmaceutical, agrochemical and petroleum industries. Earlier breakthroughs in this area have been achieved predominantly by catalysts with noble metals such as Rh¹⁻⁴ and Ir⁵ which are capable of single site multi-electron redox processes.

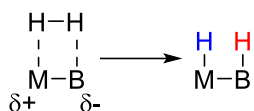
New developments that have emerged over the recent years promote the utilization of cooperative catalyst paradigms. Such systems undergo catalysis via metal-ligand (metal-base and metal-acid) cooperativity, frustrated Lewis acid-base pair cooperativity and bimetallic cooperativity. One major advantage of switching to cooperative strategies is that it allows us to abandon the use of toxic precious metals. Another is that it opens up the door to uncover unique reactivity and selectivity modes that complement the traditional single-site catalysis. This asset is remarkably exemplified by the evolution of H-H activation modes with the development of cooperative catalytic paradigms.

Single site strategy: homolytic cleavage

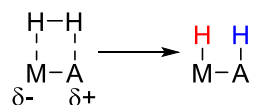


Cooperative strategies: heterolytic cleavage

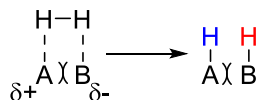
b) Metal-base cooperativity



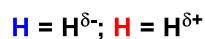
c) Metal-acid cooperativity



d) Frustrated lewis acid-base pair cooperativity



Scheme 1: Evolution of H-H activation modes with cooperative strategies



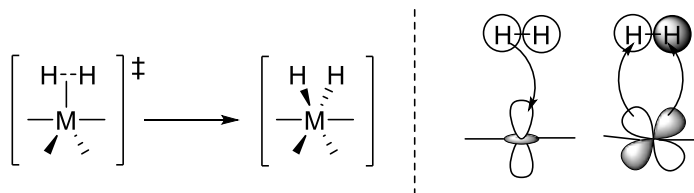
Classical single site catalysts activate H_2 via homolytic cleavage mechanisms (Scheme 1a). Cooperative catalysts however, operate mostly via heterolytic cleavage mechanisms (Scheme 1b, 1c and 1d)⁶. For example, metal-base catalysts developed by Shvo⁷, Noyori⁸ and Milstein groups⁹ feature a transition metal site which attracts the hydride and a Lewis base site which accepts the proton to collectively achieve heterolysis of H_2 (Scheme 1b). Recent reports of metal-acid catalysts by the Peters Group¹⁰ consists of an electron-deficient Lewis acid ligand and an electron-rich transition-metal which activates H_2 heterolytically in unison (Scheme 1c). Another cooperative approach that

implements heterolytic H₂ cleavage is the use of non-transition metal frustrated Lewis acid-base pairs developed by the Paradies¹¹, Stephan¹², Repo¹³ and Erker¹⁴ groups (Scheme 1d).

The chemistry accomplished by these novel cooperative catalytic paradigms and how they deviate from the traditional noble metal catalytic paradigm as it pertains to C-C hydrogenation reactions will be discussed in detail in the remainder of this chapter.

1.2.1. Single-Site Strategy

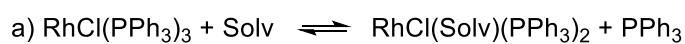
Precious metals have been utilized as hydrogenation catalysts due to their ability to homolytically activate H₂. Classical oxidative addition of H₂ in single-transition-metal-sites occur via a σ -complex formation, followed by homolysis of H₂. This is brought forward by the donation of electrons from the $\sigma_{\text{H-H}}$ orbital to an empty d-orbital of the metal and the back-donation from a filled metal d-orbital to the $\sigma^*_{\text{H-H}}$ orbital (Scheme 2).



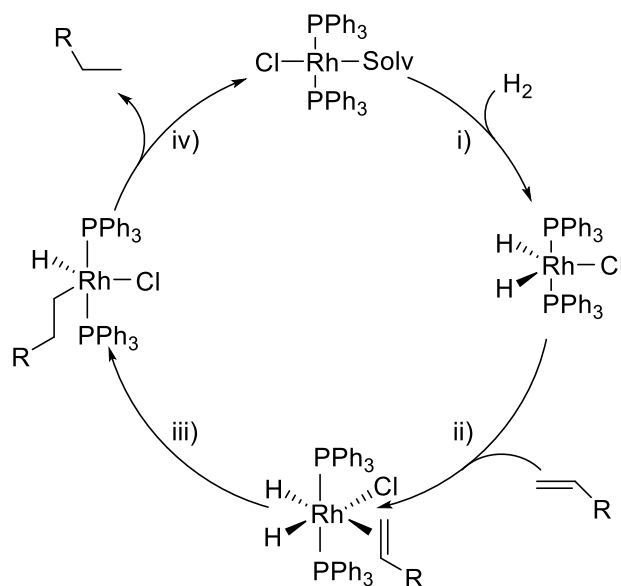
Scheme 2: Orbital interactions during single-site H₂ activation

Homogeneous catalytic hydrogenation of organic substrates with unsaturated C-C bonds was first introduced by Halpern and co-workers in 1961 using single site chlororuthenate(II) complexes.¹⁵ However, the most significant advance at the time was

made with the development of Wilkinson's catalyst $[\text{RhCl}(\text{PPh}_3)_3]$, first reported in 1966.¹ The mechanism of this single-site Rh catalyst has been studied vigorously over the years.^{16,17} The catalytic cycle depicts fundamental concepts in organometallic chemistry (Scheme 3) such as oxidative addition and reductive elimination which occur via two-electron redox processes. It is interesting to note that in the sequence of steps, the H_2 addition occurs first, followed by the alkene addition.



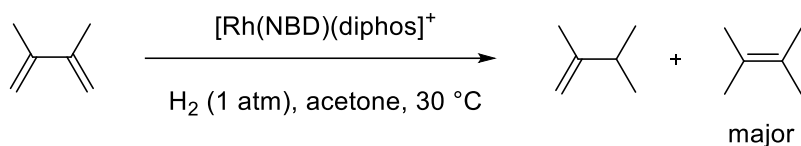
b)



Scheme 3: Olefin hydrogenation by Wilkinson's catalyst
Steps: a) ligand dissociation b) catalytic cycle
 i) H_2 addition ii) alkene addition iii) migratory insertion
 iv) reductive elimination

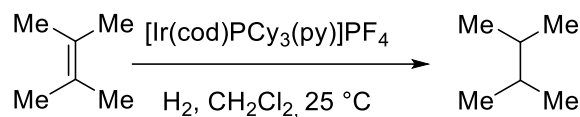
The Schrock-Osborn catalyst²⁻⁴ developed in 1977, is another catalyst that stands out in the history of alkene hydrogenation. It undergoes catalysis via a cationic Rh species

(Scheme 4). The catalyst is more active and effective than the Wilkinson's catalyst due to the cationic center being more electrophilic which facilitates the coordination of the alkene, which is the rate determining step. Mechanistic studies have shown that in Schrock-Osborn catalysts featuring bidentate ligands, alkene coordination can precede H₂ addition in the catalytic cycle.¹⁸ Selective hydrogenations were also demonstrated in converting dienes to monoenes.² Alkyne hydrogenations were also achieved yielding the *cis*-olefin.⁴ The incorporation of bidentate ligands to the Rh catalysts also enhanced its ability to control enantioselectivity in later years in asymmetric hydrogenations via chiral phosphine ligands.¹⁹



Scheme 4: Olefin hydrogenation by Schrock-Osborn catalyst

Another single site catalyst that is of noteworthy importance is the Crabtree's catalyst^{5,20} (Scheme 5). This Ir catalyst too is a cationic complex and shows higher activity especially towards the hydrogenation of hindered alkenes. Tetra-substituted olefins which were not accessible by both the Wilkinson and Crabtree catalyst were activated by it. The catalyst is also well-known for its substrate-directed hydrogenations which is a feature prominent in some Rh catalysts as well.²¹



Scheme 5: Olefin hydrogenation by Crabtree's catalyst

Since these initial reports, an array of single site noble metal catalysts have been developed for the catalytic hydrogenation of unsaturated C-C bonds in the decades that followed.^{22–24} However, precious metal catalysts come with a number of weaknesses. They are toxic, expensive and scarce. Therefore, the development of catalysts which counter these weaknesses is of paramount importance. A search for single site catalysts using earth-abundant metals has been pursued, but only a handful of successful reports remain to date^{25–29} Most of these systems promote single-site chemistry using electron rich late transition metals assisted by ligands, but, their mechanistic features and common driving forces are not well understood.

1.2.2. Cooperative Strategies

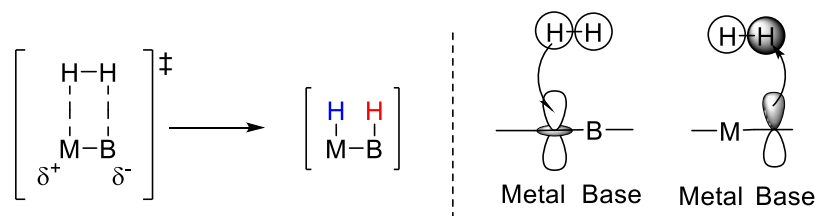
Efficient single site catalysis is promoted by the noble metals' ability to undergo two-electron redox processes such as oxidative additions and reductive eliminations. Although switching to first-row transition metals is a desirable alternative, it's proven to be challenging as 3d metals have a tendency to undergo single-electron redox reactions. An elegant solution that has surfaced in the recent years is the strategic use of two catalytic entities to cooperatively bring about two-electron redox processes. The two entities in action can be a metal/ligand pair where the ligand is either an acid or a base, a frustrated Lewis acid/base pair or a bimetallic pair.

1.2.2.1. Metal-Ligand Cooperativity

The ligands present in single site catalysts are traditionally innocent and do not participate in the redox processes during catalysis. However, switching these ligands with ligands that are non-innocent with respect to acid-base chemistry, have given rise to a new class of bifunctional catalysts in which both the metal and the ligand work cooperatively to facilitate a two-electron redox process. Initial progress was made with basic ligands.

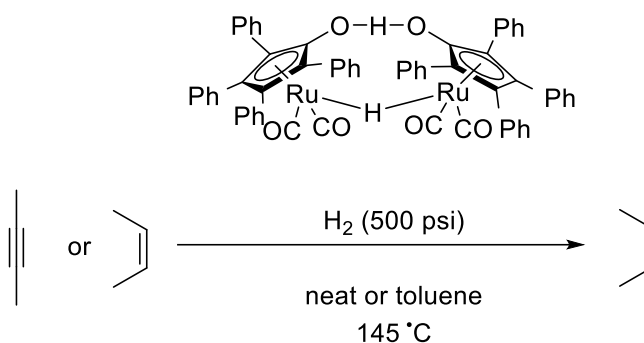
1.2.2.1.1. Metal-Base Cooperativity

Hydrogenation using metal-base cooperativity is possible due the ability of these bifunctional catalysts to heterolytically cleave H_2 . While the electron donation from the σ_{H-H} orbital to an empty d-orbital in the metal is still carried out, the back-donation to the σ^*_{H-H} orbital is actually done by a filled p-orbital in the basic residue. This brings about H_2 activation heterolytically, complementing single-site activity (Scheme 6).



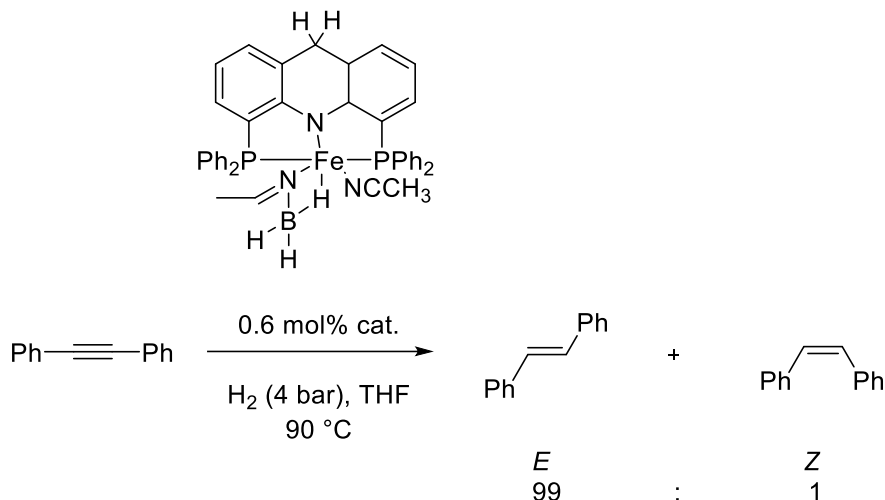
Scheme 6: Orbital interactions during H_2 activation with metal-base cooperativity

Shvo's catalyst reported in 1985 is the first example of catalytic hydrogenation of organic substrates with C-C bonds using metal-base cooperativity⁷ (Scheme 7). Both alkenes and alkynes were reduced by H₂.³⁰ Whilst it still used Ru as the metal, the catalyst showed unique reactivity by distributing the redox changes between the metal center and the redox active cyclopentadienone ligand. Similar bifunctional mechanistic features were observed in Noyori's⁸ and Morris's³¹ catalysts in the hydrogenation of C=O and C=N multiple bonds. However, their application in the hydrogenation of C-C bonds remains underdeveloped.



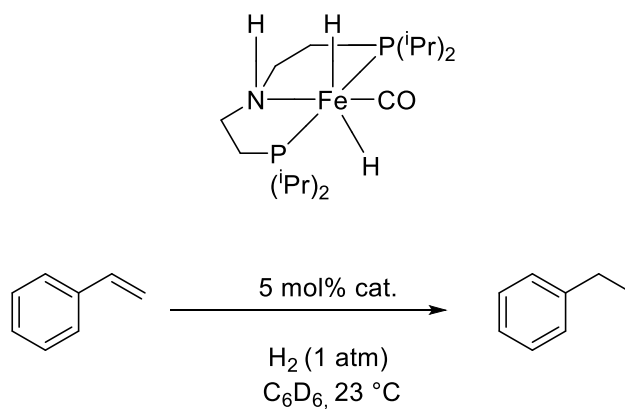
Scheme 7: Hydrogenation by Shvo's catalyst

A significant advance in the metal-base bifunctional catalysis that followed was the transition to first-row transition metals. A prominent example is Milstein's catalyst, an acridine-based PNP iron complex capable of *E*-selective semi-hydrogenation of alkynes⁹ (Scheme 8). The reaction occurs with no added base and under mild conditions.



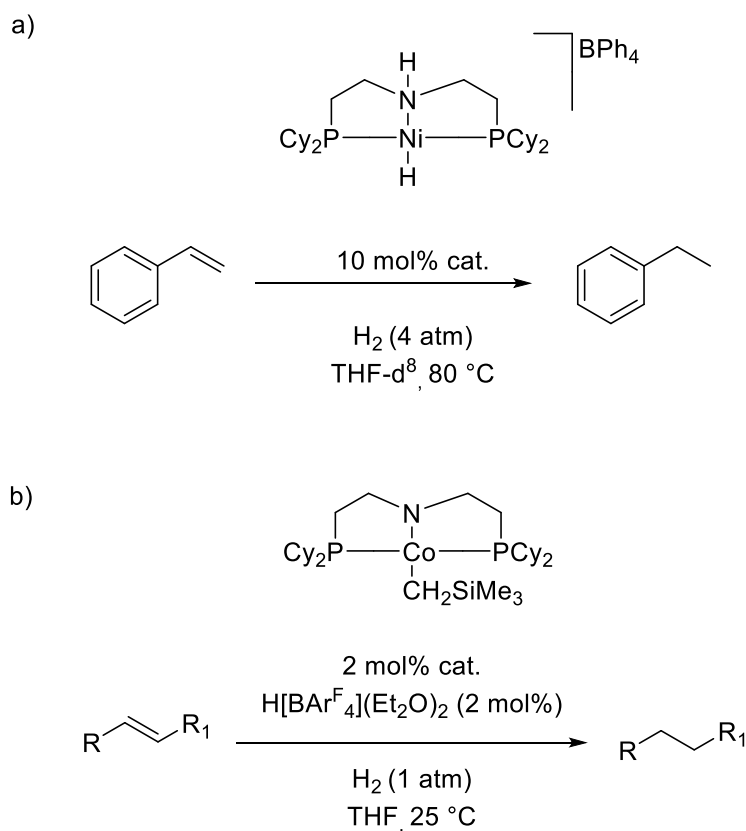
Scheme 8: *E*-selective semi-hydrogenation of alkynes by Milstein's catalyst

Iron was utilized further by the Jones group recently for the hydrogenation of polarized alkenes³² (Scheme 9). Styrenes and similar substrates were efficiently hydrogenated using an iron catalyst bearing a bis(phosphino)amine pincer ligand. DFT calculations and further experiments revealed a metal-ligand cooperative pathway.



Scheme 9: Iron catalyzed hydrogenation of alkenes by Jones's catalyst

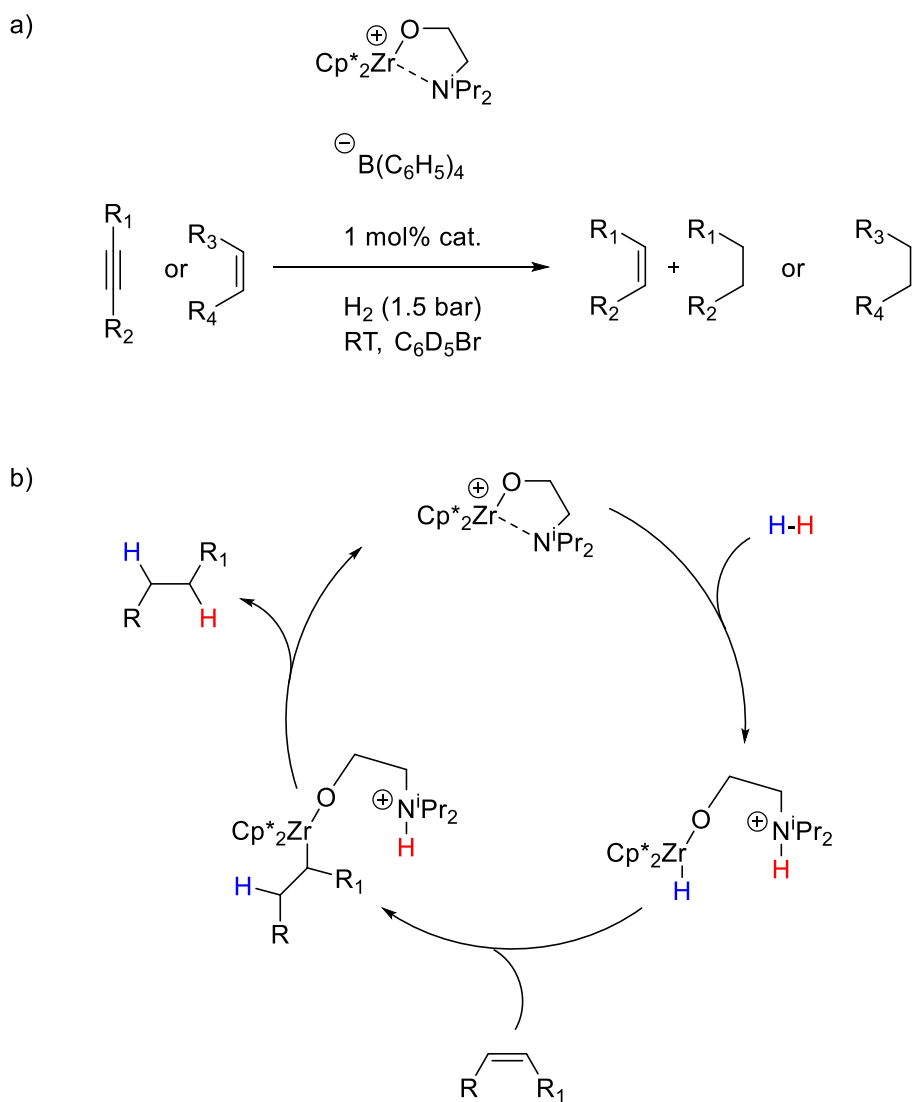
Pincer ligands have been employed for the synthesis of catalysts with other transition metals as well.³³ In 2012, Hanson and co-workers achieved alkene hydrogenation using cationic and a neutral PNP nickel hydride complexes³⁴ (Scheme 10a). Later they expanded their work to acquire the same feat using a cationic PNP cobalt(II)-alkyl complex^{35,36} (Scheme 10b).



Scheme 10: a) Nickel and b) cobalt catalyzed hydrogenation of alkenes by Hanson and co-workers

Organometallic frustrated Lewis pairs (FLPs) are another class of metal-base catalysts in which the metal acts as the Lewis acid in sync with a basic ligand. Erker and co-workers recently reported two systems based on zirconium containing cationic acidic residues and

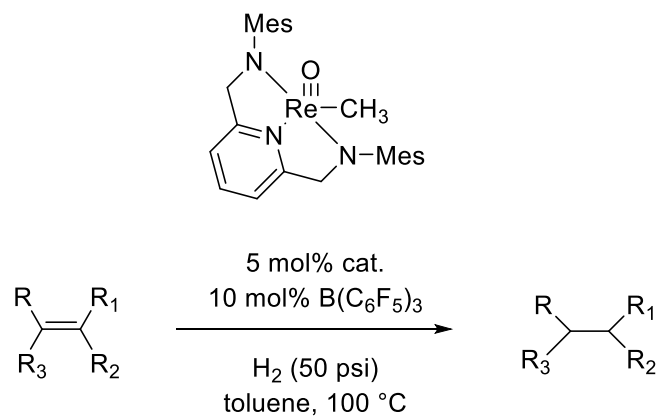
nitrogen and phosphorus containing anionic basic residues capable of hydrogenating alkenes and alkynes catalytically up to >99% yields under mild conditions.^{14,37} The proposed catalytic cycle is an excellent example which demonstrates that single site catalysis can be mimicked by metal-base cooperativity but with a redox-inactive metal center. The H₂ activation and the alkane elimination step show how the mimicking of a classical two-electron oxidative addition and a two-electron reductive elimination can be cooperatively carried out by metal-ligand cooperativity (Scheme 11).



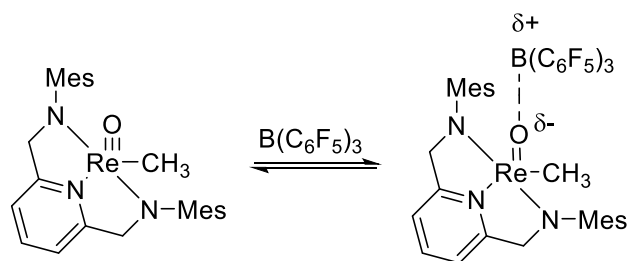
Scheme 11: Zirconium catalyzed hydrogenation by Erker and co-workers
a) reaction scheme b) catalytic cycle

Ison and co-workers enriched the organometallic FLP chemistry by introducing oxorhenium complexes with $\text{B}(\text{C}_6\text{F}_5)_3$ adducts capable of olefin hydrogenation^{38,39} (Scheme 12a and 12b). Interestingly, the H_2 activation is preceded by the alkene coordination in the mechanism elucidated by the experimental and computational investigations that followed. Mechanistic studies also showed that rhenium does not directly form or break bonds in catalysis. The addition of hydrogen and the product generation takes place across the rhenium oxo bond in the most favorable pathway (Scheme 12c). This is the first time that the incorporation of a transition-metal oxo in a FLP yielded enhanced catalytic activity through a synergistic effect.

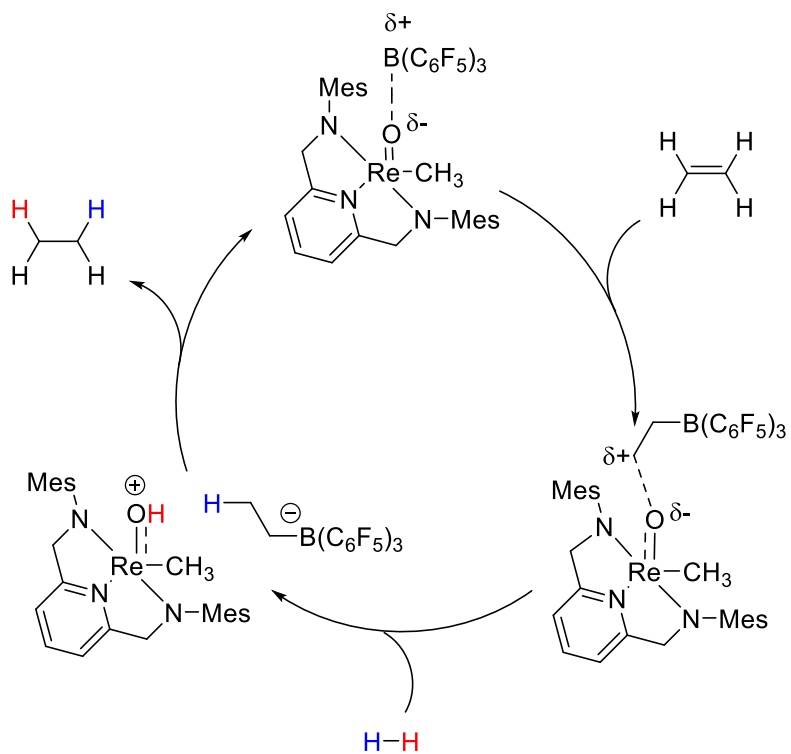
a)



b)



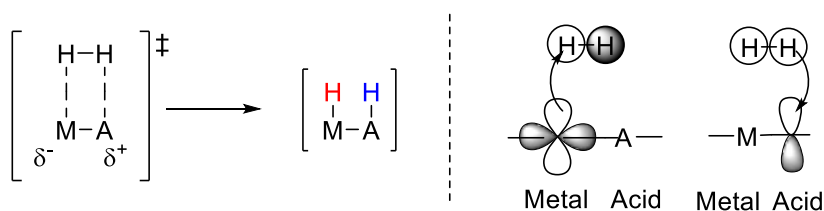
c)



Scheme 12: Rhenium catalyzed olefin hydrogenation by Ison and co-workers
 a) reaction scheme b) FLP generation c) catalytic cycle

1.2.2.1.2. Metal-Acid Cooperativity

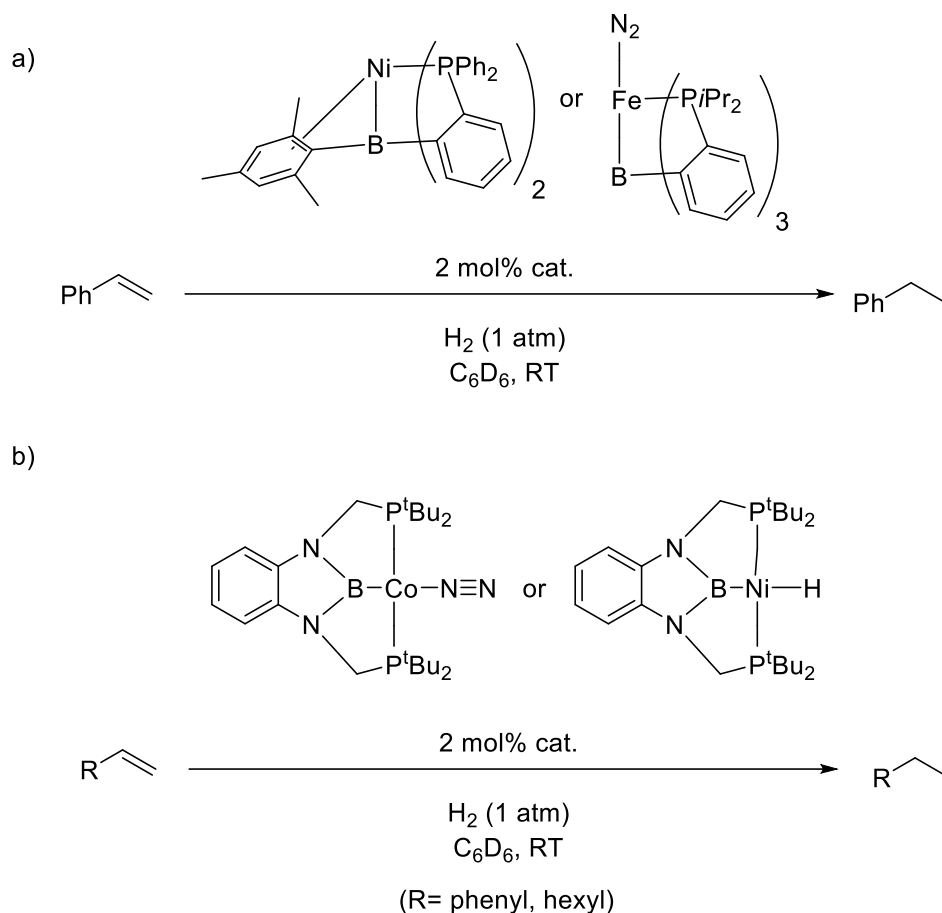
Incorporating an acidic ligand to a Lewis basic metal has recently introduced a new class of cooperative catalysts that uses metal-ligand cooperativity. These metal-acid catalysts usually consists of acidic boron ligands tethered to relatively basic and electron rich metal centers. In a typical example, the initial H_2 activation occurs by the electron donation from the $\sigma_{\text{H-H}}$ orbital to the empty orbitals in the acidic residue, and the back-donation from the filled d-orbitals of the metal center to the $\sigma^*_{\text{H-H}}$ orbital (Scheme 13) although alternative pathways have been calculated.^{6,40}



Scheme 13: Orbital interactions during H_2 activation with metal-acid cooperativity

Catalytic hydrogenation of unsaturated C-C bonds was first accomplished using this strategy by Peters and co-workers, who employed a nickel-borane bifunctional catalyst in which the borane Lewis acid was incorporated into a chelating multidentate ligand.¹⁰ The [Ni-B] unit was found to activate H_2 reversibly, to form a hydridonickel borohydride intermediate that could deliver the activated H_2 to styrene. Catalytic hydrogenation of both styrene and norbornene were achieved (Scheme 14a). Related chemistry was later reported by the same group using an iron boratrane system, where again a Lewis acidic borane moiety was held in proximity to an electron-rich metal center by chelation and

generated observable metal borohydride intermediates relevant to catalytic hydrogenation of styrene, ethylene and phenylacetylene (Scheme 14a).⁴¹

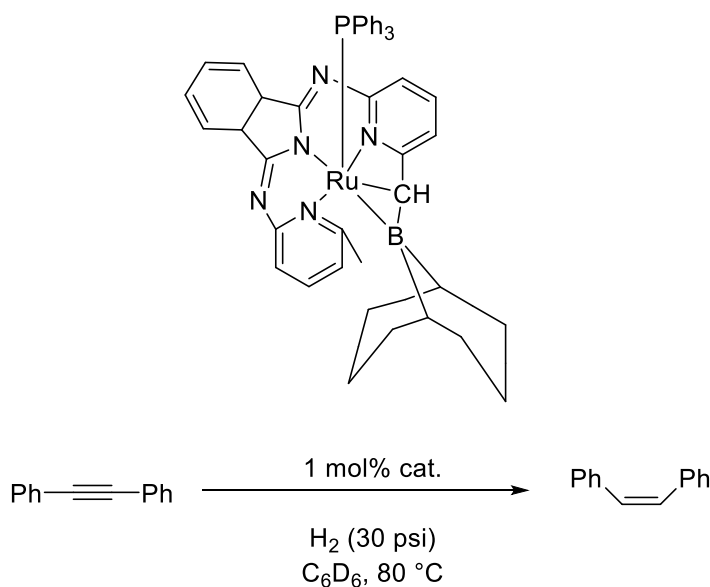


**Scheme 14: Catalytic a) Styrene hydrogenation using metal-borane complexes
 b) Alkene hydrogenation using metal-boryl complexes developed
 by Peters and co-workers.**

In addition to these chelated metal-borane catalysts, the Peters group also reported the use of chelated metal-boryl complexes as catalysts for olefin hydrogenation. A borylcobalt(I) catalyst was found to add two equivalents of H_2 to yield a dihydridoboratocobalt(II) dihydride intermediate relevant to catalytic hydrogenation of

styrene.⁴² This borylcobalt catalyst and a related borylnickel catalyst were later reported to catalyze hydrogenation reactions of styrene and some unactivated alkenes,⁴³ with turnover frequencies exceeding those of related systems lacking the metal-acid cooperative effect (Scheme 14b).

Selective alkyne hydrogenation was observed by the Szymczak group in 2016 using ruthenium-borane complexes.⁴⁴ These bifunctional metal-acid catalysts selectively semi-hydrogenated internal and terminal alkynes at high pressures of H₂ (Scheme 15) with high conversions and high reaction rates.



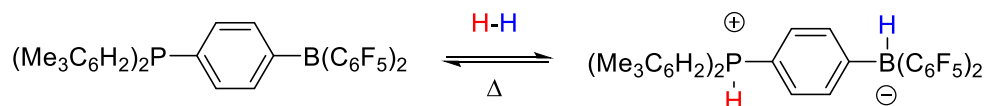
Scheme 15: Ruthenium catalyzed Z-selective semi-hydrogenation of alkynes by Szymczak and co-workers

1.2.2.2. Frustrated Lewis Acid-Base Pair Cooperativity

Perhaps the most promising and desirable alternative cooperative strategy that has emerged to replace precious metal catalysts is the use of frustrated Lewis acid/base

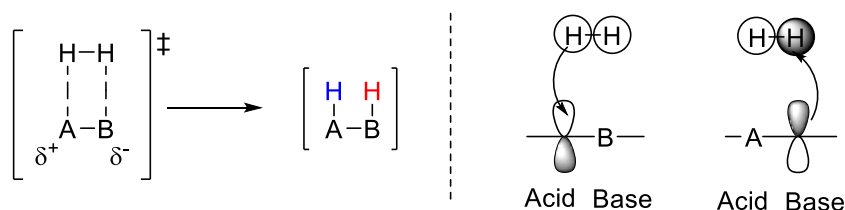
pairs.^{11,45–47} The most exciting feature that this strategy unveils is that it allows the catalysts to be free of not only precious metals, but also of all transition metals altogether. It is a solution that is simple and therefore, elegant.

In 2006, Stephan and co-workers reported the reversible activation of H₂ using a phosphonium borate species containing both Lewis acidic and basic components comprising only of main group elements⁴⁸ (Scheme 16).



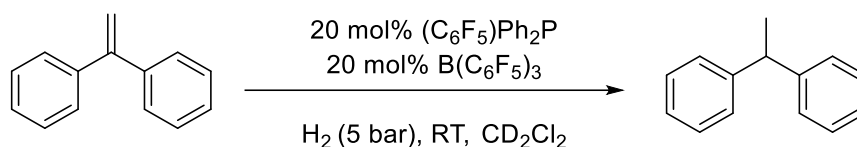
Scheme 16: Reversible H₂ activation using FLPs by Stephan and co-workers

This new class of compounds termed frustrated Lewis pairs (FLPs), were ideal candidates for catalytic hydrogenations. The H₂ interaction occurs via electron donation from the $\sigma_{\text{H-H}}$ orbital to an empty orbital in the Lewis acid and back-donation from a filled orbital in the Lewis base into the $\sigma^*_{\text{H-H}}$ orbital (Scheme 17)^{49–53}



Scheme 17: Orbital interactions during H₂ activation with FLP cooperativity

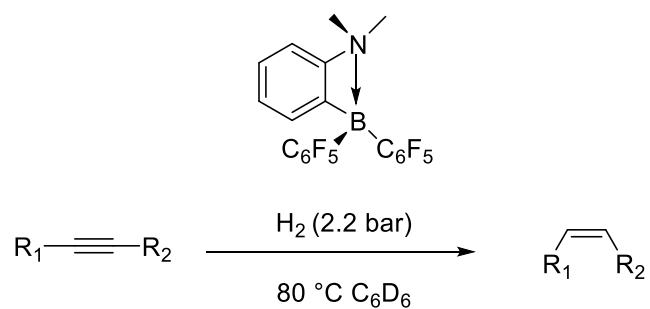
Due to the heterolytic nature of H_2 activation, catalytic hydrogenation was initially pursued successfully for polar substrates with C-O and C-N bonds.⁵⁴ Hydrogenation of non-polar C-C bonds was first reported by Paradies, Stephan, Grimm and co-workers in 2012⁵⁵ with the activation of olefin substrates at low temperatures (Scheme 18). More examples for olefin hydrogenation surfaced in the following years with modified FLPs.^{11,47,56–60}



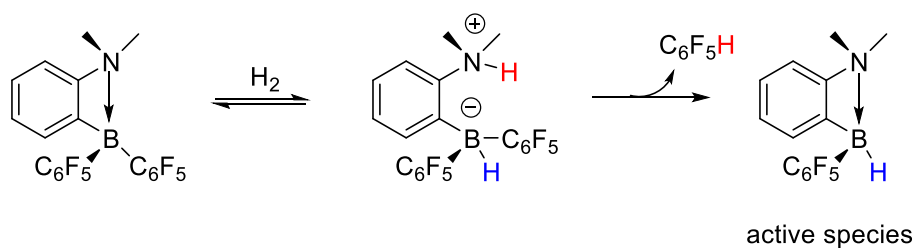
Scheme 18: Olefin hydrogenation using FLPs by Paradies, Grimm, Stephan and co-workers

Semi-hydrogenation of alkynes with FLPs were reported for the first time by Repo and co-workers in 2013.¹³ Selective formation of *cis*-alkenes was observed using mild conditions. They later switched the C_6F_5 groups in the catalyst with Cl and H atoms while retaining catalytic activity.⁶¹ In the reaction mechanism, the activation of the pre-catalyst by H_2 forms the active catalytic species. Their proposed catalytic cycle is a fine demonstration of how Lewis acid-base cooperativity is utilized in catalysis. It portrays once again that two-electron redox processes essential for catalysis such as oxidative addition and reductive elimination which previously needed precious metals can be mimicked by combining two entities that are individually only capable of mono-functional reactivity such as acid or base chemistry (Scheme 19).

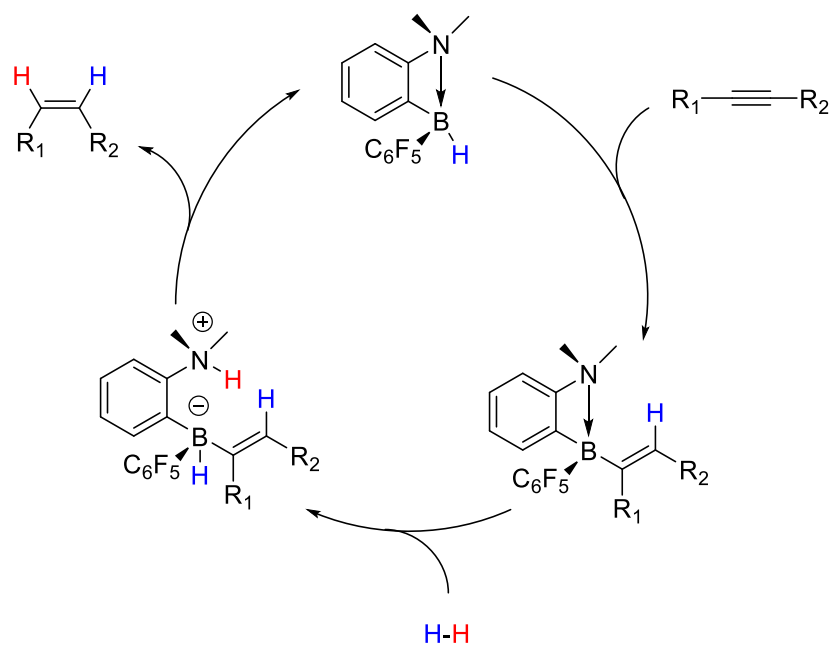
a)



b) i)

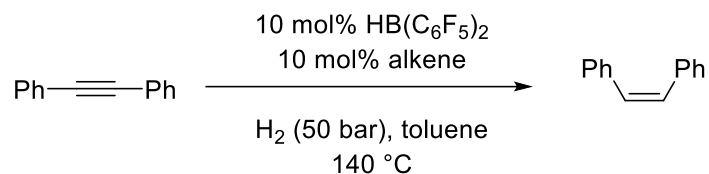


ii)



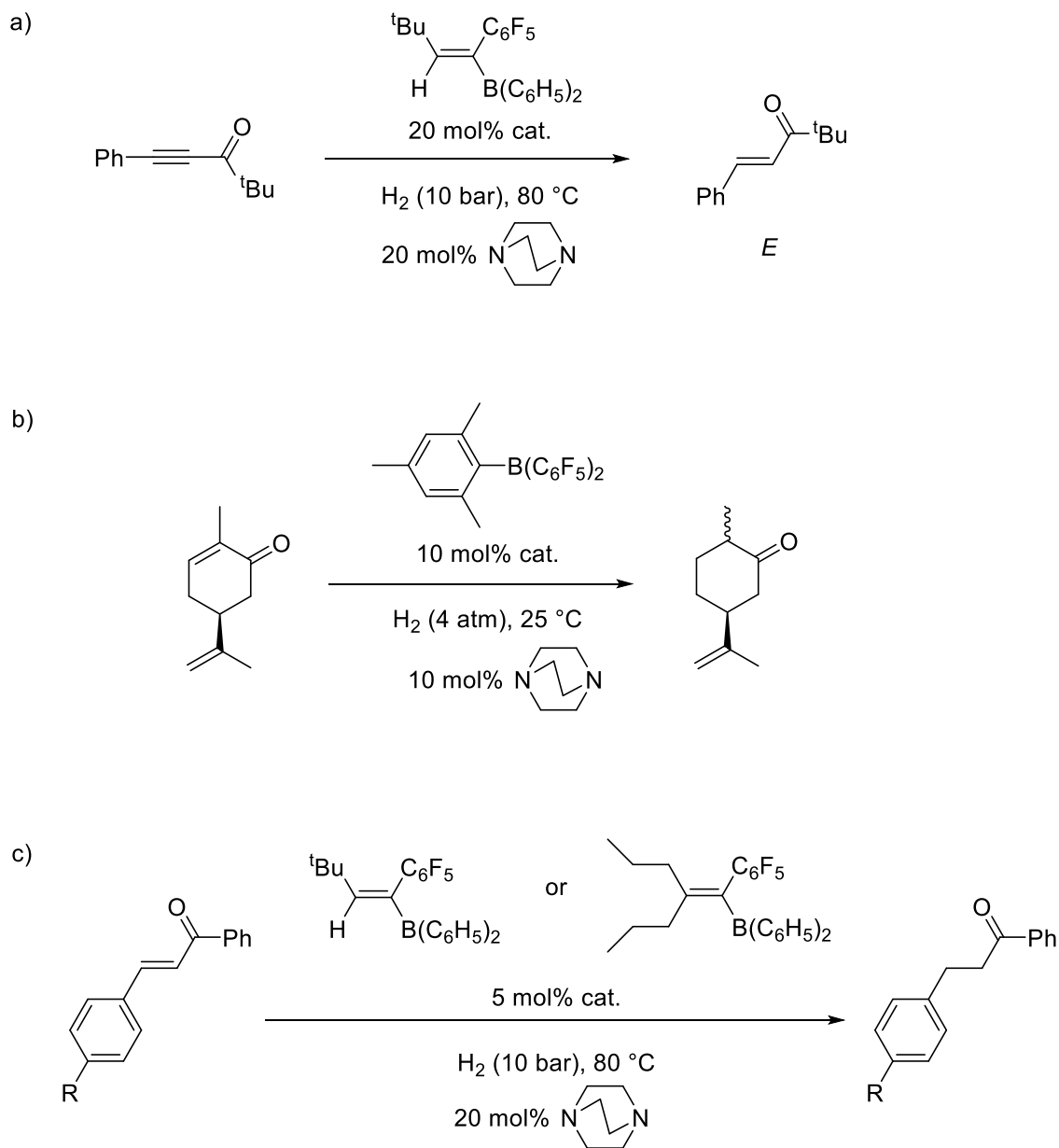
Scheme 19: Alkyne hydrogenation using FLPs by Repo and co-workers
a) reactions scheme b) i) formation of the active catalyst species
ii) catalytic cycle

In 2015, Du and co-workers showed that both *cis*- and *trans*-alkenes can be obtained in high stereoselectivities from alkynes using high temperatures and pressures⁶² (Scheme 20). Here, the cooperative role in catalysis is assumed by $\text{HB}(\text{C}_6\text{F}_5)_2$ and an alkene species interacting with a pentafluorophenyl group. Selective alkyne hydrogenation to produce *cis*-alkenes has been demonstrated by silica-supported FLP systems as well.⁶³



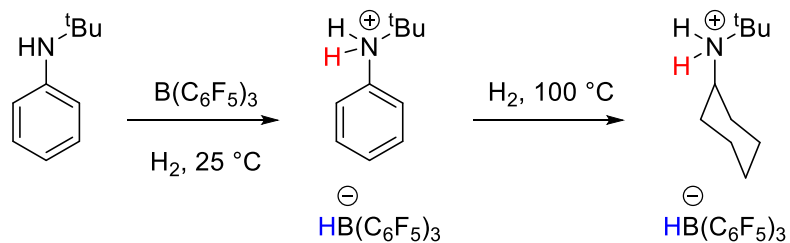
Scheme 20: Z-selective semi-hydrogenation of alkynes by Du and co-workers

FLPs have shown catalytic activity in C-C hydrogenation of electron-poor alkynes and alkenes as well.¹² Erker and co-workers have been able to selectively hydrogenate the C-C triple bonds in ynones catalytically in 2011.⁶⁴ Soós and co-workers selectively hydrogenated the C-C double bond in carvones⁴⁶ in 2012. Similarly, C-C hydrogenation in nitroolefins, acrylates⁶⁵ and enones⁴⁷ was achieved by Paradies and co-workers (Scheme 21).



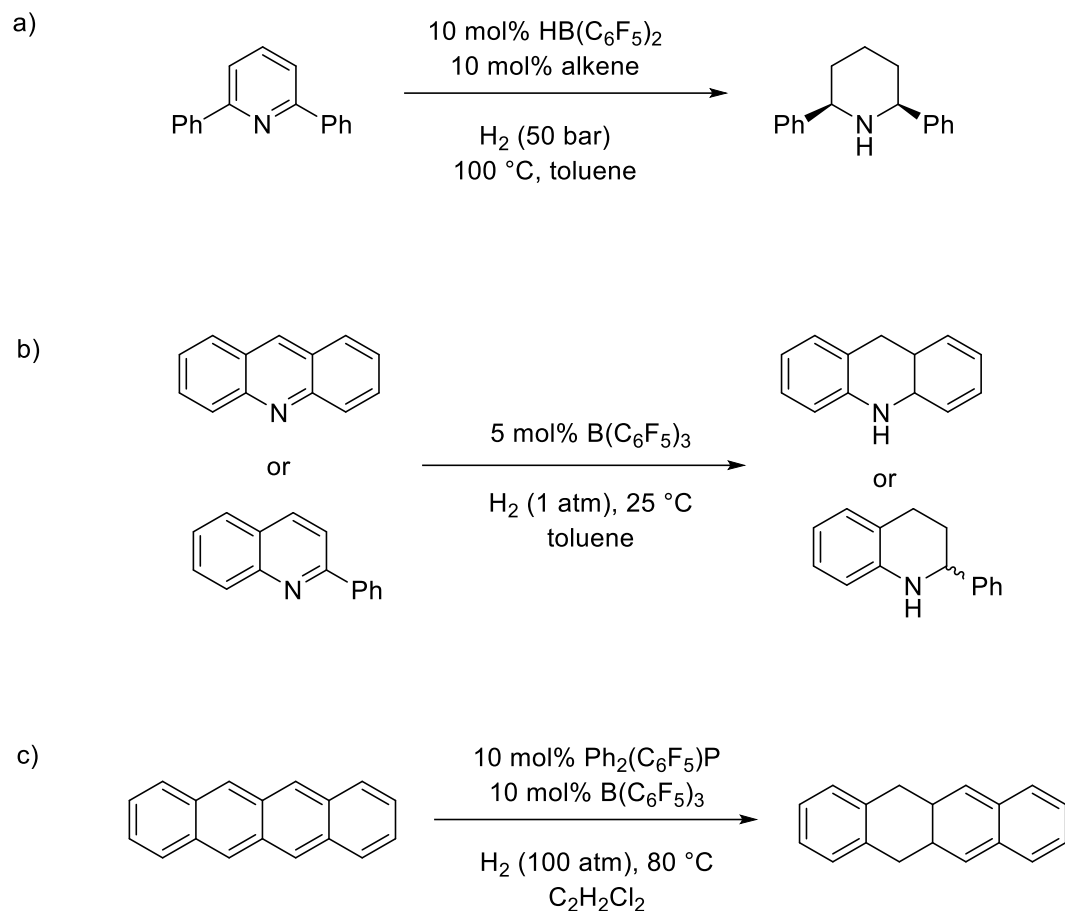
Scheme 21: Hydrogenation of electron poor alkynes and alkenes a) ynones by Erker and co-workers b) carvones by Soós and co-workers c) acrylates by Paradies and co-workers

In 2012, while studying H_2 activation reactions by FLPs, Stephan and co-workers unexpectedly uncovered that FLPs were capable of hydrogenating C-C double bonds in phenyl rings when their catalyst itself was hydrogenated⁶⁶ (Scheme 22).



Scheme 22: Hydrogenation of *tert*-butylaniline by Stephan and co-workers

This is a yet another example which demonstrates the emergence of a new and unusual mode of reactivity with the application of cooperative catalytic paradigms. The chemistry of hydrogenating aromatic systems was later extended to pyridines⁶⁷, trisubstituted quinolines⁶⁸, N-heterocycles⁶⁹ and polyaromatics⁷⁰ by Stephan and Du groups¹² (Scheme 23).



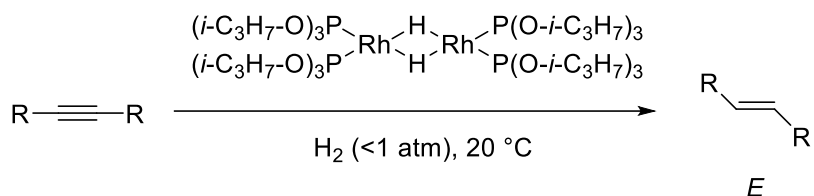
Scheme 23: Hydrogenation of a) pyridines by Du and co-workers b) N-heterocycles and c) polyaromatics by Stephan and co-workers

1.2.2.3. Bimetallic Cooperativity

Among the cooperative strategies employed for hydrogenations, the bimetallic strategy is perhaps the most underexplored. While theoretical^{71,72} and stoichiometric^{73–76} studies of bimetallic H_2 activations have been reported, their catalytic applications have been quite elusive.

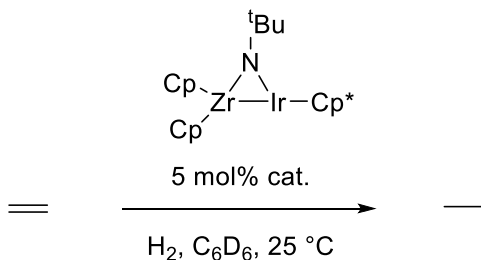
In 1982, Williams and co-workers introduced a dinuclear rhodium catalyst capable of catalytic hydrogenation of alkynes to selectively form *trans*-olefins.⁷⁷ This was again a rare

selectivity mode as the *cis*-alkene is the favored product in alkyne hydrogenation in most precious metal catalytic conversions. This system is the first and the only homobimetallic catalyst to promote hydrogenation of C-C multiple bonds. The catalyst precursor is a bridged square-planer dimer with two adjacent reactive metal centers (Scheme 24).



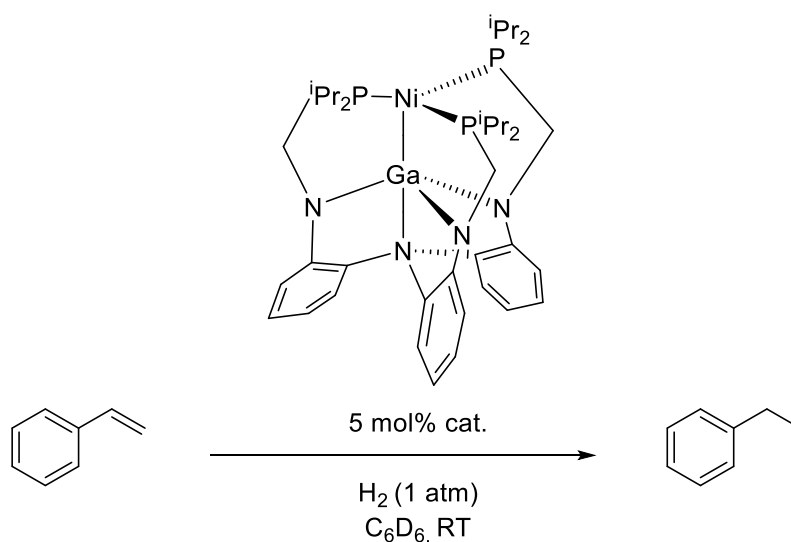
Scheme 24: *E*-selective semi-hydrogenation of alkynes by Williams and co-workers

Almost a decade later, Bergman and co-workers reported an early-late heterobimetallic complex showing catalytic reactivity towards alkene and alkyne hydrogenation.⁷⁸ This zirconium-iridium bridging imido complex hydrogenated ethylene, propylene, butane, 1-phenyl-1-propyne, 3-hexyne and *N*-phenylbenzaldimine (Scheme 25). Iridium-tantalum complexes have also shown activity towards alkene hydrogenations.^{79–81}



Scheme 25: Zirconium and iridium catalyzed hydrogenation by Bergman and co-workers

Lu and co-workers described a nickel-gallium heterobimetallic system demonstrating catalytic hydrogenation of olefins in high yields in 2015⁸² (Scheme 26). They also showed that the parallel nickel-indium system is active in olefin hydrogenation, but suffers from poor reactivity.



Scheme 26: Olefin hydrogenation by Lu and co-workers

Catalytic hydrogenation of multiple C-C bonds have also been reported by some multimetallic complexes.⁸³ However, their reaction mechanisms are poorly understood and sometimes even include heterogeneous pathways.

1.3. Heterobimetallic Catalysts as a Cooperative Strategy by Mankad Group

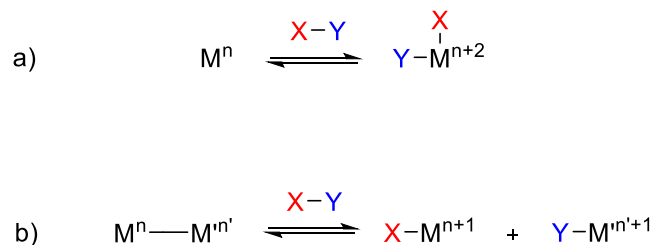
A majority of the efforts in pursuing heterobimetallic complexes as a cooperative strategy for catalysis has been focused on “early-late” heterobimetallic systems. Such complexes contain a polar metal-metal bond between an electropositive early transition metal with a low d-electron count and an electronegative late transition metal with a high

d-electron count. However, since early-transition metals form stable metal-heteroatom bonds with main group elements such as O, N and Cl, there's a penchant for stable intermediates to be formed that would prevent catalytic turnover. Therefore, even though some attempts towards catalysis has been successful^{78,84} most of the reactions reported are stoichiometric in nature.

A creative approach to evade this impediment is to switch the early transition metal with a late transition metal. The polarity of the metal-metal bond can still be maintained by keeping one of the late transition metals in a higher d-electron count than the other.

To this effect, Mankad and co-workers synthesized a new class of heterobimetallic complexes featuring polar metal-metal bonds between late transition metals in 2013.⁸⁵ They demonstrated that these complexes featuring copper-iron, copper-zinc and copper-molybdenum bonds activated methyl iodide, a polar substrate with rapid reactivity bringing about a bimetallic oxidative addition.

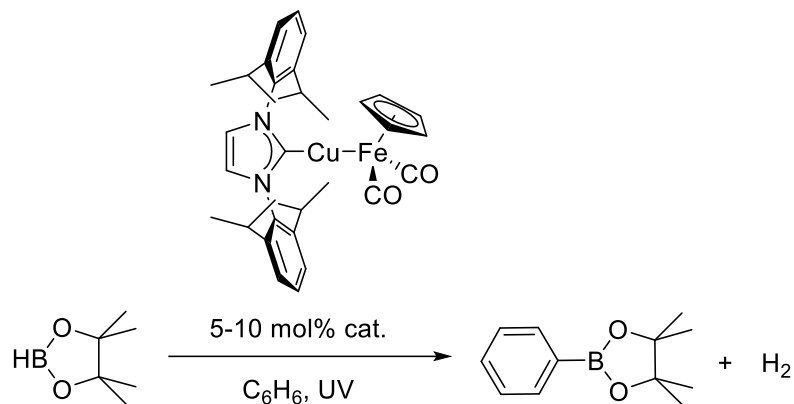
In the years that followed, they developed the chemistry of these heterobimetallic complexes further to accomplish catalytic conversions utilizing metal-metal cooperativity mimicking reactivity that was previously accomplished only by precious metals. Our original hypothesis was that this feat would be achieved as the complexes could break their metal-metal bonds and each of the metals could then undergo single-electron redox changes to cooperatively bring about two-electron redox processes (Scheme 27). However, spectroscopic and theoretical investigations have revealed that a majority of the redox changes occur in the ligands and not the metals.^{86,87} This phenomenon will be discussed in detail in chapter two.



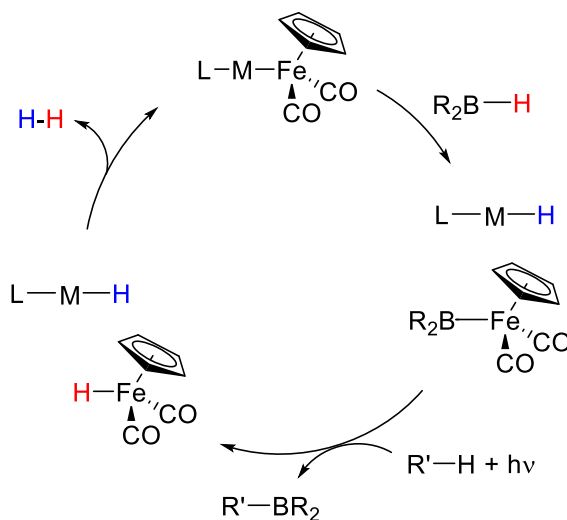
**Scheme 27: Heterobimetallic cooperative strategy to mimic bimetallic oxidative addition by Mankad and co-workers a) single site oxidative addition
b) bimetallic oxidative addition**

Photochemical C-H borylation was achieved catalytically using copper-iron and copper-zinc complexes⁸⁸ (Scheme 28a). Experimental and computational investigations revealed a mechanistic pathway with bimetallic oxidative addition and bimetallic reductive elimination steps (Scheme 28b).^{88,89}

a)

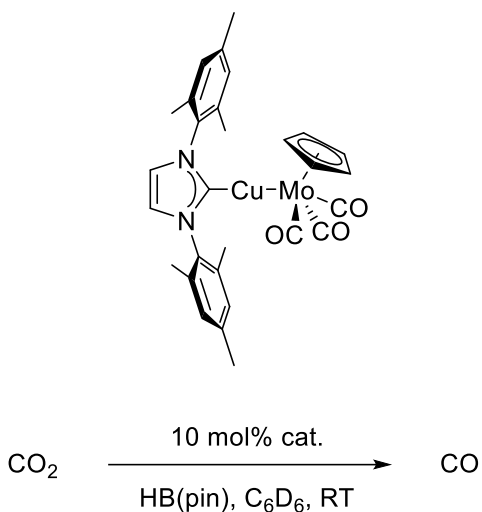


b)



Scheme 28: Heterobimetallic C-H borylation by Mankad and co-workers (L = NHC)
 a) Reaction scheme b) Catalytic cycle

Tunable catalysts for CO₂ activation were later developed with copper-iron, copper-tungsten and copper-molybdenum complexes.⁹⁰ The heterobimetallic catalysts were able to reduce CO₂ to CO with the use of HB(pin) while the analogous monometallic copper catalysts were only able to produce formate (Scheme 29). Reduction of CO₂ to CO by a monometallic copper catalyst has been reported previously, but has required the use of B₂pin₂.^{91,92}



Scheme 29: Heterobimetallic CO₂ reduction by Mankad and co-workers

1.3.1. Potential for Hydrogenation Reactions

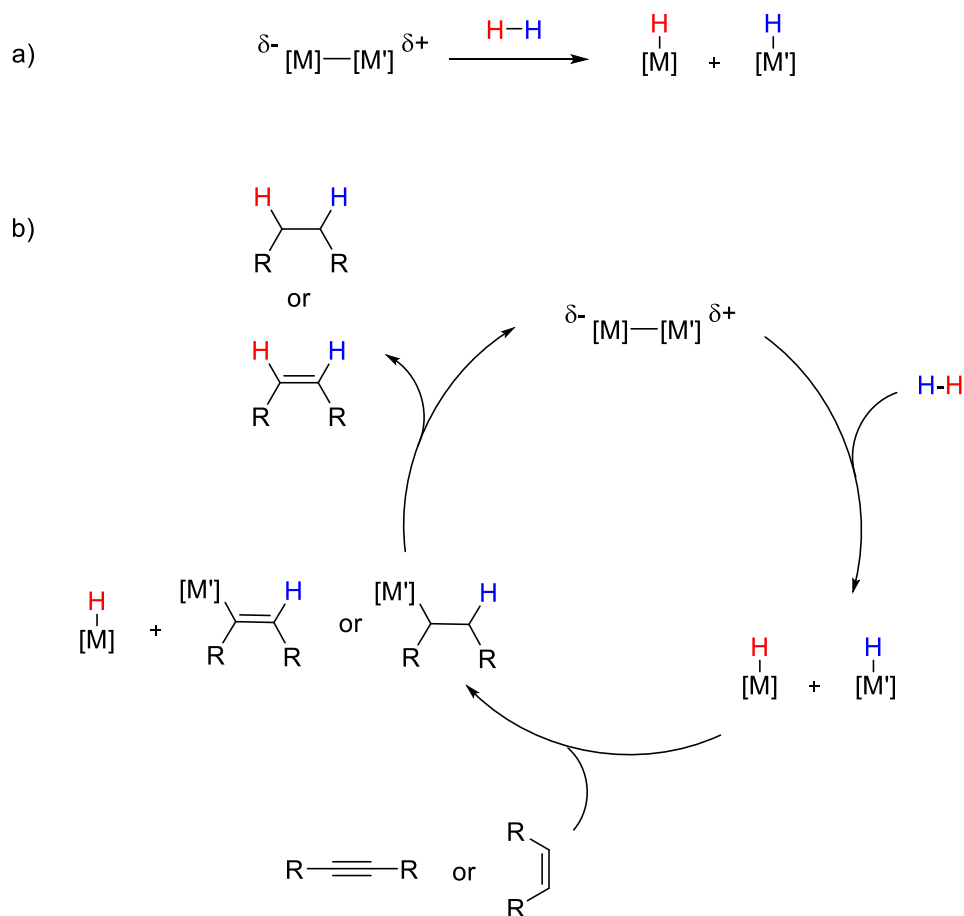
With the rapid evolution of novel reactivity modes and non-precious catalysts (section 1.2), it is evident that the hydrogenation of C-C multiple bonds can be developed and improved further using cooperative catalysts.

With the successful display of catalytic reactivity in C-H borylation and CO₂ reduction (section 1.3), it is evident that with rational design, heterobimetallic catalysts can be developed to implement fundamental and useful organic transformations as an alternative for single-site catalysts.

Combining these two trains of thoughts would naturally lead one to conclude that heterobimetallic catalysts can be developed to implement the hydrogenation of C-C multiple bonds as an alternative cooperative strategy to replace single-site catalysts.

As a starting point, we can envision activating H₂ heterolytically using polar heterobimetallic complexes introduced by the Mankad group (Scheme 30a). As in the mechanism of the bimetallic C-H borylation (Scheme 28a),⁸⁸ we can hypothesize a

bimetallic oxidative addition of H_2 across the metal-metal bond, which is coincidentally the reverse step of the reductive elimination in the C-H borylation mechanism (Scheme 28a) with a low-energy transition state⁸⁹ which could potentially be accessed from either direction. Once H_2 activation is achieved to form the corresponding metal hydrides, an alkene or an alkyne can be inserted into one of the metal hydrides as demonstrated by Erker and co-workers (Scheme 11b). The metal-alkyl/alkenyl species could then react with the remaining metal hydride to reductively eliminate the respective saturated alkane or alkene. Combining these steps together, it's plausible to conceptualize a catalytic cycle in which the two metals cooperatively engage in multi-electron redox steps to bring forward catalysis (Scheme 30b).



**Scheme 30: Proposed a) heterolytic H_2 activation by heterobimetallic complexes
b) catalytic cycle for C-C bond hydrogenations**

1.4. Research Goals

As demonstrated in the previous section of this chapter (section 1.3.1), polar heterobimetallic complexes introduced by the Mankad group have the potential to be developed for catalytic hydrogenation of organic substrates with C-C multiple bonds. However, rational design and reaction development requires a thorough understanding of these heterobimetallic systems.

Therefore, the research goals explored in this dissertation are to study the structure and reactivity features of polar heterobimetallic complexes (chapters two & three) and utilizing the insights obtained, to rationally design catalysts for C-C multiple bond hydrogenations (chapter four), and to study the mechanisms of the reactions developed (chapter five) in order to inspire future organic transformations (chapter six).

Chapter 2

Experimental Determination of Redox Cooperativity and Electronic Structures in Catalytically Active Cu-Fe and Zn-Fe Heterobimetallic Complexes

Reproduced in part with permission from Karunananda, M. K.; Vázquez, F. X.; Alp, E. E.; Bi, W.;

Chattopadhyay, S.; Shibata, T.; Mankad, N. P. *Dalton Trans.* **2014**, 43, 13661-13671.

© 2014 The Royal Society of Chemistry

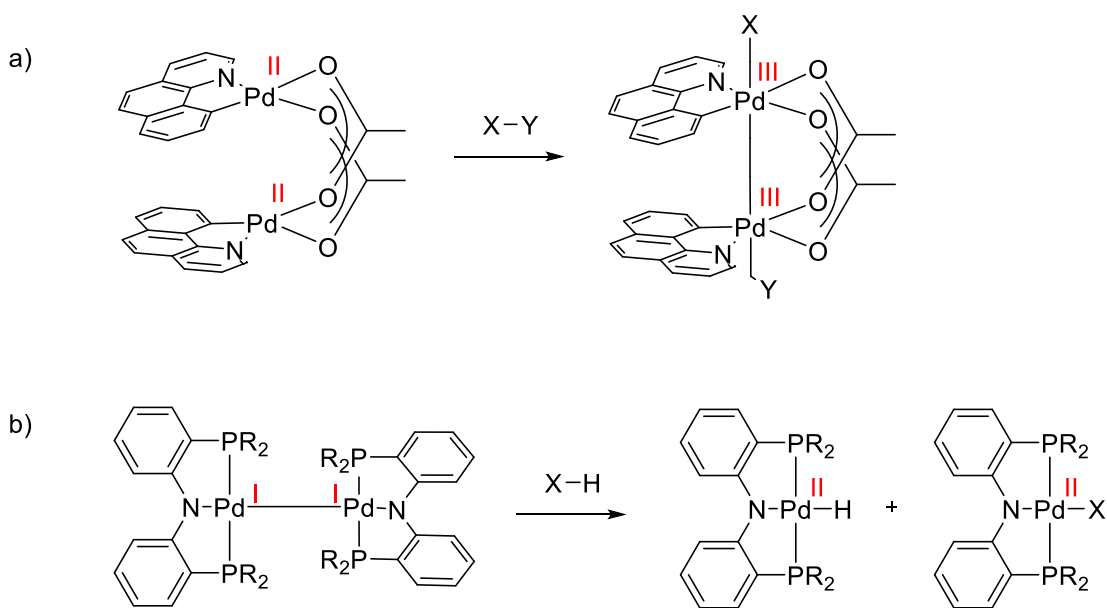
2.1. Opening Remarks

As mentioned in chapter one, the goals of chapters two and three are to investigate the structural and functional features of the polar heterobimetallic complexes introduced by the Mankad group.⁸⁵ Chapter two presents an experimental analysis. Heterobimetallic complexes competent in catalysis,⁸⁸ are studied using modern spectroscopic tools such as XANES, IR and Mössbauer spectroscopy. The electronic structures of the complexes are elucidated. The intricate roles of the individual components of a typical heterobimetallic system, as it carries out an oxidative addition, a fundamental step in catalysis, are probed. The conclusions derived aided in the expansion of the toolbox of heterobimetallic complexes available for catalysis (chapter three).

2.2. Introduction

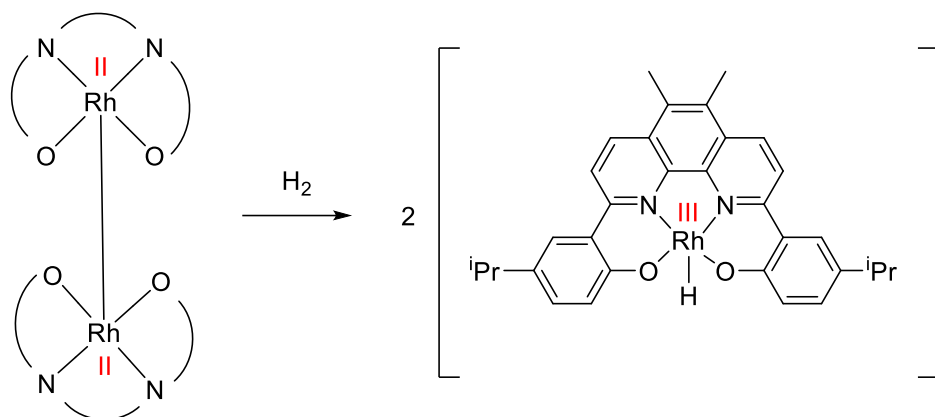
Although conventional catalytic transformations that employ multi-electron redox chemistry occur via single-site precious metal catalysis, some modern approaches utilize the use of cooperative strategies. One such approach that has been gaining momentum is the use of metal-metal cooperativity^{93–102} which has been well established in bioinorganic systems¹⁰³ and in heterogeneous catalysis.¹⁰⁴ For example, homobimetallic systems using metals such as rhodium¹⁰⁵, palladium¹⁰⁶, silver¹⁰⁷ and gold¹⁰⁸ have been developed for oxidative catalysis. In many of these examples, the ability of direct metal-metal bonds to facilitate multi-electron redox chemistry is a key feature, and understanding the electronic structures of metal-metal bonded systems as they relate to such redox processes is of fundamental importance.

Oxidative addition, a fundamental step in catalysis has been studied extensively in single-site catalysis. However, reports of bimetallic oxidative additions are rare and their mechanisms are not as well-investigated. In 2011, Ritter and co-workers reported a binuclear Pd(II) complex which undergoes bimetallic oxidative addition to yield a binuclear Pd(III) complex (Scheme 31a).¹⁰⁹ In this system, the formation of the metal-metal bond stabilizes the products of the oxidation. Ozerov and co-workers have also reported a binuclear Pd(I) complex which carried out an oxidative addition, breaking the metal-metal bond to yield separate products with Pd(II) centers (Scheme 31b).¹¹⁰



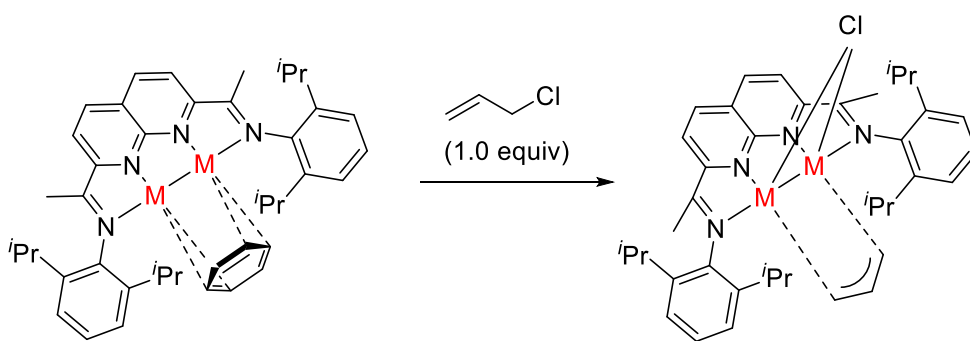
**Scheme 31: Bimetallic oxidative addition using Pd complexes by a) Ritter and co-workers
b) Ozerov and co-workers**

Similarly, oxidative addition of H_2 has been reported previously by Chan and co-workers in a dinuclear Rh(II) system in which the metal-metal bond breakage resulted in the formation of two separate Rh(III) hydrides (Scheme 32).⁷³



Scheme 32: Bimetallic oxidative addition by Chan and co-workers

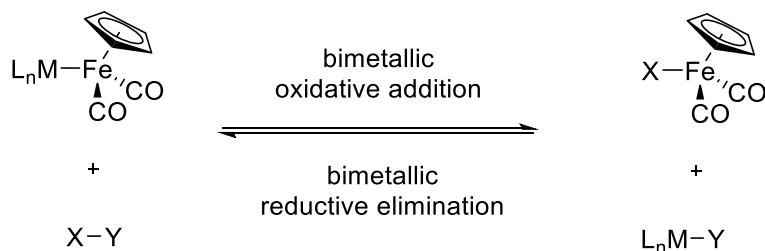
Uyeda and co-workers recently reported an isostructural series of Ni_2 , Co_2 and Fe_2 complexes capable of bimetallic oxidative addition with allyl chloride (Scheme 33).¹¹¹ A comprehensive electronic structure analysis of the Ni_2 complexes has been established previously¹¹² revealing that the bimetallic complexes can access a range of oxidation states via accommodating varying amounts of electron density in the π -system of the ligand.



Scheme 33: Bimetallic oxidative addition by Uyeda and co-workers (M = Ni, Co or Fe)

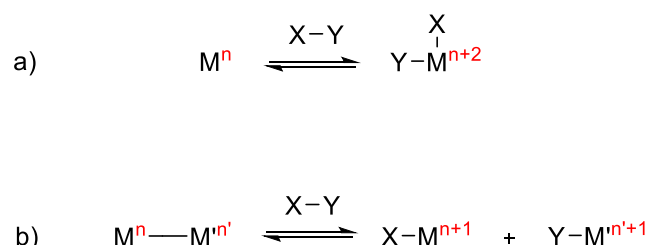
In considering systems capable of bimetallic oxidative addition, the redox participation of the different metals and ligands during reactivity has been investigated using experimental and computational studies by Ritter, Uyeda and Lu groups.^{106,111–116}

Adding to the bimetallic literature, our group has recently advanced the use of base metal heterobimetallic complexes to provide alternatives to traditional, single-site noble metal catalysts for C-H functionalization.^{88,89} These systems utilize Cu-Fe or Zn-Fe bonds constructed through salt metathesis reactions of metal-halide precursors with the anionic fragment $[\text{FeCp}(\text{CO})_2]^-$, or Fp^- .⁸⁵ Heterobimetallic M-Fp complexes constructed in this way have been known for some time,^{117–122} although they have commonly employed d^0 metal precursors to generate so-called “early-late” M-Fp systems that have generally resisted catalytic application development. Because the new Cu-Fp and Zn-Fp complexes derived from d^{10} metal precursors show promise for C-H functionalization catalysis^{88,123} and for small molecule activation processes,¹²⁴ we sought to understand the electronic structures of these complexes in detail. In particular, we have argued previously^{88,123} that heterobimetallic catalysis reminiscent of single-site noble metal systems is enabled through bimetallic oxidative addition and bimetallic reductive elimination steps that couple the single-electron redox manifolds of two base metals in order to achieve net two-electron redox changes (Scheme 34).



Scheme 34: Heterobimetallic reactivity during catalysis

As in the case of bimetallic systems with late-transition metals reported by Ozerov¹¹⁰ and Chan⁷³ groups, our original hypothesis was that our heterobimetallic systems would break their metal-metal bonds and each of the metals would then undergo single-electron redox changes to cooperatively bring about two-electron redox processes (Scheme 35).



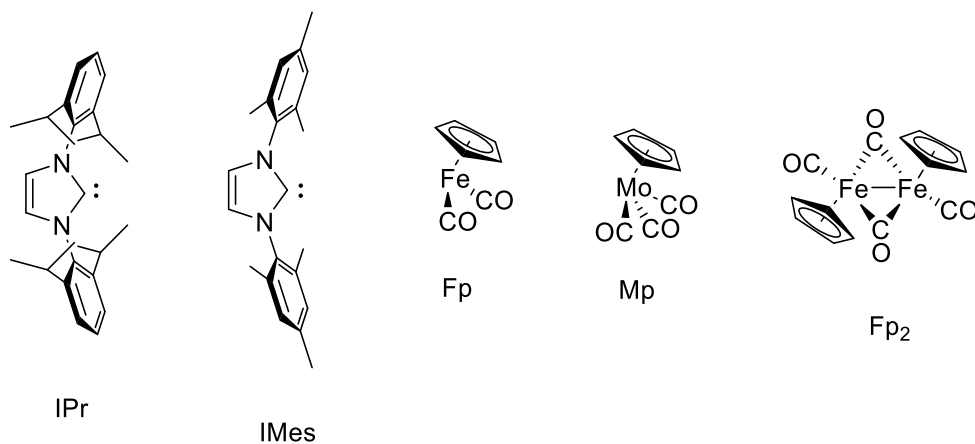
**Scheme 35: Heterobimetallic cooperative strategy to mimic bimetallic oxidative addition by Mankad and co-workers a) single site oxidative addition
b) proposed bimetallic oxidative addition**

In this chapter, a combined Mössbauer spectroscopy and X-ray absorption spectroscopy (XAS) study that examines this hypothesis experimentally by probing the unique electronic structures of Cu-Fe and Zn-Fe heterobimetallic complexes is presented highlighting the degree to which the different parts of the molecules undergo redox changes during oxidative addition.

2.3. Results & Discussion

The complexes featured in this study are composed of the fragments shown in Scheme 36, with a canonical example complex being (IPr)Cu-Fp. Collectively, the available systematic variations allow for the effects on electronic structure of the N-heterocyclic carbene (NHC) supporting ligand (IPr or IMes), the electrophilic metal (Cu or

Zn), and the nucleophilic metal (Fe or Mo) to be probed. Several benchmark complexes including (IPr)CuCl, (IPr)ZnCl₂·THF, K⁺Fp⁻, FpMe, FpI, and Fp₂ (Scheme 36) also were examined for comparison to the heterobimetallic systems.



Scheme 36: Representative fragment abbreviations

2.3.1. Mössbauer Spectroscopy

Mössbauer spectroscopy was used to probe the electronic and geometric environments of the Fe centers in Fp-containing complexes (Figure 1).¹²⁵

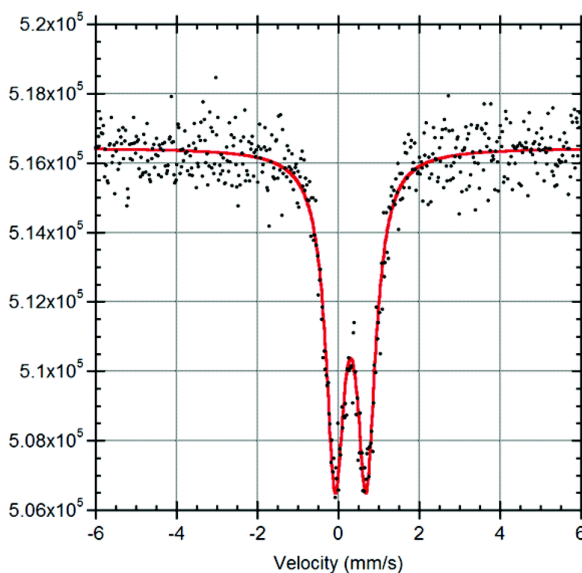


Figure 1: Mössbauer data (black) and fit (red) for (IPr)Cu-Fp¹²⁶

In addition, many Fp⁻ containing complexes have been characterized by Mössbauer spectroscopy previously.^{127,128,129} Representative data, both from literature values and from measurements reported here, are tabulated in Table 1.

Table 1: Mössbauer parameters for Fp-X complexes as a function of X^a

Entry	X	δ (mm s ⁻¹)	ΔE_Q (mm s ⁻¹)	ν_{CO} (cm ⁻¹)
1	-CH ₃ ^{129,130}	-0.008	1.753	1990, 1930
2	-CH ₂ Ph ¹²⁹	0.004	1.72	2010, 1960
3	-Cl ¹²⁷	0.148	1.836	2050, 2002
4	-Br ¹²⁷	0.148	1.849	2045, 1999
5	-I ¹²⁷	0.128	1.830	2038, 1998
6	-C(O)CH ₃ ^{128,131}	-0.15	1.68	2021, 1965
7	-CN ¹²⁷	-0.0097	1.89	2060, 2015
8	-Fp ¹³²	0.141	1.87	1925, 1750
9 ^b	-GeR ₂ ⁻¹³³	0.084	1.744	1995, 1943
10 ^c	-FeR' ¹³⁴	0.08	1.73	1958, 1902
11	-Cu(IPr)	0.30	0.77	1914, 1849
12	-Cu(IMes)	0.32	0.76	1905, 1842
13	-Zn(Cl)(IPr)	0.42	0.72	1944, 1888
14	-ZnFp ¹³⁵	0.288	1.733	1973, 1956, 1915
15	[K] ⁺	0.34 (66%), 0.13 (34%)	0.72 (66%), 1.8 (34%)	1853, 1720
16	[K(18-crown-6) ₂] ⁺	0.35	0.79	1854, 1775

^aData collected at room temperature unless otherwise indicated. ^bData collected at 78 K; R= κ^2 -[C₆H₃-2-(C(CF₃)₂O)-4(CH₃)]²⁻. ^cData collected at 190 K; R'= C₆H-2,6-(C₆H₂-2,4,6-ⁱPr₃)₂-3,5-ⁱPr₂; only parameters for the Fp iron center are shown here.¹²⁶

Typical Fp-containing complexes (entries 1–7 in Table 1) display small isomer shifts of about 0 mm s⁻¹, typically associated with a low-spin Fe(II) formulation,¹²⁵ and large quadrupole splittings of about 1.7-1.9 mm s⁻¹. The isomer shifts in typical Fp-X complexes are slightly larger than 0 mm s⁻¹ when X is a π -donor ligand (entries 3–5) and slightly smaller than 0 mm s⁻¹ when X is a π -acceptor ligand (entries 6–7). Quadrupole splittings are relatively insensitive to these electronic effects and remain consistently large due to the similar local symmetries at Fe across most Fp-X complexes (entries 1–7). Examples of previously characterized M-Fp complexes also are included in Table 1. The

Mössbauer parameters for these complexes that feature either Ge-Fp¹³³ or Fe-Fp¹³⁴ bonds are within the range observed for typical Fp-X complexes (entries 8–10). In this context, the Cu-Fe complexes (IPr)Cu-Fp and (IMes)Cu-Fp, as well as the Zn-Fe complex (IPr)(Cl)Zn-Fp, were found to have unusual Mössbauer parameters (entries 11–13): the isomer shifts are large (0.30–0.42 mm s⁻¹) and the quadrupole splittings are small (0.72–0.77 mm s⁻¹) compared to previously characterized Fp-containing complexes.

Two electronic factors known to affect the isomer shift likely are operative for the Cu-Fp and Zn-Fp complexes. Large isomer shifts can indicate a decrease in s-electron density at Fe,^{125,133} which in the current systems would arise from Fe → Cu/Zn σ -donation.⁸⁵ Large isomer shifts also can indicate an increase in d-electron density at Fe,^{125,133} which in the current systems would arise from Cu/Zn → Fe π -backdonation involving d π –d π interactions. It is well understood for Fp-X complexes that σ (Fe-X) orbitals are of the correct symmetry to mix with the Fe s-orbitals, while the π (Fe-X) orbitals are forbidden by symmetry from possessing Fe s-character.¹³⁶ When considering these two factors, it is unlikely that the anomalously large isomer shifts in the Cu–Fp complexes are due solely to a decrease in s-electron density due to Fe → Cu σ -donation, because otherwise a comparably large effect would also be observed in the Ge-Fp and Fe-Fp complexes where the same type of donor–acceptor interaction is present.^{133,134} Instead, the most likely explanation is that the large isomer shifts arise from an increase in d-electron density due to Cu → Fe π -backdonation. It is reasonable that this effect would be absent in Ge-Fp and Fe-Fp complexes, where the metals bound directly to the Fp fragment lack filled and accessible d-shells for π -backbonding, as is the case with Cu. Indeed, our previous theoretical studies of (NHC)Cu-Fp complexes indicated that the HOMO and HOMO–1 orbitals possess π^* (Cu-Fe) character (Figure 2).⁸⁵

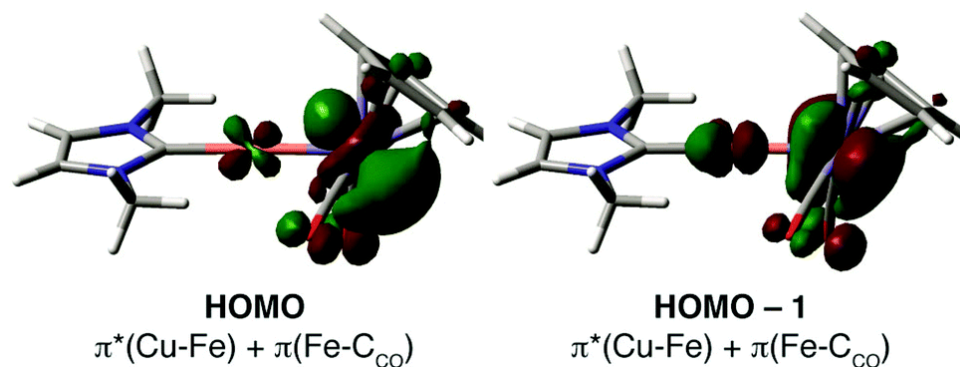


Figure 2: Cu \rightarrow Fe π -backdonation evident in calculated HOMO and HOMO-1 of a model (NHC)Cu-Fp complex. Calculated surfaces (0.04 isocontours) reproduced with permission from reference⁸⁵

It is further reasonable that X \rightarrow Fe π -donation would be more pronounced in Cu-Fp complexes than in the Fp-halide series, because of the more efficient orbital overlap available in d π -d π interactions compared to d π -p π interactions. The electron-rich nature of the Fe centers in the Cu-Fp complexes is evident from the lower-energy CO vibrational frequencies compared to other Fp-X complexes (Table 1). In addition to these bonding considerations, another important consideration is that the Cu-Fe bonding likely possesses significant electrostatic character due to the lack of empty Cu d-orbitals, thereby causing the Mössbauer parameters of the Fp fragment within the Cu-Fp complexes to resemble those for the free Fp anion (*vide infra*). The observed further increase in the isomer shift from (IPr)Cu-Fp and (IMes)Cu-Fp (0.30–0.32 mm s⁻¹) to (IPr)(Cl)Zn-Fp (0.42 mm s⁻¹) could arise from an increase in Zn \rightarrow Fe π -backdonation relative to Cu \rightarrow Fe π -backdonation (and corresponding increase in Fe d-electron density) due to the influence of the π -donor chloride ligand, an increase in Fe \rightarrow Zn σ -donation relative to Fe \rightarrow Cu σ -donation (and corresponding decrease in Fe s-electron density) due to the more Lewis-acidic Zn site, or a combination of both factors. Interestingly, ZnFp₂

exhibits a similar isomer shift (Table 1, entry 14),¹³⁵ indicating that these observations are relatively general to complexes with the [Fp] fragment bound to late transition metals centers like Cu and Zn.

Quadrupole splitting values are typically sensitive to local symmetry at Fe.¹²⁵ It is reasonable that relatively little variation is observed in most Fp–X complexes, because little variation in local symmetry at Fe is expected as a function of X. The anomalously small quadrupole splittings for (IPr)Cu-Fp and (IMes)Cu-Fp, then, may arise from the secondary Cu...CO interactions observed by X-ray crystallography and predicted by computations⁸⁵ that cause deviations from idealized Fe geometry within the Fp fragments. A similar effect is proposed for (IPr)(Cl)Zn-Fp. It is interesting to note that the quadrupole splitting for ZnFp₂ (Table 1, entry 14) falls within the more typical Fp range. Isomer shift and quadrupole splitting data computed from DFT calculations support these assertions (Table 2).

Table 2: Calculated Mössbauer parameters predicted by DFT^a

Entry	Complex	δ (mm s ⁻¹)	Q (barn) ^c	η^d	ΔE_Q (mm s ⁻¹)
1	Fp ₂	0.0971	0.182	0.835	1.59
2	FpI	0.122	0.182	-0.872	1.76
3	FpMe	-0.0107	0.182	0.684	1.90
4	(IMe)Cu-Fp ^b	0.305	0.0494	0.147	0.768
5	(IMe)(Cl)Zn-Fp ^b	0.425	0.0494	0.237	0.711

^aBVP86/LANL2TZ(f)/6-311+G(d). ^bIMe= 1,3-dimethylimidazol-2-ylidene. ^cQuadrupole moment determined by fitting. ^dAsymmetry parameter of electric field gradient determined directly from DFT calculations.¹²⁶

Computed isomer shift values reproduce the experimentally observed pattern and correctly predict an increase in the isomer shift in Fp-X complexes across the series Me <

$I < \text{Cu}(\text{NHC}) < \text{Zn}(\text{Cl})(\text{NHC})$. Similarly, the computed quadrupole splitting values correctly predict a clustering pattern of high splittings for Fp_2 , FpMe , and FpI and low splittings for $(\text{NHC})\text{CuFp}$ and $(\text{NHC})(\text{Cl})\text{ZnFp}$. From the calculations, it is evident that this effect does indeed derive from the symmetry of the ligand fields around the Fe centers, as the heterobimetallic complexes (Table 2, entries 4–5) were computed to have very different quadrupole moments (Q) and electric field gradient asymmetry parameters (η) than the Fe-only complexes (Table 2, entries 1–3).

To verify that the source of the asymmetry is distortion of the Fe environment due to semi-bridging $\text{Cu}\cdots\text{CO}$ or $\text{Zn}\cdots\text{CO}$ interactions, the calculated structural asymmetry parameters, α , for the CO ligands are tabulated in Table 3.

Table 3: Asymmetry parameters for CO ligands determined experimentally and computationally^{a,b}

Entry	Complex	α (observed)	α (calculated)
1	(NHC)Cu-Fp	0.40, 0.58	0.44, 0.48
2	(NHC)(Cl)Zn-Fp	0.56, 0.70	0.63, 0.65
3	FpI	0.76, 0.79 ^c	0.78, 0.78

^aExperimental values from X-ray crystallography of IPr derivatives; computational values from DFT of IMe derivative (BVP86/LANL2TZ(f)/6-311+G(d))¹²⁶; IMe= 1,3-dimethylimidazol-2-ylidene⁸⁶. ^bSee reference¹³⁷ for definition of α . ^cStructural data for FpI from reference¹³⁸.

The typical ranges for bimetallic carbonyl complexes are: terminal CO, $\alpha \geq 0.6$; bridging CO, $\alpha \leq 0.1$; semi-bridging CO, $0.1 < \alpha < 0.6$.¹³⁷ Both crystallographic and computational analyses of the Cu-Fe complexes reveal the presence of semi-bridging CO

ligands (Table 3, entry 1), a phenomenon that is clearly absent in Fp-I (Table 3, entry 3) when iodine is treated as a metal. The Zn-Fp complexes feature CO ligands that are borderline cases along the terminal/semi-bridging continuum, and we propose that the resulting modest distortion of the Fe environment compared to Fp-I causes the low quadrupole splitting observed. The anionic species K^+Fp^- exhibited two distinct Fe environments by Mössbauer spectroscopy (entry 15 in Table 1), consistent with previous observations¹³⁹ by IR spectroscopy of multiple contact ion pair configurations existing between Fp^- and either Na^+ or K^+ . In order to examine the bare Fp^- anion, we synthesized the cation-sequestered ion pair $[\text{K}(\text{18-crown-6})_2]^+[\text{Fp}]^-$, which was found to exhibit a clean, sharp pair of symmetric and antisymmetric CO vibrations by IR spectroscopy (Figure A1 in Appendix).

The Mössbauer spectrum for this species was modeled as having a single Fe environment (entry 16) matching the major species present in K^+Fp^- (entry 15), although some disorder was evident from the relatively large linewidth of the spectrum for $[\text{K}(\text{18-crown-6})_2]^+[\text{Fp}]^-$ (0.6 mm s^{-1} vs. $0.3\text{--}0.35 \text{ mm s}^{-1}$ in pure Fe). The observed quadrupole splitting of 0.79 mm s^{-1} is in the range observed for the Cu-Fp and Zn-Fp complexes of interest here, rather than in the range of more typical Fp-X complexes. The small quadrupole splitting can be rationalized by the observed C_{2v} geometry apparent in the solid-state structure of Fp^- that is distinct from C_s -symmetric environments observed in Fp-X complexes but similar to the local Fe symmetry in $(\text{IPr})\text{CuFp}$.^{140,141} This rationale fits the analysis of quadrupole splitting data for the Cu-Fp and Zn-Fp complexes.

2.3.2. X-Ray Absorption Spectroscopy

X-ray absorption near edge structure (XANES) spectroscopy was employed to probe the local environment around Fe, Cu and Zn atoms in the organometallic compounds of interest. XANES is used to determine the oxidation state and electronic transitions and fingerprint the element of interest. XANES spectra are usually taken from 150 eV below the edge energy to 300 eV above the edge energy of the element of interest and are sensitive to the unoccupied electronic levels near the Fermi level. In most cases the edge position shifts to higher energies with increase in effective oxidation states, and the oxidation states of unknown samples can be obtained by comparison with well-understood reference standards.^{142,143} For each heterobimetallic complex in this study, a combination of the appropriate two K-edge XANES spectra was used to construct an electronic structure model.

2.3.2.1. Cu K-Edge Spectroscopy

Selected Cu K-edge data are plotted in Figure 3, and the peak energies of the pre-edge features are tabulated in Table 4.

Table 4: Cu K-Edge data

Entry	Complex	Pre-edge Energy ^a (eV)
1	Cu foil	8983.1
2	CuCl ^b	8985.0
3	CuCl ₂ ^b	8988.0
4	(IPr)CuCl	8983.6
5	(IMes)CuCl	8983.9
6	(IPr)CuI	8983.8
7	(IPr)CuFp	8983.5
8	(IMes)CuFp	8983.5
9	(IPr)CuMp	8983.5

^aPeak energy of pre-edge feature. (Deconvolution shown in Appendix 1 Figures A2-A4 and Table A1). ^bAnhydrous.¹²⁶

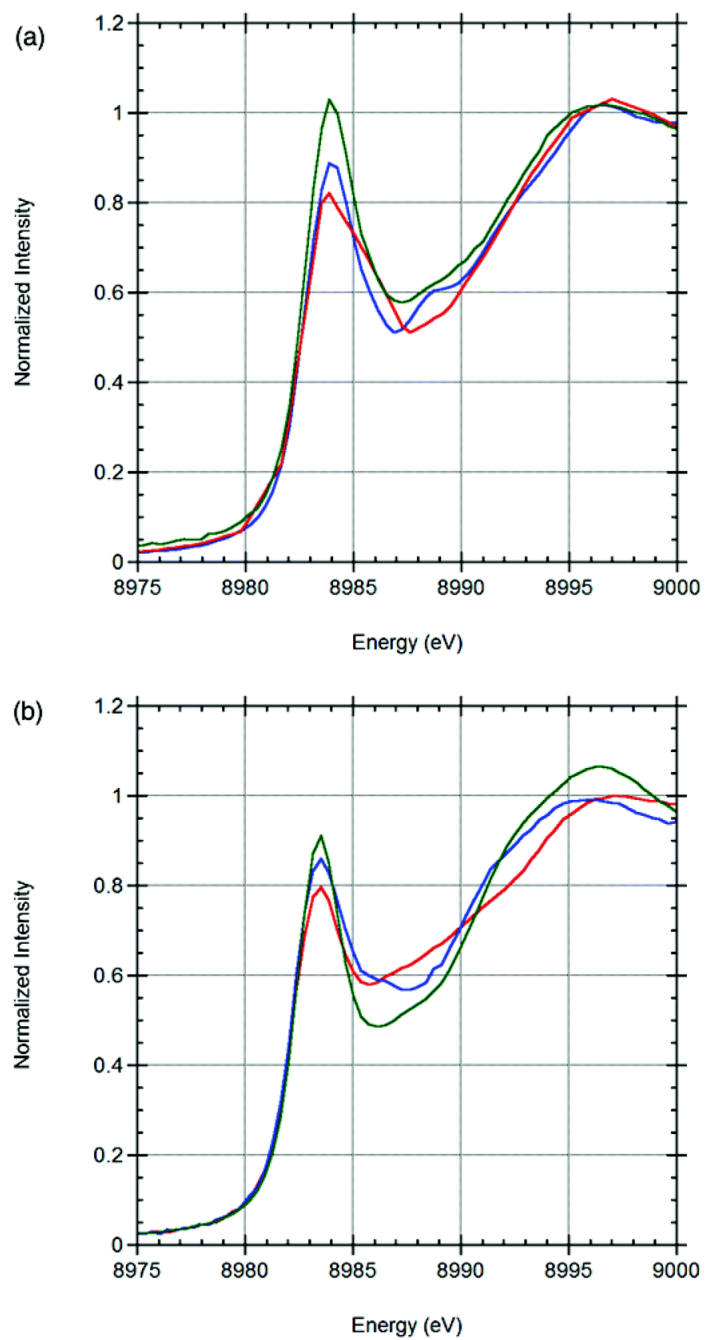


Figure 3: Cu K-edge spectra for (a) (IPr)CuCl (red), (IMes)CuCl (blue), IPrCuI (green) (b) (IPr)Cu-Fp (blue), (IMes)Cu-Fp (red) and (IPr)Cu-Mp (green)¹²⁶

The spectra for all NHC complexes were dominated by intense pre-edge features in the 8983–8984 eV range of approximately 0.8 normalized intensity, consistent with the typical spectral shape observed for two-coordinate Cu complexes.¹⁴⁴ Previous studies with covalent Cu complexes have indicated that these intense pre-edge features, which correspond to the first electric dipole allowed Cu 1s \rightarrow 4p transitions, are highly sensitive to the effective nuclear charge at Cu, with a \sim 3 eV change expected per oxidation state.^{144,145} The pre-edge energies for (NHC)CuX complexes were found to be relatively insensitive to the identity of X. The benchmark complexes (IPr)CuCl, (IMes)CuCl, and (IPr)CuI all displayed similar pre-edge positions (\sim 8984 eV) that indicated highly reduced Cu centers with effective nuclear charges lower than that in CuCl (8985.0 eV). The Cu-Fe complexes (IPr)CuFp and (IMes)CuFp displayed pre-edge energies (\sim 8983 eV) very similar to the halide complexes. The Cu-Mo complex (IPr)CuMp, which features a less nucleophilic¹⁴⁶ Mp[−] anion relative to Fp[−], also exhibited a similar pre-edge position (8983.5 eV). Overall, the effective nuclear charge of Cu in (NHC)CuX complexes is relatively insensitive to the identity of the NHC ligand, the identity of the X ligand, or the presence/absence of a Cu-M bond.

2.3.2.2. Zn K-Edge Spectroscopy

Zn K-edge data are plotted in Figure 4 and tabulated in Table 5. The spectra were relatively featureless. A modest increase in intensity at \sim 9663 eV for (IPr)(Cl)Zn-Fp relative to (IPr)ZnCl₂·THF may reflect an increase in anisotropy of the Zn 4p orbitals due to the trigonal planar (as opposed to pseudotetrahedral) coordination geometry, akin to pre-edge behavior in Cu K-edge spectroscopy.¹⁴⁴

Table 5: Zn K-Edge data

Entry	Complex	Rising edge Energy ^a (eV)
1	Zn foil	9661.2
2	ZnCl ₂ ^b	9665.4
3	(IPr)ZnCl ₂ ·THF	9665.0
4	(IPr)(Cl)Zn-Fp	9665.7

^aInflection point energy determined by analysis of first derivative spectra.¹²⁶ ^bAnhydrous.

The complexes (IPr)ZnCl₂·THF and (IPr)(Cl)Zn-Fp displayed rising edge positions (~9665 eV) very similar to that observed for anhydrous ZnCl₂ (9665.4 eV), indicating an effective oxidation state of Zn(II) for both complexes. Much like the Cu K-edge data, these Zn K-edge data were relatively insensitive to the replacement of a halide ligand for Fp⁻. When comparing derivative spectra, it is evident that the Zn K-edge position for (IPr)(Cl)Zn-Fp is modestly higher in energy than that of (IPr)ZnCl₂·THF (Figure 4b), again consistent with the proposed presence of Zn → Fe π -backdonation counterbalancing Fe → Zn σ -donation.

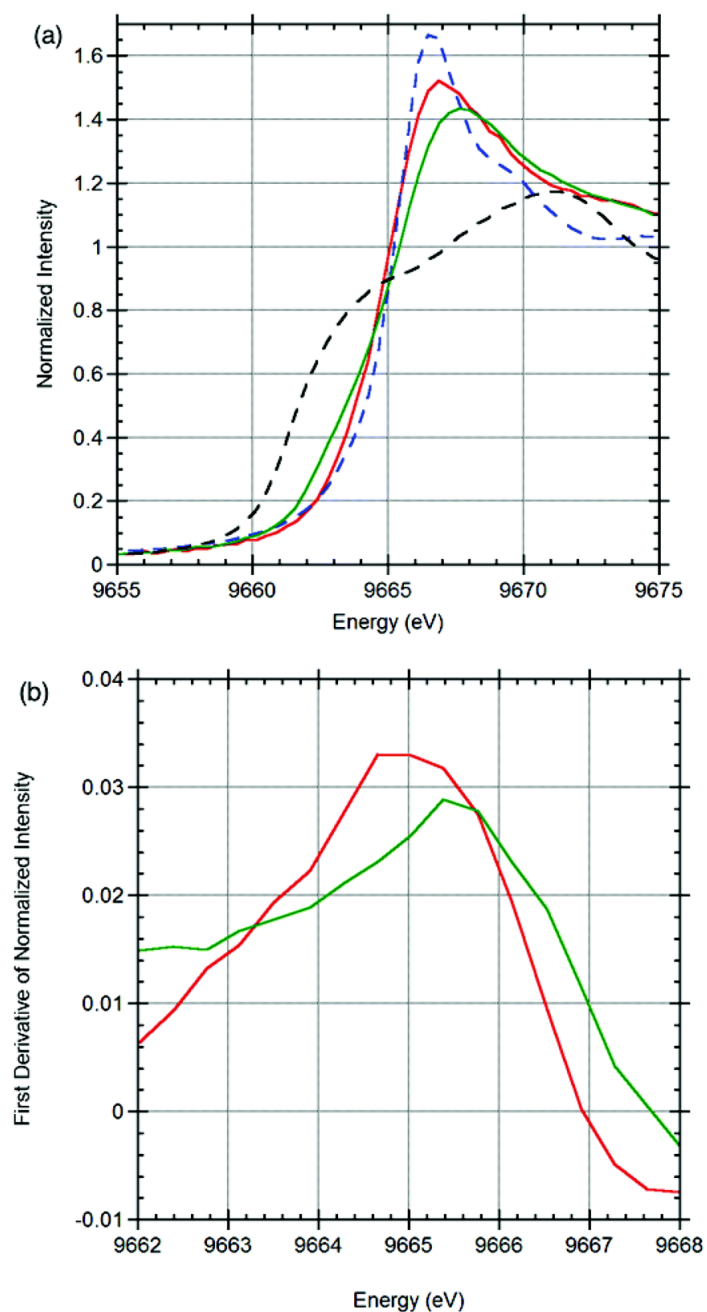


Figure 4: (a) Zn K-edge spectra for Zn foil (dashed black), anhydrous ZnCl_2 (dashed blue), $(\text{IPr})\text{ZnCl}_2\cdot\text{THF}$ (solid red), $(\text{IPr})(\text{Cl})\text{Zn-Fp}$ (solid green) (b) First derivative Zn K-edge spectra for $(\text{IPr})\text{ZnCl}_2\cdot\text{THF}$ (red) and $(\text{IPr})(\text{Cl})\text{Zn-Fp}$ (green)¹²⁶

2.3.2.3. Fe K-Edge Spectroscopy

Selected Fe K-edge data are plotted in Figure 5 and 6, and both rising edge positions and pre-edge positions are tabulated in Table 6.

Table 6: Fe K-Edge data

Entry	Complex	Rising edge Energy ^a (eV)	Pre-edge Energy ^a (eV)
1	Fe foil	7111.3	Not observed
2	FeCl ₂ ^c	7119.7	7111.8, 7113.7
3	FeCl ₃ ^c	7120.7	7113.4
4	K ⁺ Fp ⁻	7123.0	7113.7, 7114.7
5	FpI	7125.1	7112.7, 7115.0
6	FpMe	7123.3	7113.1, 7115.0
7	(IPr)CuFp	7123.9	7113.4
8	(IMes)CuFp	7123.6	7113.4
9	(IPr)(Cl)ZnFp	7124.6	7113.4
10	Fp ₂	7126.2	7114.2

..

^aInflection point energy determined by analysis of first derivative spectra. ^bPeak energies of pre-edge features.¹²⁶ ^cAnhydrous

The spectra for Fp-containing complexes exhibited pre-edge features in the 7112–7115 eV range of approximately 0.2 normalized intensity, consistent with the strong-field, low-symmetry nature of the systems.¹⁴⁷ Previous analyses of highly covalent Fe compounds have revealed that pre-edge energies do not reflect the effective nuclear charge of the Fe and remain relatively constant across multiple oxidation states.¹⁴⁸ A similar pattern was observed in the set of complexes analyzed in this study (Table 6). On the other hand, rising edge energies at the Fe K-edge have been established as reporters of effective nuclear charge at Fe, with a ~1 eV change expected per oxidation state.¹⁴⁸

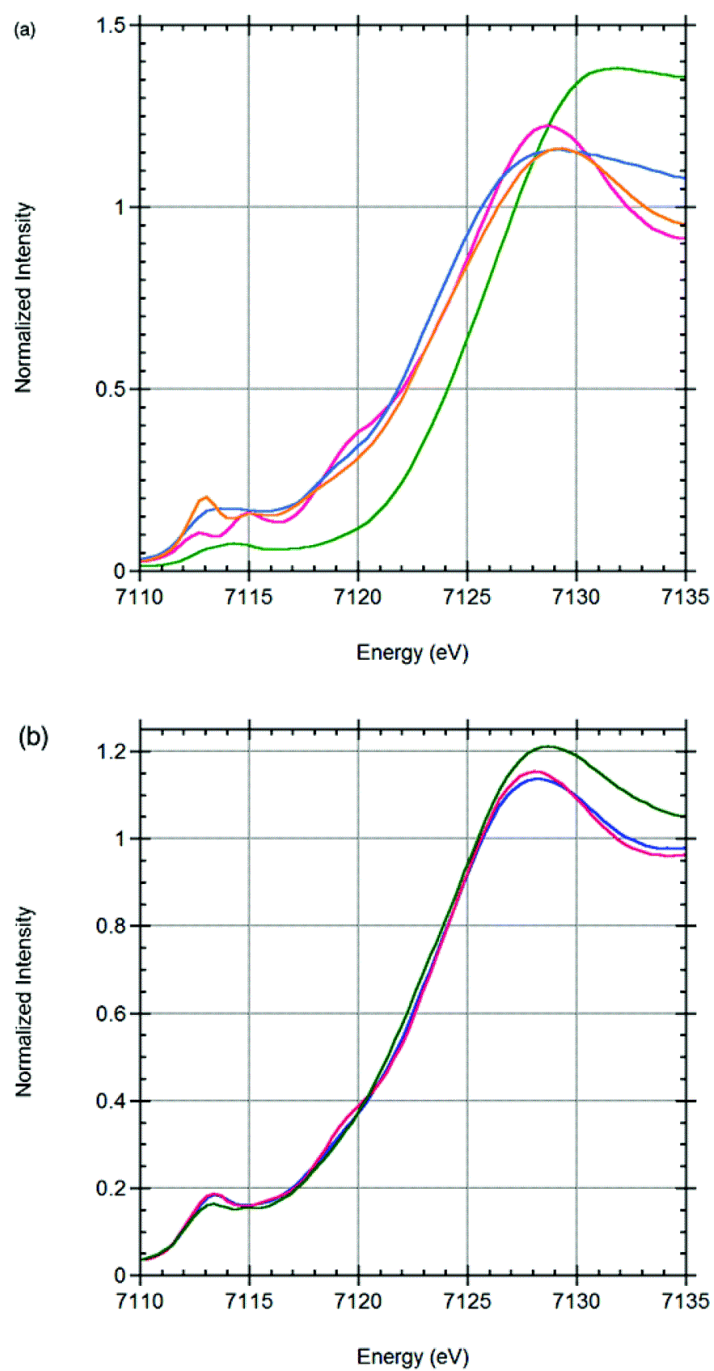


Figure 5: Fe K-edge spectra for (a) Fpl (pink), KFp (blue), FpMe (orange), Fp₂ (green) (b) (IPr)Cu-Fp (pink), (IPr)(Cl)Zn-Fp (green), (IMes)Cu-Fp (blue)¹²⁶

The benchmark complexes K^+Fp^- , FpI , and $FpMe$ (Figure 5a), which have formal oxidation states ranging from Fe(0) to Fe(II), displayed rising edge positions (7123–7125 eV) higher in energy than $FeCl_2$ (7119.7 eV) and $FeCl_3$ (7120.7 eV), indicating high effective nuclear charges at Fe in the Fp compounds resulting from π -backbonding to the carbonyl ligands. The effective nuclear charge at Fe is decreased in $FpMe$ (7123.3 eV) relative to FpI (7125.1 eV), likely due to the strong σ -donating property of the methyl ligand, making it closer in effective Fe nuclear charge to formally Fe(0) complex K^+Fp^- (7123.0 eV). The homobimetallic Fp_2 exhibited a very high-energy rising edge position (7126.2 eV), likely due to the presence of three Fe-CO linkages per metal (rather than two) in its structure (Scheme 36) resulting in anomalously high effective nuclear charge at Fe. Similar effects have been observed at the metal K-edge for systems with multiple CO ligands or other strongly π -acidic groups.^{149–151}

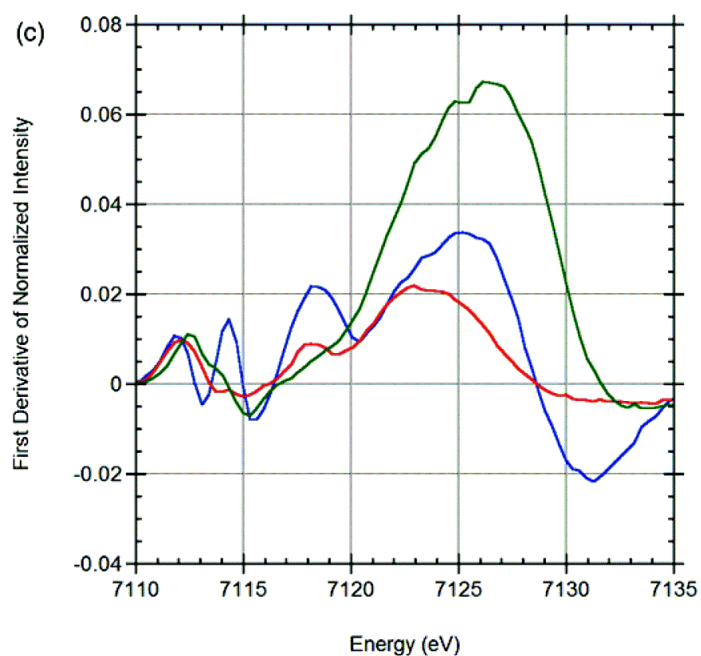


Figure 6: First derivative of Fe K-edge spectra for KfP (red), FpI (blue) and Fp_2 (green)¹²⁶

Although the observed differences in Fe K-edge position are minor when analyzing normalized Fe K-edge intensity, the differences are more pronounced when analyzing derivative spectra (Figure 6). The Cu-Fe bonded complexes (IPr)Cu-Fp and (IMes)Cu-Fp displayed slightly decreased Fe K-edge rising edge positions (~ 7124 eV) compared to FpI and slightly increased compared to K^+Fp^- and FpMe (Figure 5b and 6). This is consistent with the electronic structure description that emerged from Mössbauer analysis: these Cu-Fp complexes feature Cu \rightarrow Fe $d\pi-d\pi$ backdonation that is more pronounced than I \rightarrow Fe $p\pi-d\pi$ backdonation in FpI, counterbalancing Fe \rightarrow Cu σ -donation and making the effective nuclear charge at Fe lower rather than higher. The rising edge position for (IPr)(Cl)Zn-Fp (7124.6 eV) was very similar to those of the Cu-Fe complexes, within the resolution of these experiments.

2.3.3. Elucidation of Redox Cooperativity

We have argued previously for metal–metal cooperativity during bimetallic oxidative addition and bimetallic reductive elimination to be a key factor in facilitating productive catalysis (Scheme 34).⁸⁸ With the complete set of metal K-edge data available, the degree of redox coupling within a heterobimetallic system during such a stoichiometric reaction step can be probed. For example, we have reported previously that the Cu-Fe bonded complex (IPr)Cu-Fp is capable of activating methyl iodide to produce (IPr)CuI and FpMe as products.⁸⁵ Such a R-X bimetallic oxidative addition reaction could, in principle, be used to build a catalytic reaction involving functional group interchange at a carbon–halogen bond if coupled to the known chemistry of FpR complexes¹⁵² and can be considered a model reaction for other catalytically relevant bimetallic redox reactions.

Table 7: Experimentally determined bimetallic cooperativity during oxidative addition

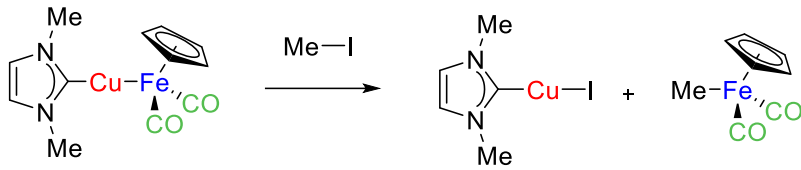
Energy parameter	Before oxidative addition	After oxidative addition	Energy change
Cu K-Edge	8983.5 eV	8983.8 eV	+0.3 eV
Fe K-Edge	7123.9 eV	7123.3 eV	-0.6 eV
νCO^a	1914, 1849 cm^{-1}	1992, 1924 cm^{-1}	+75-78 cm^{-1}

^aDetermined from IR spectroscopy in the solid state.¹²⁶

Tabulating metal K-edge data for the reactants and products in this bimetallic oxidative addition lends insight into the nature of the two-electron redox process. As shown in Table 7, the effective nuclear charges of both Cu and Fe change in subtle ways as evidenced by the minor changes in Cu and Fe K-edge positions, but the changes are not sufficient to account for the 2-electron oxidation expected for a net oxidative addition process. Therefore, despite the subtle electron effects of the Cu-Fe bonding noted from Mössbauer and XANES analyses, the supporting ligands must be participating to a significant extent in the redox process. Carbonyl ligands, in particular, are highly redox non-innocent. Indeed, an average increase of 76.5 cm^{-1} was observed for the coupled CO stretching vibrations upon oxidative addition, consistent with significantly less electron density being delocalized into the π^* (C–O) orbitals in FpMe, the product of oxidative addition, compared to (IPr)Cu-Fp, the more reduced species. The cyclopentadienyl ligand

may also participate to some extent in the redox process: the rising Fe K-edge position in ferrocene/ferrocenium is, similarly, known not to be sensitive to the redox state,¹⁵³ although strong Cp-substituent effects are well known for XAS spectroscopy of ferrocene derivatives.^{154,155} Computation of partial charges within the molecules before and after bimetallic oxidative addition supports this view (Table 8).

Table 8: Computed partial charges during bimetallic oxidative addition

			
Calculated partial charge ^a	Before oxidative addition	After oxidative addition	Change in charge
Cu	0.39	0.20	-0.19
Fe	-1.19	-1.01	+0.18
2CO ^a	0.39	0.72	+0.33
Cp	0.18	0.30	+0.13
IMe	0.23	0.24	+0.01

^aNatural charges from NBO analysis at the BVP86/LANL2TZ(f)/6-311+G(d) level of theory.¹²⁶

In a truncated model system, the calculated changes in partial charge for both Cu and Fe were <0.2e. The CO ligands, indeed, were calculated to experience significant increase in partial charge (0.33e combined). The Cp ligand also was calculated to experience a notable increase in partial charge (0.13e), while the model N-heterocyclic carbene was calculated to be redox-innocent with respect to the bimetallic oxidative addition. Extrapolating to bimetallic oxidative addition and bimetallic reductive elimination steps involving Cu-Fp and Zn-Fp complexes in catalytic scenarios,⁸⁸ one can assume that

this pattern will hold true and that the carbonyl groups will bear the majority of redox changes during catalysis. It is our assertion that this insight will aid future designs for base metal catalysis using the heterobimetallic approach promoted here.

2.4. Conclusions

Collectively, the data presented here support our previous assertion⁸⁵ that the (NHC)M-Fp complexes under study are best described as [(NHC)M]⁺/[Fp]⁻ pairs stabilized by highly polar M-Fe bonds, with the [Fp]⁻ group acting as a pseudohalide ligand with respect to effective nuclear charge at Cu or Zn. Close scrutiny of the physical data reveals that these Cu-Fe and Zn-Fe bonds have certain unique characteristics that distinguish them from M-Fe bonds in the more common “early-late” heterobimetallic M-Fp complexes.^{117–122} Most notably, spectral features reveal dependence on π -symmetry overlap involving filled d-orbitals on Cu or Zn that would be unoccupied in early metal analogues; although these interactions represent anti-bonding orbital mixing, they nonetheless serve to reduce effective nuclear charge at Fe. Additionally, Cu-Fe bond cleavage during bimetallic oxidative addition impacts the effective nuclear charges of Cu and Fe to a minimal extent and instead significantly attenuates π -backbonding into the CO ligands, providing insight into the nature of catalytically relevant multi-electron redox processes. Future strategies for base metal catalysis can be expected to leverage these conclusions in order to devise catalysts through rational design (chapter three).

2.5. Experimental Procedures⁸⁶

2.5.1. Synthesis

2.5.1.1. General Considerations

Unless otherwise specified, all reactions and manipulations were performed under purified N₂ in a glovebox or using standard Schlenk line techniques. Glassware was oven-dried prior to use. Reaction solvents were sparged with argon and dried using a Glass Contour Solvent System built by Pure Process Technology, LLC, or freshly distilled according to standard procedures.¹⁵⁶ Deuterated solvents for NMR spectroscopy were degassed by repeated freeze-pump-thaw cycles and dried by prolonged storage over activated, 3 Å molecular sieves. ¹H NMR and ¹³C{¹H} NMR spectra were recorded at ambient temperature using a Bruker Avance DPX-400 spectrometer, and chemical shifts were referenced to residual solvent peaks. FT-IR spectra were recorded on solid samples in a glovebox using a Bruker ALPHA spectrometer fitted with a diamond-ATR detection unit. Literature procedures were used to prepare the complexes (IPr)CuCl,¹⁵⁷ (IMes)CuCl,¹⁵⁷ (IPr)CuI,¹⁵⁸ KFp,¹⁵⁹ (IPr)ZnCl₂(THF),¹⁶⁰ FpI,¹⁶¹ FpMe,⁸⁵ (IPr)CuFp,⁸⁵ (IMes)CuFp,⁸⁵ (IPr)CuMp,⁸⁵ and (IPr)(Cl)ZnFp,⁸⁵. Unless otherwise indicated, all other chemicals were purchased from commercial sources and used without further purification.

2.5.1.2. Preparation of [K(18-crown-6)₂]⁺[Fp]⁻

(108.9 mg, 0.504 mmol) and 18-crown-6 (133.2 mg, 0.504 mmol) were dissolved in THF (10 mL), generating an orange-red suspension. The solution was stirred overnight and filtered through a medium-porosity fritted funnel. The resulting bright orange solid was washed with pentane and dried in vacuo. Yield: 105.7 mg (74%). ¹H NMR (400 MHz, CD₃CN): δ 4.23 (s, 5 H, Cp), 3.57 (s, 48 H, CH₂). ¹³C{¹H} NMR (400 MHz, CD₃CN): δ 229.2

(CO), 76.8 (Cp), 70.9 (CH₂). IR (solid, cm⁻¹): 2897, 1854 (ν CO), 1775 (ν CO), 1472, 1353, 1253, 1098, 959, 835, 672, 603, 586, 502.

2.5.2. Mössbauer Spectroscopy

The Mössbauer spectroscopy experiments were conducted with a ⁵⁷Co source in a Pd matrix, using constant acceleration mode. The zero velocity point is adjusted to coincide with the isomer shift of α -iron to be zero. AVORTEX silicon drift detector was used with an energy resolution of 200 eV at 14.4 keV, providing excellent background rejection. The linewidths used have varied between 0.4 and 0.6 mm s⁻¹. All data presented here were taken at room temperature. Typical data collection time was a few days, with a baseline count of several millions. The samples were synthesized using natural iron.

2.5.3. Computational Methods

All calculations were performed using Gaussian09, Revision B.01.¹⁶² Density functional theory (DFT) calculations were carried out using a hybrid functional, BVP86, consisting of Becke's 1988 gradient-corrected Slater exchange functional¹⁶³ combined with the VWN5 local electron correlation functional and Perdew's 1986 non-local electron correlation functional.¹⁶⁴ Mixed basis sets were employed: the LANL2TZ(f) triple- ζ basis set^{165,166,167} with effective core potential^{165,168,169} was used for Fe and Cu; the LANL2TZ+ triple- ζ basis set¹⁶⁶ with effective core potential^{165,168,169} was used for Zn; the LANL2DZ double- ζ basis set with effective core potential was used for Cl;^{165,168,169} and the Gaussian09 internal 6-311+G(d) basis set was used for C, H, N, and O. The 2,6-diisopropylphenyl and 2,4,6-trimethylphenyl groups on the NHC ligands were truncated

to methyl groups in order to minimize computational time. Structural geometries were optimized to energy minima, and then frequency calculations were performed to confirm that no imaginary frequencies were present. Molecular orbital surfaces were viewed using Gaussview 4.1.¹⁷⁰ Partial charges were determined by natural population analysis from NBO v. 3.1 within Gaussian09.¹⁷¹

2.5.4. X-Ray Absorption Spectroscopy

Fe K edge (7112 eV), Cu K edge (8979 eV) and Zn K edge (9659 eV) for the samples were measured at 10ID beamline at the Advanced Photon Source, Argonne National Laboratory.¹⁷² A rhodium coated harmonic rejection mirror was used to eliminate higher energy photons. Experiments were performed in transmission mode. A mixture of 70% helium and 30% nitrogen gas was used in the initial ion chamber I_0 placed before the sample and full nitrogen gas in transmission and reference ion chambers. The gases in the ion chambers were optimized for adequate absorption of photons. Samples and standards were spread uniformly on kapton tape and stacked for obtaining the right edge height for each of the three edges. The samples were loaded in an air sensitive sample holder that was kept filled with helium gas during the measurements. Metal foils were measured with the help of the reference ion chamber for every scan taken at Fe, Cu and Zn edges, respectively. The spot size of the incident X-ray beam on the sample was 500 micron \times 500 micron. Measurements were done in quick scanning mode, where the undulator gap and taper were fixed while the Bragg angle of the double crystal monochromator (with Si(111) crystal) was scanned at a constant speed. Several scans were taken on each sample and then averaged to obtain satisfactory statistics. The samples were re-measured after purposely exposed to air to establish that the data presented do not correspond to oxidized samples. Analysis of the sequential individual

scans established that the samples were not incurring any measurable radiation damage during the experiment. Data collected were processed using the Athena software.¹⁷³ Normalization of each data set was carried out in the following way. After subtracting background by fitting the pre-edge region, $\chi(\mu)$ was fit between 50 and 150 eV far enough from the post-edge features and then extrapolated to $E = 0$. Normalization was done by dividing the spectra by the edge height at $E = 0$.

Chapter 3
Theoretical Investigations of the Structure and Reactivity of Heterobimetallic
Complexes

Reproduced in part with permission from Karunananda, M. K.; Parmelee, S. R.; Waldhart, G. W.; Mankad, N. P. *Organometallics*. **2015**, 34, 3857-3864.

© 2015 American Chemical Society

Reproduced in part with permission from Banerjee, S.; Karunananda, M. K.; Bagherzadeh, S.; Jayarathne, U.; Parmelee, S. R.; Waldhart, G. W.; Mankad, N. P. *Inorg. Chem.* **2014**, 53, 11307-11315.

© 2014 American Chemical Society

3.1. Opening Remarks

As mentioned earlier in chapter one, chapter two and three are dedicated to investigating the structural and functional features of the polar heterobimetallic complexes introduced by Mankad group.⁸⁵ Chapter three presents a theoretical analysis of heterobimetallic complexes capable of polar substrate activations⁸⁵ and small molecule activations,¹⁷⁴ using DFT. The mechanisms of these reactions are investigated using transition state calculations. The charges and bond orders of the individual components of a typical heterobimetallic system, as it undergoes bimetallic oxidative addition and bimetallic N₂O activation are probed using IRC calculations. Some thermodynamic parameters such as ΔH^\ddagger , ΔG^\ddagger and ΔS^\ddagger are also calculated. The key components of the complexes functional during these reactions are identified using the theoretical analysis presented here and the experimental analysis presented earlier (chapter two). A series of new heterobimetallic complexes synthesized by the Mankad group keeping these key components intact or enhanced is also studied using DFT calculations and the structural trends present are elucidated. The trends uncovered aid in future reaction development (chapter four).

3.2. Bimetallic Oxidative Addition

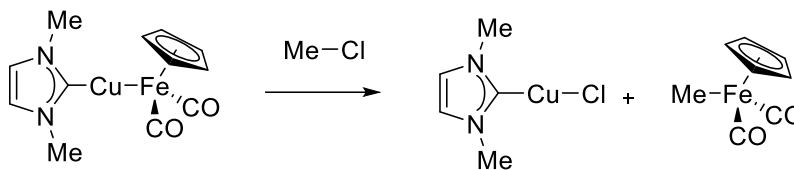
3.2.1. Introduction

As emphasized in chapter two, whilst oxidative addition (OA) and reductive elimination (RE) in single-site catalysts have been studied extensively, their mechanistic features in bimetallic catalysts remain underexplored.^{83,84,117,175} Out of the examples present, most of the studies in literature on bimetallic oxidative addition (BOA) and bimetallic reductive elimination (BRE) are focused on noble metals which are also capable of single-site OA and RE steps^{81,97,108,176–197} while studies on earth-abundant first-row transition metals which do not favor single-site mechanisms¹⁹⁸ are scarce.^{199–211}

In chapter two, an experimental study on a BOA was presented on a copper-iron heterobimetallic system capable of activating methyl iodide. The (IPr)Cu-Fp (IPr = *N,N'*-bis(2,6-diisopropylphenyl)-imidazol-2-ylidene, Fp = FeCp(CO)₂) complex studied, had previously shown catalytic activity in C-H borylation of arenes utilizing bimetallic OA and RE steps on B-H and H-H substrates respectively.

To better understand the nature of the bimetallic reaction pathways in this system, our group has conducted a thorough mechanistic study of alkyl halide activation by the Cu-Fe heterobimetallic reaction center.⁸⁷ Use of cyclopropylmethyl halide substrates as radical clocks established that alkyl halide activation occurs by a two-electron mechanism for alkyl bromides and chlorides but not iodides. Eyring analysis of the activation of benzyl chloride allowed for experimental determination of activation parameters, including a large and negative entropy of activation ($\Delta S^\ddagger = -36$ eu). A Hammett study with para-substituted benzyl chlorides revealed a reaction constant of $\rho = 1.6$, indicating accumulation of negative charge in the transition state on the alkyl halide carbon. The Ru analogue, (IPr)Cu-Rp (Rp = RuCp(CO)₂), was found to react approximately 17–25 times more slowly with selected benzyl chlorides than (IPr)Cu-Fp, indicating that the relative nucleophilicities of the free metal carbonyl anions are predictive of the relative reactivities of their heterobimetallic counterparts.

In this section, the mechanistic investigations are continued through theoretical calculations. The oxidative addition of methyl chloride into (IMe)Cu-Fp, a model of (IPr)Cu-Fp, is studied (Scheme 37) computationally. The transition state of the reaction, and the thermodynamic parameters associated with it (ΔH^\ddagger , ΔG^\ddagger and ΔS^\ddagger), are calculated and they correlate well with the experimental values deduced by the Mankad group.⁸⁷



Scheme 37: Bimetallic oxidative addition of MeCl

3.2.2. Results & Discussion

In order to examine the heterobimetallic reaction computationally, we chose to begin with gas-phase DFT calculations at the BVP86/LANL2TZ(f) level of theory on the model reaction between the reactants (IMe)Cu-Fp + CH₃Cl to yield products (IMe)Cu-Cl + Fp-CH₃ (IMe = *N,N'*-dimethylimidazol-2-ylidene) (Scheme 37). The overall reaction was calculated to be exergonic by $\Delta G_{298\text{ K}} = -20.0$ kcal/mol. A transition state (**TS1**) for this reaction was identified computationally as lying higher in energy by $\Delta G_{298\text{ K}}^{\ddagger} = +26.2$ kcal/mol than the individual reactants. A surprisingly good match was found between the calculated activation parameters for the (IMe)Cu-Fp + CH₃Cl reaction ($\Delta H^{\ddagger} = +14.6$ kcal/mol; $\Delta S^{\ddagger} = -39.0$ eu) and the experimental ones for the (IPr)Cu-Fp + benzyl chloride reaction ($\Delta H^{\ddagger} = +13(2)$ kcal/mol; $\Delta S^{\ddagger} = -36(7)$ eu).⁸⁷ When benzene solvation was included in the calculations, these energetics differed by only ~2 kcal/mol compared to the gas phase values, and so gas-phase calculations were utilized subsequently.

The calculated energetics of this pathway are consistent with the experimental observation of the reaction occurring at ambient conditions. For comparison, an alternative mechanism would involve ionization of the Cu-Fe bond to reveal [Fp]⁻, which could then react with the alkyl halide by the known S_N2 pathway.²¹² We have previously calculated that the [(IMe)Cu]⁺[Fp]⁻ ion pair is higher in energy by >80 kcal/mol than neutral (IMe)Cu-Fp in benzene solution, i.e., too high in energy to be accessible under ambient

conditions.⁸⁹ This fact, combined with the phenomenological observations regarding product profiles,⁸⁹ causes us to rule out this alternative pathway, as it is inconsistent with experimental observations.

The structure of **TS1** (Figure 7) results from approach of CH₃Cl toward a point between Cu and Fe along a trajectory that bisects one of the Cp(centroid)-Fe-CO angles. The C-Cl bond is almost fully broken (2.45 Å) relative to the calculated C-Cl distance in free CH₃Cl (1.84 Å). The [CH₃] unit is planar, resembling the stereoinvertive transition-state structure of a typical S_N2 reaction. The Cu-Fe bond is intact but slightly elongated (2.41 Å) relative to the reactant structure (2.33 Å). The Cu...CO interaction nearest to the incoming CH₃Cl molecule is elongated (2.94 Å) relative to the reactant structure (2.57 Å), while the Cu...CO interaction on the face opposite the incoming CH₃Cl molecule is contracted (2.22 Å) relative to the reactant structure (2.49 Å). Because no new Cu-CO bond ultimately forms in the products, this latter Cu...CO contraction in **TS1** highlights the templating role played by that CO ligand, holding the bimetallic transition-state structure together as the Cu-Fe bond breaks.

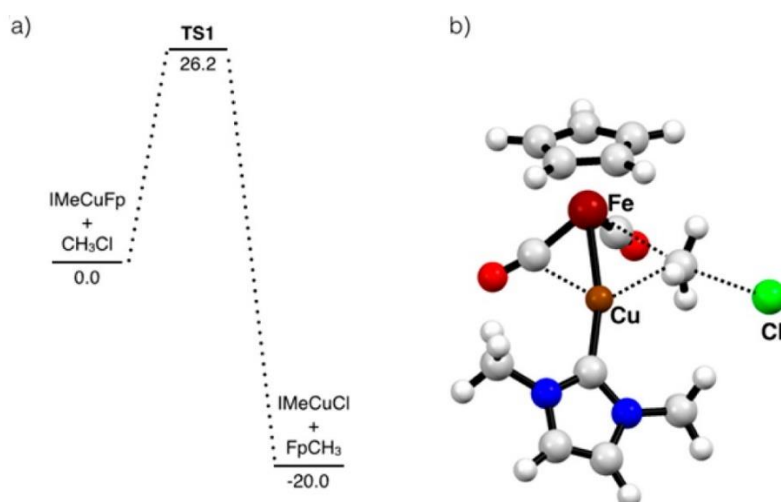


Figure 7: a) Calculated reaction coordinate diagram for reactants (IMe)Cu-Fp + CH₃Cl to products (IMe)Cu-Cl + Fp-CH₃ with relative free energies given in kcal/mol at 298 K. b) Structure of TS1⁸⁷

The Fe-CH₃ bond is only slightly formed (2.85 Å) relative to the calculated distance in the Fp-CH₃ product (2.05 Å). The [CH₃] carbon also engages in a close Cu...C contact (2.19 Å) despite the fact that no new Cu-C bond forms in the products, indicating that the Cu center plays an important role in the transition state, as well. NBO calculations on **TS1** were carried out to analyze how both natural charge distribution and bonding interactions change during the reaction pathway. For comparative purposes (see Figure 7a), we also present these data for the reactants and products.

Selected natural charge data are compiled in Table 9. Consistent with the formally BOA process, the [Fp] fragment is oxidized during the reaction. As we have noted before in chapter two,^{89,86} within the [Fp] fragment the redox chemistry is dominated by the CO ligands (Table 9) and Cp ligand, and the natural charge on Fe is relatively constant (between $q = -1.17$ and -1.00) throughout the reaction pathway. Regarding the CH₃Cl molecule undergoing BOA, there is essentially no change in natural charge residing on

the [CH₃] unit. The chloride, however, experiences dramatic ionization at **TS1** and remains largely anionic in character in the (IMe)Cu-Cl product.

Table 9: Calculated natural charges along the reaction coordinate⁸⁷

Complex	$q(\text{IMeCu})$	$q(\text{Fp})$	$q(2\text{CO})$	$q(\text{CH}_3)$	$q(\text{Cl})$
Reactants	0.62	-0.62	0.39	0.08	-0.08
TS1	0.28	-0.28	0.48	0.10	-0.50
Products	0.52	0.01	0.72	-0.01	-0.52

Selected Wiberg and Mayer bond index data are compiled in Table 10. As expected, the CH₃Cl carbon experiences a smooth increase in bonding interaction with the Fe center during the reaction. Of particular note is that while a Cu-CH₃ bond does not form in the products, there is a significant Cu-CH₃ interaction in **TS1** of equal magnitude to the Fe-CH₃ interaction. This observation indicates that **TS1** is a true bimetallic transition state, where both Cu and Fe interact with the BOA substrate equally. As expected because the [(IMe)Cu] and [Fp] fragments are separating in this reaction, the Cu...CO interaction with the carbonyl group proximal to the incoming CH₃Cl substrate experiences a smooth decrease during the reaction. Of particular note is the Cu...CO interaction distal to the incoming CH₃Cl molecule. Whereas this semi-bridging Cu...CO interaction in (IMe)Cu-Fp ultimately breaks, the interaction is actually amplified in **TS1**. In other words, the distal semi-bridging CO ligand bridges the Cu-Fe bond more significantly in the transition state than in either the reactants or the products. This observation indicates that, in addition to playing an important role in the redox changes during BOA and BRE (chapter two),^{89,86} the semi-bridging CO ligands also play a key structural role, essentially templating the bimetallic transition state to stabilize it as the metal-metal bond is breaking.

Table 10: Selected Wiberg and Mayer bond index values along the reaction coordinate^a

Complex	Cu-C(methyl)	Fe-C(methyl)	Cu-C(proximal CO) ^b	Cu-C(distal CO) ^b
Reactants	0.00/0.00	0.00/0.00	0.13/0.13	0.15/0.15
TS1	0.25/0.25	0.31/0.31	0.07/0.07	0.26/0.26
Products	0.00/0.00	0.71/0.71	0.00/0.00	0.00/0.00

^aValues are given as Wiberg/Mayer ^bProximal and distal refer to the position of a CO ligand relative to the incoming CH₃Cl molecule.⁸⁷

Lastly, we attempted to study transition states related to **TS1** with various para-substituted benzyl chloride substrates in place of CH₃Cl. A similar transition state, **TS2-H**, was located for the parent benzyl chloride, with a similar barrier height to that for CH₃Cl ($\Delta G^\ddagger_{298\text{ K}} = +28.6$ kcal/mol) and with similar activation parameters ($\Delta H^\ddagger = +15.8$ kcal/mol; $\Delta S^\ddagger = -43.0$ eu). Transition states also were located for benzyl chloride substrates with cyano, methyl, and methoxy substituents in the para position (**TS2-CN**, **TS2-Me**, **TS2-OMe**). Unlike the experimentally determined Hammett reaction constant of $\rho = 1.6(2)$,⁸⁷ the barrier heights corresponding to **TS2-H**, **TS2-CN**, **TS2-Me**, and **TS2-OMe** were very similar (between +27.1 and +28.6 kcal/mol), indicating a Hammett constant close to zero. When conducting the calculations with a different DFT functional (B3LYP instead of BVP86) or when including implicit benzene solvation, the absolute values of the energies changed, but the collective trend remained unchanged. While this inability to reproduce a kinetic parameter in the BOA reaction is likely reflective of the various sources of error associated with quantitatively correlating computational mechanisms to experimental rate constants (especially regarding entropic contributions to highly polarized systems such as this one),^{213,214} we are nonetheless confident in the ability of our model to qualitatively

reveal the detailed nature of the BOA transition state highlighted in the discussion of **TS1** above.

3.2.3. Conclusions

In conclusion, the transition states for alkyl halide BOA by (IPr)Cu-Fp and related complexes have been characterized by computational methods. Computational analysis revealed important features of the transition state unavailable from experimental data, including the dual role of the carbonyl ligands in the [Fp] group both of acting as redox non-innocent ligands during the BOA reaction and also of providing structural stability to the transition state as the metal-metal bond cleaves.

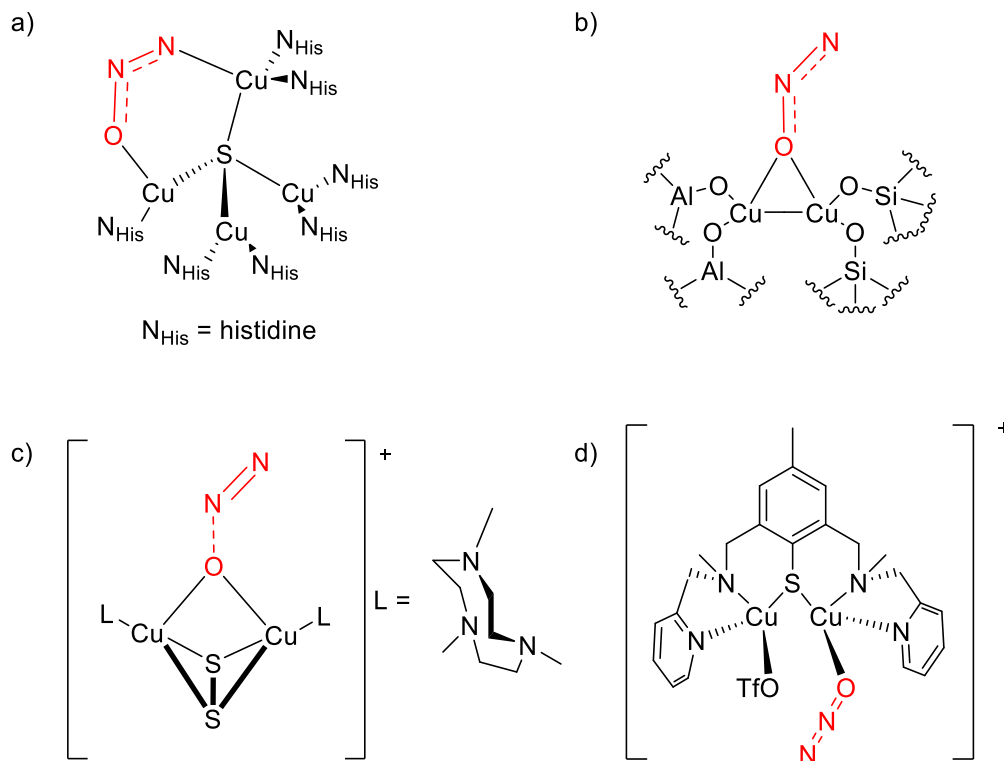
3.3. Bimetallic N₂O Activation

3.3.1. Introduction

N₂O is an ozone depletion agent and a greenhouse gas three hundred times more potent than CO₂.^{215,216} Activating N₂O and using it as an oxygen-donating agent is highly desirable, especially since the only byproduct is N₂ which is environmentally harmless. Although oxygen-atom abstraction from N₂O is thermodynamically favorable due to the stability of the byproduct N₂ with a strong N-N triple bond, it still remains a challenging conversion since it's burdened with high kinetic barriers which are hard to overcome as N₂O is a poor ligand. Nonetheless, some successful examples of stoichiometric²¹⁷ and catalytic conversions have been reported.

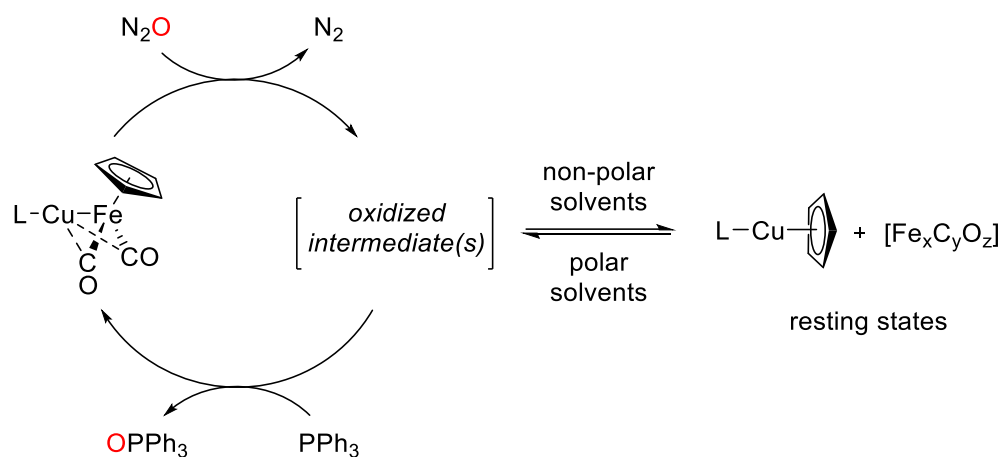
Nature catalyzes N₂O deoxygenation utilizing the enzyme, nitrous oxide reductase (N₂OR). The catalytic site of N₂OR is a tetracopper sulphide cluster that is thought to bind N₂O in a μ -1,3-N,O fashion using two adjacent Cu centers (Scheme 38a).²¹⁸ Similarly, a

Cu-ZSM-5 zeolite material capable of catalyzing oxidation reactions with N_2O ²¹⁹ is thought to bind N_2O in a μ -1,1-O fashion using pairs of Cu centers spaced at appropriate distances (Scheme 38b).²²⁰ Molecular Cu complexes capable of N_2O activation also typically utilize homobimetallic cooperativity. Cramer, Tolman and co-workers reported the stoichiometric deoxygenation of N_2O by a tricopper disulphide complex, where N_2O activation was proposed to occur by μ -1,1-O interaction with a transient dicopper intermediate (Scheme 38c).²²¹ Beloglazkina and co-workers reported electrocatalytic N_2O deoxygenation as well as catalytic oxygen-atom transfer from N_2O to PPh_3 using a dicopper catalyst, although the nature of N_2O binding to the catalyst was not addressed.²²² Torelli and co-workers reported an asymmetric dicopper thiolate species capable of stoichiometric N_2O deoxygenation, and terminal η -1-O binding of N_2O to one of the two Cu centers (Scheme 38d) was proposed.²²³



Scheme 38: Proposed homobimetallic N_2O binding to Cu-containing active sites:
a) the catalytic site of N_2OR by Solomon b) adjacent Cu sites in Cu-ZSM-5 by Solomon c) a copper disulphide model complex by Tolman d) a copper thiolate model complex by Ménage

Recently, our group reported a heterobimetallic system capable of stoichiometric oxygen atom transfer from N_2O to PPh_3 .¹²⁴ The (IMes)Cu-Fp complex (IMes = *N,N'*-bis(2,4,6-trimethylphenyl)imidazol-2-ylidene, Fp = FeCp(CO)₂) reacted with N_2O and PPh_3 to give N_2 and $OPPh_3$. The resting states of the catalyst were hypothesized to be (IMes)Cu-Cp and an unknown $Fe_xC_yO_z$ species (Scheme 39). Preliminary experiments hinted the possibility of a catalytic cycle. Since the intermediates involved in the reaction were not identified experimentally, a theoretical investigation was carried out to probe the reaction pathway using DFT calculations. The analysis is presented here.



Scheme 39: Hypothetical catalytic scheme for N₂O activation

3.3.2. Results & Discussion

Theoretical investigation of the oxygen-atom transfer reactions from N₂O to PPh₃ mediated by our Cu-Fe heterobimetallic complexes are presented here. As mentioned in the introduction, since the experimental evidence was inconclusive, we sought to model the intermediates associated with N₂O bonding and/or N₂ loss computationally. The model complex (IMe)CuFp (**A**, IMe = N,N'-dimethylimidazol-2-ylidene) was used for computations, and different N₂O-bound isomers were examined. Energy minima for (IMe)Cu(μ-N₂O)Fp with μ_{1,1}-N (**B**), μ_{1,3}-N,O (**C**), and μ_{1,2}-N,N (**D**) binding were located (Figure 8). These were identified as possible intermediates in the bimetallic N₂O activation process.

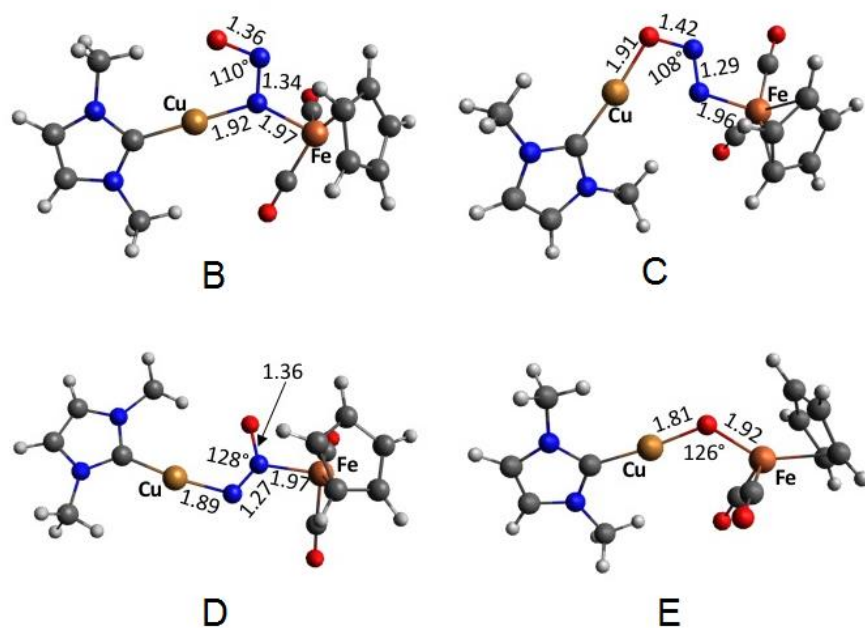


Figure 8: Intermediates of N_2O activation by (IMe)Cu-Fp **B**) μ -1,1-N isomer **C**), μ -1,3-N,O isomer **D**) μ -1,2-N,N isomer **E**) N_2 dissociated (IMe)Cu(μ -O)Fp species modelled by DFT calculations. Bond distances are shown in angstroms, and all displayed angles refer to $\angle\text{N-N-O}$. Color code: C, grey; H, white; Cu, bronze; Fe, orange; N, blue; O, red.

Of these isomers, species **B** was lowest in energy ($\Delta G = +17.3$ kcal/mol relative to **A** + N_2O). The species **C** and **D** were only slightly higher in energy (+18.2 kcal/mol and 19.2 kcal/mol respectively). Because μ -1,3-N,O and μ -1,1-O binding are most commonly invoked in the bimetallic N_2O activation literature,²²⁴ we also attempted to locate an energy minimum for a μ -1,1-O isomer. However, geometry optimizations for a such a species from different starting geometries invariably yielded the intermediate (IMe)Cu(μ -O)Fp (**E**) with a dissociated N_2 outside of bonding distance from the other atoms of the molecule. The combination of **E** and N_2 was significantly lower in energy than the intermediates **B**, **C** and **D** (Figure 9).

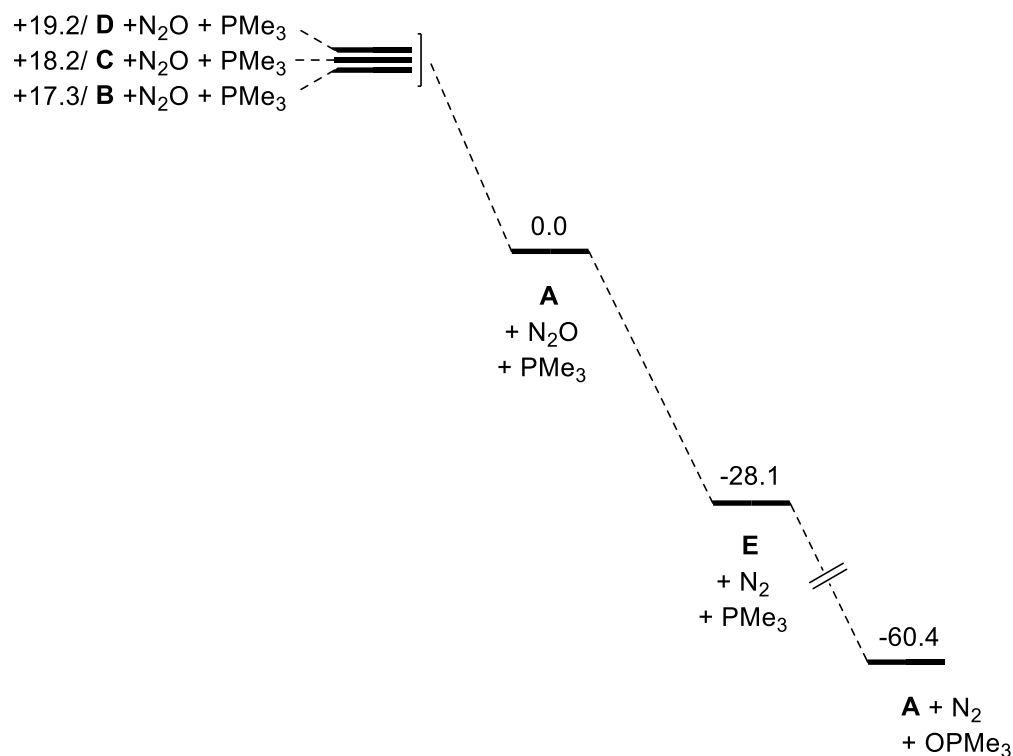


Figure 9: Reaction energy profile, determined by DFT modelling.
 Reaction free energies (ΔG at 298 K) are shown in units of kcal/mol,
 and intermediate labels refer to species in Figure 8.

When analyzed further, a transition state with μ -1,1-O binding (**TS3**) was located along the reaction coordinate connecting **A** and **E** (Figure 10). The activation energy associated with **TS3** ($\Delta G^\ddagger = +25.2$ kcal/mol) is similar in magnitude to the minimum energies for **B**, **C**, and **D**. Therefore, at this time we favor the reaction between **A** and N₂O producing species **E** via transition state **TS3** and without any N₂O-bound energy minimum along the reaction pathway (Figure 10).

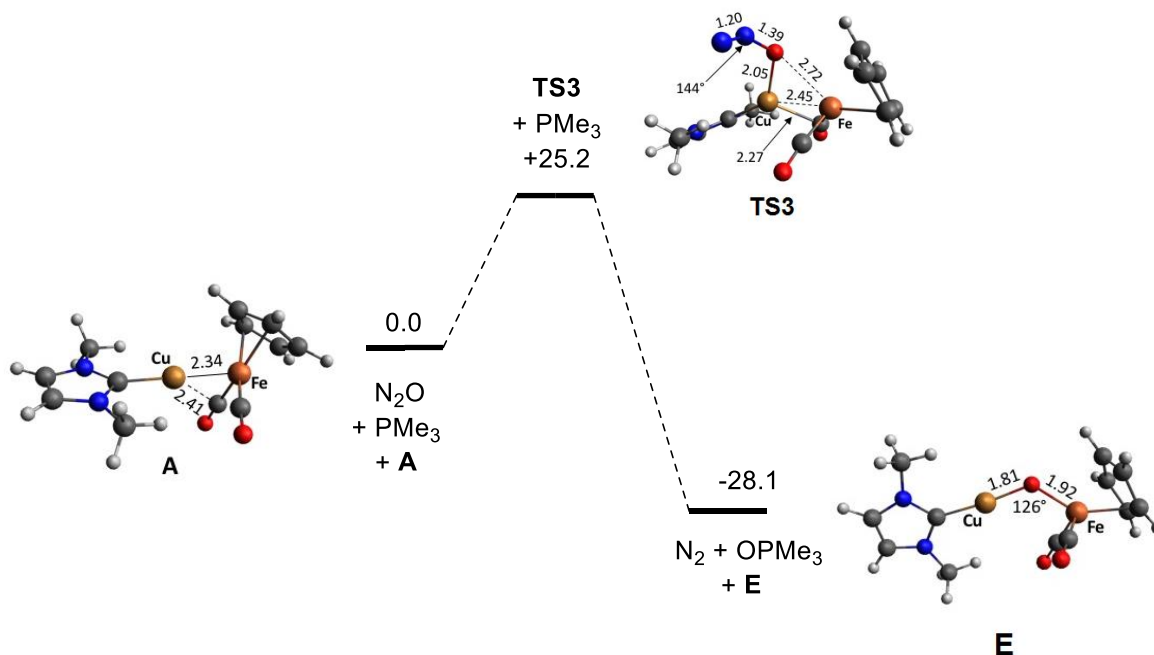


Figure 10: Calculated reaction coordinate diagram for reactants (IMe)Cu-Fp (A**) + N₂O to (IMe)Cu-(μ-O)Fp (**E**) + N₂ through transition state **TS3** with relative free energies given in kcal/mol at 298 K**

However, involvement of intermediates such as **B**, **C**, and **D** cannot be ruled out definitively at this time. Transition state **TS3** for N₂O deoxygenation by **A** is qualitatively similar to transition states previously identified for bimetallic oxidative addition reactions between **A** and CH₃Cl (section 3.2) and between (IMe)CuRp (Rp = RuCp(CO)₂) and H₂ (chapter five), in that (a) both metal centers interact with a single atom of the incoming substrate and (b) a CO ligand bridges the two metal sites in the transition state more strongly than in the ground state, presumably to provide stability to the elongating metal-metal bond.

Unlike in previous calculations, in transition state **TS3**, the incoming N₂O molecule does not approach the midpoint of the metal-metal bond but rather approaches the Cu center more directly than the Fe center. This bias of N₂O approach towards one of the two

metal sites closely resembles di-copper transition states for N₂O activation identified by Sels, Schoonheydt and Solomon²²⁰ (Scheme 38b) and by Cramer and Tolman²²¹ (Scheme 38c), the latter of which involves asymmetric μ -1,1-O binding in the transition state despite the homobimetallic di-copper species itself being completely symmetrical.

The overall catalytic transformation is calculated to be exothermic by $\Delta G = -60.4$ kcal/mol. Approximately half of this energy release ($\Delta G = -28.1$ kcal/mol) comes from N₂O deoxygenation by the catalyst and liberation of N₂ (Figure 10) The resulting species after N₂O deoxygenation is the bridging oxo complex **E**. The LUMO of **E** has Fe-O σ^* character, with large oxygen 2p contribution oriented in a way that is appropriate for backside attack by a nucleophilic phosphine (Figure 11).

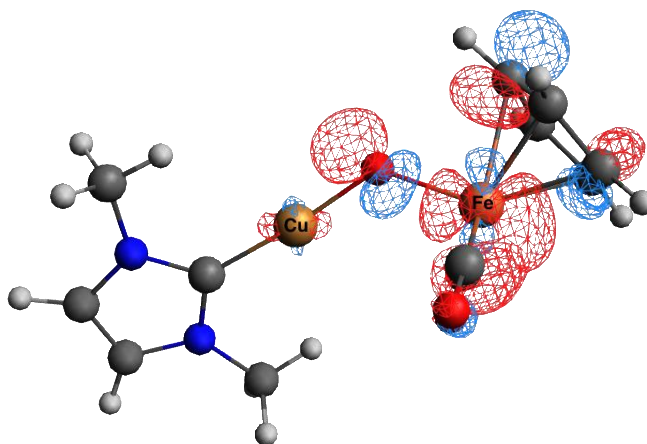


Figure 11: Orbital surface for the LUMO of **E calculated by DFT (0.04 isovalue)**

In contrast, the N₂O-bound intermediates **B**, **C**, and **D** do not possess low-energy orbitals with significant oxygen 2p character, and so P-O bond formation from these intermediates is less likely. Therefore, at this time we favor **E** as being the electrophilic oxygen-atom donor along the catalytic reaction pathway. Bimetallic M(μ -O²⁻)M' complexes with a single oxygen-atom bridging ligand are known to be quite unstable when the total d-electron count of the molecule exceeds 10,²²⁵ as it does in **E**. Consequently, it is

reasonable to expect intermediate **E** to have decomposition pathways competing with productive phosphine oxidation; one of these pathways might ultimately result in Cp migration to Cu and generation of the catalytic resting states observed experimentally.

3.3.3. Conclusions

In conclusion, a heterobimetallic oxygen-atom transfer reaction from N_2O to PPh_3 has been probed computationally using DFT calculations. Possible N_2O bound intermediates were located as well as a $(\text{IMe})\text{Cu}(\mu\text{-O})\text{Fp}$ (**E**) intermediate after a potential N_2 release step. The transition state for this heterobimetallic N_2O activation step, resulting in the oxygen-atom transfer to the heterobimetallic species, has been located. The transition state of this N_2O activation shows structural similarities to the transition states of CH_3Cl (section 3.2) and H_2 (chapter 5) activations: CO ligands play a templating role in keeping the transition state stable as the metal-metal bond breaks.

3.4. Key Functional Components of Heterobimetallic Catalysts

In conclusion, the $(\text{IPr})\text{Cu-Fp}$ complexes developed by Mankad group which are active catalysts for C-H activation⁸⁸ show some interesting functional features. Mechanistic investigations reveal that the analogous monometallic counterparts are unable to show reactivity individually, proving that both the metals are required for catalysis.^{88,89} Calculated charges and bond orders of the metals before, after and during bimetallic activations (CH_3Cl and N_2O) also confirm that both the metals do contribute to the reactivity (chapter two, sections 3.2 and 3.3).^{86,87}

Even though we originally hypothesized that the two transition metals would exclusively perform redox activity during catalysis, spectroscopic data reveals that the bulk of the redox chemistry is carried out by the non-innocent CO ligands (chapter two).

Theoretical investigations resulting in transition state calculations of both MeCl and N₂O activation reactions reveal that the CO ligands also play a bridging role, stabilizing the transition state as the metal-metal bond breaks (sections 3.2 and 3.3).

3.5. Development and Characterization of a Toolkit of Heterobimetallics

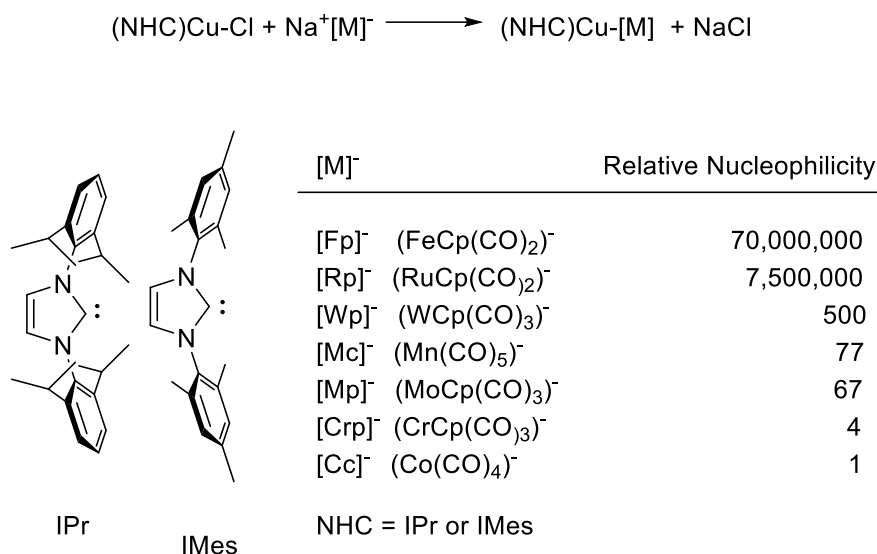
3.5.1. Introduction

The polar unsupported complexes of the type (NHC)Cu-Fp developed by Mankad group⁸⁵ have shown reactivity in both C-H activation⁸⁸ and small molecule activation reactions¹²⁴. As demonstrated earlier (chapter two, section 3.2 and 3.3), mechanistic investigations of the reactions done by these heterobimetallic complexes reveal bimetallic analogues of the classical oxidative addition and reductive elimination reactions,^{86,87} and so we have speculated that other reactions traditionally conducted with single-site noble-metal catalysts might be viable using this bimetallic approach.¹²³ In order to probe such questions and fully explore the possibilities of such heterobimetallic catalysts, it is substantial to synthesize and characterize a more comprehensive series of (NHC)Cu-[M] complexes that can collectively access a vast chemical reactivity space.^{122,226–229}

The mechanism of the bimetallic OA and RE reactions such as demonstrated in C-H activation, relies on subtle interplay between the nucleophilicity of the [Fp][−] moiety and the electrophilicity of the [(NHC)Cu]⁺ fragment and highlights the need to vary both of these parameters in a controlled manner for future reaction development. As a starting point in expanding our heterobimetallics, we sought to retain the electrophilic [(NHC)Cu]⁺ fragment and vary the nucleophilic [Fp][−] fragment. Due to their key functional role (section 3.4), retaining CO ligands in the nucleophilic metal fragment was deemed desirable.

Fortunately, [Fp][−] is but one of a series of anionic metal carbonyls whose relative nucleophilicities have been quantified and span an impressively large range (Scheme 40

).¹⁴⁶ These nucleophilicity data, which represent a kinetic parameter, also correlate well with thermodynamic reduction potentials and possibly with pK_a .^{230,231} Using this series of nucleophiles, Mankad group reported the synthesis and crystallographic characterization of a set of (NHC)Cu-[M] complexes using the same strategy as they've previously demonstrated (Scheme 40).²³²



Scheme 40: Synthesis of (NHC)Cu-[M] complexes. Abbreviations and relative nucleophilicity data for [M]⁻ anions have been taken from ref 145

This section examines these new complexes computationally. The analysis includes calculated bond indices and elucidation of molecular orbital diagrams. Structural trends that emerge with respect to nucleophilicity are also determined. Collectively, this series of complexes provides a toolbox of potential catalysts for future reaction discovery, with fine control of structure–function relationships, that will access an expansive chemical space unavailable to just the initial (NHC)Cu-Fp complexes.

3.5.2. Results & Discussion

We have previously established, through computational methods^{85,86} as well as chemical reactivity studies^{85, 174,86, 88} and spectroscopic analyses (chapter two),⁸⁶ that the Cu-Fe bond in (IPr)Cu-Fp is polarized such that the Cu retains positively charged, electrophilic character and the Fe retains negatively charged, nucleophilic character (i.e., the Cu-Fe bond possesses a significant degree of ionic character). Because of the varying nucleophilicities and reducing potentials of the $[M]^-$ anions used in this study to construct (IPr)Cu-[M] complexes,^{146,230,231} we chose to undertake computational analysis to examine how this polar, ionic Cu-M bonding is affected by the identity of $[M]^-$.

Model complexes featuring the truncated IMe ligand (where IMe = N,N'-dimethylimidazol-2-ylidene) in place of IPr were examined using density functional theory (DFT), with the BVP86 functional, the LANL2TZ(f) basis set for metal centers, and the 6-311G+(d) basis set for non-metal atoms. As demonstrated previously with (IMe)Cu-Fp, (IMe)Cu-Mp, and related complexes, this level of theory provided excellent correlation with experimentally determined structural parameters and vibrational frequencies.

Table 11: Calculated and experimental bond distances for (IMe)Cu-[M] model complexes^a

Complex ^b	Calculated ^a $d(\text{Cu-M})$ (Å) /FSR ^c	Experimental ^{a,f} $d(\text{Cu-M})$ (Å)/FSR ^c	Calculated ^a $d(\text{Cu}\cdots\text{CO})$ (Å) ^d	Experimental ^{a,f} $d(\text{Cu}\cdots\text{CO})$ (Å) ^d
(IMe)Cu-Fp ^e	2.330/0.997	2.3462(5)/1.004	2.490, 2.574	2.423(3), 2.749(3)
(IMe)Cu-Rp	2.441/1.011	2.4387(9)/1.010	2.739, 2.755	2.610(6), 2.828(5)
(IMe)Cu-Wp	2.535/1.025	2.5345(6)/1.025	1.971, 1.971, 1.975	2.272(5), 2.300(7), 2.468(6)
(IMe)Cu-Mc	2.408/1.028	2.415(1)/1.032	2.434, 2.434, 3.054, 3.055	2.63(1), 2.66(1), 2.644(6), 2.973(6)
(IMe)Cu-Mp ^e	2.588/1.050	2.5600(8)/1.039	2.194, 2.196, 3.640	2.193(7), 2.322(7), 3.861(7)
(IMe)Cu-Crp	2.468/1.052	2.4569(7)/1.048	2.172, 2.172, 3.556	2.174(4), 2.237(5), 3.547(5)
(IMe)Cu-Cc	2.315/0.994	2.3423(6)/1.005	2.486, 2.501, 2.660, 4.086	2.354(4), 2.444(4), 2.933(4), 4.077(4)

^aBVP86/LANL2TZ(f)/6-311+G(d). ^bDecreasing order of [M][−] nucleophilicity; see ref.¹⁴⁶

^cFormal shortness ratio; see ref.²³³ ^dOnly distances within van der Waals contact (<4.2 Å)²³⁴ are listed. Italicized values represent semi-bridging carbonyls (0.1 < α < 0.6), and non-italicized values represent terminal carbonyls ($\alpha \geq 0.6$); see ref.¹³⁷. ^eData taken from ref.⁸⁵ ^fIMe = IPr (*N,N'*-bis(2,6-diisopropylphenyl)-imidazol-2-ylidene)²³²

Calculated bond distances are presented in Table 11 for comparison to the IPr derivatives, and calculated vibrational data for the CO ligands is presented in Table 12. The optimized structures for the IMe supported heterobimetallic complexes featuring Fe, Ru, Mo, and Cr closely matched experimental observations for the IPr supported complexes in terms of Cu-M distances, semi-bridging CO distances, and number of semi-bridging CO interactions (see Table 11).

Table 12: **Calculated and experimental vibrational frequencies for (IMe)Cu-[M] model complexes²³²**

Complex ^{a,b}	Calculated ν_{CO} (cm ⁻¹)	Experimental ν_{CO} (cm ⁻¹) ^b
(IMe)Cu-Rp ^c	1890, 1943	1867, 1940
(IMe)Cu-Wp	1802, 1819, 1882	1784, 1818, 1920
(IMe)Cu-Mc	1890, 1912, 1964, 1965, 2040	1830, 1885, 2042
(IMe)Cu-Crp	1790, 1821, 1930	1790, 1881, 1925
(IMe)Cu-Cc	1926, 1950, 1969, 2028	1915, 1957, 2038

^aBVP86/LANL2TZ(f)/6-311+G(d). ^bDecreasing order of [M]⁻ nucleophilicity; see ref.¹⁴⁶ ^bIMe = IPr (*N,N*-bis(2,6-diisopropylphenyl)-imidazol-2-ylidene) ^cFrom ref ²³⁵

The Cu-M distances can be compared using Cotton's formal shortness ratio (FSR) calculations to correct for metal sizes (Table 11).^{233,236} As expected, FSR values for the metal-metal single bonds were all near 1. Periodic trends in FSR were not immediately evident: for example, FSR decreased going down the Group 6 triad but increased going down Group 8. However, a clear trend emerged by which FSR increased with decreasing nucleophilicity of [M]⁻, indicating that stronger nucleophiles result in shorter Cu-M bonds. An outlier in this regard was (IPr)Cu-Cc, which exhibited an anomalously short Cu-Co FSR value, despite the weakly nucleophilic character of [Cc]⁻. The trends in Cu-M FSR values, including the anomalous value for the Cu-Co bond, were successfully replicated experimentally by the crystallographic analysis.²³²

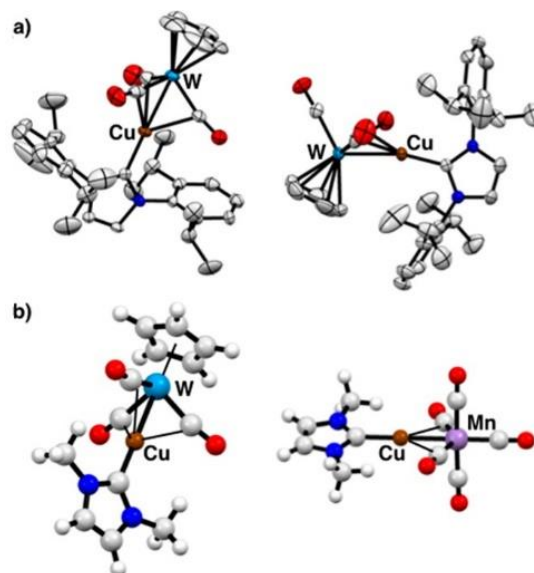


Figure 12: a) Two independent (IPr)Cu-Wp molecules found in the same asymmetric unit, depicted as 50 % probability thermal ellipsoids. Hydrogen atoms and co-crystallized solvent molecules have been omitted.²³² b) Optimized structures of (IMe)Cu-Wp and (IMe)Cu-Mc determined by density functional theory (DFT) energy minimization (BVP86/LANL2TZ(f)/6-311+G(d)).²³²

The optimized structure for (IMe)Cu-Wp closely matched the (IPr)Cu-Wp structure with the linear Cu-W-Cp(centroid) angle, shorter Cu-W distance, and three semi-bridging CO ligands rather than two (Figure 12b). The outliers were the Mn (Figure 12b) and Co cases: (IMe)Cu-Cc and (IMe)Cu-Mc were calculated to have three and two semi-bridging CO ligands, respectively, whereas, experimentally, this trend was reversed for the IPr series. This distinction apparently had little effect on the calculated Cu-Mn and Cu-Co distances, which agreed quite well with the experimental values. The latter observation implies that the semi-bridging CO interactions do not influence the Cu-M distances to a large extent.

The frontier molecular orbitals for the expanded heterobimetallic series closely mimic the previously published frontier orbitals for (IMe)Cu-Fp.⁸⁵ As an example, selected

orbital surfaces for (IMe)Cu-Mc are plotted on a computationally determined energy scale in Figure 13.

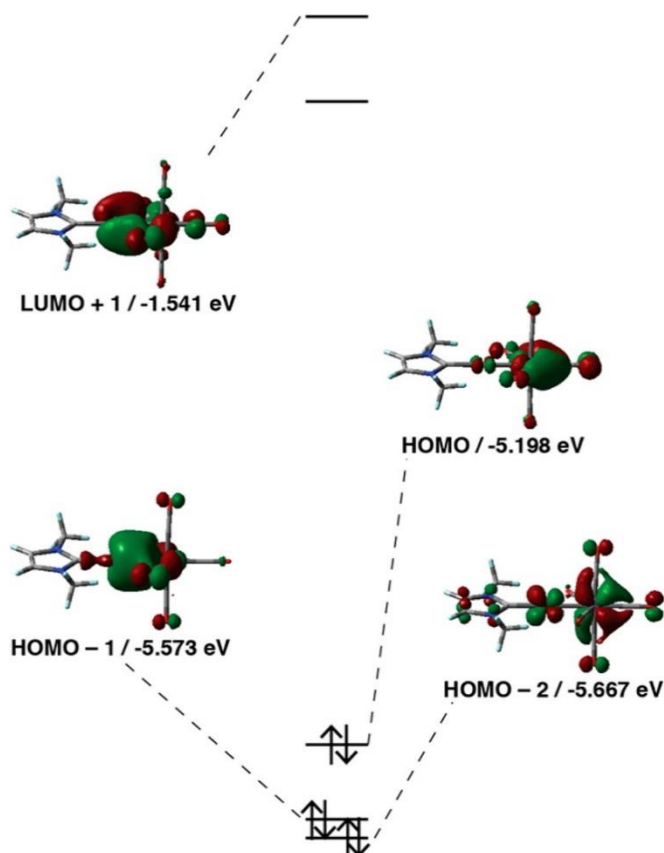


Figure 13: Frontier molecular orbital diagram calculated for (IMe)Cu-Mc (BVP86/LANL2TZ(f)/6-311+G(d), 0.04 isocontours). In this case, the HOMO and HOMO-2 orbitals possess Cu-Mn π^* character, the HOMO-1 orbital possesses Cu-Mn σ character, the LUMO (not shown) does not involve Cu-Mn or Cu-CO interactions, and the LUMO+1 exhibits Cu-CO through-space overlap.²³²

A general pattern is largely conserved throughout the series. For each complex, the three highest-lying filled molecular orbitals (MOs) have closely spaced energies; one possesses Cu-M σ character and the other two possess Cu-M π^* character. The effect of the filled Cu-Fe π^* MOs in (IPr)Cu-Fp has been detected spectroscopically.⁸⁶ A low-lying

empty MO exhibits significant through-space overlap between Cu and the semi-bridging CO ligands, and the relevant MO of Cu-M σ^* -character is invariably quite high in energy (LUMO+3 or higher).

Table 13: Calculated charges (q) from natural population analysis for (IMe)Cu-MCp_n(CO)_m model complexes^a

Complex ^b	$q[\text{Cu}]$	$q[\text{M}]$	$q[(\text{IMe})\text{Cu}]$	$q[\text{MCp}_n(\text{CO})_m]$
(IMe)Cu-Fp ^c	0.39	-1.19	0.63	-0.63
(IMe)Cu-Rp	0.40	-1.05	0.61	-0.61
(IMe)Cu-Wp	0.40	-0.95	0.69	-0.69
(IMe)Cu-Mc	0.45	-2.22	0.68	-0.68
(IMe)Cu-Mp ^c	0.45	-1.19	0.72	-0.72
(IMe)Cu-Crp	0.43	-1.66	0.70	-0.70
(IMe)Cu-Cc	0.37	-1.41	0.65	-0.65

^aBVP86/LANL2TZ(f)/6-311+G(d).²³²

^bDecreasing order of [M]– nucleophilicity; see ref.¹⁴⁶

^cData taken from ref⁸⁵

Charge distribution in the heterobimetallic series was probed using natural population analysis (Table 13). Contrary to our expectations, both the calculated Cu atomic charges and the calculated [(IMe)Cu] fragment charges were relatively invariant across the series, despite the extreme differences in relative nucleophilicities and reduction potentials of the [MCp_n(CO)_m] partners. The calculated charge of Cu ranged only from 0.37 to 0.45 e across the series, and the calculated fragment charge of [(IMe)Cu] ranged only from 0.61 e to 0.72 e. Furthermore, no discernible trends were evident. While the fragment charge of [MCp_n(CO)_m] was necessarily invariant as well, the calculated charge of M did span a large range, from –0.95 to –2.22 e. Within both the group 6 series

and the group 8 series, the atomic charge of M became less anionic going down the triad, tracking with the trends in metal electronegativities. No discernible trend was evident across the 3d series, with regard to the electronegativity of M. Instead, the dominant trend was with the number of CO ligands, with a greater number of CO ligands generally stabilizing more anionic charge localized on M. The negative charge localization on the metal centers was counterbalanced by positive charge delocalization in the Cp rings and, especially, by positive charge localization on CO carbon atoms (Table 14).

Table 14: Calculated charges (*q*) for Cp and CO ligands from natural population analysis for (IMe)Cu-[M] model complexes^a

Complex ^b	<i>q</i> [CO]	<i>q</i> [CO] _{total}	<i>q</i> [Cp]
(IMe)Cu-Rp	0.19, 0.19	0.38	0.05
(IMe)Cu-Wp	0.09, 0.04, 0.04	0.18	0.09
(IMe)Cu-Mc	0.23, 0.36, 0.36, 0.34, 0.23	1.53	
(IMe)Cu-Crp	0.17, 0.17, 0.34	0.67	0.29
(IMe)Cu-Cc	0.16, 0.19, 0.15, 0.26	0.76	

^aBVP86/LANL2TZ(f)/6-311+G(d).²³² ^bDecreasing order of [M]– nucleophilicity; see ref.¹⁴⁶

Once again, the (IMe)Cu-Cc complex was an outlier, as the Co center was calculated to hold less anionic charge than expected based on the number of CO ligands. This anomaly could be tied to the unusually short Cu-Co bond distance resulting in negative charge transfer from Co toward Cu.

NBO analysis of the Fe, W, Mn, Mo, and Cr derivatives underscored the ionic nature of the Cu-M bonds. In all of these cases, significant (3-4%) non-Lewis occupancies

were calculated, and no Cu-M bonding NBOs were located in any of these cases. Instead, significant $M \rightarrow Cu$ donor-acceptor interactions were identified, with the two predominant acceptor orbitals being Cu valence ($\sim 85\%$ Cu 4p) and Cu- C_{NHC} antibonding ($\sim 65\text{--}70\%$ Cu 4s) in nature. For the Ru and Co cases, Cu-M bonding NBOs were located. For the Ru derivative, this bonding NBO was 13% Cu $sp^{0.07}d^{0.09}$ and 87% Ru $sp^{0.79}d^{6.17}$ in nature; for the Co derivative, this bonding NBO was 20% Cu $sp^{0.72}d^{0.09}$ and 80% Co $sp^{2.66}d^{1.75}$ in nature. Apparently, the Cu-Ru and Cu-Co bonds are unusually covalent, according to NBO analysis, compared to the other Cu-M bonds. In the Co case, there may be a link between this finding and the anomalously small Cu-Co FSR and anomalously positive Co partial charge values.

Table 15: Wiberg bond indices for (IMe)Cu-MCp_n(CO)_m model complexes^a

Complex ^b	Cu-M	Cu-C _{NHC}	Cu...CO	M-CO
(IMe)Cu-Fp ^c	0.39	0.58	0.15, 0.13	1.20, 1.18
(IMe)Cu-Rp	0.40	0.57	0.11, 0.11	1.27, 1.27
(IMe)Cu-Wp	0.29	0.63	0.21, 0.21, 0.17	1.38, 1.38, 1.36
(IMe)Cu-Mc	0.28	0.58	0.17, 0.17, 0.05, 0.05, 0.03	1.08, 1.08, 1.06, 1.04, 1.04
(IMe)Cu-Mp ^c	0.28	0.59	0.24, 0.24, 0.02	1.33, 1.33, 1.29
(IMe)Cu-Crp	0.30	0.58	0.25, 0.25, 0.02	1.20, 1.20, 1.18
(IMe)Cu-Cc	0.32	0.60	0.18, 0.18, 0.13, 0.03	2.13, 2.10, 2.07, 2.06

^aBVP86/LANL2TZ(f)/6-311+G(d).²³² ^bDecreasing order of [M]– nucleophilicity; see ref.¹⁴⁶

^cData taken from ref⁸⁵

Wiberg bond index (WBI) values were calculated to further probe covalency of the bonding in the heterobimetallic series (Table 15). The (IMe)Cu-[M] complexes constructed

with the strongest nucleophiles, $[\text{Fp}]^-$ and $[\text{Rp}]^-$, were calculated to have higher Cu-M bond indices. These values were significantly $\ll 1$, indicating that the Cu-Fe and Cu-Ru bonds possess low covalent character and are best-viewed as polar bonds with significant ionic character. The WBI values decreased even further for the weaker nucleophiles, but the difference was minor and all the Cu-M WBI values span a very small range across the series. Small but significant WBI values were calculated for the semi-bridging $\text{Cu}\cdots\text{CO}$ interactions and corroborated their independent assignment using the structural asymmetry parameter, α . The asymmetry parameter (α) was used to determine the presence of so-called “semi-bridging” CO ligands ($0.1 < \alpha < 0.6$).¹³⁷ The number of semi-bridging CO ligands identified matched the number of close $\text{Cu}\cdots\text{CO}$ contacts having non-negligible WBI values in all cases.

3.5.3. Conclusions

In conclusion, a new series of Cu-M heterobimetallic complexes supported by N-heterocyclic carbene ligands that has been synthesized by the Mankad group was analyzed computationally. Structural trends that emerged were analyzed. Future stoichiometric and catalytic reactivity studies stand to leverage the tunable kinetic and thermodynamic parameters available upon construction and analysis of the heterobimetallic toolbox presented here with precise control over structure-function relationships.

3.6. Computational Methods

3.6.1. General Considerations

All calculations were performed using Gaussian09, Revision B.01.¹⁶² Density functional theory (DFT) calculations were carried out using a hybrid functional, BVP86, consisting of Becke's 1988 gradient-corrected Slater exchange functional¹⁶³ combined with the VWN5 local electron correlation functional and Perdew's 1986 non-local electron correlation functional.¹⁶⁴ Structural geometries were optimized to energy minima, and then frequency calculations were performed to confirm that no imaginary frequencies were present. Natural population analysis was used to determine atomic and fragment charges, and Wiberg and Mayer bond indices were used to determine bond orders: both were obtained from NBO v. 3.1¹⁷¹ calculations within Gaussian09. Optimized structures of (IMe)Cu-Fp and (IMe)Cu-Mp were reported previously.^{85,86}

3.6.1.1. Bimetallic Oxidative Addition

Mixed basis sets were employed for the smaller MeCl system: the LANL2TZ(f) triple- ζ basis set^{165–167} with effective core potential^{165,168,169} was used for Cu and Fe; the LANL2TZ+ triple- ζ basis set¹⁶⁶ with effective core potential^{165,168,169} was used for Zn; the LANL2DZ double- ζ basis set with effective core potential was used for Cl;^{165,168,169} and the Gaussian09 internal 6-311+G(d) basis set was used for C, H, N, and O. All geometry optimizations were performed using LANL2DZ effective core potentials (ECP) for the larger systems with BnCl and BnCl derivatives. Single-point electronic energy calculations were then carried out using larger mixed basis sets: the LANL2TZ(f) triple- ζ basis set with effective core potential for Cu and Fe, the LANL2DZ double- ζ basis set with effective core potential for Cl, and the Gaussian09 internal 6-311+G(d) basis set for C, H, N, and O. In some cases, effects of solvation by benzene were calculated with the polarizable

continuum model (PCM) using the integral equation formalism variant (IEFPCM)²³⁷ with default settings as implemented in Gaussian09. The 2,6-diisopropylphenyl and 2,4,6-trimethylphenyl groups on the NHC ligands were truncated to methyl groups in order to minimize computational time. Vibrational frequency analysis confirmed that all stationary points were correctly identified either as stable intermediates with zero imaginary frequencies or transition states with only one imaginary frequency. Intrinsic reaction coordinate calculations confirmed that each transition state was situated between its corresponding reactant and product states on the Born–Oppenheimer potential energy surface.

3.6.1.2. Bimetallic N₂O Activation

All optimizations were performed using the LANL2DZ^{165,168,169} effective core potentials (ECP).^{165–167} Single point electronic energy calculations were then carried out using larger mixed basis sets: the LANL2TZ(f) triple- ζ basis set^{165–167} with effective core potentials^{165–167} for Cu and Fe, and the Gaussian09 internal 6-311+G(d) basis set for C, H, N, P and O. The 2,6-diisopropylphenyl and 2,4,6-trimethylphenyl groups on the NHC ligands and the phenyl groups on the triphenylphosphine and triphenylphosphine oxide were truncated to methyl groups in order to minimize computational time. Vibrational frequency analysis confirmed that all stationary points were correctly identified either as stable intermediates with zero imaginary frequencies or transition states with only one imaginary frequency. Intrinsic reaction coordinate calculations confirmed that each transition state was situated between its corresponding reactant and product states on the Born–Oppenheimer potential energy surface. The sum of electronic and thermal free energies were used to calculate ΔG values at 298 K. Molecular orbital surfaces were plotted using Avogadro 1.0.3.²³⁸

3.6.1.3. Development and Characterization of a Toolkit of Heterobimetallics

Mixed basis sets were employed: the LANL2TZ(f) triple- ζ basis set^{165–167} with effective core potential^{165,168,169} was used for all transition metals, and the Gaussian 09 internal 6-311+G(d) basis set was used for all other atom types.

Chapter 4

***E*-Selective Semi-Hydrogenation of Alkynes by Heterobimetallic Catalysis**

Reproduced in part with permission from Karunananda, M. K.; Mankad, N. P. *J. Am. Chem.*

Soc. **2015**, 137, 14598-14601.

© 2015 American Chemical Society

4.1. Opening Remarks

The theme of this dissertation set forward in chapter one is that cooperative catalytic paradigms such as the late-late heterobimetallic strategy introduced by Mankad group lead to the development of novel reactivity and selectivity modes in hydrogenations. Our original hypothesis was that catalytic hydrogenation of unsaturated C-C bonds can be achieved by our bimetallic systems (chapter one). Before the reaction development, the structural and functional features of the polar heterobimetallic complexes were investigated experimentally and theoretically, and the results obtained which improved our understanding of these complexes were presented in chapter two⁸⁶ and three.^{87,232} Chapter four presents the actual implementation of the bimetallic strategy in developing hydrogenation reactions.²³⁹ The screening of catalysts was pursued initially using thermodynamic calculations of the energies of the H₂ activation step. The experiments that followed led to the discovery of a catalytic semi-hydrogenation of alkynes. Catalyst optimization, robustness screening and some isomerization studies are presented here along with the proposed mechanism.

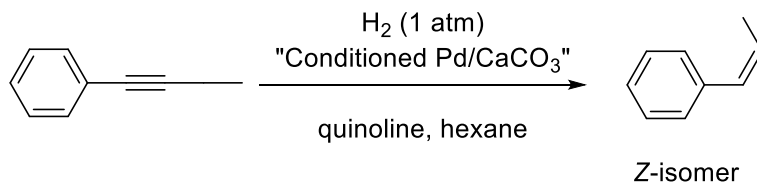
4.2. Introduction

Catalytic hydrogenation of unsaturated organic substrates remains a crucial application of homogeneous catalysis, in part due to the exquisite control of selectivity that is possible through catalyst design. The classical approach to catalytic hydrogenation involves single-site oxidative addition/reductive elimination mechanisms (chapter one). This approach is exemplified by well-known examples such as Wilkinson's catalyst,¹ the Schrock-Osborn catalyst,²⁻⁴ and Crabtree's catalyst^{5,20} that all operate by Rh^I/Rh^{III} or Ir^I/Ir^{III} cycles initiated through single-site oxidative addition of H₂. Exciting developments have

emerged through exploring non-classical approaches to H₂ activation. Representative examples include catalysts that activate H₂ using metal-base cooperativity,^{7,9,14,30,32–39} metal-acid cooperativity^{41,42,44} or non-metal frustrated Lewis acid-base cooperativity.^{11–13,47,55–64,66} Hydrogenation chemistry brought forward by these cooperative catalysts in C–C multiple-bonds have been discussed in detail in chapter one.

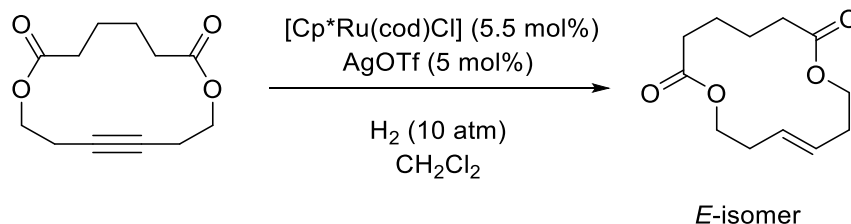
Another cooperative effect to potentially exploit is bimetallic cooperativity, wherein two metal sites within a catalyst cooperate to activate H₂ and initiate catalytic reduction of a substrate. Although bimetallic H₂ cleavage reactions have been long known,^{71–76,78} their use in catalytic transformations is underdeveloped.^{81,83,84} Previous examples of bimetallic hydrogenation catalysts often suffer from poor activity,²⁴⁰ and in some cases faster rates can actually be achieved by using monometallic analogues that omit one of the two metal sites.²⁴¹

In this chapter, a semi-hydrogenation reaction of alkynes that *requires* bimetallic cooperativity to proceed, is described. Through optimizing the nature of the bimetallic pairing within a tunable catalyst design, we have achieved unusual *E*-selectivity in the alkyne reduction, a rare selectivity mode in hydrogenation catalysis that complements the famously *Z*-selective Lindlar catalyst (Scheme 41)^{242,243} and more modern updates.^{44,244,245} as well as the *E*-selective but, stoichiometric Birch reduction reported in 1944, that utilizes sodium which is not compatible with many sensitive functional groups.²⁴⁶



Scheme 41: Z-selective semi-hydrogenation of alkynes by Lindlar and co-workers

Prior to our work, *E*-selective hydrogenation of alkynes was reported by Fürstner²⁴ and co-workers using a ruthenium/silver catalyst (Scheme 42) at elevated pressures (10 bar) under ambient temperatures (chapter one, Scheme 8).

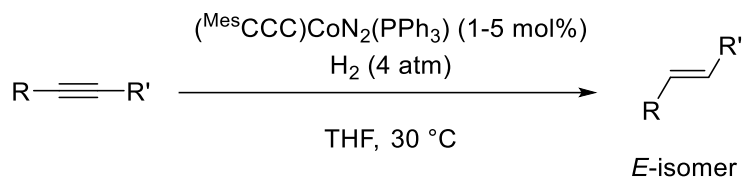


Scheme 42: E-selective semi-hydrogenation of alkynes by Fürstner and co-workers

Milstein⁹ and co-workers also reported an iron-pincer catalyst capable of *E*-selective semi-hydrogenation of alkynes under ambient temperatures of 90 °C and elevated H₂ pressures of 10 bar (chapter one, Scheme 8).

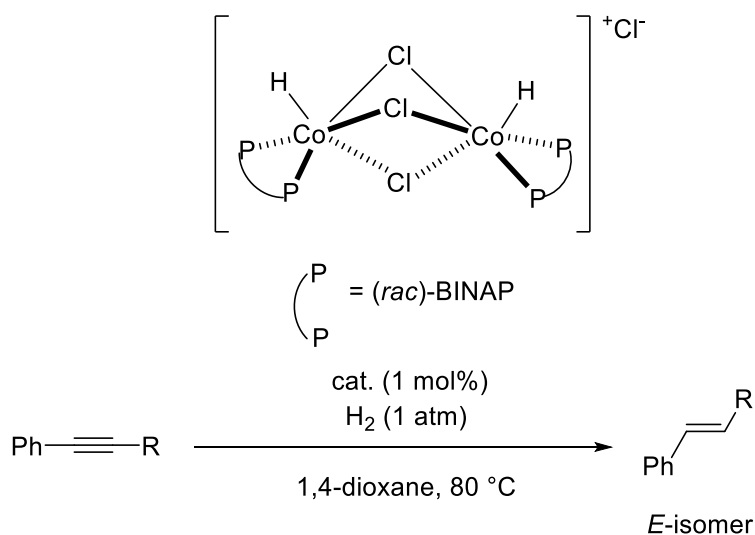
Since our initial report in 2015, several reports on *E*-selectivity has emerged in recent literature. In 2015, Fout and co-workers reported a single-site cobalt catalyst capable of hydrogenating alkynes to yield *cis*-alkenes which are subsequently isomerized to form the *trans*-alkenes (Scheme 43).²⁴⁷ The catalyst operates at mild temperatures, and requires moderate H₂ pressures up to 4 atm. A range of substrates with a variety of functional

groups were tolerated, including para-substituted diphenylacetylenes featuring electron-donating and electron-withdrawing groups. However, reactivity was not observed for terminal alkynes. Substrates with silyl, furanyl, thienyl, and imadazolyl groups were also tolerated.



Scheme 43: *E*-selective semi-hydrogenation of alkynes by Fout and co-workers

Mashima and co-workers demonstrated an iridium catalyst which hydrogenated alkynes to give *trans*-alkenes in 2016 (Scheme 44).²⁴⁸



Scheme 44: *E*-selective semi-hydrogenation of alkynes by Mashima and co-workers

While utilizing H₂ gas as the hydrogen source for hydrogenation reactions is desired due to the lack of waste products and efficient atom economy, using other hydrogen sources can sometimes be cheap and may require only mild reaction conditions. *E*-selectivity has been achieved in such transfer-hydrogenation reactions as well.²⁴⁹ For example, Jöge and co-workers showed an alkyne reduction to give *E*-alkenes using triethoxysilane in 2002.²⁵⁰ Han and co-workers demonstrated *E*-selective alkyne reduction using formic acid as the hydrogen source in a palladium catalyzed reaction in 2011.²⁵¹ In 2016, Liu and co-workers published a cobalt catalyst capable of transfer-hydrogenating alkynes to yield *cis*- and *trans*-alkenes.²⁵² Ammonia borane; a hydrogen storage material was used here as the hydrogen source. Grela and co-workers also reported ruthenium catalysts capable of transfer-hydrogenation of alkynes to yield *E*-alkenes in 2016.²⁵³

4.3. Results & Discussion

4.3.1. Catalyst Screening Using Thermodynamic Calculations

Our interest in bimetallic H₂ activation began through the study of a heterobimetallic catalyst for the dehydrogenative borylation of arenes.⁸⁸ The proposed mechanism for this transformation includes a key turnover step involving bimetallic reductive elimination from (NHC)CuH + FpH to regenerate the (NHC)Cu-Fp catalyst through loss of H₂. The calculated pathway⁸⁹ for this dehydrogenation event has a low-energy transition state that could reasonably be approached from the reverse direction, i.e., in a hypothetical H₂ cleaving reaction. We thus reasoned that a (NHC)Cu-Fp complex or one of its (NHC)Cu-[M] analogues²³² ([M] = metal carbonyl anion) might be active for bimetallic H₂ addition. To explore this possibility, we calculated the thermodynamics of this hypothetical H₂ activation, as a function of [M], using DFT methods with a truncated NHC model (Ime =

N,N'-dimethylimidazol-2-ylidene, Table 16). The relative trends that emerged (Table 16) guided our experimental catalyst development, although the energies would be more accurate by including NHC sterics, solvation, and (NHC)CuH dimerization²⁵⁴ energies.

Table 16: Thermodynamics for H₂ activation by (NHC)Cu-[M]²³⁹

Entry	[M]	Relative nucleophilicity of [M] ^{-a}	$\Delta G_{298\text{ K}}$ (kcal/mol) ^b
1	FeCp(CO) ₂	70,000,000	21.9
2	RuCp(CO) ₂	7,500.000	20.1/14.5 ^c
3	Re(CO) ₅	25,000	26.4
4	WCp(CO) ₃	500	24.8
5	Mn(CO) ₅	77	33.0
6	MoCp(CO) ₃	67	34.0
7	CrCp(CO) ₃	4	34.5
8	Co(CO) ₄	1	49.0

^aFrom ref X. ^bCalculated by DFT for H₂ cleavage. ^cFor (IMes)Ag in place of (IMe)Cu.

As expected on the basis of facile dehydrogenation reactivity observed previously,^{88,89} the H₂ activation is thermodynamically unfavorable for all systems calculated. Two key observations guided our experimental trials. First, the general trend is for H₂ activation to be less favorable with decreasing [M]⁻ nucleophilicity.¹⁴⁶ Second, among the most promising candidates, the (NHC)Cu-Rp system (Rp = RuCp(CO)₂) has an unusually low ΔG value for H₂ addition (Table 16, entry 2) considering the relative

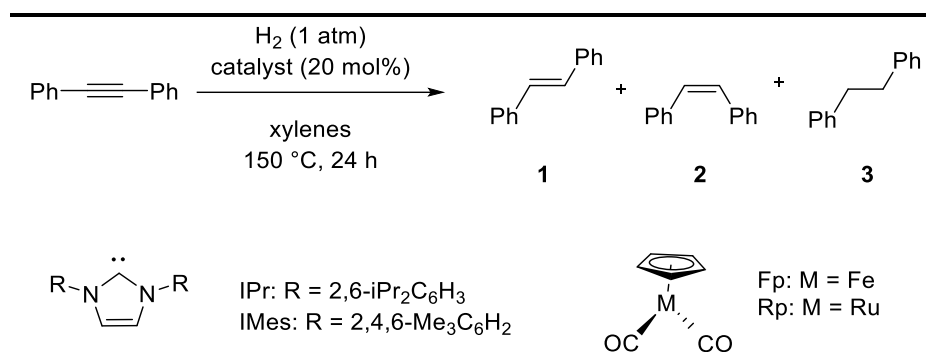
nucleophilicity of $[\text{Rp}]^-$. Based on these observations, we began experimental studies with $(\text{NHC})\text{Cu-Fp}$ and $(\text{NHC})\text{Cu-Rp}$ complexes. In a related study, Meyer recently observed stoichiometric H_2 activation based on cooperation between $[\text{Rp}]^-$ and a carbon Lewis acid.²⁵⁵

As expected, no evidence for any reaction occurring was obtained by NMR spectroscopy when different $(\text{NHC})\text{Cu-Fp}$ and $(\text{NHC})\text{Cu-Rp}$ complexes were exposed to H_2 . However, when the reactions were done in the presence of alkynes at elevated temperatures, alkene products were observed, indicating that H_2 was indeed being activated by the catalyst.

4.3.2. Catalyst Optimization

Preliminary experimentation indicated that appropriate conditions for catalytic hydrogenation would include 150 °C reaction temperature in xylenes solvent at 1 atm of H_2 pressure. Rapid catalyst decomposition was observed when polar solvents were used in place of xylenes or when higher H_2 pressures were employed. Catalysis was observed at lower temperatures, but multiple days were required for reaction progress to reach completion. When comparing diphenylacetylene hydrogenation results for $(\text{NHC})\text{Cu-Fp}$ catalysts (Table 17, entries 1 and 2) with those for $(\text{NHC})\text{Cu-Rp}$ catalysts (entries 3 and 4), we found that selectivity for *trans*-stilbene increased significantly when substituting Fe for Ru.

Table 17: Alkyne semi-hydrogenation catalyst optimization²³⁹



Entry	Catalyst	Conversion (%) ^a	1:2:3 ^a
1	(IPr)Cu-Fp	32	8:23:1
2	(IMes)Cu-Fp	64	12:50:2
3	(IPr)Cu-Rp	60	40:18:3
4	(IMes)Cu-Rp	61	42:17:2
5	(IPr)Ag-Fp	29	17:12:1
6	(IMes)Ag-Fp	32	21:11:0
7	(IPr)Ag-Rp	84	54:24:5
8	(IMes)Ag-Rp	95.7^b	90.2:4.2:1.2^b
9	(IPr)AgOAc	0	N/A
10	Rp ₂ ^c	7	4:3:0
11	(IMes)Ag-Rp + Hg drop	89	67:18:4

^aFrom ¹H NMR integration against an internal standard. ^bAveraged over two independent runs (±0.2 error bars). ^cCatalyst loading was 10 %, i.e., 20 % Ru.

In all cases, the total conversions of diphenylacetylene were low to modest, and so we proceeded to test (NHC)Ag-Fp (entries 5 and 6) and (NHC)Ag-Rp analogues (entries 7 and 8), which were predicted by DFT to activate H₂ more readily (Table 16, entry 2). Only for the (NHC)Ag-Rp catalysts were high conversions realized. The optimal catalyst was (IMes)Ag-Rp (IMes = N,N'-bis(2,4,6-trimethylphenyl)imidazol-2-ylidene), which gave 96% conversion of diphenylacetylene and yielded *trans*-stilbene as 95% of the product

mixture (Table 17, entry 8). The *cis*-stilbene was the main side product, while 1,2-diphenylethane was formed only in trace amounts.

To confirm that both metal sites are required for catalysis, we note that neither (IPr)AgOAc nor Rp_2 catalyze hydrogenation of diphenylacetylene (entries 9 and 10). Preliminary indications are that the reaction does involve homogeneous catalysis: a drop of Hg did not significantly poison catalysis (entry 11), and we believe that the modest lowering of conversion and erosion of selectivity is due to a slow background reaction between (IMes)Ag-Rp and Hg, evident from a visible color change even prior to heating (IMes)Ag-Rp + Hg with H_2 and alkyne. Quantitative conversions of both an electron-rich and an electron-poor diarylalkyne were achieved under these catalytic conditions, still with high *E:Z* selectivity (Table 18, entries 2 and 3). A terminal alkyne also underwent quantitative reduction (entry 4). 1-phenyl-1-hexyne underwent efficient reduction, but we were unable to identify the product(s) formed (entry 5).

Table 18: Alkyne semi-hydrogenation by (IMes)Ag-Rp²³⁹

$R-C\equiv C-R' \xrightarrow[\text{xylene, } 150^\circ\text{C, 24 h}]{H_2 (1 \text{ atm}), (IMes)Ag-Rp (20 \text{ mol}\%)} \begin{matrix} R-CH=CH-R' \\ \text{1} \end{matrix} + \begin{matrix} R-CH=CH-R' \\ \text{2} \end{matrix} + \begin{matrix} R-CH_2-CH_2-R' \\ \text{3} \end{matrix}$				
Entry	R	R'	Conversion (%) ^a	1:2:3 ^a
1	Ph	Ph	95.7 ^b	90.2:4.2:1.2 ^b
2	4-MeOC ₆ H ₄	4-MeOC ₆ H ₄	>99	71:24:5
3	4-F ₃ CC ₆ H ₄	4-F ₃ CC ₆ H ₄	>99	72:20:8
4	4-(n-H ₁₁ C ₅)C ₆ H ₄	H	91	91 ^c :n.d. ^d
5	Ph	nBu	>99	n.d. ^d

^aFrom ¹H NMR integration against an internal standard. ^bAveraged over two independent runs (±0.2 error bars). ^cTerminal alkene ^dNot determined.

4.3.3. Hydrogenation Mechanism

A hypothetical hydrogenation mechanism is shown in Figure 14a. Reversible H_2 activation by the $(\text{NHC})\text{M}'\text{-}[\text{M}]$ catalyst produces $(\text{NHC})\text{M}'\text{-H} + [\text{M}]\text{-H}$. This H_2 activation can be viewed as a heterolysis, producing an equilibrium mixture of a protic species and a hydridic species.

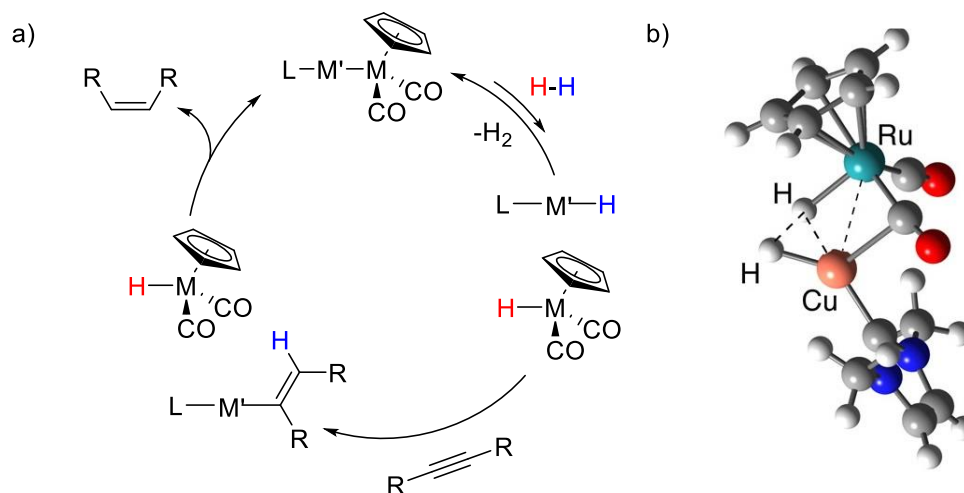


Figure 14: a) Hypothetical mechanism for alkyne semi-hydrogenation by $(\text{NHC})\text{M}'\text{-}[\text{M}]$ catalysts ($\text{M} = \text{Fe}$ or Ru , $\text{M}' = \text{Cu}$ or Ag , $\text{L} = \text{IPr}$ or IMes).
b) Transition state for H_2 activation **TS4** by $(\text{IMe})\text{Cu-Rp}$ calculated by DFT.

The calculated transition state for H_2 activation by $(\text{IMe})\text{Cu-Rp}$ **TS4** is shown in Figure 14b ($\Delta H^\ddagger = 20.1$ kcal/mol, $\Delta S^\ddagger = -29.8$ eu, $\Delta G_{298\text{K}}^\ddagger = 29.0$ kcal/mol). As expected for a late transition state, the Cu-Ru and H-H bonds are almost completely broken (2.74 and 1.28 Å, respectively, vs 2.44 and 0.75 Å in reactants). As we have noted previously for a related reaction (chapter three),⁸⁷ one of the CO ligands bridges the two metals in the transition state ($\text{Cu}\cdots\text{CO} = 2.64$ Å) to provide stability as the metals separate. As

evidence for this step occurring, we note that ^1H NMR peaks (e.g., in toluene- d_8 : δ = 4.52 and -12.04, 5:1 integration) initially assigned to RpH were observed in typical product mixtures, along with precipitation of the coinage metal consistent with known decomposition of $(\text{NHC})\text{M}'\text{-H}$ complexes.^{254,256,257} The ruthenium species assigned here as RpH was later identified as the decomposition product of hydrogenation: HRuCp(CO)(IMes) which will be discussed in detail in chapter five.

Following H_2 activation, alkyne insertion into $(\text{NHC})\text{M}'\text{-H}$ produces a σ -alkenyl intermediate. This hydro-metalation step is expected to proceed with *syn* stereochemistry, based on the known reactivity of the $(\text{IPr})\text{CuH}$ dimer.²⁵⁴ Less is known about the insertion chemistry of analogous $(\text{NHC})\text{Ag-H}$ species.^{256,257} Finally, protonolysis of the σ -alkenyl ligand by $[\text{M}]\text{-H}$ regenerates the $(\text{NHC})\text{M}'\text{-[M]}$ catalyst through bimetallic elimination of the *Z*-alkene. According to this proposal, the alkyne substrate is initially reduced to the *Z*-alkene, which must then be isomerized under the reaction conditions. To probe the validity of this proposal, we exposed *cis*-stilbene to the catalytic conditions and, indeed, observed isomerization to the *trans* isomer (Table 19, entry 1).

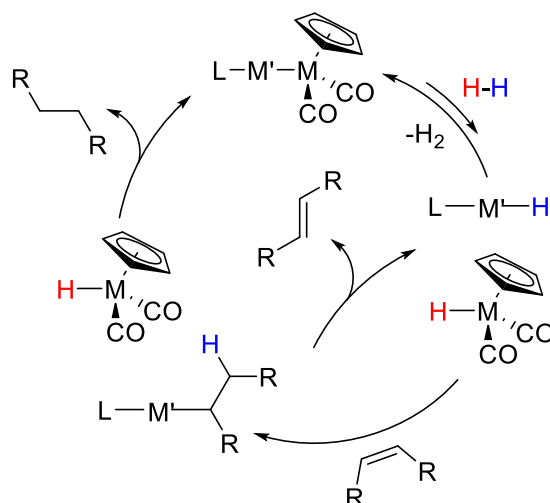
Table 19: Alkene isomerization studies²³⁹

Alkene	$\xrightarrow[\text{xylenes, 150 } ^\circ\text{C, 24 h}]{\text{H}_2 \text{ (1 atm)}, \text{ (IMes)Ag-Rp (20 mol\%)}}$		
	1	2	3

Entry	Alkene	Variation on conditions	1:2:3 ^a
1	<i>cis</i> -stilbens	None	92:4:5
2	<i>trans</i> -stilbens	None	98:0:2
3	<i>cis</i> -stilbens	Catalyst omitted	<1:99:0
4	<i>cis</i> -stilbens	H ₂ omitted	22:78:0

^aFrom ¹H NMR integration against an internal standard.

On the other hand, exposing the *trans*-stilbene to the catalytic conditions resulted in no isomerization (entry 2). The *Z*-to-*E* isomerization was stopped when the catalyst was omitted (entry 3) and slowed when H₂ was omitted (entry 4). These observations indicate that *cis*-stilbene is a viable reaction intermediate that isomerizes to *trans*-stilbene under the reaction conditions, and that the isomerization is catalyzed by a H₂ derived metal-hydride species. A proposed mechanism for isomerization is shown in Scheme 45.



Scheme 45: Hypothetical mechanism for alkene isomerization under hydrogenation conditions by (NHC)M'-[M] catalysts (M = Fe or Ru, M' = Cu or Ag, L = IPr or IMes).

The mechanism involves *Z*-alkene insertion into the (NHC)M'-H intermediate to generate a metal-alkyl species. This metal-alkyl subsequently undergoes β -hydride elimination to extrude either the *E* or *Z* alkene, the former of which is favored thermodynamically. The metal-alkyl intermediate species should also be susceptible to protonolysis by [M]-H, consistent with our observation of trace alkanes in most product mixtures. According to our catalyst optimization results (Table 17), the general trends are for the cycle in Scheme 45 to be faster for M' = Ag, M = Ru, and NHC = IMes.

4.3.4. Time-Dependent Robustness Screening

Finally, we sought to explore the functional group tolerance of the transformation using a modified version of Glorius's robustness screening method.²⁵⁸ The reduction of diphenylacetylene was conducted in the presence of various additives containing

potentially reactive functional groups. Product mixtures were analyzed at both partial (6 h) and full (24 h) conversion (Table 20).

Table 20: Time-dependent robustness screening data²³⁹

$ \begin{array}{c} \text{Ph}-\text{C}\equiv\text{C}-\text{Ph} \\ + \\ \text{additive (1 eq.)} \end{array} \xrightarrow[\text{xylene, 150 }^\circ\text{C, 24 h}]{\text{H}_2 \text{ (1 atm), (IMes)AgRp (20 mol\%)}} \begin{array}{c} \text{Ph}-\text{CH}=\text{CH}-\text{Ph} \\ \text{1} \end{array} + \begin{array}{c} \text{Ph}-\text{CH}=\text{CH}-\text{Ph} \\ \text{2} \end{array} + \begin{array}{c} \text{Ph}-\text{CH}_2\text{CH}_2-\text{Ph} \\ \text{3} \end{array} $			
Entry	additive	Conversion (%) ^{a,b}	1:2:3 ^{a,b}
1	None	55/96	49:4:1/90:4:1
2	Heptaldehyde	36/96	8:22:5/15:81:1
3	6-undecanone	74/90	61:12:1/71:16:2
4	Acetonitrile	55/94	37:17:2/78:16:2
5	Ethyl acetate	58/>99	43:13:2/92:0:8
6	1-butanol	79/99	69:8:2/84:11:4
7	Pyridine	68/79	62:5:1/66:11:2
8	1-dodecane	65/.99	48:15:2/96:1:3
9	Neopentyl chloride	54/99	39:13:2/94:2:3

^aFrom ¹H NMR integration against an internal standard. ^bListed as 6 h/24 h.

It is clear from the partial conversion data that the rate of catalysis is not slowed by any of the functional group tested, other than by aldehydes (entry 2). From the full conversion data, it is evident that the alkyne reduction is tolerant of many reactive functional groups. The *E:Z* selectivity was eroded slightly by the presence of a pyridine or a ketone (entries 3 and 7), and was actually inverted by the presence of an aldehyde (entry 2). As an illustrative example, the aldehyde additive was detected at the end of the reaction, indicating that (IMes)Ag-Rp is capable of catalyzing alkyne hydrogenation but

not aldehyde reduction. The selective reduction of alkynes in the presence of other reducible functional groups (e.g., aldehydes, ketones, alkenes, nitriles) is quite remarkable especially given the reactivity of Cu/Ag hydrides towards polar substrates such as CO₂, aldehydes and ketones.²⁵⁹

4.4. Conclusions

In conclusion, a unique cooperative H₂ activation reaction by heterobimetallic (NHC)M'-MCp(CO)₂ complexes (NHC = *N*-heterocyclic carbene, M' = Cu or Ag, M = Fe or Ru) has been leveraged to develop a catalytic alkyne semi-hydrogenation transformation. The optimal Ag-Ru catalyst operates at low pressures and gives high selectivity for converting alkynes to *E*-alkenes, a rare selectivity mode for reduction reactions with H₂. The transformation is tolerant of many reducible functional groups such as ketones and aldehydes. Computational analysis of H₂ activation was utilized to guide rational catalyst development. Bimetallic alkyne hydrogenation and alkene isomerization mechanisms are proposed. While this initial catalyst still requires ruthenium and silver metals and elevated temperatures, strategies for developing second-generation catalysts with cheaper first-row transition metals functional under lower temperatures are investigated (chapter five).

4.5. Experimental Procedures

4.5.1. General Considerations

Unless otherwise specified, all reactions and manipulations were performed under purified N₂ in a glovebox or using standard Schlenk line techniques. Glassware was oven-dried prior to use. Reaction solvents were sparged with argon and dried using a Glass Contour Solvent System built by Pure Process Technology, LLC (toluene, pentane), or

purified by repeated freeze-pump-thaw cycles followed by prolonged storage over activated, 3-Å molecular sieves (xylenes, NMR solvents). H₂ gas was purchased from PRAXAIR at a purity of 99.999% (5.0 UHP grade) and purified further by running through an O₂ removing catalyst column (RCI GetterMax 133T) and a drying column (Drierite). Literature methods were used to synthesize Rp_2 ,²³⁵ (IPr)AgOAc,²⁶⁰ (IMes)AgCl, (IPr)AgCl,²⁶¹ KFp,²⁶² NaRp, (IMes)CuFp, (IPr)CuFp, (IMes)CuRp, (IPr)CuRp, and (IPr)AgRp.²³² Unless otherwise specified, all chemicals were purchased from commercial sources and used without further purification.

4.5.2. Physical Measurements

NMR spectra were recorded at ambient temperature using Bruker Avance DPX-400 and Bruker Avance DRX-500 spectrometers. ¹H NMR and ¹³C{¹H} NMR chemical shifts were referenced to residual solvent peaks. FT-IR spectra were recorded on solid samples in a glovebox using a Bruker ALPHA spectrometer fitted with a diamond-ATR detection unit. Elemental analyses were performed by Midwest Microlab, LLC in Indianapolis, IN. Single-crystal X-ray diffraction studies were performed using a Bruker SMART X2S benchtop diffractometer fitted with an Oxford Cryostreams desktop cooler. Solution and refinement were accomplished with the SHELXTL suite of programs,²⁶³ using standard methods.²⁶⁴

4.5.3. Computational Methods

Optimized data for (IMe)Cu-[M] complexes (where [M] = FeCp(CO)₂, RuCp(CO)₂, WCp(CO)₃, Mn(CO)₅, MoCp(CO)₃, CrCp(CO)₃, CrCp(CO)₃, Co(CO)₄) were obtained from chapter three and previous literature.^{232,85} All calculations were performed using Gaussian09, Revision B.01.¹⁶² Density functional theory (DFT) calculations were carried

out using a hybrid functional, BVP86, consisting of Becke's 1988 gradient-corrected Slater exchange functional¹⁶³ combined with the VWNS local electron correlation functional and Perdew's 1986 nonlocal electron correlation functional.¹⁶⁴ Mixed basis sets were employed: the LANL2TZ(f) triple- ζ basis set^{165–167} with effective core potential^{165,168,169} was used for Cr, Mn, Fe, Co, Cu, Mo, Ru, Ag, W and Re; and the Gaussian09 internal 6-311+G(d) basis set was used for C, H, N, and O. The 2,4,6-trimethylphenyl groups on the NHC ligands were truncated to methyl groups in order to minimize computational time. Vibrational frequency analysis confirmed that all stationary points were correctly identified either as stable intermediates with zero imaginary frequencies or transition states with only one imaginary frequency. The sum of electronic and thermal free energies were used to calculate the ΔG values at 298 K. Intrinsic reaction coordinate calculations confirmed that the transition state was situated between its corresponding reactant and product states on the Born–Oppenheimer potential energy surface.

4.5.4. Synthesis of Catalysts

4.5.4.1. (IMes)Ag-Rp

(IMes)AgCl (0.1004 g, 0.224 mmol, 1 equiv) was dissolved in toluene (10 mL), and NaRp (0.1100 g, 0.448 mmol, 2 equiv) was added to the solution. The brown solution was stirred for 24 h at room temperature. The solution was filtered through Celite, and the filtrate was evaporated to dryness. The remaining solid was suspended in pentane (10 mL) and stirred vigorously for 30 min. The suspension was filtered through a fritted glass filter, and the brown-yellow solid was washed with pentane (3 \times 5 mL) and then dried *in vacuo*. Yield: 0.1052 g, 0.165 mmol, 74%. The solid was stored in a glovebox freezer at -36°C . X-ray quality crystals were grown by vapor diffusion of pentane into a concentrated

toluene solution at $-36\text{ }^{\circ}\text{C}$. ^1H NMR (400 MHz, C_6D_6): δ 6.76 (s, 4H, *m*-H), 6.05 (s, 2H, NCH), 4.80 (s, Cp), 2.08 (s, 6H, *p*-CH₃), 2.03 (s, 12H, *o*-CH₃). $^{13}\text{C}\{^1\text{H}\}$ NMR (125 MHz, C_6D_6): δ 209.1 (CO), 139.1, 135.8, 134.7, 129.3, 121.0, 80.1 (Cp), 20.7, 17.5. Note: Even after 10000 scans on a near-saturated solution, the ^{13}C signal for the carbene carbon was not detected. IR (solid, cm^{-1}): 1930 (νCO), 1864 (νCO), 788, 566. Anal. Calcd for $\text{C}_{28}\text{H}_{29}\text{N}_2\text{O}_2\text{AgRu}$: C, 53.00; H, 4.61; N, 4.42. Found: C, 52.97; H, 4.49; N, 4.46.

4.5.4.2. (IPr)Ag-Rp

(IPr)AgCl (0.0849 g, 0.160 mmol, 1 equiv) was dissolved in toluene (10 mL), and NaRp (0.0783 g, 0.320 mmol, 2 equiv) was added to the solution. The solution was stirred for 24 h at room temperature. The solution was filtered through Celite, and the filtrate was evaporated to dryness. The remaining solid was suspended in pentane (10 mL) and stirred vigorously for 30 min. The suspension was filtered through a fritted glass filter, and the off-white solid was washed with pentane (3 \times 5 mL) and then dried *in vacuo*. Yield: 0.0891 g, 0.123 mmol, 77%. The solid was stored in a glovebox freezer at $-36\text{ }^{\circ}\text{C}$. X-ray quality crystals were grown by vapor diffusion of pentane into a concentrated toluene solution at $-36\text{ }^{\circ}\text{C}$. ^1H NMR (400 MHz, C_6D_6): δ 7.21 (t, $J = 7.8\text{ Hz}$, 2H, *p*-H), 7.09 (d, $J = 7.8\text{ Hz}$, 4H, *m*-H), 6.32 (s, 2H, NCH), 4.77 (s, Cp), 2.60 (sept., $J = 6.8\text{ Hz}$, 4H, $\text{CH}(\text{CH}_3)_2$), 1.46 (d, $J = 6.9\text{ Hz}$, 12H, $\text{CH}(\text{CH}_3)_2$), 1.10 (d, $J = 6.9\text{ Hz}$, 12H, $\text{CH}(\text{CH}_3)_2$). $^{13}\text{C}\{^1\text{H}\}$ NMR (125 MHz, C_6D_6): δ 208.6 (CO), 145.7, 135.0, 130.4, 124.0, 121.0, 80.0 (Cp), 28.7, 24.5, 23.6. Note: Even after 10000 scans on a near-saturated solution, the ^{13}C signal for the carbene carbon was not detected. IR (solid, cm^{-1}): 1936 (νCO), 1868 (νCO), 755, 565. Anal. Calcd for $\text{C}_{34}\text{H}_{41}\text{AgN}_2\text{O}_2\text{Ru}$: C, 56.82; H, 5.75; N, 3.90. Found: C, 55.88; H, 5.56; N, 3.98.

4.5.4.3. (IMes)Ag-Fp

(IMes)AgCl (0.0674 g, 0.150 mmol, 1 equiv) was dissolved in toluene (10 mL), and KFp (0.0650 g, 0.300 mmol, 2 equiv) was added to the solution. The solution was stirred for 24 h at room temperature. The solution was filtered through Celite, and the filtrate was evaporated to dryness. The remaining solid was suspended in pentane (10 mL) and stirred vigorously for 30 min. The suspension was filtered through a fritted glass filter, and the yellow solid was washed with pentane (3 × 5 mL) and then dried *in vacuo*. Yield: 0.0571 g, 0.096 mmol, 64%. The solid was stored in a glovebox freezer at -36 °C. ¹H NMR (500 MHz, C₆D₆): δ 7.16 (s, 4H, *m*-H), 6.75 (s, 2H, NCH), 4.33 (s, Cp), 2.07 (s, 6H, *p*-CH₃), 2.03 (s, 12H, *o*-CH₃). ¹³C{¹H} NMR (125 MHz, C₆D₆): δ 222.4 (CO), 139.4, 136.1, 135.0, 129.6, 121.2, 76.8 (Cp), 21.0, 17.8. Note: Even after 10000 scans on a near-saturated solution, the ¹³C signal for the carbene carbon was not detected. IR (solid, cm⁻¹): 1905 (νCO), 1844 (νCO), 655, 584. Anal. Calcd for C₂₈H₂₉N₂O₂AgFe: C, 57.07; H, 4.96; N, 4.75. Found: C, 57.27; H, 4.68; N, 4.51.

4.5.5. General Procedure for Catalyst Optimization

In a nitrogen filled glovebox, the catalyst (5.0 mg, 0.2 equiv), diphenylacetylene (1 equiv) and an internal standard (hexamethylbenzene or 1,3,5-trimethoxybenzene, 1 equiv) were dissolved in xylenes (1 mL), transferred to a J-Young NMR tube, and sealed. (The transfer was done in two steps: First, the maximum amount of the solids were dissolved in 0.7 mL of xylenes and transferred. The vial was washed with another 0.3 mL of xylenes and the washings were then transferred.) The J-Young tube was inverted multiple times to make sure that all the solids dissolved and then connected to a Schlenk line containing H₂ gas (1 atm). After degassing the solution using three 5-minute freeze-

pump-thaw cycles, the sample was frozen again, exposed to H₂ and allowed to thaw and equilibrate for 30 minutes. The J-Young tube was then resealed and heated in an oil bath at 150 °C for 24 h. The J-Young tube was then transferred back into the glovebox, and the solution was transferred into a scintillation vial and dried *in vacuo*. The dried product was then dissolved in toluene-*d*₈ and pipette-filtered through Celite into a J-Young tube. The ¹H NMR spectrum was recorded. (The catalyst impurities present can be removed by pipette-filtering the product mixture through silica)

4.5.6. General Procedure for Catalytic Semi-Hydrogenation of Alkynes by (IMes)AgRp

In a nitrogen filled glovebox, (IMes)Ag-Rp (5.0 mg, 0.2 equiv), the alkyne (1 equiv) and an internal standard (hexamethylbenzene or 1,3,5-trimethoxybenzene, 1 equiv) were dissolved in xylenes (1 mL), transferred to a J-Young NMR tube, and sealed. (The transfer was done in two steps: First, the maximum amount of the solids were dissolved in 0.7 mL of xylenes and transferred. The vial was washed with another 0.3 mL of xylenes and the washings were then transferred.) The J-Young tube was inverted multiple times to make sure that all the solids dissolved and then connected to a Schlenk line containing H₂ gas (1 atm). After degassing the solution using three 5-minute freeze-pump-thaw cycles, the sample was frozen again, exposed to H₂ and allowed to thaw and equilibrate for 30 minutes. The J-Young tube was then resealed and heated in an oil bath at 150 °C for 24 h. The J-Young tube was then transferred back into the glovebox, and the solution was transferred into a scintillation vial and dried *in vacuo*. The dried product was then dissolved in toluene-*d*₈ or CDCl₃ depending on the alkyne and pipette-filtered through Celite into a J-Young tube. The ¹H-NMR spectrum was recorded.

4.5.7. General Procedure for the Alkene Isomerization

In a nitrogen filled glovebox, (IMes)Ag-Rp (5.0 mg, 0.2 equiv) (unless indicated otherwise), the *cis* or *trans*-stilbene (1 equiv), and an internal standard (hexamethylbenzene or 1,3,5-trimethoxybenzene, 1 equiv) were dissolved in xylenes (1 mL), transferred to a J-Young NMR tube, and sealed. (The transfer was done in two steps: First, the maximum amount of the solids were dissolved in 0.7 mL of xylenes and transferred. The vial was washed with another 0.3 mL of xylenes and the washings were then transferred.) The J-Young tube was inverted multiple times to make sure that all the solids dissolved and then connected to a Schlenk line containing H₂ gas (1 atm). After degassing the solution using three 5-minute freeze-pump-thaw cycles, the sample was frozen again, exposed to H₂ and allowed to thaw and equilibrate for 30 minutes. The J-Young tube was then resealed and heated in an oil bath at 150 °C for 24 h. The J-Young tube was then transferred back into the glovebox, and the solution was transferred into a scintillation vial and dried *in vacuo*. The dried product was then dissolved in toluene-*d*₈ and pipette-filtered through Celite into a J-Young tube. The ¹H-NMR spectrum was recorded.

4.5.8. Procedure for the Control of the Alkene Isomerization.

In a nitrogen filled glovebox, (IMes)Ag-Rp (5.0 mg, 0.2 equiv), *cis*-stilbene (1 equiv), and an internal standard (hexamethylbenzene or 1,3,5-trimethoxybenzene, 1 equiv) were dissolved in xylenes (1 mL), transferred to a J-Young NMR tube, sealed. (The transfer was done in two steps: First, the maximum amount of the solids were dissolved in 0.7 mL of xylenes and transferred. The vial was washed with another 0.3 mL of xylenes and the washings were then transferred.) The J-Young tube was inverted

multiple times to make sure that all the solids dissolved and then heated in an oil bath at 150 °C for 24 h. The J-Young tube was then transferred back into the glovebox, and the solution was transferred into a scintillation vial and dried *in vacuo*. The dried product was then dissolved in toluene-*d*₈ and pipette-filtered through Celite into a J-Young tube. The ¹H-NMR spectrum was recorded.

4.5.9. General Procedure for the Robustness Screen Using Additives

In a nitrogen filled glovebox, (IMes)Ag-Rp (5.0 mg, 0.2 equiv), diphenylacetylene (1 equiv), an additive (1 equiv) and an internal standard (hexamethylbenzene or 1,3,5-trimethoxybenzene, 1 equiv) were dissolved in xylenes (1 mL), transferred to a J-Young NMR tube, and sealed. (The transfer was done in two steps: First, the maximum amount of the solids were dissolved in 0.7 mL of xylenes and transferred. The vial was washed with another 0.3 mL of xylenes and the washings were then transferred.) The J-Young tube was inverted multiple times to make sure that all the solids dissolved and then connected to a Schlenk line containing H₂ gas (1 atm). After degassing the solution using three 5-minute freeze-pump-thaw cycles, the sample was frozen again, exposed to H₂ and allowed to thaw and equilibrate for 30 minutes. The J-Young tube was then resealed and heated in an oil bath at 150 °C for 6 or 24 h. The J-Young tube was then transferred back into the glovebox, and the solution was transferred into a scintillation vial and dried *in vacuo*. The dried product was then dissolved in toluene-*d*₈ and pipette-filtered through Celite into a J-Young tube. The ¹H-NMR spectrum was recorded.

Chapter 5

Mechanistic Investigations into *E*-Selective Semi-Hydrogenation of Alkynes by Heterobimetallic Catalysis

Reproduced in part with permission from Karunananda, M. K.; Mankad, N. P. *Organometallics*

2017, 36, 220-227.

© 2015 American Chemical Society

5.1. Opening Remarks

In the previous chapter, the reaction development of an *E*-selective semi-hydrogenation of alkynes was presented (chapter four). The initial catalyst screening done by DFT calculations, the catalyst optimization, substrate screening and robustness screening that followed were also discussed. A hypothetical hydrogenation mechanism was proposed and the transition state for the H₂ activation step was calculated and thermodynamic parameters were elucidated. According to the mechanism, the *Z*-alkene is first formed and isomerized to form the *E*-alkene. A mechanism for the isomerization was also proposed and confirmed using isomerization experiments.

Continuing from chapter four, the mechanistic investigations in to *E*-selective hydrogenation is further pursued in chapter five. Computationally, the bimetallic H₂ activation is analyzed further using IRC and NBO calculations. The inter-nuclear bond orders, atom/fragment charges and NBO occupancies are analyzed as functions of the reaction coordinate for H₂ activation by a model copper-ruthenium complex. Experimentally, the catalyst decomposition is studied through a series of control experiments and the alkene/alkane elimination steps in the catalytic cycle is probed using model copper-ruthenium analogues to better understand the selectivity effects at work. A kinetic study motivated by a computational analysis performed by a collaborator is also presented.

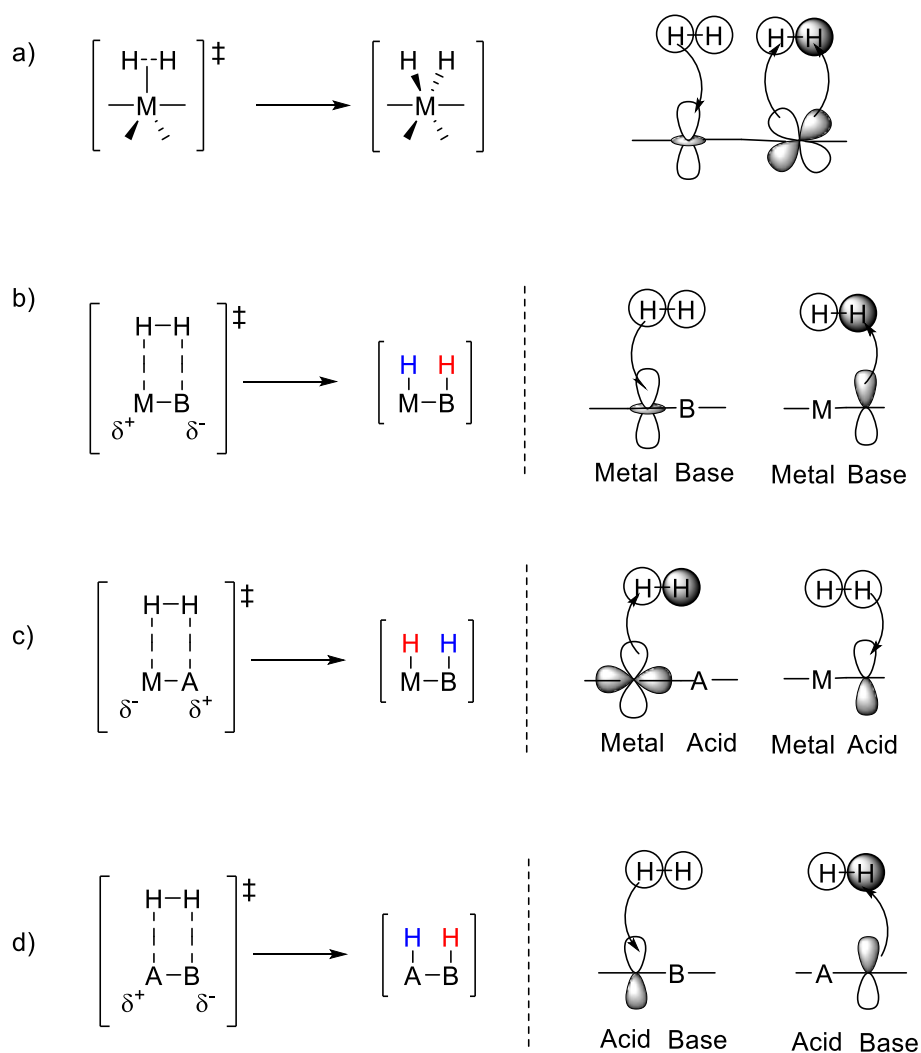
5.2. Introduction

Catalytic hydrogenation of C–C multiple bonds, one of the most studied topics in organometallic chemistry, remains crucial both for conversion of bulk hydrocarbon feedstocks and for late-stage manipulations of complex organic molecules. Advancing new technologies in this area inherently relies on identifying systems capable of H₂

activation. Many homogeneous hydrogenation catalysts rely on single-site oxidative addition of H₂.^{1,4,5,28} As emphasized in chapter one, recent advances, some of which have enabled unique catalytic selectivity and/or use of non-precious catalyst elements, move beyond the single-site paradigm to involve heterolytic H₂ activation by cooperative strategies. Examples include cooperation between a metal site and a basic residue,^{7,9,14,30,32–39} between a metal site and a Lewis acidic residue,^{41,42,44} between two different metal sites,^{71–76,78} or between non-metal frustrated Lewis acid–base pairs.^{11–13,47,55–64,66}

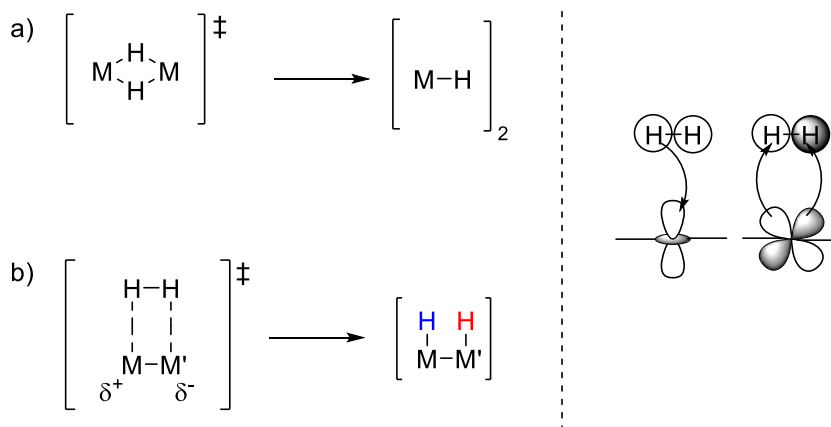
On a fundamental level, the emergence of novel selectivity modes is clearly demonstrated with the evolution of H–H activation modes with cooperative strategies. As mentioned in chapter one, the single-site oxidative addition of H₂ occurs through a σ -complex formation and the subsequent concerted homolysis of H₂. This occurs via the electron donation to an empty d-orbital of the metal from the $\sigma_{\text{H-H}}$ orbital and the back-donation to the $\sigma^*_{\text{H-H}}$ orbital from a filled metal d-orbital (Scheme 46a).

When switching to heterolytic H₂ cleavage via metal-ligand cooperativity, the orbital interactions are maintained, but using different orbital combinations. In metal-base systems, while the electron donation from the $\sigma_{\text{H-H}}$ orbital to an empty d-orbital is still operational, the back-donation to the $\sigma^*_{\text{H-H}}$ orbital is taken over by a filled p-orbital in the basic residue (Scheme 46b).⁸ In metal-acid systems, multiple orbital combinations have been calculated.^{6,40} In many examples, the electron donation occurs to the empty orbitals in the acidic residue from the $\sigma_{\text{H-H}}$ orbital, and the back-donation, to the $\sigma^*_{\text{H-H}}$ orbital from the filled d-orbitals of the metal center (Scheme 46c). In FLPs, orbital interactions show that the electron donation occurs from the $\sigma_{\text{H-H}}$ orbital to an empty orbital in the Lewis acid and back-donation from a filled orbital in the Lewis base into the $\sigma^*_{\text{H-H}}$ orbital (Scheme 46d).^{49–53}



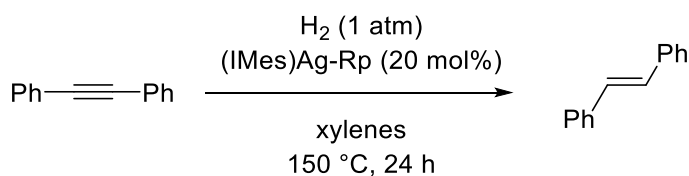
Scheme 46: Orbital interactions during H₂ activation in a) single-site b) metal-base c) metal-acid d) FLP e) bimetallic systems

In the case of bimetallic H₂ activation, both homolytic⁷⁷ and heterolytic⁷⁶ H₂ cleavage has been reported (Scheme 47). Although d-orbitals are expected to play a major role, the exact orbitals involved in electron donation and back-donation to and from $\sigma^*_{\text{H-H}}$ and $\sigma_{\text{H-H}}$ orbitals aren't well understood.



Scheme 47: Possible orbital interactions during bimetallic H₂ activation
a) homolytic cleavage b) heterolytic cleavage

In chapter four, a heterobimetallic silver-ruthenium catalyst which initially activated H₂ heterolytically was described. This catalyst displayed high stereoselectivity for *E*-alkene products, and was chemoselective for alkyne reduction in the presence of other reducible functional groups such as aldehydes, ketones, nitriles, and alkyl chlorides (Scheme 48).



Scheme 48: *E*-selective semi-hydrogenation of alkynes

The observed stereoselective *trans*-addition of H₂ to alkynes puts this catalyst in a select group of systems exhibiting *E*-selective semi-hydrogenation behavior, whether by direct hydrogenation^{9,24,62,77,264–266} or by transfer hydrogenation or indirect reduction/deprotection routes.^{246,249–253,268–270} The observed chemoselectivity for alkyne reduction in the presence of vulnerable functional groups raises the possibility of using

this technology for late-stage introduction of *trans*-alkene moieties.²⁷¹ While the optimal system utilized the precious metals Ag and Ru, non-precious metal analogues pairing Cu and/or Fe did show some activity and represent opportunities for further development. Understanding the nature of heterobimetallic H₂ activation, the catalytic mechanism, and the selectivity-determining reaction steps will aid in the design of second-generation systems featuring nonprecious metals capable of operating efficiently and selectively under mild conditions.

In this chapter, studies on the mechanism of heterobimetallic H₂ activation and on the heterobimetallic alkene/alkane elimination reactions that contribute to the observed catalytic selectivity are presented. The H₂ activation step is analyzed by computational modeling of the reaction coordinate, providing understanding of the key transition states and orbital interactions involved in H₂ cleavage. The alkene/alkane elimination steps are analyzed by stoichiometric reactivity studies of isolable models of catalytic intermediates. Additionally, new insights into catalyst decomposition pathways are disclosed. A kinetic analysis supporting predictions by a computational study by a collaborator is also presented. Inspired by the kinetic study, attempts to replace silver with copper in search for cheaper catalysts are carried out and discussed. Collectively, a mechanistic picture emerges that will aid future catalyst development in this area.

5.3. Results & Discussion

5.3.1. Control Experiments and Catalyst Decomposition

In chapter four,²³⁹ evidence for a bimetallic catalytic mechanism was provided by comparing results for diphenylacetylene hydrogenation obtained with (IMes)AgRp (Table 21, entry 1) with those obtained with (IPr)AgOAc and Rp₂, neither of which gave productive catalysis (entries 2, 3). To examine this issue further, we have subsequently

examined a larger array of Ag-free Ru catalysts, with a focus on the Ru-containing compounds produced upon catalyst decomposition under the reaction conditions.

Table 21: Ag-free and Ru-free control experiments²⁷²

$\text{Ph}-\text{C}\equiv\text{C}-\text{Ph} \xrightarrow[\text{xylene, 150 } ^\circ\text{C, 24 h}]{\text{H}_2 (1 \text{ atm}), \text{ catalyst (20 mol\%)}} \text{Ph}-\text{CH}=\text{CH}-\text{Ph} + \text{Ph}-\text{CH}=\text{CH}-\text{Ph} + \text{Ph}-\text{CH}_2-\text{CH}_2-\text{Ph}$ <div style="display: flex; justify-content: space-around; width: 100%;"> 1 2 3 </div>			
Entry	Catalyst	Conversion (%) ^a	1:2:3^a
1 ^b	(IMes)Ag-Rp	95	90:4:1
2 ^b	(IPr)AgOAc	0	N/A
3 ^b	Rp ₂ ^c	7	4:3:0
4	HRp	35	22:13:0
5	HRuCp(CO)(IMes)	47	30:17:0
6	Cp*Ru(COD)Cl/AgOTf ^d	23	6:5:12
7 ^b	(IMes)Cu-Rp	61	42:17:2
8 ^b	(IPr)Cu-Rp	60	40:18:3
9	(6Dipp)Cu-Rp	70	60:9:0

^aFrom ¹H NMR integration against an internal standard. ^bFrom ref²³⁹ ^cCatalyst loading was 10 %, i.e., 20 % Ru. ^dCatalyst loading was 20 %, i.e., 20 % Ag.

Originally, we assigned the (IMes)AgRp decomposition mixture during catalysis as involving precipitation of metallic Ag and formation of HRp (observed ¹H NMR resonances in toluene-*d*₆: δ = 4.52 and −12.04). Because a Hg drop did not poison the reaction, metallic Ag was ruled out from being catalytically relevant, but HRp was not tested as a catalyst due to initial difficulties in isolation of a pure sample. Now, we report that an isolated sample of pure HRp was found to catalyze diphenylacetylene

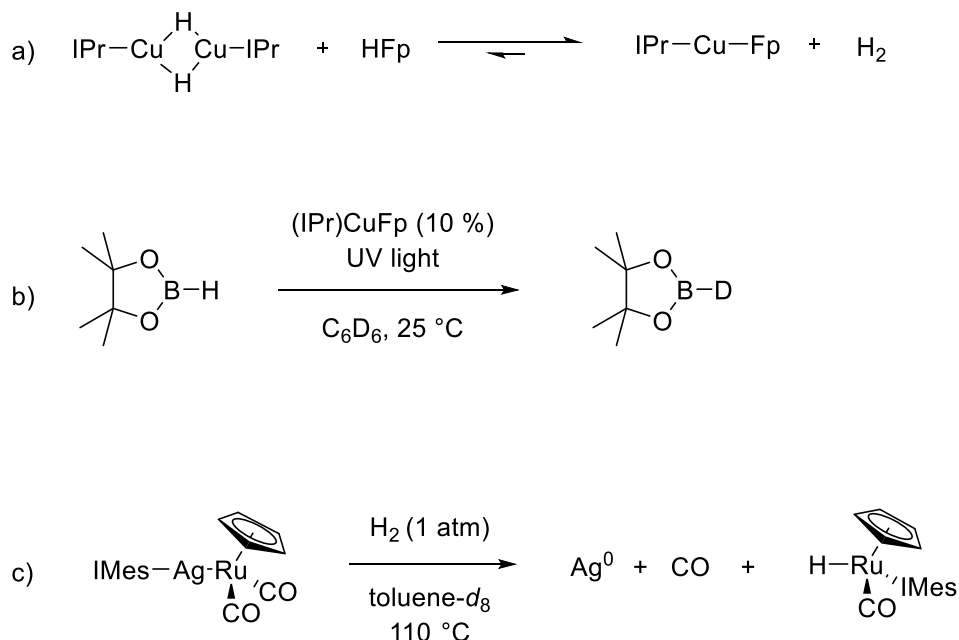
hydrogenation but did not provide high conversion of diphenylacetylene or high selectivity for *E*-stilbene (**1**) relative to the other reduction products (**2** and **3**) (entry 4). Upon examining the ^1H NMR characterization of isolated HRp, however, we noticed that its observed ^1H NMR resonances ($\delta = 4.57$ and -10.75 in toluene- d_8) did not match the resonances observed under catalytic conditions with (IMes)AgRp. Furthermore, the IMes resonances observed after catalysis with (IMes)AgRp did not match those for authentic samples of free IMes ligand. Filtration of metallic Ag and removal of organics from a catalytic product mixture provided an isolated sample of the catalyst decomposition product, which is now assigned as HRuCp(CO)(IMes) on the basis of NMR and IR characterization.

Isolating this species and re-exposing it to the catalytic conditions did provide diphenylacetylene hydrogenation (entry 5), but again the observed conversion of diphenylacetylene and selectivity for **1** were significantly lower than those for (IMes)AgRp. These two single-site Ru catalysts (entries 4, 5) likely mediate *trans*-hydrogenation of diphenylacetylene through a Ru-carbene pathway akin to that detailed by Fürstner for $[\text{Cp}^*\text{Ru}]$ catalysts at high H_2 pressure.²⁷³ One of the Fürstner catalyst mixtures utilized both Ru and Ag, but does not provide high levels of catalytic conversion or selectivity under the conditions optimal for (IMes)AgRp (entry 6). Lastly, to contextualize the Cu/Ru model studies presented below, catalytic results for (NHC)CuRp complexes are shown in entries 7 and 8.

5.3.2. Bimetallic H_2 Activation

Within the bimetallic mechanism that is operative in this system, we have proposed that the metal-metal bonded $(\text{NHC})\text{M}'\text{-}[\text{M}]$ complexes react directly with H_2 to generate

(NHC)M'-H and H[M] pairs that subsequently reduce alkyne substrates. Experimental evidence for the feasibility of this proposed bimetallic H₂ activation step comes from three observations (Scheme 49): (a) experimental observation of the microscopic reverse reaction, i.e., bimetallic H₂ elimination from 0.5 [(IPr)CuH]₂ + HFp;^{88,89} (b) H/D exchange reactivity of (IPr)CuFp observed during dehydrogenative borylation conditions,⁸⁸ which likely involves activation of HD generated in situ; and (c) observation of HRuCp(CO)(IMes) upon thermolysis of (IMes)AgRp in the absence of alkyne under H₂ (1 atm), which is presumably the result of intermediate formation of (IMes)AgH + HRp followed by thermal decomposition of (IMes)AgH by the known pathway²⁵⁶ and ligand substitution at Ru. However, experimental data on the mechanism of H₂ activation is elusive due to the thermodynamically unfavorable nature of (NHC)M'-H + H[M] relative to (NHC)M'-[M] + H₂.²³⁹ This motivated our pursuit of computationally modeling the heterobimetallic H₂ activation step.



Scheme 49: Experimental evidence for heterobimetallic H₂ activation a) Mazzacano & Mankad (2013) b) Mazzacano & Mankad (2013) c) This work

In chapter four,²³⁹ a computed transition state for H₂ activation by an (IMe)CuRp model (IMe = N,N'-dimethylimidazol-2-ylidene) was presented. The reaction between (IMe)CuRp and H₂ was calculated to be thermodynamically unfavorable ($\Delta G_{298\text{ K}} = 20.1$ kcal/mol), with an even smaller driving force than the analogous reaction involving (IMe)AgRp ($\Delta G_{298\text{ K}} = 14.1$ kcal/mol). The calculated activation barrier of $\Delta G_{298\text{ K}}^{\ddagger} = 29.0$ kcal/mol was consistent with the high temperature required for catalysis and was determined using a computational method that had been calibrated with experimental data previously.⁸⁷

The calculated activation parameters included a large and negative entropy of activation ($\Delta H^{\ddagger} = 20.1$ kcal/mol, $\Delta S^{\ddagger} = -29.8$ eu), indicating a highly organized transition-state structure. Here, to develop a deeper understanding of this H₂ activation reaction, we provide a thorough discussion of the computed reaction pathway provided by analysis of atom/fragment charges, interatomic bond orders, and natural bond orbital occupancies, all as functions of the intrinsic reaction coordinate (IRC). These results also expand on the discussions of an analogous Cu-Fe transition state for H₂ elimination⁸⁹ and of a Cu-Fe transition state for C-Cl activation,⁸⁷ both disclosed previously, the latter which was presented in chapter three.

For all the results discussed below, the various computed parameters have been tracked across several points along the computational IRC scan: the optimized reactant complex (**R**), three points from the IRC scan before the transition state, the transition state (**TS4**), three points from the IRC scan after the transition state, and the optimized product complex (**P**). The energetic profile of these states and the **TS4** structure are shown in Figure 15.

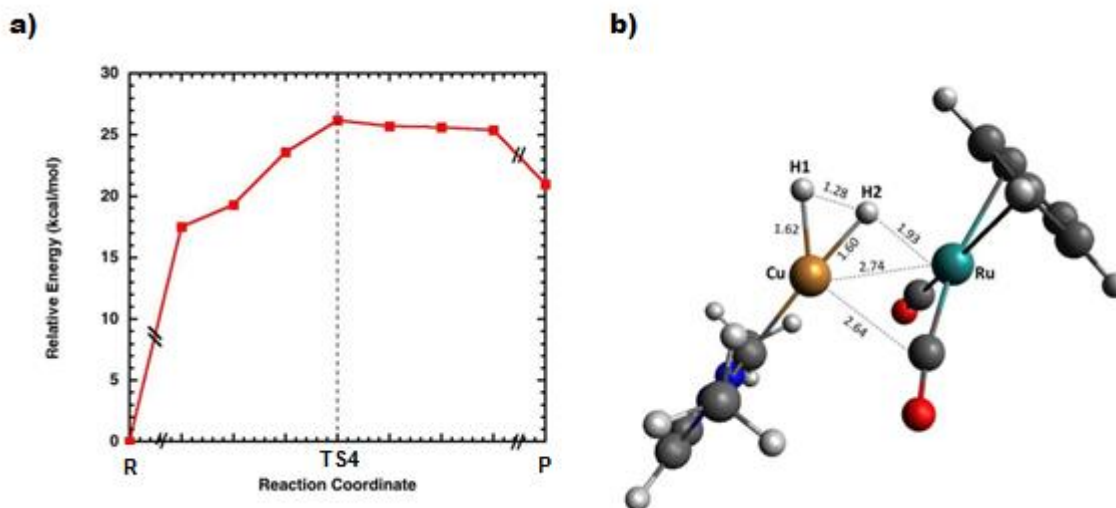


Figure 15: Computational modeling of the reaction between (IMe)-CuRp and H₂. a) Relative energies of the structures from the intrinsic reaction scan that were analyzed for this study b) Transition state structure TS4, with key inter-nuclear distances labeled in units of Å. // = discontinuity.²⁷²

Upon examining the calculated trajectory of H₂ approach, it is clear that the reaction proceeds via the H₂ substrate initially forming a σ -complex at the Cu site. As the H₂ molecule approaches Cu, it induces Cu-Ru bond dissociation as well as NHC-Cu-Ru bending (133° in **TS4** vs 179° in **R**). Structural templating of the bimetallic transition state involving semibridging carbonyl ligands seems not to be operative in this case, as both Cu...CO distances increase smoothly along the reaction coordinate without exhibiting a local minimum at the transition state that is seen in other cases.^{87,239}

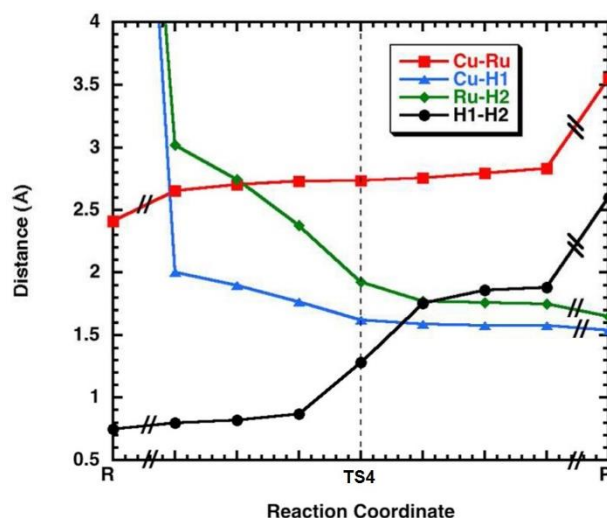


Figure 16: Selected inter-nuclear distances for the reaction between (IMe)-CuRp and H₂, plotted along the calculated intrinsic reaction coordinate scan. // = discontinuity.²⁷²

Figure 16 plots key inter-nuclear distances as functions of reaction coordinate. The Cu-Ru distances increase smoothly as the Cu-H1 distance decreases smoothly. The Ru-H2 and H1-H2 distances change more abruptly: the Ru-H2 bond is almost completely associated and the H1-H2 bond nearly dissociated at the **TS4** structure. These observations are consistent with a late transition state resembling the products and with a model that resembles deprotonation of a Cu(H2) σ -complex by the Rp fragment.

Prior to dissociation of the two metal-hydride complexes to yield the **P** state, there appears to be a locally preferred H1 \cdots H2 contact of 1.76–1.88 Å at later stages of the reaction profile. These short H \cdots H distances are in the dihydrogen-bonding regime^{274,275} and indicate polarization of the H₂ molecule. Experimental evidence for M-H \cdots H-M' dihydrogen bonding in a related system has been reported, and the accompanying

computational analysis indicated a dihydrogen bond strength of 1.7 kcal/mol in that system.²⁷⁶

The reaction profile was also analyzed using computed bond orders, determined by calculation of Wiberg bond indices (WBIs) derived from natural bond orbital (NBO) calculations. The changes in WBI values across the reaction coordinate (Figure 17) reinforce conclusions reached by analyzing bond distances. The Cu–Ru bond in **R** experiences a smooth dissociation across the reaction coordinate and is partially broken at the **TS4** state. The Cu–H1 and Ru–H2 bonds are partially formed at **TS4**, and the covalent H1–H2 bond is mostly broken at **TS4**. In the post-**TS4** portion of the reaction coordinate, a locally preferred set of WBI values again indicates the presence of dihydrogen bonding between (IMe)CuH and HRp. Only upon complete dissociation at the **P** state are the Cu–H1 and Ru–H2 bonds completely formed and the Cu–Ru and H1–H2 bonds completely broken.

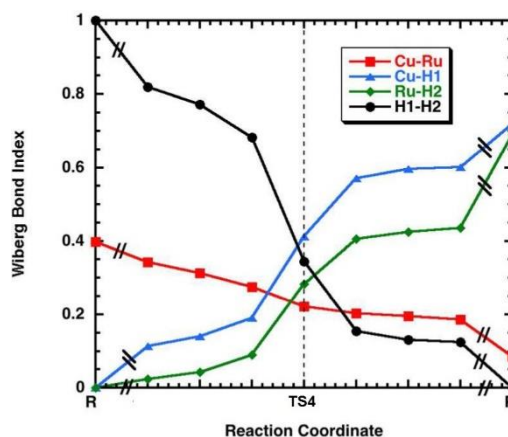


Figure 17: Selected Wiberg bond index values for the reaction between (IMe)-CuRp and H₂, plotted along the calculated intrinsic reaction coordinate scan. // = discontinuity.²⁷²

Analysis of atom/fragment charges across the reaction coordinate provides insight into the extent to which redox activity is delocalized throughout the bimetallic reaction center and its supporting ligands. Natural charge values derived from natural population analysis are plotted in Figure 18. A traditional, single-site oxidative addition process is generally thought to involve homolytic H-H bond dissociation accompanied by two-electron oxidation of the metal center. In the bimetallic H₂ cleavage reaction being examined here, the reaction clearly involves heterolytic H₂ cleavage. In addition to the computational evidence for dihydrogen bonding disclosed above, the H1-H2 bond undergoes cleavage to produce hydridic H1 ($q = -0.42$ in **P**) and protic H2 ($q = 0.18$ in **P**) as the reaction proceeds.

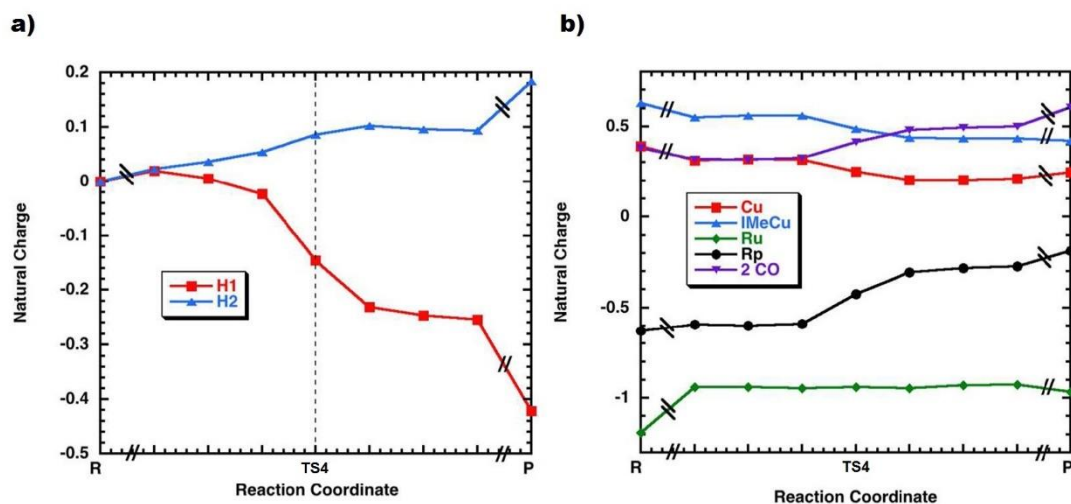


Figure 18: Selected natural charge values derived from natural population analysis for the reaction between (IMe)-CuRp and H₂, plotted along the calculated intrinsic reaction coordinate scan. // = discontinuity.²⁷²

Neither the Cu center itself nor the (IMe)Cu fragment undergoes significant oxidation during the reaction, indicating that the oxidation behavior is located mainly on the Rp fragment. Indeed, the Rp charge is calculated to increase during the reaction. The Ru center maintains constant charge throughout the reaction, indicating that redox activity is localized not on Ru but mainly on the ligands supporting Ru. The cumulative charge of the two carbonyl ligands tracks with the increase in charge of the Rp fragment during the reaction, indicating that much of the redox activity occurs at the two CO units. Similar conclusions have been reached previously during studies of bimetallic reaction pathways involving (NHC)M'[M] complexes through experimental (chapter two)¹²⁶ and computational (chapter three)^{87,89,126} analyses, and all of these studies collectively highlight the importance of redox-active carbonyl ligands in the (NHC)M'-[M] catalyst design. On the other hand, the IMe and Cp ligands have similar charges in **R** and **P** and therefore are not redox-active with regard to this reaction.

Analysis of NBO occupancies as functions of reaction coordinate provides insight into the key orbital interactions involved in bimetallic H₂ cleavage.⁶ Selected NBO occupancies are plotted in Figure 19 (left axis). As the reaction proceeds from **R** to **TS4**, the occupancy of the $\sigma_{\text{H-H}}$ orbital (labeled BD(H-H)) decreases, consistent with transfer of charge from this orbital toward the catalyst upon formation of a σ -complex.

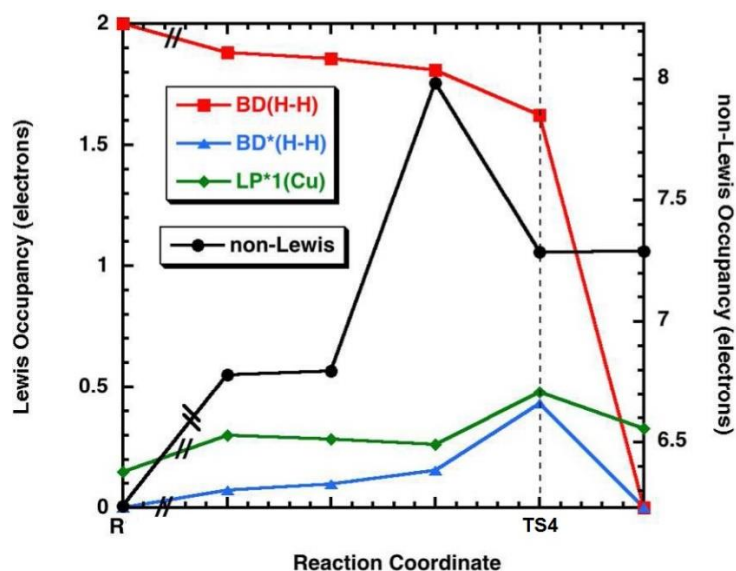


Figure 19: Selected NBO occupancy values for the reaction between (Ime)-CuRp and H₂, plotted along the calculated intrinsic reaction coordinate scan. Lewis occupancies of the H₂ bonding and antibonding NBOs and of a key Cu acceptor NBO are plotted on the left axis. Total non-Lewis occupancy of the system is plotted on the right axis. // = discontinuity.²⁷²

The loss of electron density (0.38 e) from the $\sigma_{\text{H-H}}$ orbital is almost completely matched by an increase in occupancy (0.33 e) of a Cu valence orbital (labeled LP*1(Cu)) that has $s^{0.05}p^{0.94}d^{0.01}$ hybridization (Figure 20). This is the only NBO that increases occupancy significantly as a function of reaction coordinate, and so it is assigned as the acceptor orbital to which the $\sigma_{\text{H-H}}$ orbital is donating charge. Additionally, the $\sigma^*_{\text{H-H}}$ orbital (labeled BD*(H-H)) gains occupancy (0.43 e) as the reaction proceeds, consistent with back-donation from the catalyst as the H₂ molecule coordinates and cleaves. We could not identify any NBO that experienced a corresponding decrease in occupancy over the same part of the reaction coordinate. Instead, we assign the donor orbital that transfers

charge into the $\sigma^*_{\text{H-H}}$ orbital as being the Cu-Ru bonding orbital shown in Figure 20. In the **R** state, this NBO has 87% Ru character ($s^{0.13}p^{0.01}d^{0.77}$) and 13% Cu character ($s^{0.87}p^{0.06}d^{0.08}$).

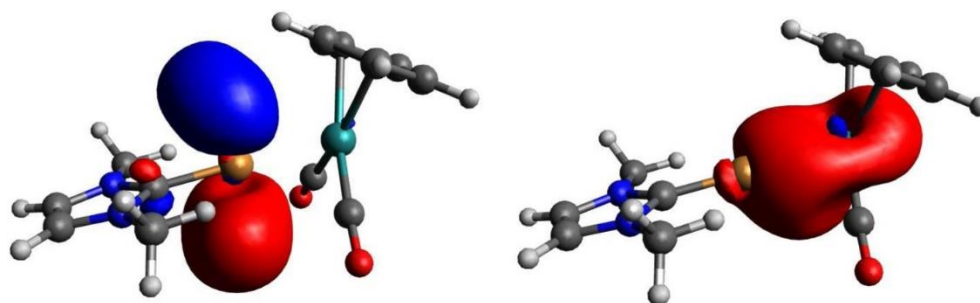
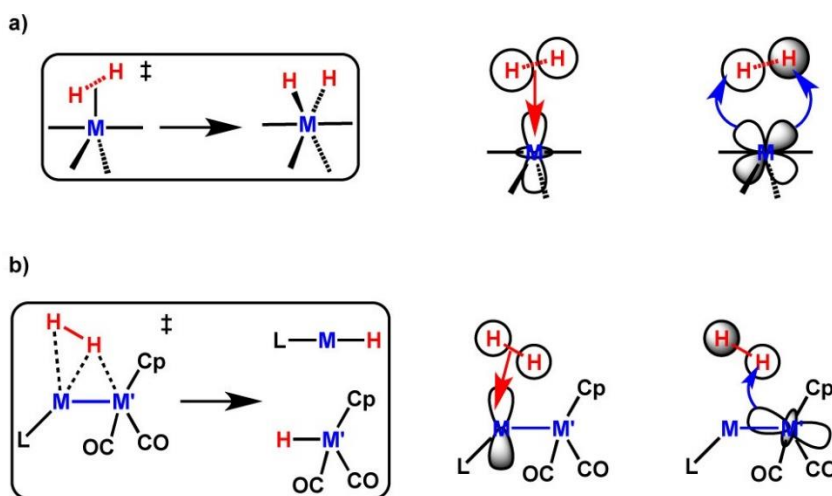


Figure 20: Surface plots (0.04 isovalues) of the LP*1(Cu) (left) and BD(Cu-Ru) (right) NBOs in **R** that are crucial acceptor and donor orbitals, respectively, for bimetallic H_2 cleavage. For clarity, the distant H_2 molecule has been omitted from the images.²⁷²

In subsequent states in the reaction profile where the Cu-Ru bond has partially dissociated, this Cu-Ru bonding NBO was not identified but instead was replaced by enhanced $\text{Rp} \rightarrow \text{Cu(Ime)}$ donor/acceptor interactions and $\text{Rp} \rightarrow \text{H}_2$ donor/acceptor interactions, with the $\text{Rp} \rightarrow \text{Cu(Ime)}$ donation decreasing and the $\text{Rp} \rightarrow \text{H}_2$ donation increasing in energetic contribution with the reaction coordinate. This behavior can be tracked using the non-Lewis occupancy of each state (Figure 20, right axis), which does increase as the reaction proceeds. The Cu-Ru bonding orbital has 1.59-e occupancy in **R**, and 1.05 e are accounted for by the increase in non-Lewis occupancy as the reaction progresses to **TS4**. The remaining 0.54 e resembles the buildup of $\sigma^*_{\text{H-H}}$ occupancy (0.43

e), allowing us to assign the Cu-Ru bonding orbital (of predominantly Ru 4d character) as the main back-donating orbital that triggers H-H cleavage.



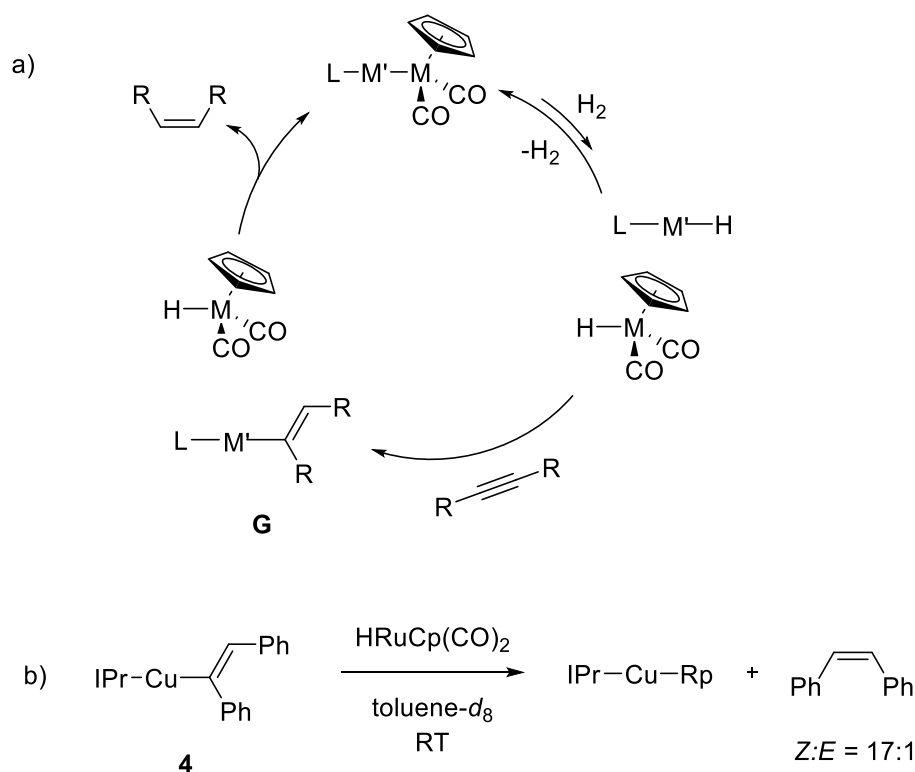
Scheme 50: Transition states and orbital interactions involved in a) monometallic and b) bimetallic H₂ addition.²⁷²

The traditional view of single-site H₂ oxidative addition involves formation of a σ-complex followed by concerted H-H homolysis that is triggered by (a) donation from σ_{H-H} to an empty metal d-orbital and (b) back-donation from a filled metal d-orbital into σ*_{H-H} (Scheme 50a). For the bimetallic H₂ activation reaction studied here, a complementary mechanistic scheme has emerged from the computational data above (Scheme 50b). Heterobimetallic H₂ addition involves formation of a σ-complex at the electrophilic metal site, followed by H-H heterolysis via H⁺ transfer to the proximal nucleophilic metal site. The key orbital interactions that trigger this heterolytic H₂ cleavage are (a) donation from σ_{H-H} to an empty orbital at the electrophilic metal site and (b) back-donation into σ*_{H-H} from a filled orbital predominantly located at the nucleophilic metal site. Such separation of the key orbital interactions across two reactive sites strongly resembles H₂ activation

by p-block frustrated Lewis pairs (FLPs), which involves donation from $\sigma_{\text{H-H}}$ to a Lewis acid and from a Lewis base to $\sigma^*_{\text{H-H}}$.^{49–53} In this regard, the (NHC)M'-[M] catalysts can be viewed as d-block analogues of the classical p-block FLPs.

5.3.3. Alkene/Alkane Elimination and Selectivity Effects

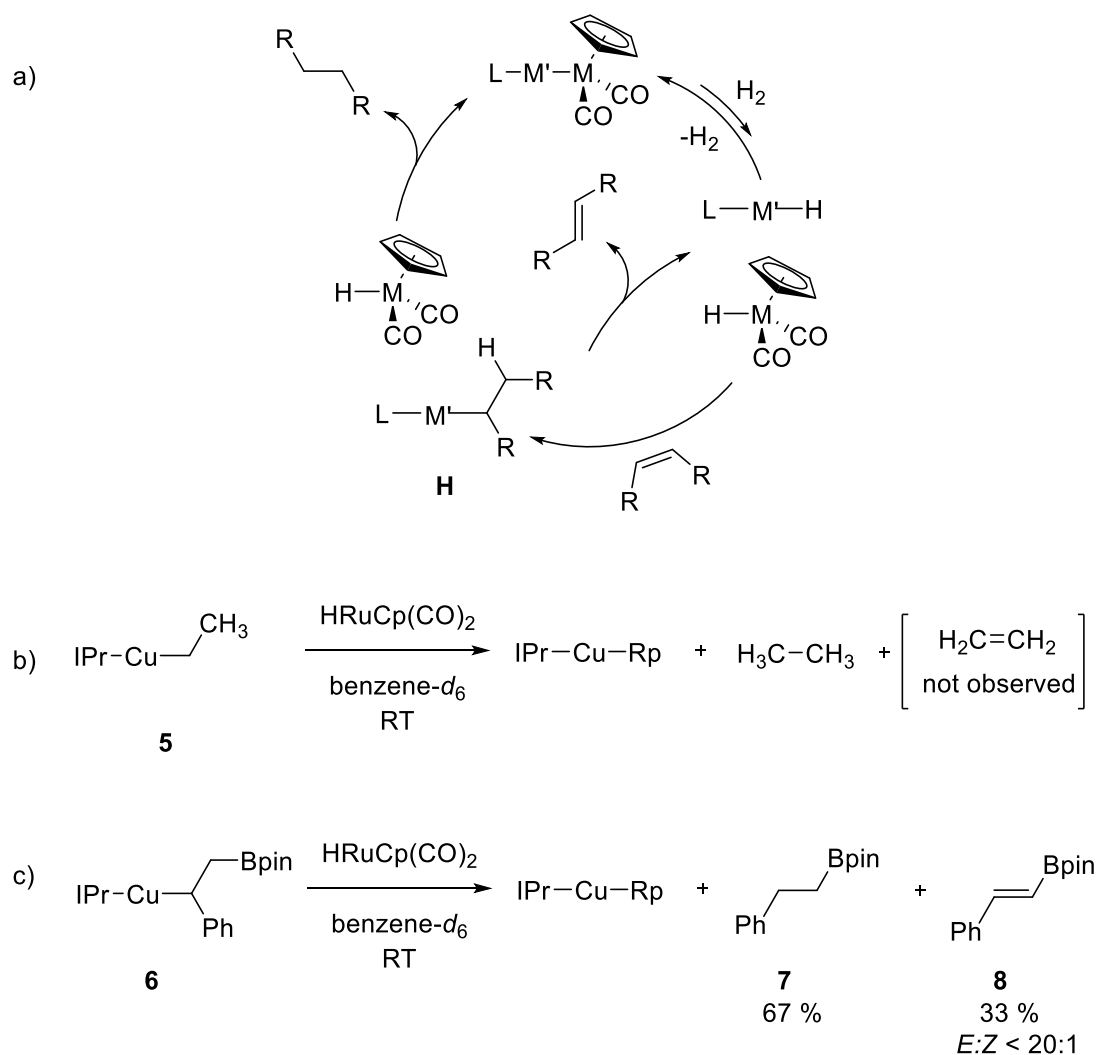
Upon heterobimetallic H_2 activation under catalytic conditions, our proposal is that the alkyne substrate undergoes 1,2-insertion with the transient (IMes)AgH intermediate to yield an alkenyl species. On the basis of stoichiometric *syn*-hydrocupration behavior reported for [(IPr)CuH]₂,²⁷⁷ we propose that this 1,2-insertion reaction produces the C=C geometry shown in structure **G** (Scheme 51a).



Scheme 51: a) Proposed alkyne hydrogenation mechanism b) Model alkene elimination reaction

Under catalytic conditions, bimetallic alkene elimination is proposed to occur through reaction of **G** with HRp, producing a *Z*-alkene and regenerating the bimetallic catalyst. To test the feasibility of this proposed step, we prepared alkenyl-copper complex **4** by *syn*-hydrocupration of diphenylacetylene. Complex **4** was found to react with HRp to produce (IPr)CuRp and generate stilbene with high *Z*-selectivity (Scheme 51b).

The fact that both the hydrocupration and alkene elimination steps proceed at room temperature implies that H₂ activation is the turnover-limiting step in the catalytic process. The generation of *Z*-alkene from this model reaction is consistent with our model of a cascade alkyne \rightarrow *Z*-alkene \rightarrow *E*-alkene process. The feasibility of *Z* \rightarrow *E* alkene isomerization was supported by experiments reported in our initial communication,²³⁹ showing that *cis*-stilbene was isomerized to *trans*-stilbene under catalytic conditions provided that both the catalyst and H₂ were present. The proposed mechanism of isomerization (Scheme 52a) involves 1,2-insertion of alkene with (IMes)AgH to produce an alkyl intermediate (**H**).



**Scheme 52: a) Proposed alkene isomerization mechanism
b and c) Model reactions for alkene vs alkane elimination**

The key, selectivity determining step then involves single-site β -hydride elimination from **H** to produce the final *E*-alkene product. In order to produce high selectivity for *E*-alkene relative to *Z*-alkene and alkane, this β -hydride elimination reaction must (a) be under thermodynamic control to suppress reversion to *Z*-alkene by β -hydride elimination and (b) outcompete bimetallic alkane elimination from reaction between **H** and HRp. To probe these factors, we conducted model reactions with two known alkyl-copper species

that have β -hydrogens. The ethyl complex **5**²⁷⁸ was found to react with HRp to produce (IPr)CuRp and ethane (Scheme 52b). This observation establishes that bimetallic alkane elimination from intermediate **H** is feasible, consistent with the small amounts of alkane formed in typical catalytic trials.²³⁹ No evidence for ethylene formation was observed in this experiment, indicating that for model complex **5** the bimetallic alkane elimination reaction outcompetes the desired β -hydride elimination reaction. We conducted an analogous experiment with alkyl-copper complex **6** (Scheme 52c), which has been shown to undergo reversible β -hydride elimination under mild conditions.²⁷⁹ Complex **6** was found to react with HRp to produce (IPr)CuRp and generate a 2:1 mixture of alkane **7** and *E*-alkene **8**. No evidence for *Z*-alkene was observed.

These observations show that, in a model system with an alkyl ligand that more closely resembles the catalytically relevant intermediate, β -hydride elimination can outcompete alkane elimination and furthermore that it is selective for extrusion of *E*-alkene products. These results show that the relative rates of β -hydride elimination and bimetallic alkane elimination are very sensitive to steric effects, and an optimal steric environment must be used in the catalyst design in order to produce high selectivity for *E*-alkene generation. The real catalytic system, which features less stable alkyl intermediates **H**, is thus finely tuned to favor β -hydride elimination over bimetallic alkane elimination, unlike the model systems **5** and **6**, which are stable enough for stoichiometric reactivity studies. These observations are consistent with the dramatic impact that the NHC steric bulk has on catalytic selectivity.²³⁹ In addition, the use of Ag in place of Cu in the optimal catalyst may derive, in part, from the more facile rate of β -hydride elimination from a 4d metal compared to a 3d metal. Lastly, the use of Rp in place of Fp in the optimal catalyst may derive, in part, from the fact that HRp is a weaker acid than HFp by $\sim 2\text{pKa}$ units,²⁸⁰ which serves to suppress the bimetallic alkane elimination process that is in

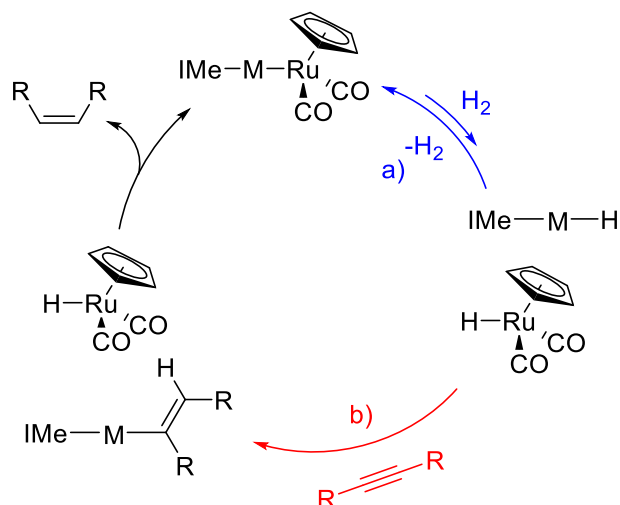
competition with productive β -hydride elimination. All of these factors need to be held in consideration when designing second-generation catalysts.

5.3.4. Kinetic Studies

Transition metal heterobimetallic catalysts have been gaining attention in the recent years as a cooperative strategy to mimic single-site catalysis. Therefore, mechanistic studies of such reactions are of broad interest. However, some of the mechanistic inquiries are not always accessible by conventional experimental approaches. Thus, computational calculations are utilized in the modern era to aid mechanistic studies and add insight to experimental findings.

For example, Ess group has been studying both heterobimetallic and homobimetallic catalytic reactions via computational calculations. Their work includes hydrogenation of alkenes by iridium-tantalum systems⁸¹, allylic amination by palladium-titanium systems,¹⁷⁸ and alkyne cyclotrimerization reactions by di-nickel systems.²⁸¹

Recently, our hypothetical hydrogenation mechanism was probed computationally by the Ess group. The transition states and the energy barriers (ΔG^\ddagger) associated with the steps in the catalytic cycle were calculated for both copper-ruthenium and silver-ruthenium catalysts. Preliminary calculations revealed that the energy barrier for H₂ activation by the metal-metal bond was indeed relatively high for the copper-ruthenium system making it the rate-limiting step in the cycle (Scheme 53a), in agreement with our calculations and experiments presented earlier (chapter four and five).^{239,272} However, an interesting new finding that surfaced was that when the catalytic cycle of the silver-ruthenium system was probed, the alkyne insertion into the metal-hydride step had the overall higher energy barrier (Scheme 53b) implying this step to be the rate-determining step.



Scheme 53: Calculated rate limiting steps for the catalytic cycle of alkyne semi-hydrogenation by $(\text{IMe})\text{M}[\text{RuCp}(\text{CO})_2]$ catalysts ($\text{IMe} = \text{N,N'-dimethylimidazol-2-ylidene}$) a) for $\text{M} = \text{Cu}$ (denoted by blue) b) for $\text{M} = \text{Ag}$ (denoted by red)

In order to examine this experimentally, a series of kinetic experiments was carried out (Table 22) using diphenylacetylene as the starting material. First, the kinetic isotope effects (KIEs) were analyzed. For the copper-ruthenium system, a primary KIE was observed with a value of 4.9 (entry 1). This is consistent with the H_2 activation step being the rate determining step²⁸² as predicted by the calculations and our previous experiments. For the silver-ruthenium system, an inverse KIE of 0.6 (entry 1) was observed. An inverse KIE can occur if the coordination of the reaction center increases at the transition state.²⁸² This again fits nicely with the calculations as the reaction center, the alkyne, is converted to a metal-alkenyl product in the proposed rate determining alkyne insertion step in to the metal.

Table 22: Kinetic parameters for hydrogenation by (IMes)M-Rp; (M=Cu, Ag)

$\text{Ar}-\text{C}\equiv\text{C}-\text{Ar} \xrightarrow[\text{toluene-}d_8, 90^\circ\text{C}, 12\text{ h}]{\text{H}_2 \text{ or D}_2 (1\text{ atm}), (\text{IMes})\text{M-Rp} (20\text{ mol}\%)}$ $\text{Ar}-\text{CH}=\text{CH}-\text{Ar} + \text{Ar}-\text{CH}=\text{CH}-\text{Ar} + \text{Ar}-\text{CH}_2\text{CH}_2-\text{Ar}$			
Entry	Kinetic parameter ^a	M =Cu	M =Ag
1	Kinetic Isotope Effect (k_H/k_D) ^b	4.9	0.6
2	Rate of reaction (k_{OMe}/k_H) ^c	2.0	7.4

^aDetermined by initial rates using in-situ NMR ^bAr = Ph ^cAr = *p*-MeOC₆H₄ for OMe and Ph for H.

The substitution effects of the alkyne on the reaction rate was explored next by comparing the initial rates for two different alkynes. The *para*-hydrogens of diphenylacetylene were switched with methoxy groups and the initial rates were determined. The effect on the rate of the copper-ruthenium system was minimal as only a k_{OMe}/k_H ratio of 2.0 was observed (entry 2). However, the effect on the rate of the silver-ruthenium system was significantly higher with a k_{OMe}/k_H ratio of 7.4 (entry 2). This further validates the projection from the calculation that the rate determining step for the silver-ruthenium system is in fact the alkyne insertion step.

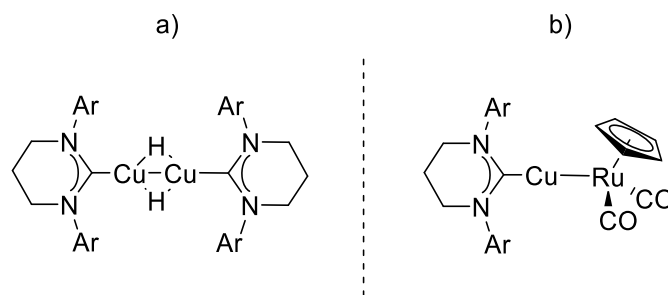
5.3.4.1. Potential for Cheaper Hydrogenation Catalyst Development

Another interesting and unanticipated result that we stumbled upon with the kinetic experiments was that the initial reaction rate of hydrogenation was actually three times faster in copper-ruthenium systems than in silver-ruthenium systems. This is quite unexpected as we know that the final yields of the silver-ruthenium catalysts are actually

much higher than the copper-ruthenium ones (Table 23, entries 1 and 2). Our rationale for this result and how to manipulate it is as follows.

NHC-copper-hydrides are known to be extremely unstable and sometimes even un-isolable.²⁵⁹ Our working theory is that even though the initial rate of hydrogenation is higher for the copper-ruthenium catalysts, due to the unstability of the copper-hydride intermediates, they actually decompose readily before reaction completion is achieved. Therefore, despite their efficiency, they end up performing poorly in the end due to their short lifetime. However, if we can move towards accessing more stable copper hydrides, we can expect to improve the overall yield by the copper-ruthenium systems and ultimately aim to even out-perform the silver-ruthenium catalysts.

Whilst most of the NHC-copper-hydrides are unstable, Sadighi group recently reported relatively stable copper-hydrides using expanded-ring-N-heterocyclic carbenes 6Dipp (Scheme 54a) and 7Dipp (6Dipp = 1,3-bis(2,6-isopropylphenyl)-3,4,5,6-tetrahydropyrimidin-2-ylidene and 7Dipp = 1,3-bis(2,6-isopropylphenyl)-4,5,6,7-tetrahydro-1,3-diazepin-2-ylidene).²⁸³ Therefore, we synthesized heterobimetallic analogues using these NHC-copper precursors. As a proof of concept, (6Dipp)Cu-Rp (Scheme 54b) was synthesized.



Scheme 54: a) Stable $[(6Dipp)Cu-H]_2$ reported by Sadighi group b) Analogous heterobimetallic catalyst $(6Dipp)Cu-Rp$: Ar = 2,6-isopropylphenyl

Catalytic hydrogenation was then attempted with this newly synthesized catalyst (Table 23, entry 3). As predicted, the overall yield of the reaction as well as the *E*-alkene production increased from 60 to 70 percent and 42 to 60 percent respectively, in comparison to the previous best copper-ruthenium catalyst, (IMes)Cu-Rp (Table 23, entry 2). So, an improvement on both the yield and selectivity was evident. However, the silver-ruthenium system remains as the best catalyst (Table 23, entry 1). Still, this is a promising result as this (6Dipp)Cu-Rp catalyst is the best copper-ruthenium catalyst to date and could be utilized in pursuing future hydrogenation reactions.

Table 23: Catalytic hydrogenation of alkynes

$\text{Ph}-\text{C}\equiv\text{C}-\text{Ph} \xrightarrow[\text{xylene, 150 } ^\circ\text{C, 24 h}]{\text{H}_2 \text{ (1 atm), catalyst (20 mol\%)}} \text{Ph}-\text{CH}=\text{CH}-\text{Ph} + \text{Ph}-\text{CH}=\text{CH}-\text{Ph} + \text{Ph}-\text{CH}_2\text{CH}_2-\text{Ph}$ <div style="display: flex; justify-content: space-around; width: 100%;"> 1 2 3 </div>			
Entry	Catalyst	Conversion (%) ^a	1:2:3^a
1 ^b	(IMes)Ag-Rp	95	90:4:1
2 ^b	(IMes)Cu-Rp	61	42:17:2
3	(6Dipp)Cu-Rp	70	60:9:0

^aFrom ¹H NMR integration against an internal standard. ^bFrom ref²³⁹

5.4. Conclusions

In conclusion, in this study we have disclosed further details regarding catalyst decomposition pathways, the mechanism of H₂ activation, the feasibility of the proposed mechanistic cascade, and the factors relating to *E*-alkene selectivity in the catalytic semi-

hydrogenation of alkynes using heterobimetallic catalysts of the type (NHC)M'-[M]. The conclusions drawn from this study will inform future catalyst designs related to hydrogenation catalysis. Specifically, in order to improve catalytic activity (possibly with earth-abundant metals) and operate at milder temperatures, it will be necessary both to (a) lower the barrier for heterobimetallic H₂ activation and (b) stabilize the vulnerable (NHC)M'H intermediates. Knowledge gained here about the key transition states and orbital interactions involved in heterobimetallic H₂ activation can serve to guide development of second-generation systems that activate H₂ more readily, and known methods for stabilizing (NHC)M'H can be pursued in concert.^{284,283} In order to maintain high selectivity for *E*-alkenes, it will be necessary for such systems to allow for efficient alkene 1,2-insertion and β -hydride elimination processes while suppressing heterobimetallic alkane elimination. The experimental results disclosed here indicate that the relative rates of these processes will be highly sensitive not only to the steric demands of the substrate but also to the steric and electronic properties of the NHC, M', and [M] fragments in the catalyst species. A kinetic study was also presented revealing a possibility of switching the expensive metals with cheaper ones. Development of new hydrogenation catalysts, with these factors in mind, is in progress in our laboratories.

5.5. Experimental Procedures

5.5.1. General Considerations

Unless otherwise specified, all reactions and manipulations were performed under purified N₂ in a glovebox or using standard Schlenk line techniques. Glassware was oven-dried prior to use. Toluene was sparged with argon and dried using a Glass Contour Solvent System built by Pure Process Technology, LLC. Xylenes, benzene, and all deuterated solvents were purified by repeated freeze-pump-thaw cycles followed by

prolonged storage over activated 3 Å molecular sieves. H₂ gas was purchased from Praxair at a purity of 99.999% (5.0 UHP grade) and purified further by running through an O₂-removing catalyst column (RCI GetterMax 133T) and a drying column (Drierite). Literature methods were used to synthesize **5**,²⁷⁸ **6**,²⁷⁹ (IMes)AgRp,²³⁹ (IPr)CuOtBu,²⁷⁷ 6DippCuCl²⁸³ and NaRp.²³² Unless otherwise specified, all other chemicals were purchased from commercial sources and used without further purification.

5.5.2. Physical Measurements

NMR spectra were recorded at ambient temperature using Bruker Avance DPX-400 and Bruker Avance DRX500 spectrometers. ¹H NMR and ¹³C{¹H} NMR chemical shifts were referenced to residual solvent peaks. FT-IR spectra were recorded on solid samples in a glovebox using a Bruker ALPHA spectrometer fitted with a diamond-ATR detection unit. GC-MS data were obtained using an Agilent Technologies 7890A GC system interfaced to an Agilent Technologies 5975C VL mass selective detector. Elemental analyses were performed by Midwest Microlab, LLC (Indianapolis, IN, USA).

5.5.3. Computational Methods

Optimized structures for the reactants, products, and transition state for (IMe)CuRp + H₂ were obtained from our previous study (chapter four),²³⁹ along with the IRC scan data. All calculations were performed using Gaussian09, revision B.01.¹⁶² Density functional theory calculations were carried out using a hybrid functional, BVP86, consisting of Becke's 1988 gradient-corrected Slater exchange functional¹⁶³ combined with the VWNS local electron correlation functional and Perdew's 1986 nonlocal electron correlation functional.¹⁶⁴ Mixed basis sets were employed: the LANL2TZ(f) tripleζ basis

set^{165–167} with effective core potential^{165,168,169} was used for Cu and Ru and the 6-311+G(d) basis set^{285,286} was used for C, H, N, and O. The sum of electronic and thermal free energies was used to calculate ΔG values at 298 K. Natural population analysis was used to determine atom/fragment charges, and Wiberg bond indices were used to determine bond orders. Both were obtained from NBO v. 3.165 calculations within Gaussian09.

5.5.4. Preparation of HRp

A modified version of the literature procedure²⁸⁰ was used. NaRp (0.0380 g, 0.155 mmol, 1 equiv) was mixed with toluene (5 mL), and 4.0 M HCl in dioxane (0.038 mL, 0.155 mmol, 1 equiv) was added. The resulting mixture was stirred overnight at room temperature. The solution was filtered through a Celite pad, and the filtrate was evaporated to dryness. Yield: 0.0131 g, 0.59 mmol, 38%. The solid was stored in a glovebox freezer at $-36\text{ }^{\circ}\text{C}$. ^1H NMR (400 MHz, toluene- d_8): δ 4.57 (s, 5H, Cp), -10.75 (s, 1H, Ru–H).

5.5.5. Preparation of HRu(Cp)(CO)(IMes)

In a nitrogen-filled glovebox, (IMes)AgRp (0.0051 g, 0.00788 mmol) was dissolved in xylenes (1 mL), transferred to a J. Young NMR tube, and sealed. (The transfer was done in two steps: First, the maximum amount of catalyst was dissolved in 0.7 mL of xylenes and transferred. The vial was washed with another 0.3 mL of xylenes to transfer remaining solids.) The J. Young tube was inverted multiple times to make sure that all solids dissolved; then the tube was connected to a Schlenk line containing H_2 gas (1 atm). After degassing the solution using three 5 min freeze–pump–thaw cycles, the sample was frozen again, exposed to H_2 , and allowed to thaw and equilibrate for 30 min.

The J. Young tube was then resealed and heated in an oil bath at 150 °C for 24 h. The tube was then transferred back into the glovebox, filtered through Celite, and dried in vacuo. Yield: 0.0026 g, 0.00520 mmol, 66%. ^1H NMR (400 MHz, benzene- d_6): δ 7.08 (s), 7.04 (s, 4H), 6.85 (s), 6.28 (s), 4.58 (s, Cp), 2.21 (s), 2.18 (s), 2.14 (s), -11.98 (s, Ru-H). $^{13}\text{C}\{^1\text{H}\}$ NMR (125 MHz, benzene- d_6): δ 208.8 (CO), 139.0, 138.5, 136.4, 136.4, 136.1, 129.4, 121.8, 82.1 (Cp), 21.3, 18.8, 18.5. IR (solid, cm^{-1}): 1885 (CO). Anal. Calcd for $\text{C}_{27}\text{H}_{30}\text{N}_2\text{RuO}$: C, 64.91; H, 6.05; N, 5.61. Found: C, 64.78; H, 6.20; N, 4.36.

5.5.6. Catalytic Trials

Catalytic hydrogenation trials with HRp and HRuCp(CO)(IMes) were conducted using the procedure we published previously and mentioned in chapter four,²³⁹ under identical reaction conditions, and using the same method of product analysis by ^1H NMR integration.

5.5.7. Preparation of 4.

This species was prepared by hydrocupration of diphenylacetylene using the procedure reported for hydrocupration of 3-hexyne.²⁷⁷ In a scintillation vial, (IPr)CuOtBu (0.0633 g, 0.12 mmol, 1 equiv) and diphenylacetylene (0.0215 g, 0.12 mmol, 1 equiv) were dissolved in benzene (10 mL). Triethoxysilane (40.5 μL , 0.23 mmol, 1.9 equiv) was added to the solution, which was then stirred overnight at room temperature. The solution was concentrated in vacuo to afford an off-white powder. Yield: 0.0574 g, 0.091 mmol, 76%. The solid was stored in a glovebox freezer at -36 °C. ^1H NMR (400 MHz, benzene- d_6): δ 7.26 (t, $^3J_{\text{H-H}} = 4.0$ Hz, 2H, *p*-H), 7.19 (s, 2H), 7.08 (d, $^3J_{\text{H-H}} = 4.0$ Hz, 4H, *m*-H), 7.05 (d, $^3J_{\text{H-H}} = 4.0$ Hz, 2H), 6.99–6.87 (m, 3H), 6.86–6.74 (m, 4H), 2.56 (sept, $^3J_{\text{H-H}} = 4.0$

Hz, 4H, CH(CH₃)₂), 1.32 (d, ³J_{H-H} = 4.0 Hz, 12H, CH(CH₃)₂), 1.08 (d, ³J_{H-H} = 4.0 Hz, 12H, CH(CH₃)₂). ¹³C{¹H} NMR (125 MHz, benzene-*d*₆): δ 185.6 (NCCu), 177.1, 154.7, 145.8, 141.3, 135.3, 133.9, 130.5, 129.6, 126.0, 124.3, 122.3, 121.4, 29.0, 25.0, 23.7. Anal. Calcd for C₄₁H₄₇N₂Cu: C, 78.00; H, 7.50; N, 4.44. Found: C, 77.70; H, 7.61; N, 4.06.

5.5.8. Alkene/Alkane Elimination Reactions with HRp

In a nitrogen filled glovebox, HRp (~5 mg, 1 equiv) and either **4**, **5**, or **6** (1 equiv) were dissolved separately in either toluene-*d*₈ or benzene-*d*₆ (0.5 mL each), transferred to the same J. Young NMR tube, and sealed. The tube was inverted several times to mix the solutions. The reactions were monitored by ¹H NMR until all HRp was consumed. For the reactions with **4** and **5**, the organic products were detected by ¹H NMR. For the reaction with **6**, the product mixture was transferred to a vial under air, pipet-filtered through silica gel, diluted with THF, and analyzed by calibrated GC-MS (with dodecane internal standard).

5.5.9. General Procedure for the Kinetic Runs

In a nitrogen filled glovebox, the catalyst (5.0 mg, 0.2 equiv), the alkyne substrate (1 equiv) and an internal standard (hexamethylbenzene or 1,3,5-trimethoxybenzene, 1 equiv) were dissolved in toluene-*d*₈ (1 mL), transferred to a J-Young NMR tube, and sealed. (The transfer was done in two steps: First, the maximum amount of the solids were dissolved in 0.7 mL of toluene-*d*₈ and transferred. The vial was washed with another 0.3 mL of toluene-*d*₈ and the washings were then transferred.) The J-Young tube was inverted multiple times to make sure that all the solids dissolved and then connected to a Schlenk line containing H₂ or D₂ gas (1 atm). After degassing the solution using three 5-minute

freeze-pump-thaw cycles, the sample was frozen again, exposed to H₂ or D₂ and allowed to thaw and equilibrate for 30 minutes. The J-Young tube was then resealed and monitored by ¹H NMR at 90 °C overnight (experiments = 600, delay time = 30 s, scans per experiment = 8). Initial rates were determined by monitoring the starting materials by ¹H NMR integration using stacked plots. A sample NMR stack plot (Figure A5) and a sample concentration vs time plot (Figure A6) is presented in the appendix.

5.5.10. Preparation of (6Dipp)Cu-Rp

(6Dipp)CuCl (0.0160 g, 0.032 mmol, 1 equiv) was dissolved in toluene (10 mL), and NaRp (0.0156 g, 0.064 mmol, 2 equiv) was added to the solution. The brown solution was stirred for 24 h at room temperature. The solution was filtered through Celite, and the filtrate was evaporated to dryness. The remaining solid was suspended in pentane (10 mL) and stirred vigorously for 30 min. The suspension was filtered through a fritted glass filter, and the brown-yellow solid was washed with pentane (3 × 5 mL) and then dried *in vacuo*. Yield: 0.0153 g, 0.021 mmol, 68%. The solid was stored in a glovebox freezer at -36 °C.. ¹H NMR (500 MHz, C₆D₆): δ 7.24 (m, 2H, *p*-CH), 7.14 (m, 4H, *m*-CH), 4.55 (s, 5H, Cp), 3.08 (sept, *J* = 8.0 Hz, 4H, CH(CH₃)₂), 2.74 (t, *J* = 8.0 Hz, 4H, NCH₂), 1.60 (d, *J* = 6.9 Hz, 12H, CH(CH₃)₂), 1.49 (quin, *J* = 8.0 Hz, 2H, NCH₂CH₂), 1.20 (d, *J* = 6.9 Hz, 12H, CH(CH₃)₂).

Chapter 6

Conclusions and Current/Future Directions

6.1. Conclusions

The preceding chapters in this thesis have unfolded the stepwise development of a heterobimetallic catalytic hydrogenation reaction. The initial hypothesis was that the hydrogenation of C-C multiple bonds can be developed using the cooperative bimetallic strategy popularized by Mankad group. Before beginning the reaction development, initial spectroscopic and computational studies were carried out in order to understand these late-late heterobimetallic systems.

Our initial hypothesis was that the bimetallic systems would carry out multi-electron redox steps like oxidative addition via the activity of the transition-metals. However, spectroscopic studies revealed that the participation of the metals was minimal and the non-innocent CO ligands were playing the major role in redox chemistry (chapter two).¹²⁶

The computational analysis carried out next, reiterated the importance of the CO ligands by revealing their structural templating role in stabilizing the two metal fragments via bridging, after the metal-metal bond was broken (chapter three).^{87,232} While retaining the CO ligands, a series of heterobimetallic complexes were synthesized by Mankad group and computational studies revealed that some structural trends can be deduced in the series as a function of nucleophilicity of the anionic metal fragment (chapter three).

^{87,232}

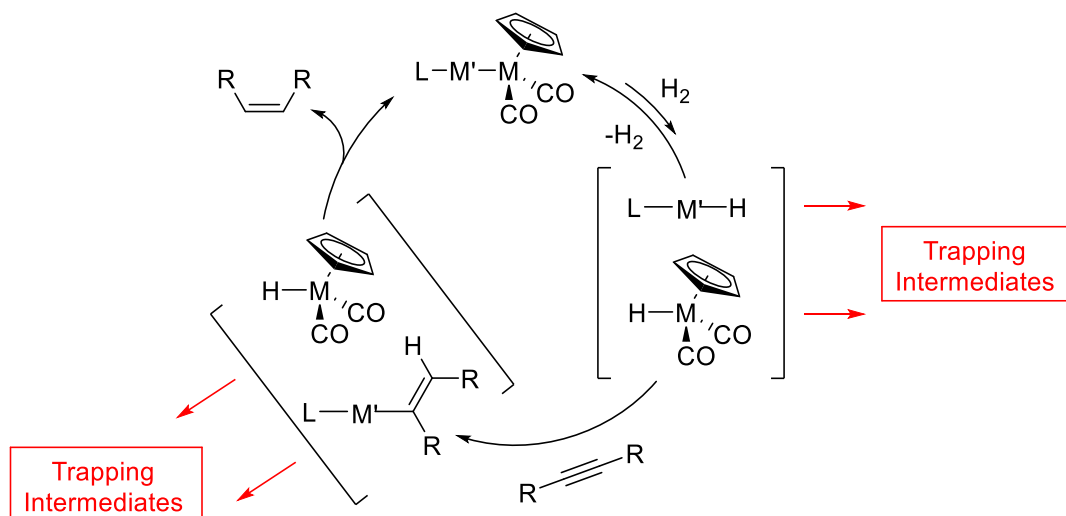
Further analysis of these trends demonstrated how computations can be utilized for catalytic screening (chapter four).²³⁹ In the pursuit of ideal candidates for H₂ activation, calculating the reaction energies yielded the most plausible metal-metal combinations reducing the experimental effort drastically. Optimizations that followed resulted in the development of an *E*-selective semi-hydrogenation reaction of alkynes (chapter four)²³⁹ which was studied extensively unveiling interesting insight into its mechanism (chapter five).²⁷²

In conclusion, the initial goals set forward in this dissertation have been accomplished as catalytic hydrogenation of C-C multiple bonds has been demonstrated. The main theme highlighted in chapter one was that switching to cooperative strategies^{7,9,32,33,38,42,44,46,55,62,64,66,77,78,82} from the single-site catalytic paradigm^{1,2,5,15} would lead to cheaper catalysts and/or yield unique selectivity and reactivity modes. The emergence of the rare *E*-selectivity in the semi-hydrogenation, supports and verifies the latter point in this claim. This work also sets precedent for future hydrogenation reactions to be pursued using this bimetallic strategy in search of unique/rare reactivity modes.

6.2. Current/Future Directions

6.2.1. Trapping Intermediates of Hydrogenation to Develop Bifunctional Reactions

As demonstrated in chapter four, the heterobimetallic complexes preform catalytic semi-hydrogenation of alkynes to yield *E*-alkenes at low pressures of H₂.²³⁹ Mechanistic investigations that followed (chapter five) has allowed us to determine the catalytic cycle at work (Scheme 55).^{239,272} The intermediates in the cycle includes metal hydrides (Cu, Ag, Fe, Ru) and metal alkyl/alkenyl species (Cu-alkyl/alkenyl and Ag-alkyl/alkenyl). Each of these intermediates are capable of a multitude of stoichiometric reactions including substrate insertions.^{287–293} Accessing these intermediates through such substrates would inherently lead to new reaction pathways to further functionalize the hydrogenated product (Scheme 55).

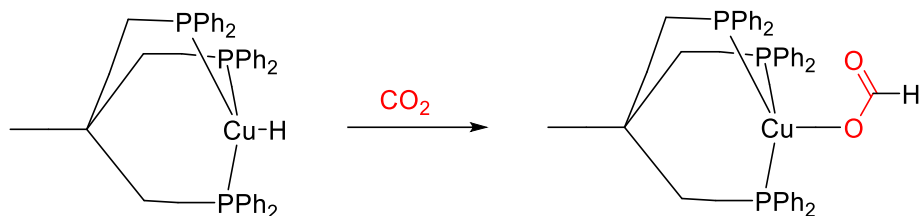


Scheme 55: Trapping intermediates of hydrogenation for bifunctional reactions

6.2.1.1. CO₂ Activation

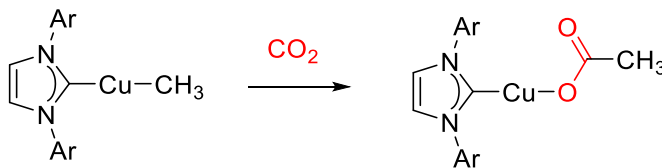
One of the substrates that has potential to trap a number of these intermediates is CO₂. Utilizing CO₂ as feedstock for organic transformations is highly desirable as CO₂ is a renewable, readily available and an inexpensive carbon source and a greenhouse gas with a major impact on climate change.^{294–297}

CO₂ insertion has been reported into a triphos-Cu-hydride (Scheme 56) by Appel and co-workers in 2015 when they demonstrated a catalytic CO₂ hydrogenation reaction producing formate.²⁹⁸ CO₂ has also shown insertion chemistry towards silver-hydride species.²⁵⁶



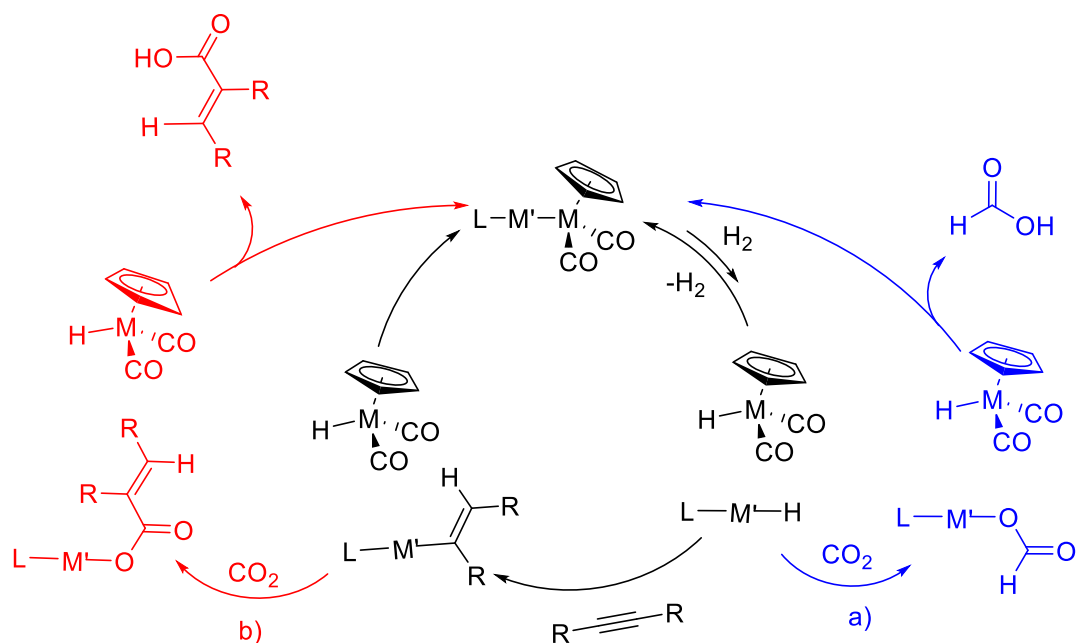
Scheme 56: Proposed CO₂ insertion step in the catalytic cycle of CO₂ hydrogenation by Appel and co-workers

Stoichiometric insertion of CO₂ has also been reported into a Cu-C bond in a (NHC)Cu-alkyl species (Scheme 57) by Sadighi group in 2004.²⁹⁹ CO₂ has been inserted into copper-silicon bonds as well.⁹²



Scheme 57: CO₂ insertion into a Cu-C bond by Sadighi and co-workers

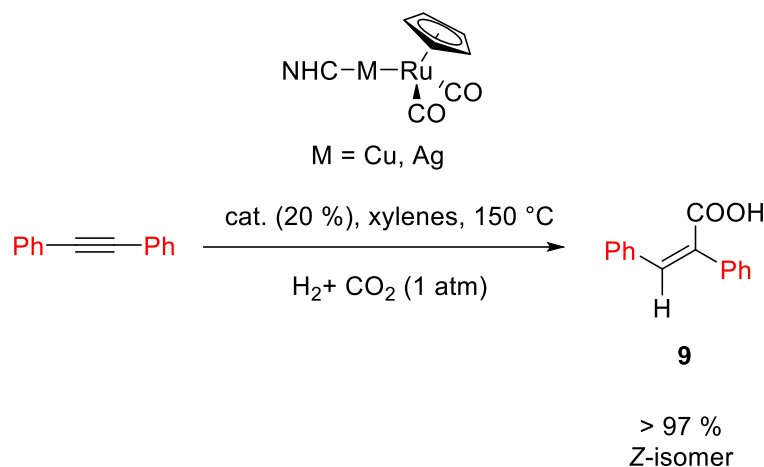
Therefore, CO₂ has two possible access points to the catalytic cycle: (NHC)Cu/Ag-H and/or (NHC)Cu/Ag-alkenyl species. Thus, trapping CO₂ and completing the cycle through a reductive elimination by the Fe/Ru hydride would allow us to catalytically form either a formate, the hydrogenated product of CO₂ (Scheme 58a) or an acrylic acid, the hydro-carboxylated product of the alkyne (Scheme 58b) or both. To test this hypothesis, we conducted our catalytically optimized hydrogenation reaction with the addition of CO₂.



Scheme 58: Potential CO₂ trapping pathways a) through the metal hydride intermediate b) through metal-alkenyl intermediate (M= Fe, Ru and M'=Cu, Ag)

6.2.1.2. Hydrocarboxylation of Alkynes

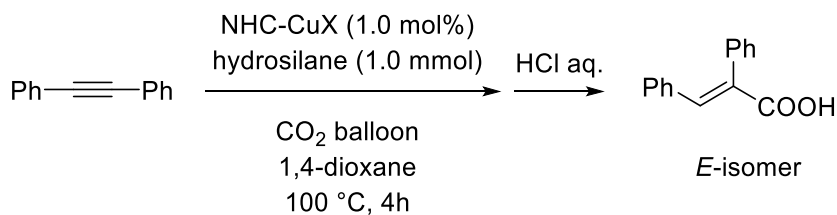
Our preliminary studies reveal the selective formation of the hydrocarboxylated product of the alkyne; the acrylic acid, **9** (Scheme 59). Monometallic controls did not yield catalytic results indicating that the mechanism is bimetallic. Initial experiments show that the rare *Z*-isomer, is formed selectively. Further optimization, reaction development and mechanistic studies are currently underway.



Scheme 59: Hydrocarboxylation of alkynes by heterobimetallic catalysis

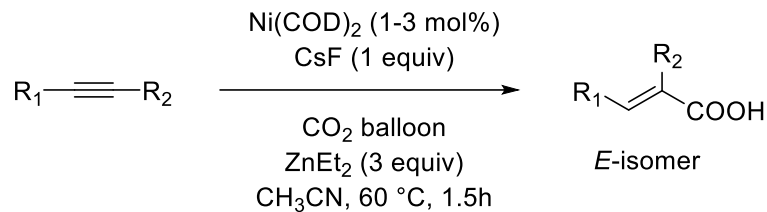
Hydrocarboxylation of alkynes using CO_2 as a substrate has been reported previously. However, none of these systems use molecular H_2 as the hydrogen source. While all these systems utilize separate reductants which produce waste products, our system utilizes H_2 as the reductant and leaves behind no byproducts, creating perfect atom economy. Also, in all of these previous reports, the *E*-isomer is selectively formed while our system produces the unprecedented *Z*-isomer catalytically.

In 2011, Tsuji and co-workers used a $(\text{NHC})\text{Cu-X}$ species to achieve catalysis, but their hydrogen source was hydro-silane (Scheme 60) and the reductant was the silane.³⁰⁰



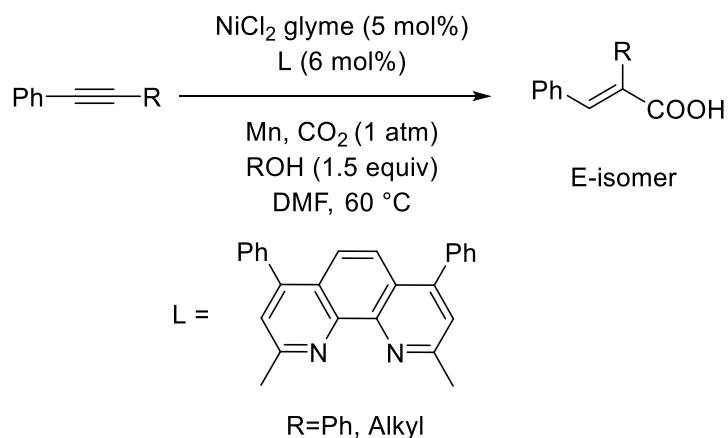
Scheme 60: Hydrocarboxylation of alkynes by Tsuji and co-workers

Ma group also demonstrated hydrocarboxylation using a nickel system the same year using HCl as the final H source and ZnEt₂ as the reductant (Scheme 61).³⁰¹



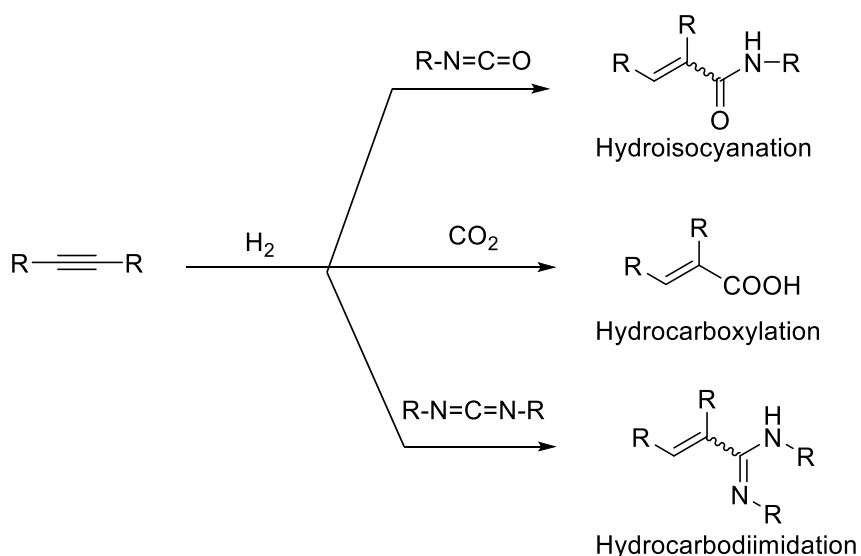
Scheme 61: Hydrocarboxylation of alkynes by Ma and co-workers

In 2015, Martin and co-workers also published a nickel catalyst for hydrocarboxylation of alkynes using an alcohol as the hydrogen source and Mn(0) as the reductant (Scheme 62).³⁰²



Scheme 62: Hydrocarboxylation of alkynes by Martin and co-workers

Whilst development of the hydrocarboxylation reaction is currently pursued, the initial results demonstrate another instance in which the use of bimetallic cooperative catalysts has given rise to a rare selectivity mode. In continuing this theme, other substrates isoelectronic to CO₂ such as isocyanates and carbodiimides can be pursued for reactivity. Thus, we can envision synthetic routes to a variety of selective hydro-functionalization reactions of alkynes which could be accessible using this bimetallic strategy (Scheme 63).



Scheme 63: Proposed heterobimetallic hydro-functionalization reactions

6.2.2. Hydrogenation of Unsaturated C=E (E = C, O, N) Double Bonds

On a more general note, the initial development of the H_2 activation reaction has revealed that a combination of metal-hydrides (Cu, Ag, Fe, Ru), some of which, too unstable to be isolated, can be accessed with this bimetallic strategy.

Even though the initial calculations reveal that switching to other metal combinations might be energetically unfavorable for H_2 activation (Chapter 4, Table 16), changing the

ligands bound to the metals could potentially change the energetics of the reaction providing a new set of metal-hydrides not accessed here.²⁹²

Therefore, while this initial work only shows catalytic activity towards alkyne hydrogenations, in varying the metal & ligand combinations, bimetallic catalysts which can hydrogenate C=E double bonds through other metal hydride combinations could potentially be developed, possibly opening the door to even asymmetric hydrogenations.

6.3. Concluding Remarks

In considering the lessons learned and evaluating the bigger picture, the work presented in this dissertation is a fine demonstration of how understanding fundamentals, such as structural and functional features of organometallic complexes, can aid in the development of catalytic applications. On a more specific note, the work presented here can be considered as an inception point into hydrogenations via cooperative late-late heterobimetallic catalysis which can lead to, and inspire many future developments.

References

- (1) Osborn, J. A.; Jardine, F. H.; Young, J. F.; Wilkinson, G. *J. Chem. Soc. A Inorganic, Phys. Theor.* **1966**, 1711.
- (2) Schrock, R. R.; Osborn, J. A. *J. Am. Chem. Soc.* **1976**, 98, 4450.
- (3) Schrock, R. R.; Osborn, J. A. *J. Am. Chem. Soc.* **1976**, 98, 2134.
- (4) Schrock, R. R.; Osborn, J. A. *J. Am. Chem. Soc.* **1976**, 98, 2143.
- (5) Crabtree, R. H.; Felkin, H.; Morris, G. E. *J. Organomet. Chem.* **1977**, 141, 205.
- (6) Li, Y.; Hou, C.; Jiang, J.; Zhang, Z.; Zhao, C.; Page, A. J.; Ke, Z. *ACS Catal.* **2016**, 6, 1655.
- (7) Blum, Y.; Czarkle, D.; Rahamim, Y.; Shvo, Y. *Organometallics* **1985**, 4, 1459.
- (8) Doucet, H.; Ohkuma, T.; Murata, K.; Yokozawa, T.; Kozawa, M.; Katayama, E.; England, A. F.; Ikariya, T.; Noyori, R. *Angew. Chemie Int. Ed.* **1998**, 37, 1703.
- (9) Srimani, D.; Diskin-Posner, Y.; Ben-David, Y.; Milstein, D. *Angew. Chemie Int. Ed.* **2013**, 52, 14131.
- (10) Hill Harman, W.; Peters, J. C. *J. Am. Chem. Soc.* **2012**, 134, 5080.
- (11) Paradies, J. *Synlett* **2013**, 24, 777.
- (12) Stephan, D. W.; Erker, G. *Angew. Chemie Int. Ed.* **2015**, 54, 6400.
- (13) Chernichenko, K.; Madarász, D.; Pápai, I.; Nieger, M.; Leskelä, M.; Repo, T. *Nat. Chem.* **2013**, 5, 718.
- (14) Xu, X.; Kehr, G.; Daniliuc, C. G.; Erker, G. *J. Am. Chem. Soc.* **2015**, 137, 4550.

- (15) Halpern, J.; Harrod, J. F.; James, B. R. *J. Am. Chem. Soc.* **1961**, 83, 753.
- (16) Halpern, J.; Wong, C. S. *J. Chem. Soc. Chem. Commun.* **1973**, 629.
- (17) Halpern, J. *Inorganica Chim. Acta* **1981**, 50, 11.
- (18) Halpern, J.; Riley, D. P.; Chan, A. S. C.; Pluth, J. J. *J. Am. Chem. Soc.* **1977**, 99, 8055.
- (19) Halpern, J. *Science* **1982**, 217, 401.
- (20) Crabtree, R. *Acc. Chem. Res.* **1979**, 12, 331.
- (21) Hoveyda, A. H.; Evans, D. A.; Fu, G. C. *Chem. Rev.* **1993**, 93, 1307.
- (22) Bennie, L. S.; Fraser, C. J.; Irvine, S.; Kerr, W. J.; Andersson, S.; Nilsson, G. N. *Chem. Commun.* **2011**, 47, 11653.
- (23) Margarita, C.; Andersson, P. G. *J. Am. Chem. Soc.* **2017**, 139, 1346.
- (24) Radkowski, K.; Sundararaju, B.; Fürstner, A. *Angew. Chemie Int. Ed.* **2013**, 52, 355.
- (25) Bart, S. C.; Lobkovsky, E.; Chirik, P. J. *J. Am. Chem. Soc.* **2004**, 126, 13794.
- (26) Tokmic, K.; Fout, A. R. *J. Am. Chem. Soc.* **2016**, 138, 13700.
- (27) Tokmic, K.; Markus, C. R.; Zhu, L.; Fout, A. R. *J. Am. Chem. Soc.* **2016**, 138, 11907.
- (28) Friedfeld, M. R.; Shevlin, M.; Hoyt, J. M.; Krska, S. W.; Tudge, M. T.; Chirik, P. J. *Science* **2013**, 342, 1076.
- (29) Ma, X.; Lei, M. *J. Org. Chem.* **2017**, 82, 2703.
- (30) Conley, B. L.; Pennington-Boggio, M. K.; Boz, E.; Williams, T. J. *Chem. Rev.* **2010**, 110, 2294.
- (31) Morris, R. H. *Chem. Soc. Rev.* **2009**, 38, 2282.

- (32) Xu, R.; Chakraborty, S.; Bellows, S. M.; Yuan, H.; Cundari, T. R.; Jones, W. D. *ACS Catal.* **2016**, 6, 2127.
- (33) Werkmeister, S.; Neumann, J.; Junge, K.; Beller, M. *Chem. - A Eur. J.* **2015**, 21, 12226.
- (34) Vasudevan, K. V.; Scott, B. L.; Hanson, S. K. *Eur. J. Inorg. Chem.* **2012**, 2012, 4898.
- (35) Zhang, G.; Scott, B. L.; Hanson, S. K. *Angew. Chemie Int. Ed.* **2012**, 51, 12102.
- (36) Zhang, G.; Vasudevan, K. V.; Scott, B. L.; Hanson, S. K. *J. Am. Chem. Soc.* **2013**, 135, 8668.
- (37) Normand, A. T.; Daniliuc, C. G.; Wibbeling, B.; Kehr, G.; Gendre, P. Le; Erker, G. *J. Am. Chem. Soc.* **2015**, 137, 10796.
- (38) Lambic, N. S.; Sommer, R. D.; Ison, E. A. *J. Am. Chem. Soc.* **2016**, 138, 4832.
- (39) Lambic, N. S.; Sommer, R. D.; Ison, E. A. *J. Am. Chem. Soc.* **2017**, 7, 1170.
- (40) Harman, W. H.; Lin, T.-P.; Peters, J. C. *Angew. Chemie Int. Ed.* **2014**, 53, 1081.
- (41) Fong, H.; Moret, M.-E.; Lee, Y.; Peters, J. C. *Organometallics* **2013**, 32, 3053.
- (42) Lin, T.-P.; Peters, J. C. *J. Am. Chem. Soc.* **2013**, 135, 15310.
- (43) Lin, T.-P.; Peters, J. C. *J. Am. Chem. Soc.* **2014**, 136, 13672.
- (44) Tseng, K.-N. T.; Kampf, J. W.; Szymczak, N. K. *J. Am. Chem. Soc.* **2016**, 138, 10378.
- (45) Hounjet, L. J.; Stephan, D. W. *Org. Process Res. Dev.* **2014**, 18, 385.
- (46) Erős, G.; Nagy, K.; Mehdi, H.; Pápai, I.; Nagy, P.; Király, P.; Tárkányi, G.; Soós, T. *Chem. - A Eur. J.* **2012**, 18, 574.
- (47) Paradies, J. *Angew. Chemie Int. Ed.* **2014**, 53, 3552.
- (48) Welch, G. C.; San Juan, R. R.; Masuda, J. D.; Stephan, D. W. *Science* **2006**, 314, 1124.

- (49) Rokob, T. A.; Hamza, A.; Stirling, A.; Soós, T.; Pápai, I. *Angew. Chemie Int. Ed.* **2008**, *47*, 2435.
- (50) Guo, Y.; Li, S. *Inorg. Chem.* **2008**, *47*, 6212.
- (51) Grimme, S.; Kruse, H.; Goerigk, L.; Erker, G. *Angew. Chemie Int. Ed.* **2010**, *49*, 1402.
- (52) Rokob, T. A.; Bakó, I.; Stirling, A.; Hamza, A.; Pápai, I. *J. Am. Chem. Soc.* **2013**, *135*, 4425.
- (53) Mück-Lichtenfeld, C.; Grimme, S. *Dalt. Trans.* **2012**, *41*, 9111.
- (54) Stephan, D. W.; Greenberg, S.; Graham, T. W.; Chase, P.; Hastie, J. J.; Geier, S. J.; Farrell, J. M.; Brown, C. C.; Heiden, Z. M.; Welch, G. C.; Ullrich, M. *Inorg. Chem.* **2011**, *50*, 12338.
- (55) Greb, L.; Oña-Burgos, P.; Schirmer, B.; Grimme, S.; Stephan, D. W.; Paradies, J. *Angew. Chemie Int. Ed.* **2012**, *51*, 10164.
- (56) Hounjet, L. J.; Bannwarth, C.; Garon, C. N.; Caputo, C. B.; Grimme, S.; Stephan, D. W. *Angew. Chemie Int. Ed.* **2013**, *52*, 7492.
- (57) Greb, L.; Daniliuc, C.-G.; Bergander, K.; Paradies, J. *Angew. Chemie Int. Ed.* **2013**, *52*, 5876.
- (58) vom Stein, T.; Pérez, M.; Dobrovetsky, R.; Winkelhaus, D.; Caputo, C. B.; Stephan, D. W. *Angew. Chemie Int. Ed.* **2015**, *54*, 10178.
- (59) Stephan, D. W. *J. Am. Chem. Soc.* **2015**, *137*, 10018.
- (60) Wang, Y.; Chen, W.; Lu, Z.; Li, Z. H.; Wang, H. *Angew. Chemie Int. Ed.* **2013**, *52*, 7496.
- (61) Chernichenko, K.; Kótai, B.; Nieger, M.; Heikkinen, S.; Pápai, I.; Repo, T. *Dalt. Trans.* **2017**, *46*, 2263.

- (62) Liu, Y.; Hu, L.; Chen, H.; Du, H. *Chem. - A Eur. J.* **2015**, *21*, 3495.
- (63) Szeto, K. C.; Sahyoun, W.; Merle, N.; Castelbou, J. L.; Popoff, N.; Lefebvre, F.; Raynaud, J.; Godard, C.; Claver, C.; Delevoye, L.; Gauvin, R. M.; Taoufik, M. *Catal. Sci. Technol.* **2014**, *6*, 882.
- (64) Xu, B.-H.; Kehr, G.; Fröhlich, R.; Wibbeling, B.; Schirmer, B.; Grimme, S.; Erker, G. *Angew. Chemie Int. Ed.* **2011**, *50*, 7183.
- (65) Greb, L.; Daniliuc, C.-G.; Bergander, K.; Paradies, J. *Angew. Chemie Int. Ed.* **2013**, *52*, 5876.
- (66) Mahdi, T.; Heiden, Z. M.; Grimme, S.; Stephan, D. W. *J. Am. Chem. Soc.* **2012**, *134*, 4088.
- (67) Liu, Y.; Du, H. *J. Am. Chem. Soc.* **2013**, *135*, 12968.
- (68) Zhang, Z.; Du, H. *Org. Lett.* **2015**, *17*, 2816.
- (69) Geier, S. J.; Chase, P. A.; Stephan, D. W. *Chem. Commun.* **2010**, *46*, 4884.
- (70) Segawa, Y.; Stephan, D. W. *Chem. Commun.* **2012**, *48*, 11963.
- (71) Versluis, L.; Ziegler, T. *Organometallics* **1990**, *9*, 2985.
- (72) Solà, M.; Ziegler, T. *Organometallics* **1996**, *15*, 1611.
- (73) Feng, M.; Chan, K. S. *Organometallics* **2002**, *21*, 2743.
- (74) Gray, T. G.; Veige, A. S.; Nocera, D. G. *J. Am. Chem. Soc.* **2004**, *126*, 9760.
- (75) Riddlestone, I. M.; Rajabi, N. A.; Lowe, J. P.; Mahon, M. F.; Macgregor, S. A.; Whittlesey, M. K. *J. Am. Chem. Soc.* **2016**, *138*, 11081.
- (76) Campos, J. *J. Am. Chem. Soc.* **2017**, *139*, 2944.

- (77) Burch, R. R.; Muetterties, E. L.; Teller, R. G.; Williams, J. M. *J. Am. Chem. Soc.* **1982**, *104*, 4257.
- (78) Baranger, A. M.; Bergman, R. G. *J. Am. Chem. Soc.* **1994**, *116*, 3822.
- (79) Hostetler, M. J.; Bergman, R. G. *J. Am. Chem. Soc.* **1990**, *112*, 8621.
- (80) Wheatley, N.; Kalck, P. *Chem. Rev.* **1999**, *99*, 3379.
- (81) Zhang, Y.; Roberts, S. P.; Bergman, R. G.; Ess, D. H. *ACS Catal.* **2014**, *5*, 1840.
- (82) Cammarota, R. C.; Lu, C. C. *J. Am. Chem. Soc.* **2015**, *137*, 12486.
- (83) Buchwalter, P.; Rosé, J.; Braunstein, P. *Chem. Rev.* **2015**, *115*, 28.
- (84) Cooper, B. G.; Napoline, J. W.; Thomas, C. M. *Catal. Rev.* **2012**, *54*, 1.
- (85) Jayarathne, U.; Mazzacano, T. J.; Bagherzadeh, S.; Mankad, N. P. *Organometallics* **2013**, *32*, 3986.
- (86) Karunananda, M. K.; Vázquez, F. X.; Ercan Alp, E.; Bi, W.; Chattopadhyay, S.; Shibata, T.; Mankad, N. P. *Dalt. Trans.* **2014**, *43*, 13661.
- (87) Karunananda, M. K.; Parmelee, S. R.; Waldhart, G. W.; Mankad, N. P. *Organometallics* **2015**, *34*, 3857.
- (88) Mazzacano, T. J.; Mankad, N. P. *J. Am. Chem. Soc.* **2013**, *135*, 17258.
- (89) Parmelee, S. R.; Mazzacano, T. J.; Zhu, Y.; Mankad, N. P.; Keith, J. A. *ACS Catal.* **2015**, *5*, 3689.
- (90) Bagherzadeh, S.; Mankad, N. P. *J. Am. Chem. Soc.* **2015**, *137*, 10898.
- (91) Laitar, D. S.; Müller, P.; Sadighi, J. P. *J. Am. Chem. Soc.* **2005**, *127*, 17196.
- (92) Kleeberg, C.; Cheung, M. S.; Lin, Z.; Marder, T. B. *J. Am. Chem. Soc.* **2011**, *133*, 19060.

- (93) Powers, I. G.; Uyeda, C. *ACS Catal.* **2017**, 7, 936.
- (94) Pye, D. R.; Mankad, N. P. *Chem. Sci.* **2017**, 8, 1705.
- (95) Mankad, N. P. *Chem. - A Eur. J.* **2016**, 22, 5822.
- (96) Sabater, S.; Mata, J. A.; Peris, E. *Nat. Commun.* **2013**, 4, 1.
- (97) Choy, S. W. S.; Page, M. J.; Bhadbhade, M.; Messerle, B. A. *Organometallics* **2013**, 32, 4726.
- (98) Uyeda, C.; Peters, J. C. *J. Am. Chem. Soc.* **2013**, 135, 12023.
- (99) Radlauer, M. R.; Day, M. W.; Agapie, T. *J. Am. Chem. Soc.* **2012**, 134, 1478.
- (100) Pérez-Temprano, M. H.; Casares, J. A.; Espinet, P. *Chem. - A Eur. J.* **2012**, 18, 1864.
- (101) Schmidt, J. A. R.; Lobkovsky, E. B.; Coates, G. W. *J. Am. Chem. Soc.* **2005**, 127, 11426.
- (102) Jacobsen, E. N. *Acc. Chem. Res.* **2000**, 33, 421.
- (103) Tolman, W. B. *Activation of small molecules : organometallic and bioinorganic perspectives*; Wiley-VCH: Weinheim, 2006.
- (104) Ananikov, V. P.; Beletskaya, I. P. *Organometallics* **2012**, 31, 1595.
- (105) Doyle, M. P. *J. Org. Chem.* **2006**, 71, 9253.
- (106) Powers, D. C.; Ritter, T. *Acc. Chem. Res.* **2012**, 45, 840.
- (107) Tang, P.; Furuya, T.; Ritter, T. *J. Am. Chem. Soc.* **2010**, 132, 12150.
- (108) Tkatchouk, E.; Mankad, N. P.; Benitez, D.; Goddard, W. A.; Toste, F. D. *J. Am. Chem. Soc.* **2011**, 133, 14293.
- (109) Powers, D. C.; Ritter, T. *Organometallics* **2013**, 32, 2042.

- (110) Fafard, C. M.; Adhikari, D.; Foxman, B. M.; Mindiola, D. J.; Ozerov, O. V. *J. Am. Chem. Soc.* **2007**, *129*, 10318.
- (111) Behlen, M. J.; Zhou, Y.-Y.; Steiman, T. J.; Pal, S.; Hartline, D. R.; Zeller, M.; Uyeda, C. *Dalt. Trans.* **2017**, *46*, 5493.
- (112) Zhou, Y.-Y.; Hartline, D. R.; Steiman, T. J.; Fanwick, P. E.; Uyeda, C. *Inorg. Chem.* **2014**, *53*, 11770.
- (113) Uyeda, C.; Steiman, T.; Pal, S. *Synlett* **2016**, *27*, 814.
- (114) Tereniak, S. J.; Carlson, R. K.; Clouston, L. J.; Young, V. G.; Bill, E.; Maurice, R.; Chen, Y.-S.; Kim, H. J.; Gagliardi, L.; Lu, C. C. *J. Am. Chem. Soc.* **2014**, *136*, 1842.
- (115) Eisenhart, R. J.; Carlson, R. K.; Clouston, L. J.; Young, V. G.; Chen, Y.-S.; Bill, E.; Gagliardi, L.; Lu, C. C. *Inorg. Chem.* **2015**, *54*, 11330.
- (116) Eisenhart, R. J.; Clouston, L. J.; Lu, C. C. *Accounts Chem. Research* **2015**, *48*, 2885.
- (117) Gade, L. H. *Angew. Chemie Int. Ed.* **2000**, *39*, 2658.
- (118) Pinkes, J. R.; Steffey, B. D.; Vites, J. C.; Cutler, A. R. *Organometallics* **1994**, *13*, 21.
- (119) Friedrich, S.; Gade, L. H.; Scowen, I. J.; McPartlin, M. *Angew. Chemie Int. Ed. English* **1996**, *35*, 1338.
- (120) Gade, L. H.; Schubart, M.; Findeis, B.; Fabre, S.; Bezougli, I.; Lutz, M.; Scowen, I. J.; McPartlin, M. *Inorg. Chem.* **1999**, *38*, 5282.
- (121) Vites, J. C.; Steffey, B. D.; Giuseppetti-Dery, M. E.; Cutler, A. R. *Organometallics* **1991**, *10*, 2827.
- (122) Blake, M. P.; Kaltsoyannis, N.; Mountford, P.; Li, W.-S.; Scowen, I. J.; McPartlin, M.; Housecroft, C. E.; Alvarez, S.; Rio, D. del; Andersen, R. A. *Chem. Commun.* **2013**, *49*,

3315.

- (123) Mankad, N. *Synlett* **2014**, 25, 1197.
- (124) Jayarathne, U.; Parmelee, S. R.; Mankad, N. P. *Inorg. Chem.* **2014**, 53, 7730.
- (125) Gütlich, P.; Garcia, Y. In *Mössbauer Spectroscopy*; Springer Berlin Heidelberg: Berlin, Heidelberg, 2013; pp 23–89.
- (126) Karunananda, M. K.; Vázquez, F. X.; Ercan Alp, E.; Bi, W.; Chattopadhyay, S.; Shibata, T.; Mankad, N. P. *Dalt. Trans.* **2014**, 43, 13661.
- (127) Long, G. J.; Alway, D. G.; Barnett, K. W. *Inorg. Chem.* **1978**, 17, 486.
- (128) Piper, M. R. J.; Stephenson, G. R.; Taylor, R. J. K.; Breen, C.; Brooks, J. S.; Williams, G. L. *J. Chem. Soc. Chem. Commun.* **1989**, 23, 1798.
- (129) Pannell, K. H.; Wu, C. C.; Long, G. J. *J. Organomet. Chem.* **1980**, 186, 85.
- (130) Li, H.; Turnbull, M. M. *J. Organomet. Chem.* **1991**, 419, 245.
- (131) Mackie, S. C.; Park, Y.-S.; Shurvell, Herbert, F.; Baird, M. C. *Organometallics* **1991**, 10, 2993.
- (132) Wright, M. E.; Long, G. J.; Tharp, D. E.; Nelson, G. O. *Organometallics* **1986**, 5, 779.
- (133) Kano, N.; Yoshinari, N.; Shibata, Y.; Miyachi, M.; Kawashima, T.; Enomoto, M.; Okazawa, A.; Kojima, N.; Guo, J.-D.; Nagase, S. *Organometallics* **2012**, 31, 8059.
- (134) Lei, H.; Guo, J.-D.; Fettingner, J. C.; Nagase, S.; Power, P. P. *J. Am. Chem. Soc.* **2010**, 132, 17399.
- (135) Burlitch, J. M.; Ferrari, A. *Inorg. Chem.* **1970**, 9, 563.
- (136) Schilling, B. E. R.; Hoffmann, R.; Lichtenberger, D. L. *J. Am. Chem. Soc.* **1979**, 101, 585.

- (137) Curtis, M. D.; Han, K. R.; Butler, W. M. *Inorg. Chem.* **1980**, *19*, 2096.
- (138) Zeller, M.; Lazich, E.; Hunter, A. D. *Acta Crystallogr. Sect. E* **2003**, *E59*, m914.
- (139) Ellis, J. E.; Flom, E. A. *J. Organomet. Chem.* **1975**, *99*, 263.
- (140) Blake, M. P.; Kaltsoyannis, N.; Mountford, P. *J. Am. Chem. Soc.* **2011**, *133*, 15358.
- (141) Hey-Hawkins, E.; von Schnering, H. G. *Z. Naturforsch.* **1991**, *46 b*, 621.
- (142) Glaser, T.; Hedman, B.; Hodgson, K. O.; Solomon, E. I. *Acc. Chem. Res.* **2000**, *33*, 859.
- (143) Solomon, E. I.; Hedman, B.; Hodgson, K. O.; Dey, A.; Szilagyi, R. K. *Coord. Chem. Rev.* **2005**, *249*, 97.
- (144) Kau, L.-S.; Spira-Solomon, D. J.; Penner-Hahn, J. E.; Hodgson, K. O.; Solomon, E. I. *J. Am. Chem. Soc.* **1987**, *109*, 6433.
- (145) Mankad, N. P.; Antholine, W. E.; Szilagyi, R. K.; Peters, J. C. *J. Am. Chem. Soc.* **2009**, *131*, 3878.
- (146) King, R. B. *Acc. Chem. Res.* **1970**, *3*, 417.
- (147) Westre, T. E.; Kennepohl, P.; Dewitt, J. G.; Hedman, B.; Hodgson, K. O.; Solomon, E. I. *J. Am. Chem. Soc.* **1997**, *119*, 6297.
- (148) Milsmann, C.; Sproules, S.; Bill, E.; Weyhermüller, T.; George, S. D.; Wieghardt, K. *Chem. - A Eur. J.* **2010**, *16*, 3628.
- (149) Yan, Y.; Keating, C.; Chandrasekaran, P.; Jayarathne, U.; Mague, J. T.; Debeer, S.; Lancaster, K. M.; Sproules, S.; Rubtsov, I. V.; Donahue, J. P. *Inorg. Chem.* **2013**, *52*, 6743.
- (150) Palmer, J. H.; Lancaster, K. M. *Inorg. Chem.* **2012**, *51*, 12473.

- (151) Lu, T. Te; Lai, S. H.; Li, Y. W.; Hsu, I. J.; Jang, L. Y.; Lee, J. F.; Chen, I. C.; Liaw, W. F. *Inorg. Chem.* **2011**, *50*, 5396.
- (152) Pannell, K. H.; Sharma, H. K. *Organometallics* **2010**, *29*, 4741.
- (153) Iwai, K.; Iwai, M.; Suto, K.; Nakashima, S.; Motoyama, I.; Sano, H.; Ikemoto, I.; Kosugi, N.; Kuroda, H. *Bull. Chem. Soc. Jpn.* **1986**, *59*, 2675.
- (154) Otero, E.; Wilks, R. G.; Regier, T.; Blyth, R. I. R.; Moewes, A.; Urquhart, S. G. *J. Phys. Chem. A* **2008**, *112*, 624.
- (155) Wen, A. T.; Rühl, E.; Hitchcock, A. P. *Organometallics* **1992**, *11*, 2559.
- (156) Armarego, W. L. F.; Chai, C. C. L. *Purification of Laboratory Chemicals*, 6th Edition.; Butterworth-Heinemann: Burlington, MA, 2009.
- (157) Citadelle, C. A.; Nouy, E. Le; Bisaro, F.; Slawin, A. M. Z.; Cazin, C. S. J.; Lin, I. J. B.; Douthwaite, R. E.; Morel, L.; Boyer, D.; Mahiou, R.; Gautier, A. *Dalt. Trans.* **2010**, *39*, 4489.
- (158) Delp, S. A.; Goj, L. A.; Pouy, M. J.; Munro-Leighton, C.; Lee, J. P.; Gunnoe, T. B.; Cundari, T. R.; Petersen, J. L. *Organometallics* **2011**, *30*, 55.
- (159) Ohishi, T.; Shiotani, Y.; Yamashita, M. *J. Org. Chem.* **1994**, *59*, 250.
- (160) Wang, D.; Wurst, K.; Buchmeiser, M. R. *J. Organomet. Chem.* **2004**, *689*, 2123.
- (161) Yasuda, S.; Yorimitsu, H.; Oshima, K. *Organometallics* **2008**, *27*, 4025.
- (162) Frisch, M. J.; Trucks, G. W.; Schlegel, H. B.; Scuseria, G. E.; Robb, M. A.; Cheeseman, J. R.; Scalmani, G.; Barone, V.; Mennucci, B.; Petersson, G. A.; Nakatsuji, H.; Caricato, M.; Li, X.; Hratchian, H. P.; Izmaylov, A. F.; Bloino, J.; Zheng, G.; Sonnenberg, J. L.; Hada, M.; Ehara, M.; Toyota, K.; Fukuda, R.; Hasegawa, J.; Ishida, M.; Nakajima, T.;

Honda, Y.; Kitao, O.; Nakai, H.; Vreven, T.; Montgomery, Jr., J. A.; Peralta, J. E.; Ogliaro, F.; Bearpark, M.; Heyd, J. J.; Brothers, E.; Kudin, K. N.; Staroverov, V. N.; Kobayashi, R.; Normand, J.; Raghavachari, K.; Rendell, A.; Burant, J. C.; Iyengar, S. S.; Tomasi, J.; Cossi, M.; Rega, N.; Millam, J. M.; Klene, M.; Knox, J. E.; Cross, J. B.; Bakken, V.; Adamo, C.; Jaramillo, J.; Gomperts, R.; Stratmann, R. E.; Yazyev, O.; Austin, A. J.; Cammi, R.; Pomelli, C.; Ochterski, J. W.; Martin, R. L.; Morokuma, K.; Zakrzewski, V. G.; Voth, G. A.; Salvador, P.; Dannenberg, J. J.; Dapprich, S.; Daniels, A. D.; Farkas, Ö.; Foresman, J. B.; Ortiz, J. V.; Cioslowski, J.; Fox, D. J. *Gaussian 09, Revision B.01*; Gaussian, Inc.: Wallingford CT, 2010.

(163) Becke, A. D. *Phys. Rev. A* **1988**, 38, 3098.

(164) Perdew, J. P. *Phys. Rev. B* **1986**, 33, 8822.

(165) Hay, P. J.; Wadt, W. R. *J. Chem. Phys.* **1985**, 82, 299.

(166) Roy, L. E.; Hay, P. J.; Martin, R. L. *J. Chem. Theory Comput.* **2008**, 4, 1029.

(167) Ehlers, A. W.; Böhme, M.; Dapprich, S.; Gobbi, A.; Höllwarth, A.; Jonas, V.; Köhler, K. F.; Stegmann, R.; Veldkamp, A.; Frenking, G. *Chem. Phys. Lett.* **1993**, 208, 111.

(168) Hay, P. J.; Wadt, W. R. *J. Chem. Phys.* **1985**, 82, 270.

(169) Wadt, W. R.; Hay, P. J. *J. Chem. Phys.* **1985**, 82, 284.

(170) Dennington, R.; Keith, T.; Millam, J. *GaussView, Version 4.1*; Semichem Inc.: Shawnee Mission, KS, 2009.

(171) Glendening, E. D.; Reed, A. E.; Carpenter, J. E.; Weinhold, F. *NBO Version 3.1*.

(172) Segre, C. U.; et al. In *The MRCAT Insertion Device Beamline at Advanced Photon Source*; 2000; pp 419–422.

- (173) Ravel, B.; Newville, M. *J. Synchrotron Radiat.* **2005**, *12*, 537.
- (174) Jayarathne, U.; Parmelee, S. R.; Mankad, N. P. *Inorg. Chem.* **2014**, *53*, 7730.
- (175) Pérez-Temprano, M. H.; Casares, J. A.; Espinet, P. *Chem. - A Eur. J.* **2012**, *18*, 1864.
- (176) Bruno, G.; Schlavo, S. L.; Rotondo, E.; Grazla, C.; Faraone, F. *Organometallics* **1989**, *8*, 886.
- (177) Ariafard, A.; Hyland, C. J. T.; Canty, A. J.; Sharma, M.; Yates, B. F. *Inorg. Chem.* **2011**, *50*, 6449.
- (178) Walker, W. K.; Kay, B. M.; Michaelis, S. A.; Anderson, D. L.; Smith, S. J.; Ess, D. H.; Michaelis, D. J. *J. Am. Chem. Soc.* **2015**, *137*, 7371.
- (179) Yin, G.; Kalvet, I.; Schoenebeck, F. *Angew. Chemie* **2015**, *127*, 6913.
- (180) Pei, X.-L.; Yang, Y.; Lei, Z.; Chang, S.-S.; Guan, Z.-J.; Wan, X.-K.; Wen, T.-B.; Wang, Q.-M. *J. Am. Chem. Soc.* **2015**, *137*, 5520.
- (181) Klä, M.; Garland, M. V. *ACS Catal.* **2015**, *5*, 2301.
- (182) Powers, D. C.; Anderson, B. L.; Hwang, S. J.; Powers, T. M.; Peez, L. M.; Hall, M. B.; Zheng, S.-L.; Chen, Y.-S.; Nocera, D. G. *J. Am. Chem. Soc.* **2014**, *136*, 15346.
- (183) Romashov, L. V.; Khemchyan, L. L.; Gordeev, E. G.; Koshevoy, I. O.; Tunik, S. P.; Ananikov, V. P. *Organometallics* **2014**, *33*, 6003.
- (184) Levin, M. D.; Toste, F. D. *Angew. Chemie Int. Ed.* **2014**, *53*, 6211.
- (185) Wolf, W. J.; Winston, M. S.; Toste, F. D. *Nat. Chem.* **2013**, *6*, 159.
- (186) Sabater, S.; Mata, J. A.; Peris, E.; Mahon, M. F.; Whittlesey, M. K. *Nat. Commun.* **2013**, *4*, 1112.

- (187) Takahashi, K.; Yamashita, M.; Nozaki, K. *J. Am. Chem. Soc.* **2012**, *134*, 18746.
- (188) Bauer, J.; Braunschweig, H.; Damme, A.; Radacki, K. *Angew. Chemie Int. Ed.* **2012**, *51*, 10030.
- (189) Oishi, M.; Kino, M.; Saso, M.; Oshima, M.; Suzuki, H. *Organometallics* **2012**, *31*, 4658.
- (190) Teets, T. S.; Nocera, D. G. *J. Am. Chem. Soc.* **2011**, *133*, 17796.
- (191) Powers, D. C.; Benitez, D.; Tkatchouk, E.; Goddard, W. A.; Ritter, T. *J. Am. Chem. Soc.* **2010**, *132*, 14092.
- (192) Reed, S. A.; White, M. C. *J. Am. Chem. Soc.* **2008**, *130*, 3316.
- (193) Cui, W.; Wayland, B. B. *J. Am. Chem. Soc.* **2004**, *126*, 8266.
- (194) Heyduk, A. F.; Nocera, D. G. *Science* **2001**, *293*, 1639.
- (195) Hanna, T. A.; Baranger, A. M.; Bergman, R. G. *J. Am. Chem. Soc.* **1995**, *117*, 11363.
- (196) Broussard, M. E.; Juma, B.; Train, S. G.; Peng, W.-J.; Laneman, S. A.; Stanley, G. G. *Science* **1993**, *260*, 1784.
- (197) Coleman, A. W.; Eadie, D. T.; Stobart, S. R.; Zaworotko, M. J.; Atwood, J. L. *J. Am. Chem. Soc.* **1982**, *104*, 922.
- (198) van der Vlugt, J. I. *Eur. J. Inorg. Chem.* **2012**, *2012*, 363.
- (199) Breitenfeld, J.; Ruiz, J.; Wodrich, M. D.; Hu, X. *J. Am. Chem. Soc.* **2013**, *135*, 12004.
- (200) Ahmed, S. M.; Poater, A.; Childers, M. I.; Widger, P. C. B.; LaPointe, A. M.; Lobkovsky, E. B.; Coates, G. W.; Cavallo, L. *J. Am. Chem. Soc.* **2013**, *135*, 18901.
- (201) Huang, W.; Dulong, F.; Khan, S. I.; Cantat, T.; Diaconescu, P. L. *J. Am. Chem. Soc.* **2014**, *136*, 17410.

- (202) Rabinowitz, H. N.; Karlin, K. D.; Lippard, S. J. *J. Am. Chem. Soc.* **1977**, 99, 1420.
- (203) Bauer, G.; Wodrich, M. D.; Scopelliti, R.; Hu, X. *Organometallics* **2015**, 34, 289.
- (204) Gavrilova, A. L.; Qin, C. J.; Sommer, R. D.; Rheingold, A. L.; Bosnich, B. *J. Am. Chem. Soc.* **2002**, 124, 1714.
- (205) Grant, D. J.; Stewart, T. J.; Bau, R.; Miller, K. A.; Mason, S. A.; Gutmann, M.; McIntyre, G. J.; Gagliardi, L.; Evans, W. J. *Inorg. Chem.* **2012**, 51, 3613.
- (206) Crowley, J. D.; Goldup, S. M.; Gowans, N. D.; Leigh, D. A.; Ronaldson, V. E.; Slawin, A. M. Z. *J. Am. Chem. Soc.* **2010**, 132, 6243.
- (207) Yuan, J.; Wang, J.; Zhang, G.; Liu, C.; Qi, X.; Lan, Y.; Miller, J. T.; Kropf, A. J.; Bunel, E. E.; Lei, A. *Chem. Commun.* **2015**, 51, 576.
- (208) Schley, N. D.; Fu, G. C. *J. Am. Chem. Soc.* **2014**, 136, 16588.
- (209) Marquard, S. L.; Bezpalko, M. W.; Foxman, B. M.; Thomas, C. M. *J. Am. Chem. Soc.* **2013**, 135, 6018.
- (210) Steiman, T. J.; Uyeda, C. *J. Am. Chem. Soc.* **2015**, 137, 6104.
- (211) Trinquier, G.; Hoffmann, R. *Organometallics* **1984**, 3, 370.
- (212) Theys, R.; Dudley, M.; Hossain, M. *Coord. Chem. Rev.* **2009**, 253, 180.
- (213) Plata, R. E.; Singleton, D. A. *J. Am. Chem. Soc.* **2015**, 137, 3811.
- (214) Winter, A. *Nat. Chem.* **2015**, 7, 473.
- (215) Thomson, A. J.; Giannopoulos, G.; Pretty, J.; Baggs, E. M.; Richardson, D. J. *Philos. Trans. R. Soc. London B Biol. Sci.* **2012**, 367, 1157.
- (216) Ravishankara, A. R.; Daniel, J. S.; Portmann, R. W. *Science* **2009**, 326, 123.

- (217) Johnson, B. J.; Antholine, W. E.; Lindeman, S. V.; Graham, M. J.; Mankad, N. P. *J. Am. Chem. Soc.* **2016**, *138*, 13107.
- (218) Gorelsky, S. I.; Ghosh, S.; Solomon, E. I. *J. Am. Chem. Soc.* **2006**, *128*, 278.
- (219) Woertink, J. S.; Smeets, P. J.; Groothaert, M. H.; Vance, M. A.; Sels, B. F.; Schoonheydt, R. A.; Solomon, E. I. *Proc. Natl. Acad. Sci. U. S. A.* **2009**, *106*, 18908.
- (220) Tsai, M.-L.; Hadt, R. G.; Vanelderen, P.; Sels, B. F.; Schoonheydt, R. A.; Solomon, E. I. *J. Am. Chem. Soc.* **2014**, *136*, 3522.
- (221) Bar-Nahum, I.; Gupta, A. K.; Huber, S. M.; Ertem, M. Z.; Cramer, C. J.; Tolman, W. B. *J. Am. Chem. Soc.* **2009**, *131*, 2812.
- (222) Majouga, A. G.; Beloglazkina, E. K.; Moiseeva, A. A.; Shilova, O. V.; Manzheliy, E. A.; Lebedeva, M. A.; Davies, E. S.; Khlobystov, A. N.; Zyk, N. V. *Dalt. Trans.* **2013**, *42*, 6290.
- (223) Esmieu, C.; Orio, M.; Torelli, S.; Le Pape, L.; Pécaut, J.; Lebrun, C.; Ménage, S. *Chem. Sci.* **2014**, *5*, 4774.
- (224) Tolman, W. B. *Angew. Chemie Int. Ed.* **2010**, *49*, 1018.
- (225) Stauber, J. M.; Bloch, E. D.; Vogiatzis, K. D.; Zheng, S.-L.; Hadt, R. G.; Hayes, D.; Chen, L. X.; Gagliardi, L.; Nocera, D. G.; Cummins, C. C. *J. Am. Chem. Soc.* **2015**, *137*, 15354.
- (226) Hicks, J.; Hoyer, C. E.; Moubarak, B.; Manni, G. L.; Carter, E.; Murphy, D. M.; Murray, K. S.; Gagliardi, L.; Jones, C. *J. Am. Chem. Soc.* **2014**, *136*, 5283.
- (227) Ma, M.; Sidiropoulos, A.; Ralte, L.; Stasch, A.; Jones, C.; Radacki, K. *Chem. Commun.* **2013**, *49*, 48.
- (228) Molon, M.; Gemel, C.; Seidel, R. W.; Jerabek, P.; Frenking, G.; Fischer, R. *Inorg. Chem.* **2013**, *52*, 7152.

- (229) Rgen Bauer, J.; Braunschweig, H.; Dewhurst, R. D. *Chem. Rev.* **2012**, 112, 4329.
- (230) Dessy, R. E.; Pohl, R. L.; King, B. *J. Am. Chem. Soc.* **1966**, 88, 5121.
- (231) Lai, C.-K.; Feighery, W. G.; Zhen, Y.; Atwood, J. D. *Inorg. Chem.* **1989**, 28, 3929.
- (232) Banerjee, S.; Karunananda, M. K.; Bagherzadeh, S.; Jayarathne, U.; Parmelee, S. R.; Waldhart, G. W.; Mankad, N. P. *Inorg. Chem.* **2014**, 53, 11307.
- (233) Cotton, F. A.; Daniels, L. M.; Murillo, C. A.; Zhou, H.-C. *Inorganica Chim. Acta* **2000**, 300, 319.
- (234) Alvarez, S. *Dalt. Trans.* **2013**, 42, 8617.
- (235) Kalz, K. F.; Kindermann, N.; Xiang, S.-Q.; Kronz, A.; Lange, A.; Meyer, F. *Organometallics* **2014**, 33, 1475.
- (236) Pauling, L. *J. Am. Chem. Soc.* **1947**, 69, 542.
- (237) Tomasi, J.; Mennucci, B.; Cammi, R. *Chem. Rev.* **2005**, 105, 2999.
- (238) Hanwell, M. D.; Curtis, D. E.; Lonie, D. C.; Vandermeersch, T.; Zurek, E.; Hutchison, G. R. *Comput. Phys. Commun.* **2011**, 182, 372.
- (239) Karunananda, M. K.; Mankad, N. P. *J. Am. Chem. Soc.* **2015**, 137, 14598.
- (240) Man, M. L.; Zhou, Z.; Ng, S. M.; Lau, C. P. *Dalt. Trans.* **2003**, 1, 3727.
- (241) Kato, H.; Seino, H.; Mizobe, Y.; Hidai, M. *J. Chem. Soc. Dalt. Trans.* **2002**, 98, 1494.
- (242) Lindlar, H. *Helv. Chim. Acta* **1952**, 35, 446.
- (243) Lindlar, H.; Dubuis, R. *Org. Synth.* **1966**, 46, 89.
- (244) Pape, F.; Thiel, N. O.; Teichert, J. F. *Chem. - A Eur. J.* **2015**, 21, 15934.
- (245) Wakamatsu, T.; Nagao, K.; Ohmiya, H.; Sawamura, M. *Organometallics* **2016**, 35, 1354.

- (246) Birch, A. J. *J. Chem. Soc.* **1944**, 0, 430.
- (247) Tokmic, K.; Fout, A. R. *J. Am. Chem. Soc.* **2016**, 138, 13700.
- (248) Higashida, K.; Mashima, K. *Chem. Lett.* **2016**, 45, 866.
- (249) Richmond, E.; Moran, J. *J. Org. Chem.* **2015**, 80, 6922.
- (250) Trost, B. M.; Ball, Z. T.; Jöge, T. *J. Am. Chem. Soc.* **2002**, 124, 7922.
- (251) Shen, R.; Chen, T.; Zhao, Y.; Qiu, R.; Zhou, Y.; Yin, S.; Wang, X.; Goto, M.; Han, L.-B. *J. Am. Chem. Soc.* **2011**, 133, 17037.
- (252) Fu, S.; Chen, N.-Y.; Liu, X.; Shao, Z.; Luo, S.-P.; Liu, Q. *J. Am. Chem. Soc.* **2016**, 138, 8588.
- (253) Kusy, R.; Grela, K. *Org. Lett.* **2016**, 18, 6196.
- (254) Mankad, N. P.; Laitar, D. S.; Sadighi, J. P. *Organometallics* **2004**, 23, 3369.
- (255) Kalz, K. F.; Brinkmeier, A.; Dechert, S.; Mata, R. A.; Meyer, F. *J. Am. Chem. Soc.* **2014**, 136, 16626.
- (256) Tate, B. K.; Wyss, C. M.; Bacsa, J.; Kluge, K.; Gelbaum, L.; Sadighi, J. P. *Chem. Sci.* **2013**, 4, 3068.
- (257) Tate, B. K.; Nguyen, J. T.; Bacsa, J.; Sadighi, J. P. *Chem. - A Eur. J.* **2015**, 21, 10160.
- (258) Collins, K. D.; Glorius, F. *Nat. Chem.* **2013**, 5, 597.
- (259) Jordan, A. J.; Lalic, G.; Sadighi, J. P. *Chem. Rev.* **2016**, 116, 8318.
- (260) Partyka, D. V.; Deligonul, N. *Inorg. Chem.* **2009**, 48, 9463.
- (261) de Fremont, P.; Scott, N. M.; Stevens, E. D.; Ramnial, T.; Lightbody, O. C.; Macdonald, C. L. B.; Clyburne, J. A. C.; Abernethy, C. D.; Nolan, S. P. *Organometallics* **2005**, 24,

6301.

- (262) Ohishi, T.; Shiotani, Y.; Yamashita, M. *J. Org. Chem.* **1994**, *59*, 250.
- (263) Sheldrick, G. M. *Acta Crystallogr. Sect. A* **2008**, *64*, 112.
- (264) Müller, P. *Crystallogr. Rev.* **2009**, *15*, 57.
- (265) Abley, P.; McQuillin, F. J. *J. Chem. Soc. D Chem. Commun.* **1969**, No. 24, 1503.
- (266) Schleyer, D.; Niessen, H. G.; Bargon, J. *New J. Chem.* **2001**, *25*, 423.
- (267) Furukawa, S.; Komatsu, T. *ACS Catal.* **2016**, *6*, 2121.
- (268) Tani, K.; Iseki, A.; Yamagata, T. *Chem. Commun.* **1999**, *37*, 1821.
- (269) Shirakawa, E.; Otsuka, H.; Hayashi, T. *Chem. Commun.* **2005**, *88*, 5885.
- (270) Luo, F.; Pan, C.; Wang, W.; Ye, Z.; Cheng, J. *Tetrahedron* **2010**, *66*, 1399.
- (271) Fuchs, M.; Fürstner, A. *Angew. Chemie Int. Ed.* **2015**, *54*, 3978.
- (272) Karunananda, M. K.; Mankad, N. P. *Organometallics* **2017**, *36*, 220.
- (273) Leutzsch, M.; Wolf, L. M.; Gupta, P.; Fuchs, M.; Thiel, W.; Farès, C.; Fürstner, A. *Angew. Chemie Int. Ed.* **2015**, *54*, 12431.
- (274) Crabtree, R. H.; Siegbahn, P. E. M.; Eisenstein, O.; Rheingold, A. L.; Koetzle, T. F. *Acc. Chem. Res.* **1996**, *29*, 348.
- (275) Custelcean, R.; Jackson, J. E. *Chem. Rev.* **2001**, *101*, 1963.
- (276) Levina, V. A.; Rossin, A.; Belkova, N. V.; Chierotti, M. R.; Epstein, L. M.; Filippov, O. A.; Gobetto, R.; Gonsalvi, L.; Lledós, A.; Shubina, E. S.; Zanobini, F.; Peruzzini, M. *Angew. Chemie Int. Ed.* **2011**, *50*, 1367.
- (277) Mankad, N. P.; Laitar, D. S.; Sadighi, J. P. *Organometallics* **2004**, *23*, 3369.

- (278) Goj, L. A.; Blue, E. D.; Munro-Leighton, C.; Gunnoe, T. B.; Petersen, J. L. *Inorg. Chem.* **2005**, *44*, 8647.
- (279) Laitar, D. S.; Tsui, E. Y.; Sadighi, J. P. *Organometallics* **2006**, *25*, 2405.
- (280) Estes, D. P.; Vannucci, A. K.; Hall, A. R.; Lichtenberger, D. L.; Norton, J. R. *Organometallics* **2011**, *30*, 3444.
- (281) Kwon, D.-H.; Proctor, M.; Mendoza, S.; Uyeda, C.; Ess, D. H. *ACS Catal.* **2017**, 4796.
- (282) Carey, F. A.; Sundberg, R. J. *Advanced Organic Chemistry: Part A: Structure and Mechanisms - Francis A. Carey, Richard J. Sundberg - Google Books*, 5th Edition.; Springer: New York, 2007.
- (283) Jordan, A. J.; Wyss, C. M.; Bacsá, J.; Sadighi, J. P. *Organometallics* **2016**, *35*, 613.
- (284) Frey, G. D.; Donnadieu, B.; Soleilhavoup, M.; Bertrand, G. *Chem. - An Asian J.* **2011**, *6*, 402.
- (285) Krishnan, R.; Binkley, J. S.; Seeger, R.; Pople, J. A. *J. Chem. Phys.* **1980**, *72*, 650.
- (286) Clark, T.; Chandrasekhar, J.; Spitznagel, G. W.; Schleyer, P. V. R. *J. Comput. Chem.* **1983**, *4*, 294.
- (287) Jordan, A. J.; Lalic, G.; Sadighi, J. P. *Chem. Rev.* **2016**, *116*, 8318.
- (288) Field, L. D.; Lawrenz, E. T.; Shaw, W. J.; Turner, P. *Inorg. Chem.* **2000**, *39*, 5632.
- (289) Maity, A.; Teets, T. S. *Chem. Rev.* **2016**, *116*, 8873.
- (290) Wang, L.; Sun, H.; Zuo, Z.; Li, X.; Xu, W.; Langer, R.; Fuhr, O.; Fenske, D. *Eur. J. Inorg. Chem.* **2016**, 2016, 5205.
- (291) Eberhardt, N. A.; Guan, H. *Chem. Rev.* **2016**, *116*, 8373.

- (292) Wiedner, E. S.; Chambers, M. B.; Pitman, C. L.; Bullock, R. M.; Miller, A. J. M.; Appel, A. M. *Chem. Rev.* **2016**, *116*, 8655.
- (293) Norton, J. R.; Sowa, J. *Chem. Rev.* **2016**, *116*, 8315.
- (294) Tsuji, Y.; Fujihara, T.; Iwasawa, N.; Cazin, C. S. J.; Nolan, S. P.; Pfluger, F.; Fauvarque, J.-F.; Mostafa, A. E.; Luo, J.; Yamada, T. *Chem. Commun.* **2012**, *48*, 9956.
- (295) Aresta, M. In *Carbon Dioxide as Chemical Feedstock*; Wiley-VCH Verlag GmbH & Co. KGaA: Weinheim, Germany; pp 1–13.
- (296) Olah, G. A.; Goepfert, A.; Prakash, G. K. S. *J. Org. Chem.* **2009**, *74*, 487.
- (297) Ravishankara, A. R.; Rudich, Y.; Pyle, J. A. *Chem. Rev.* **2015**, *115*, 3679.
- (298) Zall, C. M.; Linehan, J. C.; Appel, A. M. *ACS Catal.* **2015**, *5*, 5301.
- (299) Mankad, N. P.; Gray, T. G.; Laitar, D. S.; Sadighi, J. P. *Organometallics* **2004**, *23*, 1191.
- (300) Fujihara, T.; Xu, T.; Semba, K.; Terao, J.; Tsuji, Y. *Angew. Chemie Int. Ed.* **2011**, *50*, 523.
- (301) Li, S.; Yuan, W.; Ma, S. *Angew. Chemie Int. Ed.* **2011**, *50*, 2578.
- (302) Wang, X.; Nakajima, M.; Martin, R. *J. Am. Chem. Soc.* **2015**, *137*, 8924.

Appendix

Supplementary Data

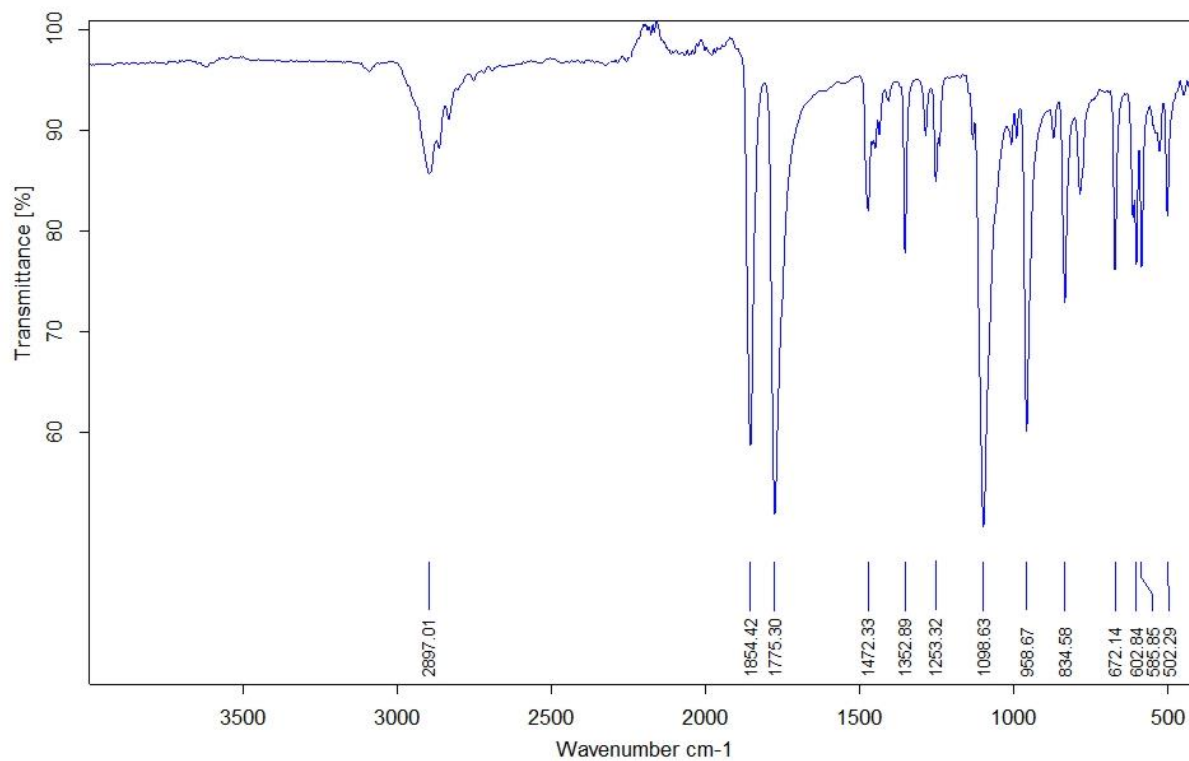


Figure A1: IR Spectrum of [K(18-crown-6)₂][Fp]

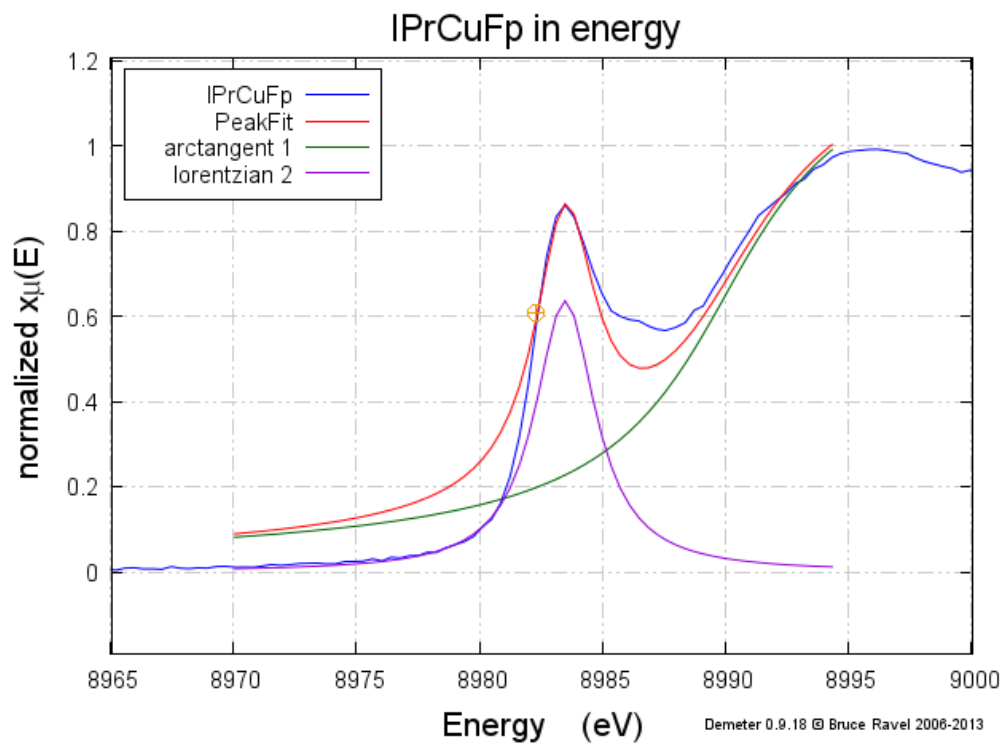


Figure A2: Deconvoluted Cu K-edge spectrum for (IPr)CuFp

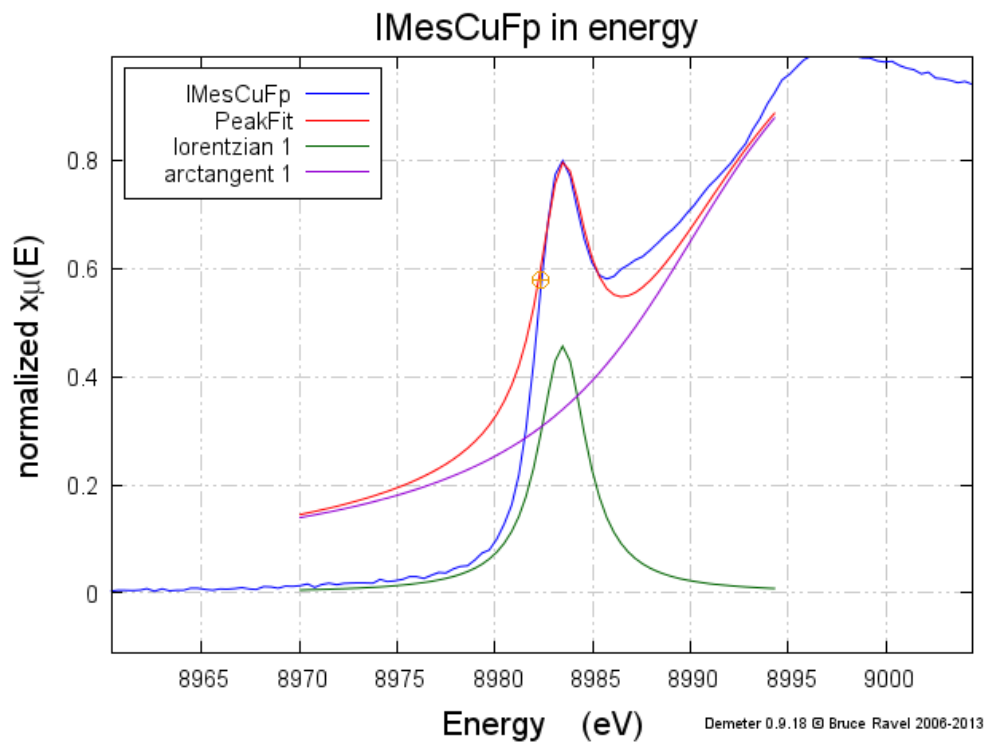


Figure A3: Deconvoluted Cu K-edge spectrum for (IMes)CuFp

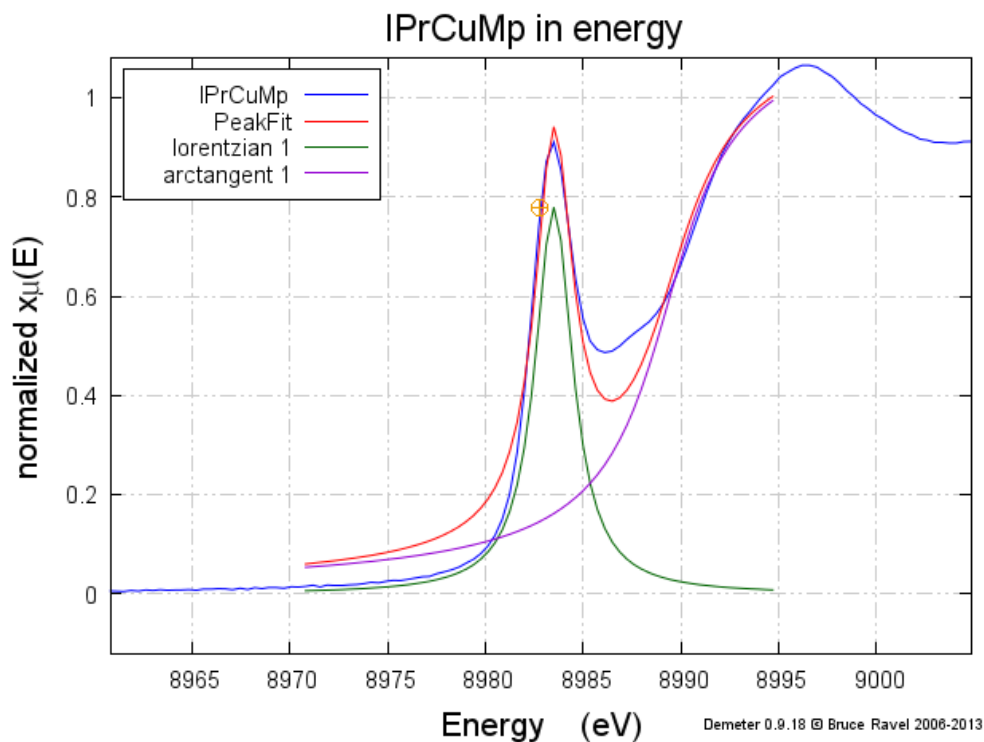


Figure A4: Deconvoluted Cu K-edge spectrum for (IPr)CuMp

Table A1: Deconvolution parameters used for XAS spectra analysis using Athena software

Complex	Fit range	Arctangent			Lorentzian			
		Height	Center	Width	Height	E0	σ	y
(IPr)CuFp	(-12)-12	1.30	8990.0	4.0	3.00	8983.48	3.0	0.5
(IMes)CuFp	(-12)-12	1.30	8990.0	7.0	2.15	8983.46	3.0	0.5
(IPr)CuMp	(-12)-12	1.17	8989.3	2.6	1.17	8983.50	2.4	0.5
(IMes)CuCl	(-12)-12	1.20	8990.0	3.5	3.70	8983.86	3.4	0.5
(IPr)CuI	(-12)-12	1.20	8990.0	3.5	4.00	8983.84	3.0	0.5
(IPr)CuCl	(-12)-12	1.10	8990.0	3.6	3.50	8983.62	3.3	0.5

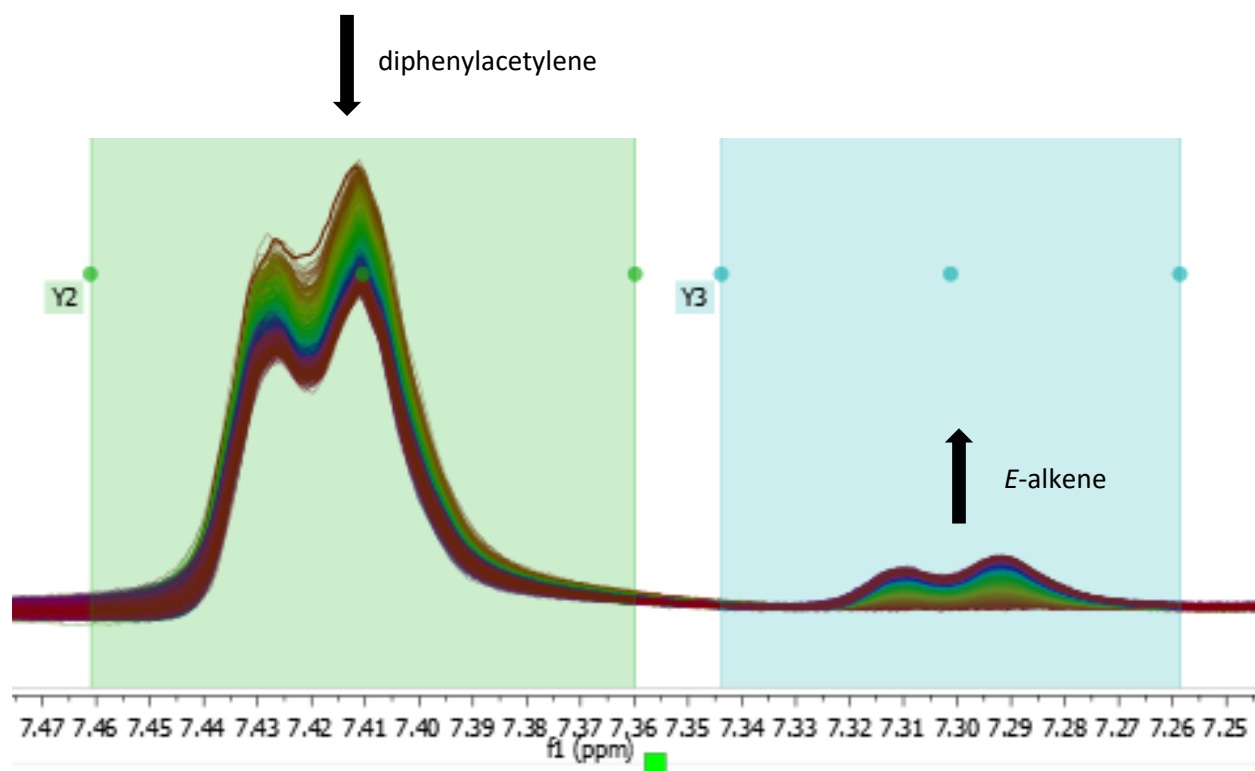


Figure A5: Sample stacked plot for the kinetic run for the hydrogenation of diphenylacetylene by (IMes)AgRp: Y2 = Disappearance of monitored peak for diphenylacetylene and Y3 = Appearance of the monitored peak for *E*-stilbene.

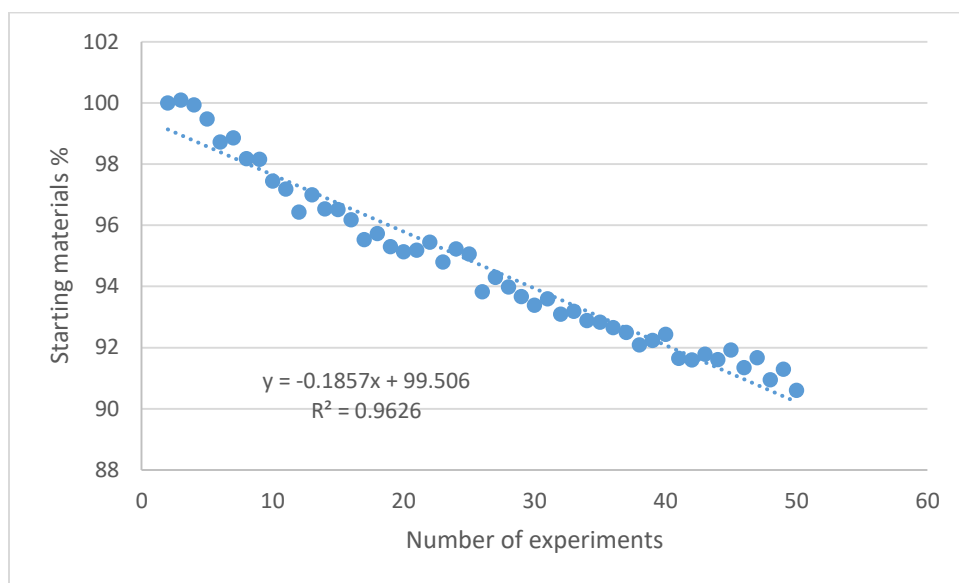


Figure A6: Sample concentration vs time plot for the kinetic run for the hydrogenation of Diphenylacetylene by (IMes)AgRp: Time per one experiment = 30 s.

Copyright Permissions

7/4/2017

Experimental determination of redox cooperativity and electronic structures in catalytically active Cu–Fe and Zn–Fe heterobimetallic complexes

M. K. Karunananda, F. X. Vázquez, E. E. Alp, W. Bi, S. Chattopadhyay, T. Shibata and N. P. Mankad, *Dalton Trans.*, 2014, **43**, 13661

DOI: 10.1039/C4DT01841A

If you are not the author of this article and you wish to reproduce material from it in a third party non-RSC publication you must [formally request permission](#) using RightsLink. Go to our [Instructions for using RightsLink page](#) for details.

Authors contributing to RSC publications (journal articles, books or book chapters) do not need to formally request permission to reproduce material contained in this article provided that the correct acknowledgement is given with the reproduced material.

Reproduced material should be attributed as follows:

- For reproduction of material from NJC:
Reproduced from Ref. XX with permission from the Centre National de la Recherche Scientifique (CNRS) and The Royal Society of Chemistry.
- For reproduction of material from PCCP:
Reproduced from Ref. XX with permission from the PCCP Owner Societies.
- For reproduction of material from PPS:
Reproduced from Ref. XX with permission from the European Society for Photobiology, the European Photochemistry Association, and The Royal Society of Chemistry.
- For reproduction of material from all other RSC journals and books:
Reproduced from Ref. XX with permission from The Royal Society of Chemistry.

If the material has been adapted instead of reproduced from the original RSC publication "Reproduced from" can be substituted with "Adapted from".

In all cases the Ref. XX is the XXth reference in the list of references.

If you are the author of this article you do not need to formally request permission to reproduce figures, diagrams etc. contained in this article in third party publications or in a thesis or dissertation provided that the correct acknowledgement is given with the reproduced material.

Reproduced material should be attributed as follows:

- For reproduction of material from NJC:
[Original citation] - Reproduced by permission of The Royal Society of Chemistry (RSC) on behalf of the Centre National de la Recherche Scientifique (CNRS) and the RSC
- For reproduction of material from PCCP:
[Original citation] - Reproduced by permission of the PCCP Owner Societies
- For reproduction of material from PPS:
[Original citation] - Reproduced by permission of The Royal Society of Chemistry (RSC) on behalf of the European Society for Photobiology, the European Photochemistry Association, and RSC
- For reproduction of material from all other RSC journals:
[Original citation] - Reproduced by permission of The Royal Society of Chemistry

If you are the author of this article you still need to obtain permission to reproduce the whole article in a third party publication with the exception of reproduction of the whole article in a thesis or dissertation.

Information about reproducing material from RSC articles with different licences is available on our [Permission Requests page](#).

<http://pubs.rsc.org/en/content/articlelanding/2014/dt/c4dt01841a#!divAbstract>

7/4/2017



RightsLink®

Home

Create Account

Help



ACS Publications
Most Trusted. Most Cited. Most Read.

Title: Experimental and Computational Characterization of the Transition State for C-X Bimetallic Oxidative Addition at a Cu-Fe Reaction Center

Author: Malkanthi K. Karunananda, Sean R. Parmelee, Greyson W. Waldhart, et al

Publication: Organometallics

Publisher: American Chemical Society

Date: Aug 1, 2015

Copyright © 2015, American Chemical Society

LOGIN

If you're a [copyright.com](#) user, you can login to RightsLink using your [copyright.com](#) credentials. Already a [RightsLink](#) user or want to [learn more?](#)

PERMISSION/LICENSE IS GRANTED FOR YOUR ORDER AT NO CHARGE

This type of permission/license, instead of the standard Terms & Conditions, is sent to you because no fee is being charged for your order. Please note the following:



- Permission is granted for your request in both print and electronic formats, and translations.
- If figures and/or tables were requested, they may be adapted or used in part.
- Please print this page for your records and send a copy of it to your publisher/graduate school.
- Appropriate credit for the requested material should be given as follows: "Reprinted (adapted) with permission from (COMPLETE REFERENCE CITATION). Copyright (YEAR) American Chemical Society." Insert appropriate information in place of the capitalized words.
- One-time permission is granted only for the use specified in your request. No additional uses are granted (such as derivative works or other editions). For any other uses, please submit a new request.


BACK


CLOSE WINDOW

Copyright © 2017 Copyright Clearance Center, Inc. All Rights Reserved. [Privacy statement](#). [Terms and Conditions](#). Comments? We would like to hear from you. E-mail us at customercare@copyright.com

7/4/2017



[Home](#) [Create Account](#) [Help](#) 

**ACS Publications**
Most Trusted. Most Cited. Most Read.

Title: Synthesis and Characterization of Heterobimetallic Complexes with Direct Cu-M Bonds (M = Cr, Mn, Co, Mo, Ru, W) Supported by N-Heterocyclic Carbene Ligands: A Toolkit for Catalytic Reaction Discovery
Author: Suparna Banerjee, Malkanthi K. Karunananda, Sharareh Bagherzadeh, et al
Publication: Inorganic Chemistry
Publisher: American Chemical Society
Date: Oct 1, 2014
Copyright © 2014, American Chemical Society

[LOGIN](#)
If you're a [copyright.com](#) user, you can login to RightsLink using your copyright.com credentials. Already a [RightsLink](#) user or want to [learn more?](#)

PERMISSION/LICENSE IS GRANTED FOR YOUR ORDER AT NO CHARGE
This type of permission/license, instead of the standard Terms & Conditions, is sent to you because no fee is being charged for your order. Please note the following:

- Permission is granted for your request in both print and electronic formats, and translations.
- If figures and/or tables were requested, they may be adapted or used in part.
- Please print this page for your records and send a copy of it to your publisher/graduate school.
- Appropriate credit for the requested material should be given as follows: "Reprinted (adapted) with permission from (COMPLETE REFERENCE CITATION). Copyright (YEAR) American Chemical Society." Insert appropriate information in place of the capitalized words.
- One-time permission is granted only for the use specified in your request. No additional uses are granted (such as derivative works or other editions). For any other uses, please submit a new request.

[BACK](#) [CLOSE WINDOW](#)

Copyright © 2017 Copyright Clearance Center, Inc. All Rights Reserved. [Privacy statement](#). [Terms and Conditions](#). Comments? We would like to hear from you. E-mail us at customer@copyright.com



RightsLink®

[Home](#)
[Create Account](#)
[Help](#)


ACS Publications
Most Trusted. Most Cited. Most Read.

Title: E-Selective Semi-Hydrogenation of Alkynes by Heterobimetallic Catalysis
Author: Malkanthi K. Karunananda, Neal P. Mankad
Publication: Journal of the American Chemical Society
Publisher: American Chemical Society
Date: Nov 1, 2015
Copyright © 2015, American Chemical Society

[LOGIN](#)

If you're a [copyright.com](#) user, you can login to RightsLink using your copyright.com credentials. Already a RightsLink user or want to [learn more?](#)

PERMISSION/LICENSE IS GRANTED FOR YOUR ORDER AT NO CHARGE

This type of permission/license, instead of the standard Terms & Conditions, is sent to you because no fee is being charged for your order. Please note the following:

- Permission is granted for your request in both print and electronic formats, and translations.
- If figures and/or tables were requested, they may be adapted or used in part.
- Please print this page for your records and send a copy of it to your publisher/graduate school.
- Appropriate credit for the requested material should be given as follows: "Reprinted (adapted) with permission from (COMPLETE REFERENCE CITATION). Copyright (YEAR) American Chemical Society." Insert appropriate information in place of the capitalized words.
- One-time permission is granted only for the use specified in your request. No additional uses are granted (such as derivative works or other editions). For any other uses, please submit a new request.

[BACK](#)
[CLOSE WINDOW](#)

Copyright © 2017 Copyright Clearance Center, Inc. All Rights Reserved. [Privacy statement](#). [Terms and Conditions](#). Comments? We would like to hear from you. E-mail us at customercare@copyright.com



RightsLink®

[Home](#)
[Create Account](#)
[Help](#)


ACS Publications
Most Trusted. Most Cited. Most Read.

Title: Heterobimetallic H₂ Addition and Alkene/Alkane Elimination Reactions Related to the Mechanism of E-Selective Alkyne Semihydrogenation

Author: Malkanthi K. Karunananda, Neal P. Mankad

Publication: Organometallics

Publisher: American Chemical Society

Date: Jan 1, 2017

Copyright © 2017, American Chemical Society

[LOGIN](#)

If you're a [copyright.com](#) user, you can login to RightsLink using your copyright.com credentials. Already a RightsLink user or want to [learn more?](#)

PERMISSION/LICENSE IS GRANTED FOR YOUR ORDER AT NO CHARGE

This type of permission/license, instead of the standard Terms & Conditions, is sent to you because no fee is being charged for your order. Please note the following:

- Permission is granted for your request in both print and electronic formats, and translations.
- If figures and/or tables were requested, they may be adapted or used in part.
- Please print this page for your records and send a copy of it to your publisher/graduate school.
- Appropriate credit for the requested material should be given as follows: "Reprinted (adapted) with permission from (COMPLETE REFERENCE CITATION). Copyright (YEAR) American Chemical Society." Insert appropriate information in place of the capitalized words.
- One-time permission is granted only for the use specified in your request. No additional uses are granted (such as derivative works or other editions). For any other uses, please submit a new request.

[BACK](#)
[CLOSE WINDOW](#)

Copyright © 2017 [Copyright Clearance Center, Inc.](#) All Rights Reserved. [Privacy statement](#). [Terms and Conditions](#). Comments? We would like to hear from you. E-mail us at customercare@copyright.com

8/8/2017



RightsLink®

Home

Create Account

Help



Title: Cooperative Strategies for Catalytic Hydrogenation of Unsaturated Hydrocarbons
Author: Malkanthi K. Karunananda, Neal R. Mankad
Publication: ACS Catalysis
Publisher: American Chemical Society
Date: Aug 1, 2017
Copyright © 2017, American Chemical Society

LOGIN

If you're a [copyright.com](#) user, you can login to RightsLink using your [copyright.com](#) credentials. Already a [RightsLink](#) user or want to [learn more](#)?

PERMISSION/LICENSE IS GRANTED FOR YOUR ORDER AT NO CHARGE

This type of permission/license, instead of the standard Terms & Conditions, is sent to you because no fee is being charged for your order. Please note the following:

- Permission is granted for your request in both print and electronic formats, and translations.
- If figures and/or tables were requested, they may be adapted or used in part.
- Please print this page for your records and send a copy of it to your publisher/graduate school.
- Appropriate credit for the requested material should be given as follows: "Reprinted (adapted) with permission from (COMPLETE REFERENCE CITATION). Copyright (YEAR) American Chemical Society." Insert appropriate information in place of the capitalized words.
- One-time permission is granted only for the use specified in your request. No additional uses are granted (such as derivative works or other editions). For any other uses, please submit a new request.

BACK

CLOSE WINDOW

Copyright © 2017 [Copyright Clearance Center, Inc.](#) All Rights Reserved. [Privacy statement.](#) [Terms and Conditions.](#) Comments? We would like to hear from you. E-mail us at customer@copyright.com

8/8/2017

Figure 2: Reproduced with permission from Jayarathne, U.; Mazzacano, T. J.; Bagherzadeh, S.; Mankad, N. P. *Organometallics* **2013**, 32, 3986. © 2013 American Chemical Society.



[Home](#) [Create Account](#) [Help](#)



Title: Heterobimetallic Complexes with Polar, Unsupported Cu-Fe and Zn-Fe Bonds Stabilized by N-Heterocyclic Carbenes

Author: Upul Jayarathne, Thomas J. Mazzacano, Sharareh Bagherzadeh, et al

Publication: *Organometallics*

Publisher: American Chemical Society

Date: Jul 1, 2013

Copyright © 2013, American Chemical Society

LOGIN

If you're a copyright.com user, you can login to RightsLink using your copyright.com credentials. Already a RightsLink user or want to learn more?

PERMISSION/LICENSE IS GRANTED FOR YOUR ORDER AT NO CHARGE

This type of permission/license, instead of the standard Terms & Conditions, is sent to you because no fee is being charged for your order. Please note the following:

- Permission is granted for your request in both print and electronic formats, and translations.
- If figures and/or tables were requested, they may be adapted or used in part.
- Please print this page for your records and send a copy of it to your publisher/graduate school.
- Appropriate credit for the requested material should be given as follows: "Reprinted (adapted) with permission from (COMPLETE REFERENCE CITATION). Copyright (YEAR) American Chemical Society." Insert appropriate information in place of the capitalized words.
- One-time permission is granted only for the use specified in your request. No additional uses are granted (such as derivative works or other editions). For any other uses, please submit a new request.

If credit is given to another source for the material you requested, permission must be obtained from that source.

[BACK](#)

[CLOSE WINDOW](#)

Copyright © 2017 Copyright Clearance Center, Inc. All Rights Reserved. [Privacy statement](#). [Terms and Conditions](#).
Comments? We would like to hear from you. E-mail us at customer@copyright.com

VITA

NAME: Malkanthi K. Karunananda

EDUCATION: Ph. D., Chemistry, University of Illinois at Chicago, IL, 2017.
B. Sc., Chemistry, University of Kelaniya, Sri Lanka, 2010.

TEACHING: *Teaching Assistant*, Department of Chemistry, University of Illinois at Chicago, Chicago, IL, 2012-2015.
Temporary Lecturer, University of Kelaniya, Sri Lanka, 2011-2012.
Temporary Demonstrator, University of Kelaniya, Sri Lanka, 2010-2011.

HONORS: *Benjamin B. Freud Fellowship*, University of Illinois at Chicago, 2016-2017.

PROFESSIONAL MEMEBERSHIPS: American Chemical Society

PUBLICATIONS: "Cooperative Strategies for Catalytic Hydrogenation of Unsaturated Hydrocarbons" Karunananda, M. K.; Mankad, N. P. *ACS catal.* **2017**. *Just Accepted Manuscript*, DOI: 10.1021/acscatal.7b02203.
"Heterobimetallic H₂ Addition and Alkene/Alkane Elimination Reactions Related to the Mechanism of *E*-selective Alkyne Semihydrogenation" Karunananda, M. K.; Mankad, N. P. *Organometallics* **2017**, 36, 220-227.
"*E*-selective Semi-Hydrogenation of Alkynes by Heterobimetallic Catalysis" Karunananda, M. K.; Mankad, N. P. *J. Am. Chem. Soc.* **2015**, 137, 14598-14601.
"Experimental and Computational Characterization of the Transition State for C-X Bimetallic Oxidative Addition at a Cu-Fe Reaction Center" Karunananda, M. K.; Parmelee, S. R.; Waldhart, G. W.; Mankad, N. P. *Organometallics*. **2015**, 34, 3857-3864.

"Synthesis and Characterization of Heterobimetallic Complexes with Direct Cu-M Bonds, (M = Cr, Mn, Co, Mo, Ru, W) Supported by *N*-Heterocyclic Carbene Ligands: A Toolkit for Catalytic Reaction Discovery" Banerjee, S.; Karunananda, M. K. (co-first author); Bagherzadeh, S.; Jayarathne, U.; Parmelee, S. R.; Waldhart, G. W.; Mankad, N. P. *Inorg. Chem.* **2014**, 53, 11307-11315.

"Experimental Determination of Redox Cooperativity and Electronic Structure in Catalytically Active Cu-Fe and Zn-Fe Heterobimetallic Complexes" Karunananda, M. K.; Vázquez, F. X.; Alp, E. E.; Bi, W.; Chattopadhyay, S.; Shibata, T.; Mankad, N. P. *Dalton Trans.* **2014**, 43, 13661-13671.

ORAL PRESENTATIONS:

"Mechanistic Insights into *E*-selective Semi-Hydrogenation of Alkynes by Heterobimetallic Catalysis" *Gordon Research Seminar-Inorganic Reaction Mechanisms*, Galveston, TX, **2017**. (Invited)

"Structural and Reactivity Trends of Heterobimetallic Complexes Featuring Direct Cu-M bonds (M=Cr, Mn, Co, Mo, Ru, W, Re)." *249th American Chemical Society National Meeting & Exposition*: Denver, CO, **2015**.

"Combined XANES, Mössbauer, and DFT Analysis of Cu-Fe and Zn-Fe Heterobimetallic Complexes Featuring Polar Metal-Metal Bonds." *247th American Chemical Society National Meeting & Exposition*, Dallas, TX, **2014**.

POSTER PRESENTATIONS:

"Mechanistic Insights into *E*-selective Semi-Hydrogenation of Alkynes by Heterobimetallic Catalysis" *Gordon Research Conference-Inorganic Reaction Mechanisms*, Galveston, TX, **2017**.

"Mössbauer and XANES Analysis of Catalytically Active Cu-Fe and Zn-Fe Heterobimetallic Complexes" *Chicago Regional Inorganic Colloquium*: University of Illinois at Chicago, Chicago, IL, **2014**.